Dynamical Simulation of a Linear Sigma Model near the Chiral Phase Transition

Dissertation
zur Erlangung des Doktorgrades
der Naturwissenschaften

vorgelegt beim Fachbereich Physik
der Johann Wolfgang Goethe-Universität
in Frankfurt am Main

von

Christian Wesp
aus Gelnhausen

Frankfurt am Main 2015
(D30)

vom Fachbereich Physik (13)
der Johann Wolfgang Goethe - Universität
als Dissertation angenommen.

Dekan: Prof. Dr. Rene Reifarth
Gutachter: Prof. Dr. Carsten Greiner, Prof. Dr. Jürgen Schaffner-Bielich
Datum der Disputation : 13.11.2015

Contents

Chapter 1

Introduction and Motivation

> Die Physik erklärt die Geheimnisse der Natur nicht, sie führt sie auf tieferliegende Geheimnisse zurück.
>
> Carl Friedrich von Weizsäcker

The topic of this thesis is the investigation of the chiral phase transition of nuclear matter, andnon-equilibrium effects within this transition and the search for its potential signatures. Most of the questions are explored with the linear σ-model which is theoretical and effective model, implemented in a numerical simulation.

Chiral symmetry is a conjectured symmetry within quantum chromodynamics (QCD), a fundamental theory of nuclear matter and elementary particles. QCD is part of a bigger theory, called the standard model of physics. It describes all known elementary particles, their properties and interactions between them, covering three of four fundamental forces of nature: electromagnetism, the force of electromagnetic interactions, the weak nuclear force, responsible for radioactive decay and the strong nuclear force, responsible for the stability of all known matter around us. Quantum chromodynamics covers the part of the strong nuclear force in the standard model. It describes six different quarks which make up all known compound matter in the universe. Their gauge bosons which are responsible for the interactions between the quarks are called gluons.

The theoretical prediction of sub-atomic particles inside the proton and other "elementary" particles was already given in 1964 by Gell-Mann [1] and Zweig [2]. They introduced these sub-atomic particle to describe the known "particle-zoo" with several dozen particles at time by using a set of fewer and underlying quantum numbers. The predicted quarks have been discovered in 1968 at the Stanford Linear Accelerator Center (SLAC), in which deep elastic scattering experiments have showed signatures of point-like particles inside the proton [3, 4]. The

Lagrangian of QCD reads [5–7]

$$\mathcal{L}_{\mathrm{QCD}} = \bar{\psi}_i \left(i \left(\gamma_\mu D^\mu \right)_{ij} - m\delta_{ij} \right) \psi_j - \frac{1}{4} G^a_{\mu\nu} G^{\mu\nu}_a \ , \tag{1.1}$$

with the the gauge invariant gluon field strength tensor $G^a_{\mu\nu}$

$$G^a_{\mu\nu} = \partial_\mu \mathcal{A}^a_\nu - \partial_\nu \mathcal{A}^a_\mu + g f^{abc} \mathcal{A}^b_\mu \mathcal{A}^c_\nu \ . \tag{1.2}$$

It describes six different elementary quarks with a quantum spinor ψ_i and eight gauge bosons with their color field $\mathcal{A}^a$. Quarks carry a quantum number called color, which is an intrinsic property of QCD elementary particles. It is of course not a real color but a name for three possible quantum states: red, green and blue. Gluons can carry color by swapping the color between two interacting quarks.

QCD is a complicated theory and many of their properties are only conjectured or can only be derived vaguely from approximations. The mathematical proof of several properties is in active research and even subject to the Millennium problems, worth a million dollar for the one who finds an analytic solution of QCD [8]. Exploring QCD from the theoretical side is challenging because of a mathematical fact of the theory, which also has an important physical meaning. In other theories elementary forces can exchange particles not interact with each other. An example is the electro-magnetism where photons can not interact with other photons. In QCD, interactions between quarks and gluons are described by the field strength tensor $G^a_{\mu\nu}$. A self-coupling between gluons is possible and described by $f^{abc}\mathcal{A}^b_\mu \mathcal{A}^c_\nu$. These self-interactions, which are generated by the non-Abelian Lie groups, increase the complexity of interactions between quarks and gluons enormously. Another problem arises here, because interaction of QCD are very strong, meaning the coupling strength of interactions is of order 1. Multiple scattering between gluons is as likely as a single interaction. This implies that a color exchange between two quarks by a single gluon can lead to potentially infinite interactions with other gluons by this single gluon. At high temperatures the interaction coupling becomes weaker and perturbation quantum thermodynamic (pQCD) can be used to expand interactions by the number of their intermediate interactions, introducing a cutoff at some order. This approach is an approximation and is able to describe several phenomena but does not cover many non-perturbative phenomena like chiral phase transition.

Beside the approach of finding a direct solution for QCD, its general properties can be explored with the help of symmetries. Symmetries are a very powerful tool in quantum field theory (QTF) as they confine basis properties and possible interactions within a theory. I will restrict the discussion of QCD to the topics important for this thesis, especially the chiral symmetry.

Chiral symmetry is a fundamental symmetry of the QCD Lagrangian. The total six quarks of QCD can be grouped into light and heavy flavor quarks by regarding their masses. Heavy quarks

have a mass several orders of magnitudes higher than light quarks. The masses of light quarks can be approximated with

$$m_u = m_d = m_s \approx 0 \ , \tag{1.3}$$

which is called the chiral limit. The already introduced QCD Lagrangian (1.1) is reformulated for massless quarks

$$\mathcal{L}_{\mathrm{QCD}} = \sum_{i=u,d,s} \bar{\psi}_i \gamma_\mu D^\mu \psi_i - \frac{1}{2} \mathrm{Tr}_c \left(G^a_{\mu\nu} G^{\mu\nu}_a \right) \ . \tag{1.4}$$

Left- and right-handed quark projectors are introduced by

$$q_{R/L} = \frac{1}{2} \left(1 \pm \gamma_5 \right) \psi \tag{1.5}$$

and can be used to decompose the above Lagrangian in a left- and right-handed part

$$\mathcal{L}_{\mathrm{QCD}} = \sum_{i=u,d,s} \left(\bar{\psi}_{i,L} \gamma_\mu D^\mu \psi_{i,L} + \bar{\psi}_{i,R} \gamma_\mu D^\mu \psi_{i,R} \right) - \frac{1}{2} \mathrm{Tr}_c \left(G^a_{\mu\nu} G^{\mu\nu}_a \right) \ . \tag{1.6}$$

Both transformations $\psi_L \to L\psi_L$ and $\psi_R \to R\psi_R$ build a new symmetry $SU(2)_L \times SU(2)_R$. For the chiral symmetry an order parameter can be introduced, the chiral condensate. In case of an established chiral symmetry, this parameter becomes zero

$$\langle \bar{\psi}\psi \rangle = \langle 0 | \bar{\psi}_R \psi_L + \bar{\psi}_L \psi_R | 0 \rangle = 0 \tag{1.7}$$

and no vacuum expectation value for a bound state between left and right handed quarks exists. In fact, the chiral symmetry is not perfectly realized in QCD, it is broken in two ways. The quark masses are not exactly zero in the Lagrangian, so (1.3) is not given. The reason are contributions from the weak interaction by the Higgs mechanism, giving the quarks a small mass and breaking the symmetry explicitly. This explicit is quite small which justifies the symmetry as an approximated symmetry. Yet, the system find its stable vacuum state in a very asymmetric configuration, breaking the symmetry additionaly. The second mechanism is called spontaneous symmetry breaking. Figure 1.1 shows a sketch of this mechanism.

Nambu [9] and Goldstone [10] discovered that the spontaneous breakdown of a global continuous symmetry leads to massless bosonic particles, called Goldstone particles. Nambu received the Nobel-price in 2008 for his work. These Goldstone bosons can be identified in detector experiments as the three pions π^+, π^- and π^0. Their mass is not zero but approximately $m_\pi = 135$ MeV, being still very light in comparison to other hadrons (the proton is seven times heavier). In QCD the chiral symmetry is explicitly broken by the quark mass in (1.1), which is the reason for the non-zero mass of the Goldstone bosons.

The high mass of the hadrons is another phenomenon which is originated in the spontaneous breaking of the chiral symmetry. Hadrons like the proton consist of three quarks. The symmetry

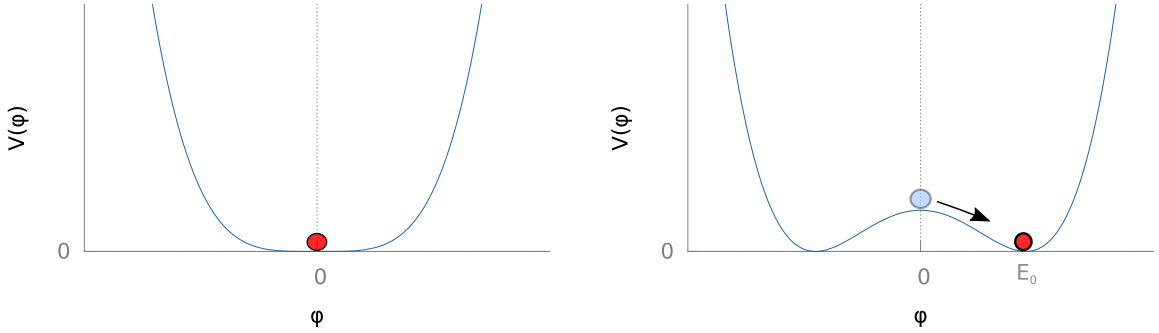

Figure 1.1: Examples of chiral potentials. Both potentials are symmetric around the center of the potential. The potential on the left has its stable expectation value at $\langle\varphi\rangle = 0$. The right potential is still symmetric around $\varphi = 0$ but has its stable expectation value at $\langle\varphi\rangle = \pm E_0$. The system will spontaneously fall into one of the two possible states $+E_0$ or $-E_0$ and break the symmetry of the system.

breaking leads to the fascinating phenomena that the proton's mass is much higher than the mass of its single constituent quarks with

$$m_q \approx 5 \text{ MeV} \quad m_P(q_d, q_u, q_u) \approx 938 \text{ MeV} \; . \tag{1.8}$$

In fact, only 1.5% of the protons mass is created by the three quarks. The remaining 98.5% of the mass is created in a dynamical, non-linear interaction between the quarks and virtual quarks and gluons given by vacuum fluctuations inside the proton. Due to the broken chiral symmetry, the chiral condensate inside protons becomes a quite large value with an estimation of [11]

$$\langle \bar{\psi}^a_R \psi^b_L \rangle = \nu \delta^{ab} \approx -\left(250 \text{ MeV}^3\right) \delta^{ab} \; . \tag{1.9}$$

Exploring the questions of nuclear physics is a big challenge for theoretical physics. Nevertheless the experimental side sees challenges of the same difficulty. Quarks and gluons can only be observed indirectly inside compound objects, the hadrons. All particles carrying a color-charge have to be caged inside a bound hadron which has to be color neutral, carrying all three colors or a color and its anti-color. This phenomena is called color-confinement [12] and creates a color-string between quarks. The binding energy of this string increases proportional to the distance between two quarks. If two quarks are separated, the string energy raises until there is enough to create a new particle-anti-particle pair of quarks, creating two separate and again confined hadrons. Therefore no free quarks should be able to exist in principle. However, Hagedorn [13] derived in his statistical model a limiting temperature. Hadrons above this temperature could melt into a plasma of quarks and gluons [14]. A similar argumentation is given by the MIT bag model [15], hadrons are described as finite region bags, containing massless quarks. Inside the bag a critical energy density an pressure can be derived which keeps the bag stable and prevents it from collapsing. Beyond this critical pressure, some change of the system state should be expected.

To study such potential of nuclear matter at hot temperatures or high densities, experiments with particle accelerators are an excellent tool. Heavy-ions like lead $^{207}_{82}\mathrm{Pb}$ are collided at the LHC with an enormous amount of energy. Within the collision, the nuclei break up and create a new type of matter which decays into a vast amount of newly created elementary particles. Studying the traces of these particles gives information about the processes at and after the collision.

The experimental challenge, beside the great technical difficulties of such a collider facility, lies in the very short lifespan of the newly created type of matter. A typically half-life of instable elementary particles and the probable quark gluon plasma lies in the order of magnitude of $10^{-15}s$, making a direct observation impossible.

Therefore several indirect probes have been proposed to indirectly observe any change of state. In 1986 it was proposed to observe the suppression of J/Ψ particles [16] as a signature of a colored plasma. This plasma should screen color charges and would inhibit color-attracting forces between charm and anti-charm quarks, decreasing the production of J/Ψ. Jet-quenching is another observable given by the energy loss of a high-energy particle propagating and interacting with a surrounding medium [17].

Such a medium would consist of quasi-free quarks and gluons, which move in a plasma of color charges. This qualitatively very unique state of nuclear matter must go through a transition from a hot and unbound state to a cold and bound state. From the theoretical side, there are two aspects of this phase transition. In QCD this transition can be split into two completely different transitions. The first transition is the confinement transition, from which the color-confined matter evolves into a state of quasi-confinement, the underlying process is the spontaneous breaking of the $Z(3)$ center symmetry of QCD [18]. The second transition is the chiral phase transition. The exact relation between these two transitions is still not completely clear, e.g. if they occur at the same temperature. One can create a phase diagram for these transition phenomena in QCD, describing the different stability regions of QCD matter and their properties. Figure 1.2 shows the sketch of such a phase diagram, dividing the phases in the $T - \mu$ plane. T declares the temperature, the chemical potential μ describes the equilibrium ratio between quarks and anti-quarks. For $T = 0$ can μ be translated to an effective quark-density.

The exploration of such a phase diagram raises different questions: In which temperature and density region exists which phase? What are the properties of the different phases? Where are the boundaries between the phases and how can the transition be described? In terms of classical theories a phase transition can be characterized by different types of orders. Possible orders are first-order, second-order or a crossover. They characterize if the phases are separated by a sharp transition at a given point, like the transition from hot water to steam, or by a smooth crossover where a real transition point can not be defined.

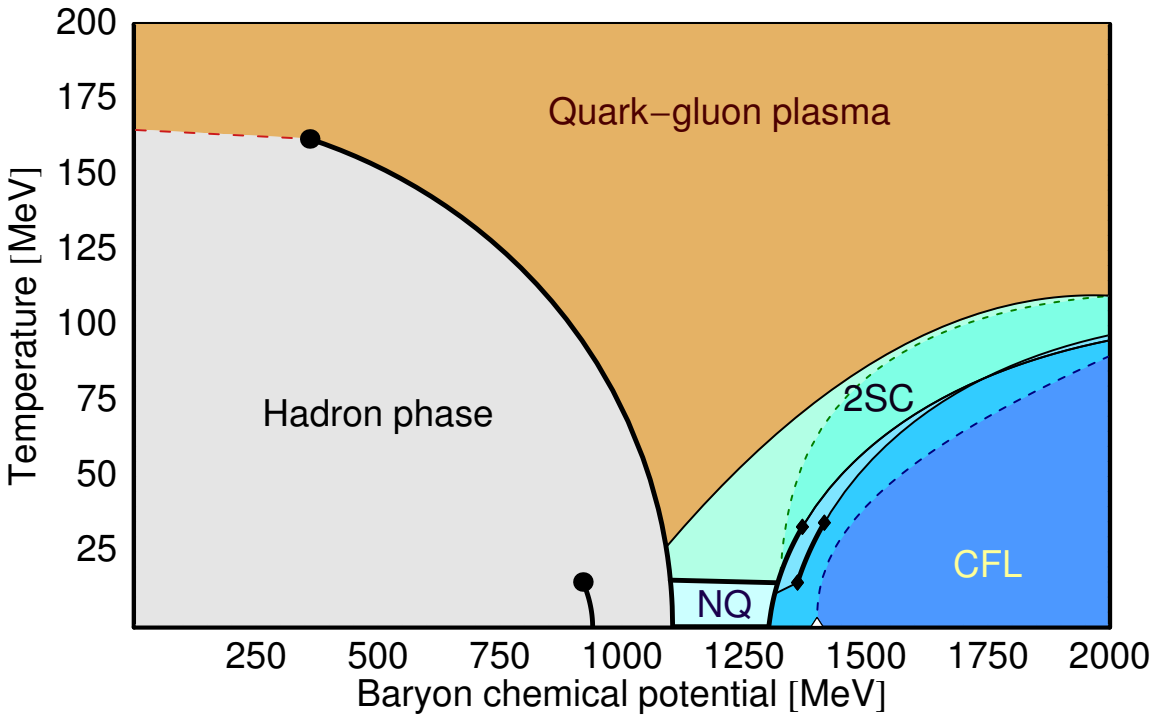

Figure 1.2: A sketch of the QCD phase diagram [19]. At low temperatures and baryon chemical potential it shows a phase of stable hadronic matter. Above a temperature and chemical potential threshold the bound matter dissociates into a plasma of quasi-free quarks and gluons.

Experiments at the SPS at CERN indicated the existence of a QGP plasma [20] but energies were too low for a consistent observation. The later Relativistic Heavy Ion Collider (RHIC) at Brookhaven National Laboratory's with energies around 200 GeV center of mass energy per nucleon was a breakthrough in search for the Quark Gluon Plasma. Within the collision a new type of medium was created, showing effects of strong collective flow and very large energy-densities [21–23]. The ATLAS, CMS and ALICE experiments at CERN confirmed these findings at even higher energies, solidifying the picture of a perfect liquid in the high-temperature phase of the transition.

What remains is the questions on the phase transition itself. To tackle this problems, different theoretical approaches have been made. Trying to solve the QCD with as little approximations as possible, the lattice quantum chromodynamics (LQCD) gained a lot of momentum in the last years. By discretizing space-time and solving the QCD action-integrals on a numerical lattice, non-perturbative observables can be calculated. However, this technique has its own difficulties, like the sign-problem at finite chemical potential [24], but for $\mu = 0$ reliable calculations can be made. These calculations can be related to high-energy collisions at the LHC at which a low μ can be assumed. For $\mu = 0$ the results show a crossover transition [25] at the quark gluon plasma. Any calculations for $\mu > 0$ are very vague and only valid for very small chemical potentials or rely on other numerical extrapolations. From the lattice QCD point of view, its is still unclear if

the crossover transition changes to some first- order second-order phase transition at some point and if these transistors end in a critical point. Some calculations even show findings against such a critical point [26].

Recent lattice calculations give an estimation for the chiral transition temperature of $T_c = (150 - 170)$ MeV [27] or $T_c = (154 \pm 9)$ MeV [28]. However, the exact results depend on the type of chosen order-parameter observable. Another disadvantage of lattice QCD is its constrain to static systems in the thermodynamical limit. Dynamical properties like fluctuations can only be derived from thermal susceptibilities, non-equilibrium or dynamical effects can not be addressed at all.

To answer such questions other approaches have to be used. Effective models have shown to be a very effective tool. Effective models have similar symmetries like QCD but have an overall more simple structure, allowing analytic solutions or efficient numerical implementations. Many ideas have been developed at such models to find other possible observables and indicators for the chiral phase transition. If the phase diagram has a critical point, the medium's fluctuations could change there, leading to an visible correlation pattern in the experimental data [29]. Such a change of fluctuations is driven by a change of the correlation length ζ in the thermal medium. Observables could be fluctuations in the multiplicity of soft pions [30], non-Gaussian fluctuations [31] or critical slowing down of different modes. The authors of [30, 31] derived a microscopic relation for fluctuations in the pion-occupation numbers n_p and $n_k$and the mean square deviations from the average occupation number v_p^2, driven by interactions between π and σ-fields

$$\langle \delta n_p \delta n_k \rangle = \langle n_p \rangle (1 + \langle n_p \rangle) \delta_{pk} + \frac{1}{m_\sigma^2} \frac{G^2}{T} \frac{v_p^2 v_k^2}{\omega_p \omega_k} \ . \tag{1.10}$$

The interesting aspect of this relation is the divergence of the correlation length at the point where the mass of the σ goes to zero $m_\sigma^2 \to 0$ which can occur at the chiral point of the chiral phase transition. Critical slowing down of equilibration processes are also discussed [32], resulting in a relation describing the dynamics of the order parameter's mass m_σ and it's correlation length ξ_{eq} within a 3D Ising model

$$\frac{\mathrm{d}}{\mathrm{d}t} m_\sigma(t) = -\Gamma(m_\sigma(t)) \left(m_\sigma(t) - \frac{1}{\xi_{\mathrm{eq}}(t)} \right) \ . \tag{1.11}$$

This study shows a possible weakening of the critical effects at the phase transition because of slowing down of critical modes which result in slower creation of fluctuations in systems with short time scales.

In experiments, several approaches have been taken to measure fluctuations of physical observables. NA49 and the still ongoing NA61 are measuring multiplicity and chemical fluctuations in heavy-ion collisions at the CERN Super Proton Synchrotron (SPS) [33–35]. First results are shown in

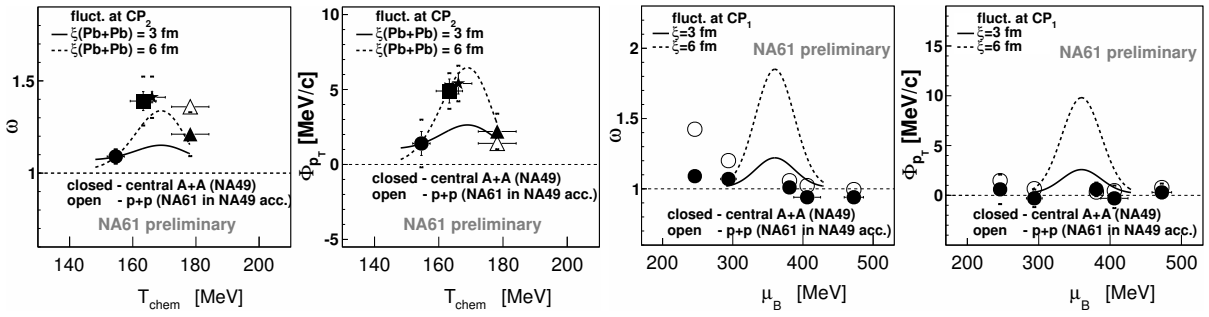

Figure 1.3: Event-by-event fluctuations of mean transverse momentum in comparison to T_{chem} (system size) and and μ_B (collision energy) for charged hadron, measured by NA49/NA61 [36] (preliminary data). Solid and dashed lines indicate estimated according to different correlation lengths.

Figure 1.3 which looks promising but still much more statistic has to be collected.

The next step in the research of the QCD phase diagram will be seen in the FAIR facility at GSI. The CBM (Compressed Baryonic Matter) experiment will have a focus on heavy-ion collisions at very high densities and therefore high chemical potential μ [37–39]. While experiments at the LHC probably create a quark-gluon plasma in the crossover region of the phase transition, experiments at GSI will try to create a plasma in the region where a phase transition of first- or second order with a critical point is assumed.

In this thesis, the linear σ-model is used to address some of the discussed questions. The model is introduced and explained in Section 2.1 and has been used widely in literature under the names σ-model or quark-meson model [40–52]. A numerical simulation is developed, employing the equations of motion of the linear σ-model. Scope of this development was the simulation of a full three-dimensional system with arbitrary initial conditions, allowing the study of non-equilibrium system evolution which could resemble the conditions within a heavy-ion collision. By comparing both equilibrium calculations and different stages of non-equilibrium systems, different effects and signatures of non-equilibrium effects can be studied. Beside the physical questions, several mathematical and numerical aspects are addressed in this thesis. Within the development of a new type of simulation, several questions and problems concerning the simulation of interactions between particles and classical fields were found. A large part of this thesis takes care of these questions and a novel framework for numerical simulations of these physical and mathematical problems is developed and is discussed.

This thesis is structured as follows: Chapter 2 introduces the linear σ-model and its basic physical properties, the numerical implementation is given in Section 2.2. In Chapter 3 equilibrium and equilibration calculations are presented within the numerical model. Thermal and chemical non-equilibrium effects and their impact are discussed in Chapater 4. This and the previous chapter include discussions on possible problems with a simple mean-field approximation of the model. In chapter 5 extensions of the numerical σ-model with chemical processes between fields and

particles are introduced and discussed. Using these extensions, calculations with non-equilibrium scenarios are presented in chapter 6, including calculations for the rapid expansion of a hot fireball. To implement interactions between particles and field in the model, new numerical methods had to be developed. These methods, their derivation and mathematical properties are discussed in Chapter 7, including example calculations to demonstrate these techniques. Chapter 8 gives detailed information about the implementation of the numerical model. A summary and conclusion is given in Chapter 9.

Chapter 2

Introduction of the Model

> Begriffe aber gewinnen in der Wissenschaft einen scharfen Sinn erst im Rahmen eines umfassenden Wissens, letztlich einer Theorie.
>
> Carl Friedrich von Weizsäcker

In this chapter, the physics of the linear σ-model and its properties is introduced. Additionally, the employed approximations for a numerical simulation are discussed.

2.1 The Linear σ-Model

The linear σ-model was first introduced by Gell-Mann and Lévy as an effective model for low energy pion-nucleon interactions [53]. For $N_f = 2$ flavors, the symmetry in QCD can be studied quite extensively because the $SU(2)_L \times SU(2)_R$ symmetry is isomorphic to $O(4)\ /\ = (N)$ models, like the σ-model [47, 54].

In this work the linear σ-model with constituent quarks is used, it describes a system of quarks, anti-quarks and chiral fields. Quarks ψ and anti-quarks $\bar{\psi}$ are defined in two light flavors $\psi = (u, d)$ and have no intrinsic mass in this model. All particles couple to the mesonic field ϕ which is decomposed in a scalar meson field σ and three pseudo-scalar mesonic fields $\boldsymbol{\pi}$. This decomposing is done due the chiral symmetry breaking feature of the model, the chiral field ϕ is expanded to a scalar component σ with a non-vanishing vacuum expectation value $\langle\sigma\rangle \neq 0$ and three pseudoscalar fields $\boldsymbol{\pi}$, which are typically set to zero in this work with $\langle\boldsymbol{\pi}\rangle = 0$

The Lagrangian with the expanded field σ and $\boldsymbol{\pi}$ reads

$$\mathcal{L} = \bar{\psi}\left[i\partial\!\!\!/ - g\left(\sigma + i\gamma_5 \boldsymbol{\pi}\cdot\boldsymbol{\tau}\right)\right]\psi + \frac{1}{2}\left(\partial_\mu\sigma\partial^\mu\sigma + \partial_\mu\boldsymbol{\pi}\partial^\mu\boldsymbol{\pi}\right) - U\left(\sigma,\boldsymbol{\pi}\right) \ . \tag{2.1}$$

The potential of the chiral fields is given by

$$U_\phi\left(\sigma,\boldsymbol{\pi}\right) = \frac{\lambda^2}{4}\left(\sigma^2 + \boldsymbol{\pi}^2 - \nu^2\right)^2 - f_\pi m_\pi^2\sigma - U_0 \tag{2.2}$$

and describes the interactions between the different fields. The potential can be split into the part of spontaneous symmetry breaking $\left(\sigma^2 + \boldsymbol{\pi}^2 - \nu^2\right)^2$ and explicit symmetry breaking $(-f_\pi m_\pi^2\sigma)$, the later term is given by the PCAC relation [55].

The expectation values can be calculated from the potential

$$\frac{\partial U(\sigma,\boldsymbol{\pi})}{\partial\sigma} \equiv 0 = -\lambda^2\left(\sigma^2 - \nu^2\right)\sigma + f_\pi m_\pi^2 + g\left\langle\bar{\psi}\psi\right\rangle \tag{2.3}$$

The scalar density $\left\langle\bar{\psi}\psi\right\rangle$ is given at one-loop level as

$$\rho_\sigma \equiv \left\langle\bar{\psi}\psi\right\rangle \sim \sigma\int\frac{\mathrm{d}^3\mathbf{p}}{(2\pi)^3}\frac{n_\psi + n_{\bar{\psi}}}{E(\mathbf{p})} \tag{2.4}$$

and is discussed in Section 2.3 in more detail. In the limit $T \to 0$ the scalar density approaches $\left\langle\bar{\psi}\psi\right\rangle \to 0$ for $\mu_B = 0$and can be neglected in (2.3) for the calculation of the vacuum expectation value.

The chiral symmetry breaking term is defined as $\nu^2 = f_\pi^2 - \frac{m_\pi^2}{\lambda^2}$, with some algebra we arrive at

$$f_\pi m_\pi^2 = \sigma\left(\lambda^2\sigma^2 - \lambda^2 f_\pi^2 - m_\pi^2\right) \ . \tag{2.5}$$

Beside two negative solutions, the physical solution of this equation is the vacuum expectation value or the pion decay constant f_π

$$\langle\sigma\rangle = f_\pi \ . \tag{2.6}$$

The vacuum mass of the scalar field is given by

$$m_\sigma^0 = 2\lambda^2 f_\pi^2 + m_\pi^2 \ . \tag{2.7}$$

Without the explicit symmetry breaking, the pion mass would be a massless Goldstone boson. In case of the explicitly broken model the mass of the pion is given by the parameter m_π.

We use the following definitions within the linear σ-model:

Model Parameter		
λ^2	$= 20$	Self-coupling parameter
g	$= 3.3$ to 5.5	Quark-sigma coupling
U_0	$= m_\pi^4/\left(4\lambda^2\right) - f_\pi^2 m_\pi^2$	Ground state
f_π	$= 93$ MeV	Pion decay constant
		/ Sigma vacuum expectation value
m_π	$= 138$ MeV	Pion mass
ν^2	$= f_\pi^2 - m_\pi^2/\lambda^2$	Field shift term

A coupling of $\lambda^2 = 20$ results in a sigma mass of about $m_\sigma \approx 600$ MeV which is a reasonable value for the resonance particle $f_0(600)$ according to the data available at the time this thesis was startet [56]. In the current PDG review [57] the σ-resonance is now labeled $f_0(500)$ and has an estimated Breit-Wigner mass of 400-550 MeV and a width of 400-700 MeV. The dominant decay channel is $\sigma \to \pi\pi$. However, the $f_0(500)$ state indeed seems to be a very broad and unstable resonance without a real particle description in terms of a naive Breit-Wigner parameterization.

The quark masses in the linear σ-model are given by the Yukawa-like coupling with the chiral fields

$$m_q^2 = g^2 \left(\sigma^2 + \boldsymbol{\pi}^2\right) \ . \tag{2.8}$$

In case of the vacuum system state $\boldsymbol{\pi} = 0$ and $\sigma = \langle\sigma_0\rangle$ the quark masses become

$$m_q \approx \begin{cases} 310 \text{ MeV for } g = 3.3 \\ 338 \text{ MeV for } g = 3.63 \\ 512 \text{ MeV for } g = 5.5 \end{cases} \tag{2.9}$$

which is consistent with constituent-quark masses for a proton, given by the particle data book

$$m_q^{\text{constituent}} \approx \frac{m_p}{3} = \frac{1007.4 \text{ MeV}}{3} \approx 335.8 \text{ MeV} \ . \tag{2.10}$$

The current-quark masses are given as [57]

$$\begin{aligned} m_u &= 2.3^{+0.7}_{-0.5} \text{ MeV} \\ m_d &= 4.8^{+0.5}_{-0.3} \text{ MeV} \end{aligned} \tag{2.11}$$

which is consistent with the assumption of massless quarks in the linear σ-model.

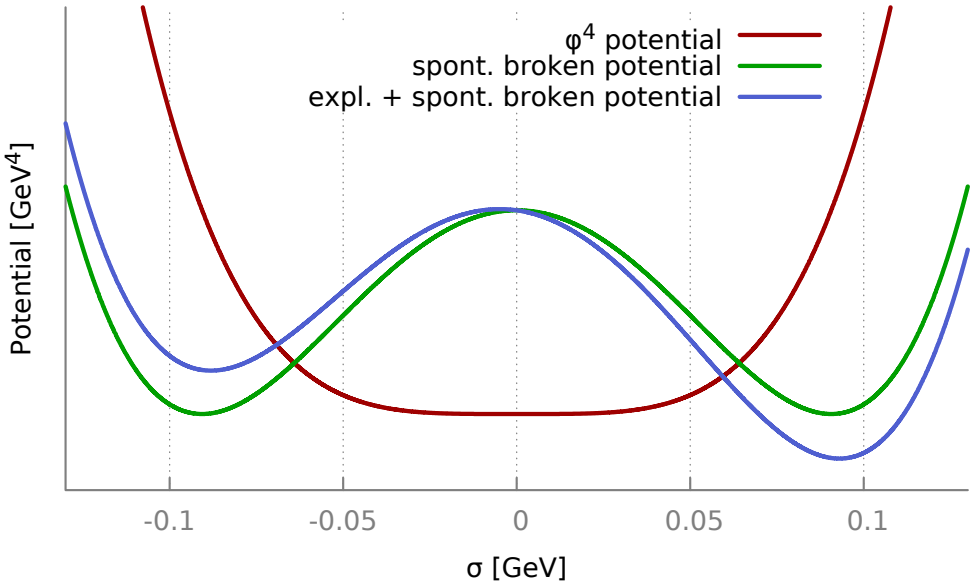

Figure 2.1: Plot of different chiral potentials for the linear sigma model. The ϕ^4 potential shows no symmetry breaking and has its only extremum at $\phi = 0$. The spontaneously broken potential, known as the famous Mexican hat potential, has still an extremum for $\phi = 0$ but its stable vacuum states are at $\phi = \pm\nu$. Symmetric and spontaneous broken potentials create massless Goldstone bosons. The potential with both spontaneously and explicit symmetry breaking is almost symmetrical but has its global minimum at $\phi = f_\pi$. The explicit symmetry breaking leads to a small but non-vanishing mass for the pions.

2.1.1 Thermal Properties

In this section the mean field dynamics of the linear sigma model is investigated.

The general grand-potential partition function for the system with the chemical potential μ reads in terms of path integrals

$$Z = \int \mathcal{D}\bar{\psi}\mathcal{D}\psi\mathcal{D}\sigma\mathcal{D}\vec{\pi}\ \exp\left(\int \mathrm{d}^4x\ \mathcal{L} + \mu\bar{\psi}\gamma_0\psi\right) \tag{2.12}$$

with the Lagrangian given in (2.1). For further calculations the thermodynamical potential is an useful quantity. By assuming the existence of a system temperature T, a volume V and the mean-field approximation for the chiral field potential $U(\sigma, \vec{\pi})$ we derive

$$\Omega(T, \mu) = -\frac{T}{V} \ln Z = U(\sigma, \vec{\pi}) + \Omega_{\bar{\psi}\psi}\ . \tag{2.13}$$

The quark potential $\Omega_{\bar{\psi}\psi}$ can be derived from the Fermi distribution with

$$\Omega_{\bar{\psi}\psi} = -d_n \int \frac{\mathrm{d}^3p}{(2\pi)^3} \left(E + T\ln\left(1 + e^{-\beta(-\mu-E)}\right) + T\ln\left(1 + e^{\beta(\mu-E)}\right)\right) \tag{2.14}$$

and the assumption of spin, color and flavor degeneracy $d_n = 2N_f N_c = 12$. The energy of the quarks is given by the dispersion relation with the effective quark mass

$$E^2 = p^2 + m^2 = p^2 + g^2 \left(\sigma^2 + \vec{\pi}^2\right) \ . \tag{2.15}$$

The thermodynamical expectation values are calculated by deriving Ω,

$$\frac{\partial \Omega}{\partial \sigma} = \lambda^2 \sigma \left(\sigma^2 + \vec{\pi}^2 - \nu^2\right) - f_\pi m_\pi^2 + g\rho_\sigma \equiv 0 \ , \tag{2.16}$$

$$\frac{\partial \Omega}{\partial \vec{\pi}} = \lambda^2 \vec{\pi} \left(\sigma^2 + \vec{\pi}^2 - \nu^2\right) + g\rho_{\vec{\pi}} \equiv 0 \ , \tag{2.17}$$

The one-loop scalar density ρ_σ or pseudo-scalar density $\rho_{\vec{\pi}}$ is calculated at mean-field level with

$$\rho_\sigma = \langle \bar{\psi}\psi \rangle = g d_n \sigma \int \frac{\mathrm{d}^3\mathbf{p}}{(2\pi)^3} \frac{f(T,\mu) + \bar{f}(T,\mu)}{E(\mathbf{p})} \ . \tag{2.18}$$

The distribution function for quarks f and anti-quarks is given by the Fermi distribution

$$f(T,\mu) = \left(1 + e^{(E-\mu)/T}\right)^{-1} \ , \tag{2.19}$$

$$\bar{f}(T,\mu) = f(T,-\mu) \ , \tag{2.20}$$

$$m_\sigma^2 = \left.\frac{\partial^2 \Omega}{\partial \sigma^2}\right|_{\sigma=\langle\sigma\rangle} \ . \tag{2.21}$$

This relation uses a mean-field approach for the mass, derived from the model's potential. Using renormalized techniques in a variational approach, similar but slightly different values are obtained [58].

2.1.2 Phase Diagram of the Linear σ-Model

To derive the phase diagram, (2.16) has to be solved self-consistently. The mean-field value $\langle\sigma\rangle$ can be defined as an order parameter for the chiral-phase transition of the linear sigma-model. By plotting the temperature dependence for the order parameter $\langle\sigma\rangle(T)$, a phase diagram of the model can be created, results are shown in Figure 2.2. The phase diagram is plotted for different field-quark coupling strengths with $g = 3.3$, $g = 3.63$ and $g = 5.5$. In all three couplings the system can be separated in a chiral broken phase with $\langle\sigma\rangle \neq 0$ at low temperatures and a chiral restored phase with $\langle\sigma\rangle \approx 0$ at high temperatures. Depending on the coupling parameter, the phase transition is from a different type or order. For $g = 3.3$ the phase diagram shows a smooth crossover transition between the broken and restored phase. A phase transition temperature can not directly be defined, but by choosing the temperate of the phase transition as the point of the inflection in the phase diagram, $T_c = 148$ MeV can be defined. For $g = 3.63$ the dependence of

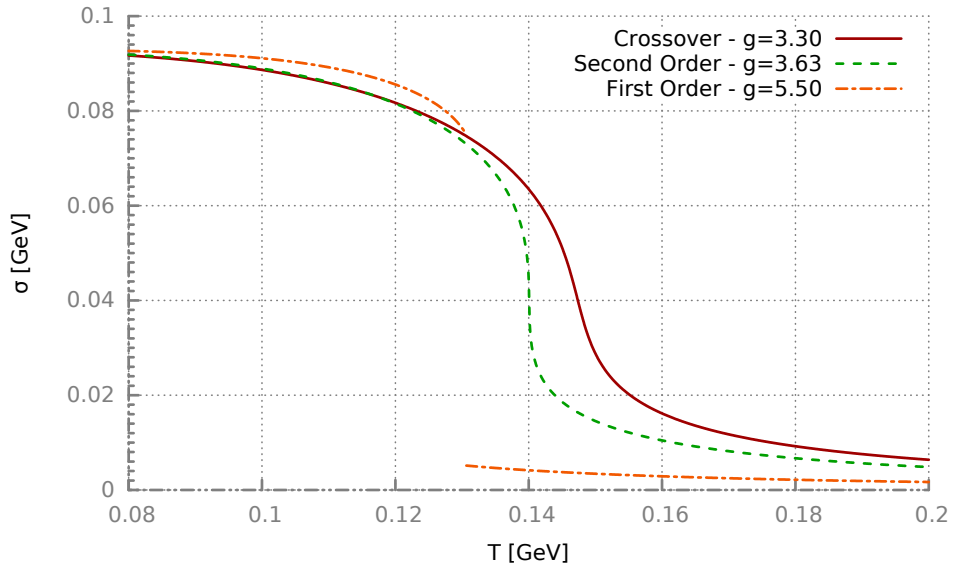

Figure 2.2: Phase-diagram of the order-parameter $\langle\sigma\rangle$ of the linear σ-model for different coupling strengths g. The temperature of the phase transition and its order is altered by changing the value of the coupling parameter. The asymptotic behavior of the order parameter for $T \to 0$ and $T \to \infty$ is independent of the coupling.

the σ mean-field shows a second-order phase transition at $T_c = 140$ MeV, at this point the slope of the order-parameter grows to infinity, resulting in a discontinuity in the first derivative of the order parameter. For the highest coupling $g = 5.5$ the phase diagram shows a first-order phase transition, as indicated by the discontinuity of the order parameter. The transition temperature is $T_c = 127$ MeV. In all cases these temperatures are too low in comparison of the suggested transition temperatures in QCD. The reason is the lack of of color-confinement in the linear σ-model. This issue can be challenged by extending the model with a Polyakov-loop mechanism [59–64]. Nevertheless, this approach only introduces a statistical confinement, fitted to lattice data, which is not directly applicable to test-particles used in this work.

Another interesting quantity is the mass of the sigma m_σ, which is defined by (2.21) and is shown in Figure 2.3 for the different couplings. The mass of the sigma is important for the whole system dynamics as it influences the interactions between quarks and the field, as shown in Chapter 5. In thermal models the mass is directly related to thermal fluctuations of the σ-field, for Gaussian fluctuations around an equilibrium value σ_{eq} one finds

$$\Pr\left(\sigma - \sigma_{\mathrm{eq}}\right) \sim \exp\left(\frac{T\left(\sigma - \sigma_{\mathrm{eq}}\right)^2}{V m_\sigma^2}\right) . \tag{2.22}$$

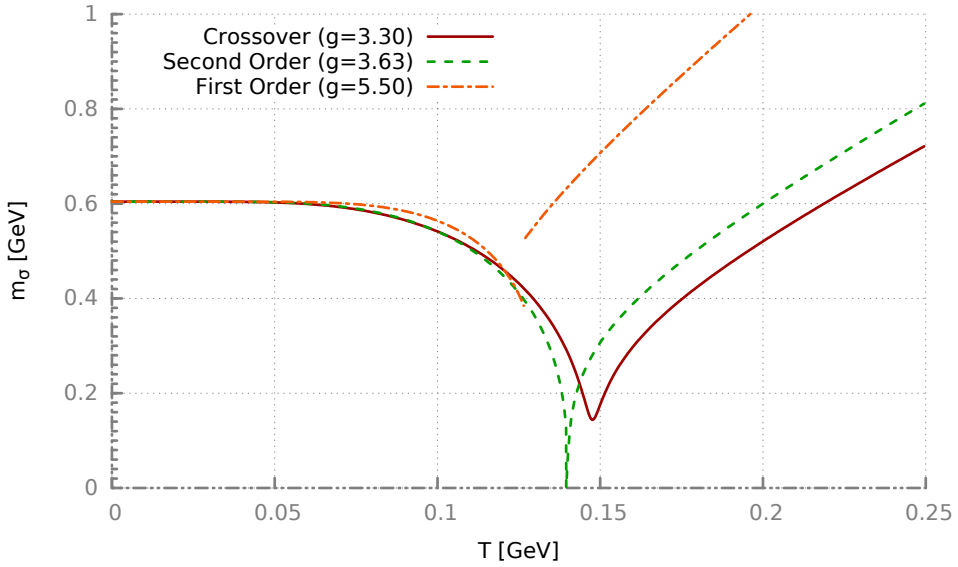

Figure 2.3: Mass of the σ-mesons in the linear σ-model in dependence to the system temperature. For the crossover transition, the mass is always defined and shows a minimum at the phase transition of the order parameter. For the second-order phase transition, the mass goes to zero at the phase transition. For the first-order transition, the mass jumps with a discontinuity.

2.2 DSLAM - Numerical Implementation of the Linear σ-Model

Thermal and equilibrium studies on the linear σ-model can be done with the fields thermodynamic potential (2.2) and thermal functions for the quark energy distributions. To investigate any non-equilibrium situations and effects, numerical models like transport simulations have to be employed. In this section the transport model DSLAM (**D**ynamical **S**imulation of a **L**inear Sigm**A** **M**odel) is introduced. It can solve the equations of motion for particles and chiral fields which are derived from the linear σ-model and can be employed to simulate different kinds of non-equilibrium situations, both thermal and chemically, to study equilibration effects, fluctuations and the dynamical behavior at and near the phase transition.

2.2.1 Physical Approximations

In principle a numerical simulation should implement the complete system's dynamics given by the Lagrange density (2.1), describing the full quantum dynamics of the equations up to all orders. A direct approach to this problem is the use of lattice field theory on a numerical grid [65–67], but this is out of scope of this work and not very suitable for non-equilibrium real-time dynamics.

In this thesis, several approximations are employed to reduce the full physical model. The quantum fields ϕ are expanded to the scalar sigma field σ and the three pion-fields $\boldsymbol{\pi}$. These fields are approximated in two steps. The first is to reduce the complex quantum fields with infinite many orders to its lowest order, the mean field. This sounds like a crude approximation but mean field approximations are a successful approach in quantum field theory [68, 69].

$$\begin{aligned} \sigma(\mathbf{x},t) &\to \langle\sigma(\mathbf{x},t)\rangle \ , \\ \boldsymbol{\pi}(\mathbf{x},t) &\to \langle\boldsymbol{\pi}(\mathbf{x},t)\rangle \ . \end{aligned} \tag{2.23}$$

In a second approach these mean fields are represented as classical, scalar fields

$$\begin{aligned} \langle\sigma(\mathbf{x},t)\rangle &\to \sigma_c(\mathbf{x},t) \ , \\ \langle\boldsymbol{\pi}(\mathbf{x},t)\rangle &\to \boldsymbol{\pi}_c(\mathbf{x},t) \ . \end{aligned} \tag{2.24}$$

which is not always the same as the mean field representation, because the mean field can still include quantum self-energy corrections. These scalar, classical fields are represented as numbers on a numerical grid. In the following the subscript c will be dropped, and all numerical fields will be assumed to be the classical mean field representation of their quantum pendants. In quantum field theory the mean field represents the average field excitation, given by the coherent state of the system. Higher-order fluctuations can be interpreted as fluctuations or additional particle-like excitations in the quantum fields. In the DSLAM model the fluctuations will be represented by kinetic energy fluctuations of the classical mean field.

In the linear σ-model quarks are represented as Dirac spinors ψ and $\bar{\psi}$ within a quantum description and spin 1/2. In this thesis quarks are represented within several approximations. From all six quark flavors only the two light quarks up and down are implemented. The model is used for temperatures $T < 200$ MeV, in this region the more massive quarks are barely excited and can be neglected. Up and down quarks are assumed to have no intrinsic mass, so their quantum numbers are assumed to be degenerated. Additionally the quantum spin is neglected and only used as a degeneracy factor in the distribution function. In a last approximation, quarks and anti-quarks are represented by uncorrelated particles, so their thermal state can be described by the Fermi-Dirac distribution

$$f^F_{\psi,\bar{\psi}}(\mathbf{p},T) = \frac{1}{\exp\left(\frac{E\mp\mu}{k_B T}\right)+1} \ . \tag{2.25}$$

In all simulation scenarios with strongly interacting particles, the quarks' distribution function is approximated with the Maxwell-Boltzmann-distribution, which is valid for high temperatures and low densities

$$f^B_{\psi,\bar{\psi}}(\mathbf{p},T) = \exp\left(-\frac{E\mp\mu}{k_B T}\right) \ . \tag{2.26}$$

Employing these approximations, particles can be described within a test-particle ansatz [70, 71] in which the phase-space dimensional distribution functions are represented by a finite sum of Dirac-delta distributions

$$f(\mathbf{r},\mathbf{p},t_0) = \frac{1}{N_{\text{test}}}\sum_i^N \delta^3(\mathbf{r}-\mathbf{r}_i(t_0))\delta^3(\mathbf{p}-\mathbf{p}_i(t_0)) \ , \tag{2.27}$$

quarks are thereby approximated to be on-shell at any moment.

An global approximation both for fields and particles is the Markov-approximation, in which all memory terms are neglected and the evolution of the system's dynamics relies only on a 'current' state of the system. In general a quantum system has a complex dependency on its own history

$$\frac{\mathrm{d}f(\mathbf{r},\mathbf{p},t)}{\mathrm{d}t} = \int_{-\infty}^{t} k(t')I\left(f(\mathbf{r},\mathbf{p},t),\mathcal{L},t\right)\mathrm{d}t' \ , \tag{2.28}$$

where $k(t')$ is the memory kernel of the system and I an interaction kernel describing the change of the distribution function given by interactions. In the case the system evolution depends only on its current state with $k(t') = \delta(t-t')$, the history of the distribution function can be neglected

$$f(\mathbf{r},\mathbf{p},t) \to f(\mathbf{r},\mathbf{p},t_0) \ , \tag{2.29}$$

and the distribution function is reduced to a 6-dimensional object instead of the 6+1 dimensions for a full memory history.

In most of the calculations, the chemical potential is set to zero $\mu = 0$, leading to a balanced number of particles and anti-particles, although the numerical implementation is generic for all μ. $\mu_B = 0$ was chosen as a first starting point for general investigations. The pionic fields $\boldsymbol{\pi}$ were also generically implemented, but in most of the simulation runs they were set to zero $\boldsymbol{\pi} = \mathbf{0}$ to have stable and time-invariant equilibrium states. In case of $\boldsymbol{\pi} \neq \mathbf{0}$ the system has no stable state and the chiral fields σ and $\boldsymbol{\pi}$ oscillate non-linearly around a meta-stable state.

2.3 Equations of Motion

The equations of motion of the fields are derived by employing the derivative of the chiral potential (2.3), here for the σ-field

$$\frac{\partial U(\sigma,\boldsymbol{\pi})}{\partial\sigma} \equiv 0 = -\lambda^2\left(\sigma^2-\nu^2\right)\sigma + f_\pi m_\pi^2 + g\left\langle\bar{\psi}\psi\right\rangle_\sigma \ , \tag{2.30}$$

resulting in the equation of motion for the mean field

$$\left(\frac{\partial^2}{\partial t^2} - \nabla_{\mathbf{x}}^2\right)\sigma(\mathbf{x},t) = -\left[\frac{\partial U(\sigma,\boldsymbol{\pi})}{\partial\sigma} + g\ \left\langle\bar{\psi}\psi\right\rangle_\sigma\right]\sigma(\mathbf{x},t) + f_\pi m_\pi^2 \tag{2.31}$$

with the scalar density

$$\rho_\sigma \equiv \left\langle\bar{\psi}\psi\right\rangle_\sigma = g\cdot d_q\cdot\sigma(\mathbf{x})\int\frac{\mathrm{d}^3\mathbf{p}}{(2\pi)^3}\ \frac{f_q(\mathbf{x},\mathbf{p},T,\mu)+f_{\bar{q}}(\mathbf{x},\mathbf{p},T,\mu)}{E(\mathbf{x},\mathbf{p},\sigma,\boldsymbol{\pi})}\ , \tag{2.32}$$

with the coupling constant g, the quark degeneracy factor $d_q = 2\cdot 2\cdot 3$ (spin, flavor and color), the quark distribution function f_q, the anti-quark distribution function $f_{\bar{q}}$ and the particles' energy

$$E(\mathbf{x},\mathbf{p},\sigma,\boldsymbol{\pi}) = \sqrt{\mathbf{p}^2+m} = \sqrt{\mathbf{p}^2+g^2\left(\sigma^2+\boldsymbol{\pi}^2\right)}\ . \tag{2.33}$$

For the pion fields the equation of motion is derived from its chiral potential

$$\frac{\partial U(\sigma,\boldsymbol{\pi})}{\partial\boldsymbol{\pi}} \equiv 0 = -\lambda^2\left(\sigma^2-\nu^2\right)\boldsymbol{\pi} + +g\left\langle\bar{\psi}i\gamma_5\psi\right\rangle_\pi\ , \tag{2.34}$$

resulting in

$$\left(\frac{\partial^2}{\partial t^2} - \nabla_{\mathbf{x}}^2\right)\boldsymbol{\pi}(\mathbf{x},t) = -\left[\frac{\partial U(\sigma,\boldsymbol{\pi})}{\partial\pi} + g\left\langle\bar{\psi}i\gamma_5\tau\psi\right\rangle_\pi\right]\boldsymbol{\pi}(\mathbf{x},t)\ . \tag{2.35}$$

The one-loop pseudo-scalar density is defined as

$$\rho_\pi \equiv \left\langle\bar{\psi}i\gamma_5\tau\psi\right\rangle_\pi = g\cdot d_q\cdot\boldsymbol{\pi}(\mathbf{x})\int\frac{\mathrm{d}^3\mathbf{p}}{(2\pi)^3}\ \frac{f_q(\mathbf{x},\mathbf{p},T,\mu)+f_{\bar{q}}(\mathbf{x},\mathbf{p},T,\mu)}{E(\mathbf{x},\mathbf{p},\sigma,\boldsymbol{\pi})} \tag{2.36}$$

which uses the assumption for isospin saturation here. Equation (2.35) describes the three pionic fields $\boldsymbol{\pi} = (\pi^+,\pi^0,\pi^-)$, but by using isospin saturation, the three fields are assumed to be evenly excited and can be approximated by a single effective field

$$\boldsymbol{\pi}(\mathbf{x}) = n_\pi\cdot\pi(\mathbf{x}) = 3\cdot\pi(\mathbf{x})\ . \tag{2.37}$$

Quarks and anti-quarks are represented by their distribution functions using the test-particle ansatz (2.27). To derive equations of motion, the Vlasov-equation is employed [72]. A discussion on the Vlasov-equation can be found in Subsection 7.2.1 the of the particle-field method in Section 7.2.1.

$$\left[\partial_t + \frac{\mathbf{x}}{E(\mathbf{x},\mathbf{p},t)}\cdot\nabla_{\mathbf{r}} - \nabla_{\mathbf{x}}\ E(\mathbf{x},\mathbf{p},t_0)\nabla_{\mathbf{p}}\right]f(\mathbf{x},\mathbf{p},t_0) = 0 \tag{2.38}$$

The time t_0 is the time of the current system state, the equations of motion do not contain any global memory kernels depending on t. The quarks' energies are defined in (2.33). Employing the test-particle ansatz, the particles can be easily propagated with (2.38). The details on the numerical implementation are given in section 8.2.2.

Chapter 3

Equilibrium and Equilibration Calculations

> There exists everywhere a medium in things, determined by equilibrium.
>
> Dmitri Iwanowitsch Mendelejew

This part of the thesis covers the physical calculations using the DSLAM model with a focus on thermal equilibrium and equilibration processes. Section 3.1 will contain calculations with the model in perfect thermal and chemical equilibrium to test its stability and consistency compared to existing thermal calculations. Section 3.2 covers a scenario in which a non-equilibrium distribution of quarks will thermalize via elastic collisions. In Section 3.3 two scenarios in which the system temperature is changed by a sudden quench and by an external heat-bath are investigated.

3.1 Equilibrium Calculations / Test Calculations

The first and absolutely mandatory test for a numerical model is an equilibrium calculation. Besides the test for numerical stability, checking for conserved quantities like energy is fundamental for later calculations.

The model is tested against thermal equilibrium initial conditions. The system is initialized at a given temperature and started, the simulation must stay at the stable, thermal-equilibrium point.

Initial conditions are set up by choosing a temperature T_{Eq} and setting all physical quantities consistent to that value.

In thermal and chemical equilibrium, the equations of motion for the chiral fields do not depend on time and space and are therefore

$$\left(\frac{\partial^2}{\partial t^2} - \nabla^2_{\mathbf{x}}\right) \sigma_{\mathrm{Eq}}(\mathbf{x}, t) \equiv 0 \ , \tag{3.1}$$

and

$$\pi(\mathbf{x}, t) = 0 \ . \tag{3.2}$$

Stable solutions only exist for $\pi = 0$, otherwise the pion fields would slowly oscillate around a non-periodic state.

The equilibrium value of the mean-field σ_{eq} has to be derived self-consistently with the equations of motion and the equilibrium distribution for the quarks, which is given by the thermal Fermi-Dirac distribution:

$$f_\psi(\mathbf{x}, \mathbf{p}, t) = \frac{2N_c N_f}{(2\pi)^3} \left(1 + \exp\left(\frac{E - \mu}{T_{\mathrm{Eq}}}\right)\right)^{-1} \tag{3.3}$$

with the number of colors $N_c = 3$, the number of flavors $N_f = 2$ and the chemical potential μ. σ_{Eq} is found by solving the equations of motion with the equilibrium condition (3.1)

$$\left[\lambda^2\left(\sigma^2_{\mathrm{Eq}} - \nu^2\right) + g^2 \int \mathrm{d}^3\mathbf{p} \ \frac{f_\psi(\mathbf{x}, \mathbf{p}, t) + \tilde{f}_\psi(\mathbf{x}, \mathbf{p}, t)}{E(\mathbf{x}, \mathbf{p}, t)}\right] \sigma_{\mathrm{Eq}} - f_\pi m^2_\pi = 0 \ . \tag{3.4}$$

Equation (3.4) has to be solved with a numerical root finder as the field and particles are coupled self-consistent. A change in σ changes the quark mass, which changes the particle number in f_π which changes σ again. After finding σ^2_{Eq}, the quark density can be calculated with the dispersion relation:

$$E_{f_\psi} = \sqrt{p^2 + m^2_{\mathrm{eff}}} = \sqrt{p^2 + g^2\sigma^2_{\mathrm{Eq}}} \ . \tag{3.5}$$

The particles are sampled isotropically in space, the momentum is sampled according to the Fermi distribution and the direction of the momenta are isotropic, as well.

Figure 3.1a to 3.1f show the result of the equilibrium calculation. The system is initialized in thermal equilibrium and stays unchanged over time. Figure 3.1c and 3.1d show the very small spatial variance of the σ-field and the scalar density $\langle\bar{\psi}\rangle$ which is induced by local density fluctuations of the particles. The system parameters are: temperature $T = 110$ MeV, system size $V = 1$ fm^3, test-particle multiplication $N_{test} = 1 \cdot 10^6$, chiral coupling $g = 3.63$, simulation run time $t_{\mathrm{run}} = 10$ fm/c, size of time step $\Delta t = 0.002$ fm/c, grid size $N_{\mathrm{Grid}} = 128^3$. Small global fluctuations in the σ-field are related with discretization effects of the test particle number, see Figure 3.1a. . The higher the number of test particles, the more accurate equation (3.4) can be solved.

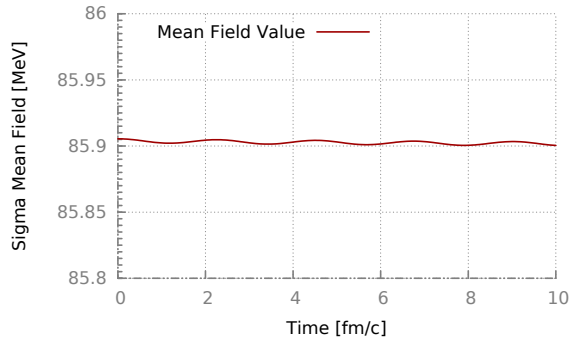

(a) Mean field value $\langle\sigma\rangle$ of the sigma field with respect to time.

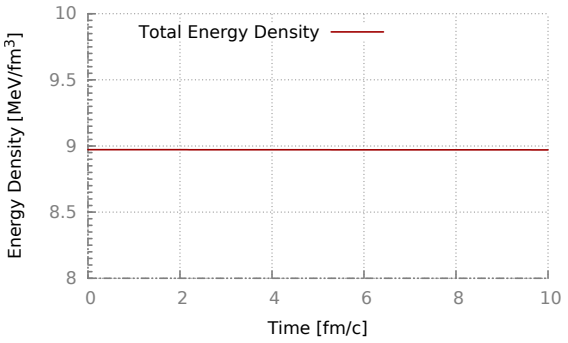

(b) Total energy of the system.

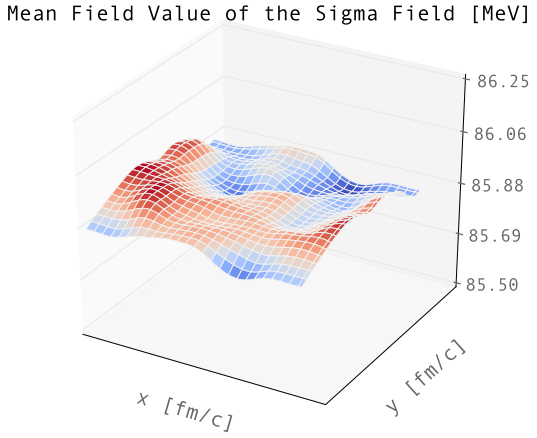

(c) Spatial distribution of the sigma mean field $\langle\sigma(\mathbf{x})\rangle$ at time $t = 1.3$ fm/c.

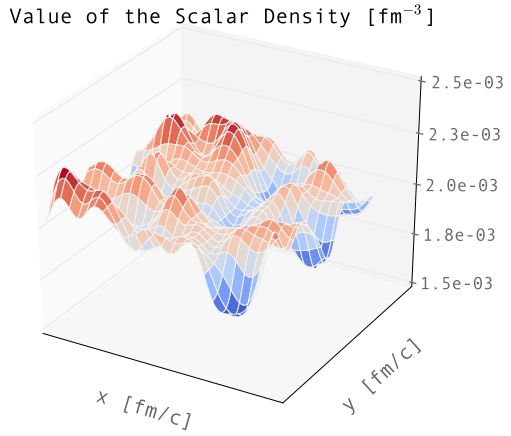

(d) Spatial distribution of the scalar density $\langle\bar{\psi}\psi\rangle(\mathbf{x})$ at time $t = 1.3$ fm/c.

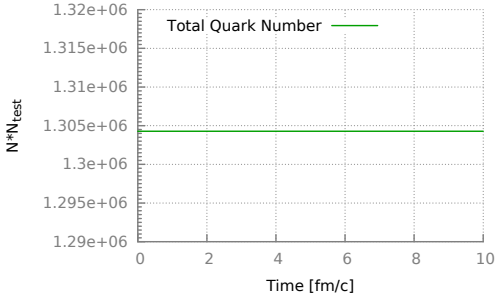

(e) Total quark and anti-quark number of the system. The number is scaled by the number of test-particles N_{test}.

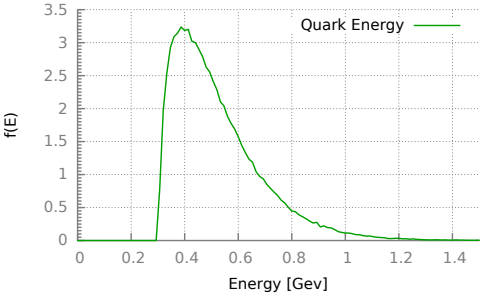

(f) Energy distribution of the quarks and anti-quarks at $t = 1.3$ fm/c. The distribution showing a thermal distribution with a quark rest mass of about 300 MeV.

Figure 3.1: Calculation for a box in thermal and chemical equilibrium.

Figures 3.1a to 3.1f show calculations for the chiral coupling $g = 3.63$, but for any other coupling the result show the same stable equilibrium behavior.

3.2 Thermalization of the Quark Distribution

Within the simulation, quarks and anti-quarks can collide via binary, elastic interactions. This allows the system to evolve an arbitrary distribution function to an equilibrium distribution. For massive and massless particles, this equilibrium distribution function is the Boltzmann-distribution

$$f(E) = \exp\left(-\frac{E}{T}\right) \ . \tag{3.6}$$

To test this behavior, a simulation is initialized in a thermal non-equilibrium scenario. The chosen initial-distribution is a distribution with a delta-peak in momentum space,

$$f(E) \sim \delta(E - E_0) \ , \tag{3.7}$$

with an arbitrary $E_0 > m$. In the test-particle ansatz, this becomes:

$$f(E, \mathbf{x}) = \sum_{i=1}^{N} \delta(E_i - E_0) = \sum_{i=1}^{N} \delta\left(\sqrt{\mathbf{p}^2 + g^2\sigma^2} - E_0\right) \ . \tag{3.8}$$

The direction of the momentum and the position of the particles is sampled uniformly in all directions. The interaction cross-section σ_{22} was chosen to be 15 mbarn. Figure 3.2 and 3.3 show the distribution function of the thermalization process at different time snapshots. The initial distribution is sharply peaked at E_0.

3.2.1 Particle Thermalization with a Virtual Heat Bath

In this section particles are initialized as described in the previous section with the difference that the particles are thermalized with a canonical heat bath. The particles are coupled to a reservoir of virtual particles which are treated as potential interaction partners sampled from a thermal distribution. This method can be imaged as a heat bath of virtual particles, the details are discussed in Section 8.3.1. The system can dynamically gain or lose thermal energy from or to the heat bath. In this test the interactions between the "real" quarks are switched off and particles only interact with the heat bath. This leads to the same thermal distribution with a slightly different equilibration behavior. In binary collisions, the equilibration process takes more time because the thermal background of particles has to be generated from the initial delta-distribution. In the heat bath scenario, particles with the initial momentum-peak can collide with already thermalized particles. This reduces the required number of collisions

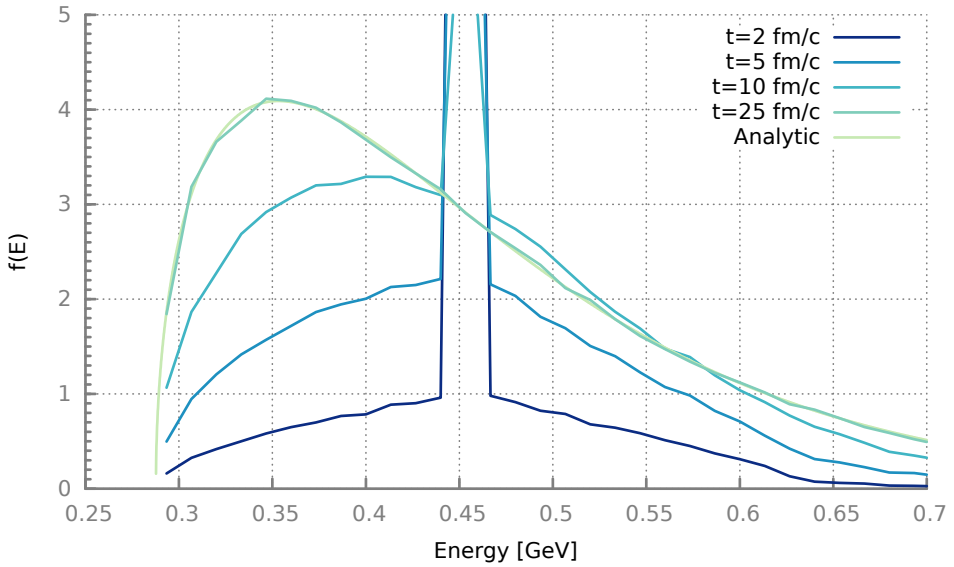

Figure 3.2: Thermalization of a delta-distribution in momentum space. The system is initialized in the chiral broken phase with a finite quark rest-mass. $g = 3.63$, $T = 120$ MeV, $N_{\text{test}} = 2 \cdot 10^6$ and $\sigma_{22} = 15$ mbarn. The distribution functions are rescaled for a better optical rendering, with $t = 2$ fm/c having the smallest norm and $t = 25$ fm/c having the largest norm.

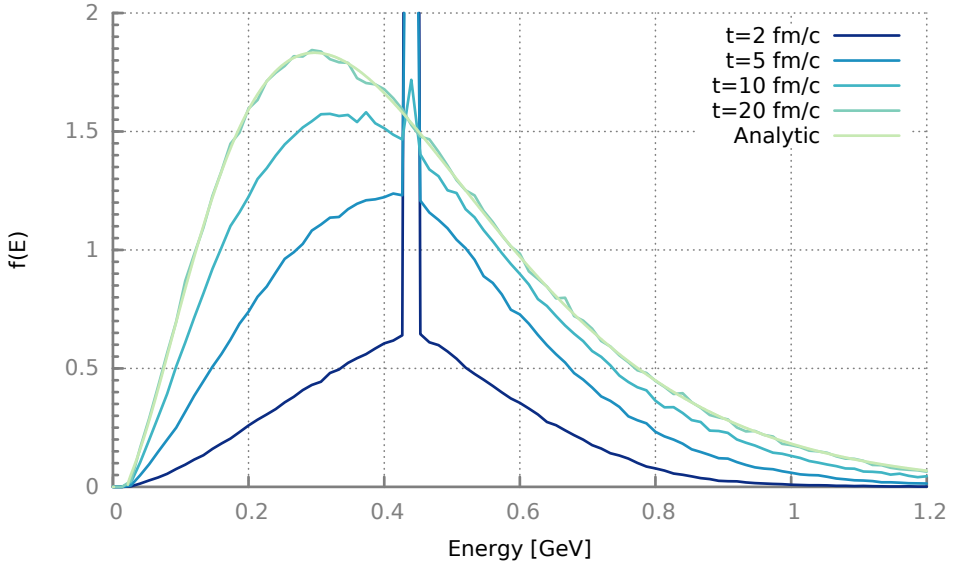

Figure 3.3: Thermalization of a delta-distribution in momentum space. The system is initialized in the chiral restored phase with a very small quark rest-mass. $g = 3.63$, $T = 150$ MeV, $N_{\text{test}} = 2 \cdot 10^6$ and $\sigma_{22} = 15$ mbarn. The distribution functions are rescaled for a better optical rendering, with $t = 2$ fm/c having the smallest norm and $t = 20$ fm/c having the largest norm.

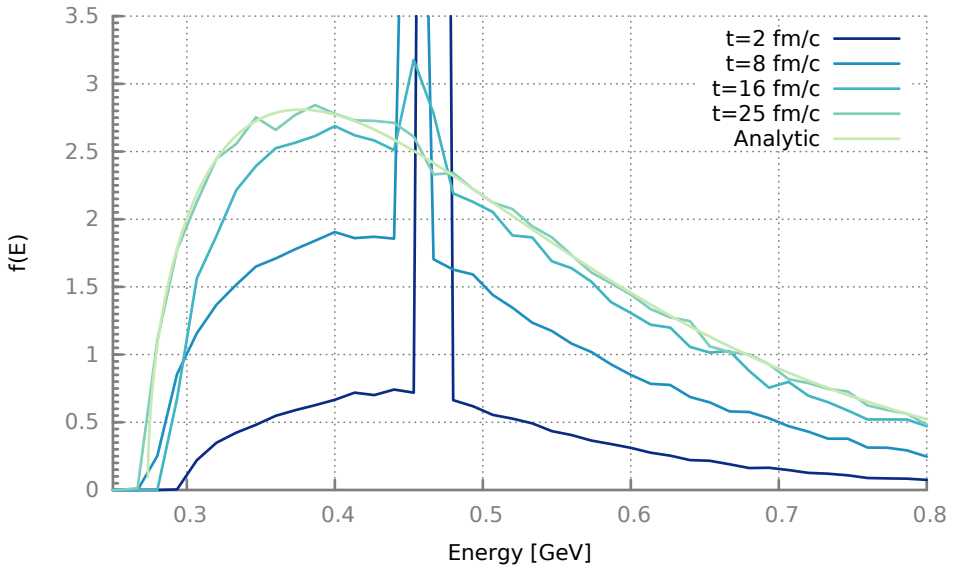

Figure 3.4: Energy distributions of the quarks at different times showing the thermalization with a virtual heat bath. Particles have been initialized with a delta distribution $f(E) = \delta(E - E_0)$. Particles can interact with a virtual heat bath, leading to a thermalization which is more efficient than binary scatterings because particles collide with an already thermal background. The following parameter were chosen $g = 3.63$, $T = 120$ MeV, $N_{\text{test}} = 1 \cdot 10^5$ and $\sigma_{22} = 15$ mbarn and a total number of 93000 particles. The distribution functions are rescaled for a better optical rendering, with $t = 2$ fm/c having the smallest norm and $t = 25$ fm/c having the largest norm.

per particle until a thermal distribution is reached. The overall time, until all particles have scattered at least once, is the same for the same interaction cross-section, but the number of needed collisions per particle is lower.

Intermediate Summary

The presented calculations show the numerical and physical stability of the DSLAM model. Initialized in equilibrium, the model shows no deviations from this state and stays stable over the run time. Particle distributions which are initialized with non-equilibrium conditions can be effectively thermalized by both binary inter-particle collisions and by interactions with a thermal heat bath.

3.3 Thermal Quench and Temperature Change

In this section two calculations will be done to investigate the behavior of the model at the chiral phase-transition. The first calculation will be a thermal quench in which the system is initialized at different temperatures for the fields and the particles. The second scenario will be a

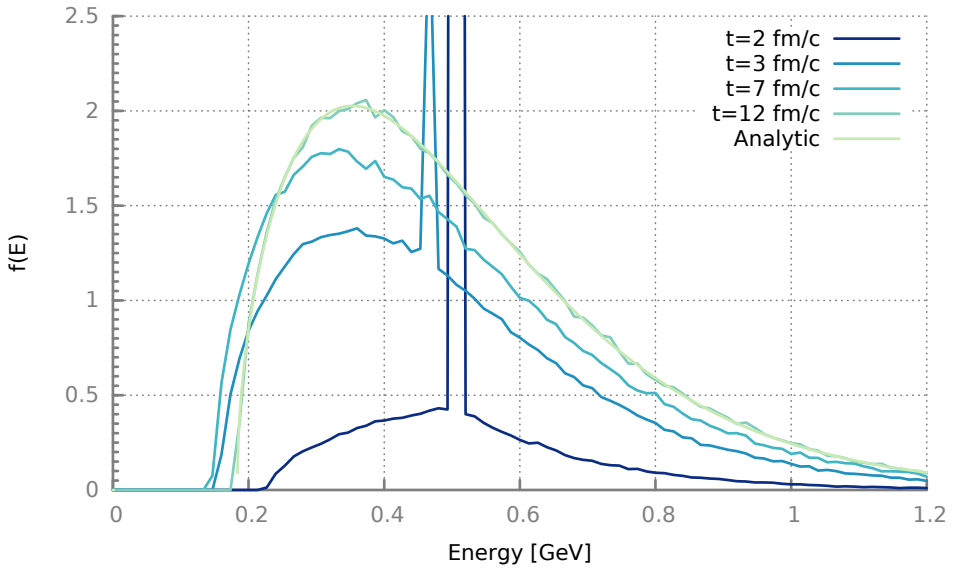

Figure 3.5: The same calculation as in Figure 3.4 but with a high temperature in the chiral restored phase as initial condition. The following parameter were chosen: $g = 3.63$, $T = 150$ MeV, $N_{\text{test}} = 1 \cdot 10^5$ and $\sigma_{22} = 15$ mbarn and a total number of 29000 particles The distribution functions are rescaled for a better optical rendering, with $t = 2$ fm/c having the smallest norm and $t = 12$ fm/c having the largest norm.

temperature shift with a heat bath. In both cases the system starts in the hot, chiral-restored phase and the quarks will be cooled. From equilibrium calculations in Section 3.1 it is expected to see a phase transition for the chiral order-parameter $\langle\sigma\rangle$ from the chiral-restored back to the chiral-broken phase.

3.3.1 Temperature Quench

In the temperature-quench scenario both fields and particles are initialized with equilibrium conditions for a given initial temperature T_i. After initialization, the particles are resampled at a new, lower temperature T_q while keeping the fields unchanged. The result is a non-equilibrium state between the fields and particles. Effectively this leads to the situation

$$\left\langle \bar{\psi}\psi \right\rangle_i \neq \left\langle \bar{\psi}\psi \right\rangle_q , \tag{3.9}$$

in which the overall potential of the σ-field changes and induces a mean-field force on the fields and the field moves away from its initial value σ_i.

Figure 3.6 shows results of such a calculation. The system was initialized with the following parameters:

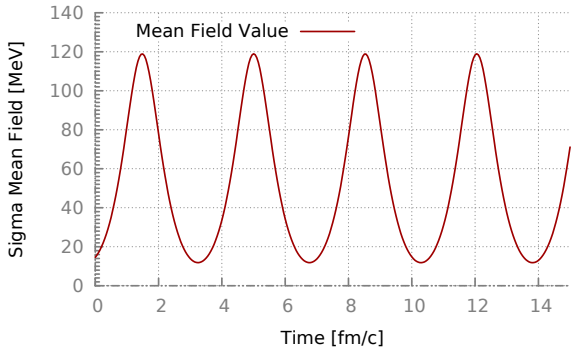

(a) Mean field value $\langle\sigma\rangle$ of the sigma field with respect to time.

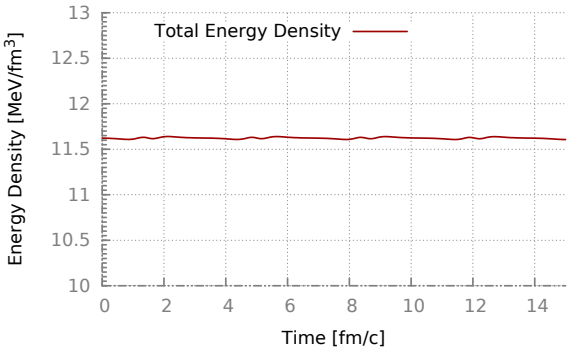

(b) Total energy of the system.

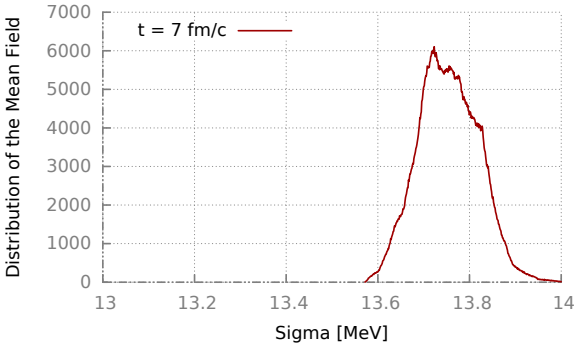

(c) Spatial distribution of the sigma mean field $\langle\sigma(\mathbf{x})\rangle$ at time $t = 7$ fm/c.

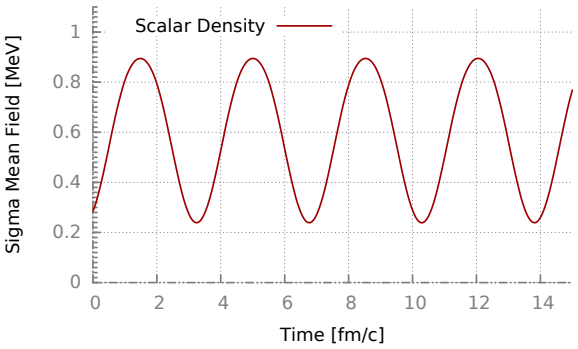

(d) Spatial distribution of the scalar density $\langle\bar{\psi}\psi\rangle(\mathbf{x})$ at time $t = 1.3$ fm/c.

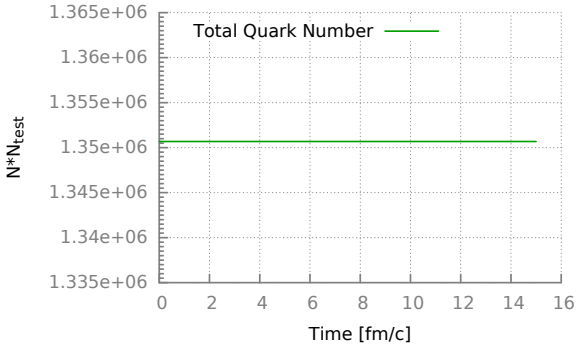

(e) Total quark and anti-quark number of the system. The number is scaled by the number of test-particles N_{test}.c

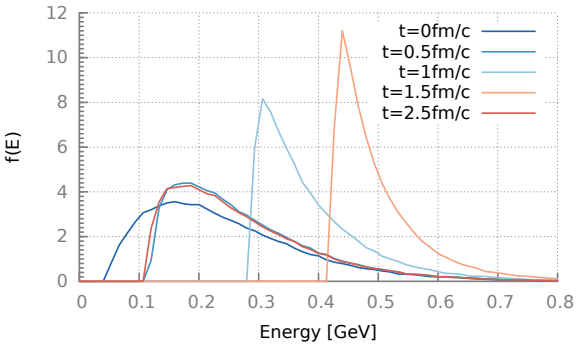

(f) Energy distribution of the quarks and anti-quarks at different times.

Figure 3.6: Results for calculation with the quenched-scenario. Particles and field are initialized at different temperatures, leading to a non-equilibrium situation.

Parameter	System Value
T_σ	150 MeV
$T_{\bar{q}q}$	80 MeV
V_{system}	1 fm^3
coupling g	3.63
N_{test}	10^6
Δt	0.002 fm/c
elastic collisions	none
heat bath	disabled

From the equations of motion of the σ-field, the field expected to deviate from its initial distribution. Subfigure 3.6a shows the time evolution of the order parameter $\langle\sigma\rangle$, which shows an oscillation. The fields and particles have different temperatures and are expected to equilibrate at some point. However, the σ-field starts a non-linear oscillation which does not seem to be damped even though a mean-field coupling with the particles should lead to an equilibrated system at some point. Even at large time scales for $t \to 300$ fm/c the system is not damped and thus does not equilibrate. The explanation for this behavior can be found in the kind of initial conditions and the coupling itself. The quarks are initialized in thermal equilibrium, so the quark spatial distribution shows very little anisotropy. This "flat" distribution does not induce any gradients in the fields and leads to an isotropic spatial distribution of the fields itself. With both the fields and particle having an isotropic distribution, the system dynamics can be approximated by a single equation of motion

$$\frac{\partial^2\sigma(t)}{\partial t^2} = --\sigma(t)\,\frac{\partial U(\sigma)}{\partial\sigma} + g\cdot\sigma(t)\cdot\left\langle\bar{\psi}\psi\right\rangle_\sigma(t) + f_\pi m_\pi^2\ , \tag{3.10}$$

which describes an anharmonic oscillator without damping.

The energy-distribution function of the quarks in Subfigure 3.6f show a periodic oscillation of the rest mass which is given by the oscillating mean field

$$m_q^2(t) = g^2\sigma^2(t)\ . \tag{3.11}$$

The overall temperature of the particles however does not change and stays at the initial temperature of 80 MeV.

Another important physical effect does not occur, either. By changing the overall temperature, the system is expected to change its phase. While the quarks have the temperature of the chiral-broken phase with $T_q \ll T_c$ (with $T_c = 140$ MeV), the order-parameter oscillates between the chiral broken and chiral restored phase but this effect should not be seen as a phase transition because it does not develop a stable phase.

The coupling constant for this system was chosen to be $g = 3.63$, which corresponds to a second-order phase transition. However, for the other couplings ($g = 3.3$ and $g = 5.5$) the system qualitatively behaves not any different. No equilibration or damping of the field can be observed and no phase transition takes place.

In summary a phase transition can not be achieved within this scenario. A temperature quench leads to a system with a global and coherent oscillation of the mean-fields. No phase transition can be observed and neither the fields nor the quarks develop towards chemical or thermal equilibrium. The reason lies in the lack of collisions or other processes which could equilibrate the system between particles and fields. A propagation of particles via a Vlasov equation with mean-field interactions does not generate any entropy, the system's equations of motion remain time-reversible.

In the next section a different approach with a heat bath will be tested.

3.3.2 Temperature Shift with an External Heat Bath

In the previous scenario the system was initialized in a quenched state which changed the energy of the particles instantaneously at the start of the time evolution, afterwards the total energy was conserved. This initial hard change induced a global oscillation in the mean-field.

Employing a different approach in this section, the system is initialized in global thermal and chemical equilibrium in the chiral restored phase. The total energy is reduced slowly and smoothly by cooling the quarks via the coupling to an external heat bath with a time dependent temperature

$$T_{\text{heatbath}}(t) = T_I \left(1 - \frac{t}{\tau_T}\right) , \tag{3.12}$$

where $1/\tau_T$ is the change rate of the heat bath temperature, cooling the heat bath over the run time of the simulation. The time dependence in (3.12) is an arbitrarily chosen ansatz.

In the beginning the heat bath and the particles have the same temperature. Within the time evolution the heat bath cools down and reduces the particle temperature as well. This slow and smooth change should minimize oscillations of the σ-field as this leads to a slow change of the chiral potential and a slow shift of the chiral field. Therefore strong oscillations as in the previous chapter are not expected and a damping of the kinetic energy of the field is not necessary. Without the undamped oscillation the system might change its chiral phase.

The following initial conditions have been chosen:

Parameter	System Value
T_I	150 MeV
Simulation run time	25 fm/c
V_{system}	1 fm^3
coupling g	3.63
N_{test}	10^6
Δt	0.002 fm/c
elastic collisions	15 mbarn
heat bath	15 mbarn
τ_T	35 fm/c

The cross sections of the elastic interactions and the interactions between quarks and the heat bath have been chosen to a large value to guarantee a fast thermalization and temperature change of the quark-medium. All other parameters have been chosen to be the same as in the thermal-quench scenario.

Results of this calculation are shown in Figure 3.7. Figure 3.7f shows the temperature change of the quarks. The initial temperature starts at $T = 150$ MeV and changes smoothly with the simulation time. The heat bath reaches a final temperature of $T_f = 80$ MeV at the end of the simulation, at this time the quarks have thermalized at 87 MeV. A slight delay between the heat bath and the quark temperature can be observed. The particles and the heat bath exchange energy by collisions, therefore the system gets a kind of relaxation-time scale between particles and the virtual heat bath.

With the quarks cooled below the phase-transition temperature, the system is expected to change its chiral phase. This would be indicated by the order parameter $\langle\sigma\rangle$ which should be in the order of the vacuum expectation value of 93 MeV. Figure 3.7a shows the time evolution of the order parameter. Surprisingly, the order parameter shows the diametrical behavior and decreases, instead of increasing. Even though the temperature is decreased, the order-parameter evolves further towards the chiral-restored regime which is expected for even hotter media. This behavior is contra-intuitive at first thought as Figure 3.7b shows a monotonic decrease of the total energy. Although the σ-field shows only very little fluctuations and seems to be in a stable phase, it is far from the expected thermodynamical state.

Comparing the quenched scenario from Section 3.3.1 with the heat bath scenario, two differences come to mind. The scalar density $\left\langle\bar{\psi}\psi\right\rangle$ oscillates between 0.3 GeV and 0.9 GeV in the quenched scenario, while it decreases from 1 GeV to 0.75 GeV in the heat bath scenario. The second difference is the particle number, which is about threefold smaller in the quenched scenario. In the heat bath scenario only the quark temperature is changed while in the quenched scenario both the temperature and the quark density are changed.

The explanation why the order-parameter does not show a phase-transition can be found in the particle density. If the system can not change the quark-density upon a temperature change, it will not be able to change its chiral phase.

The next section will investigate the effects of the particle density on the chiral-phase transition.

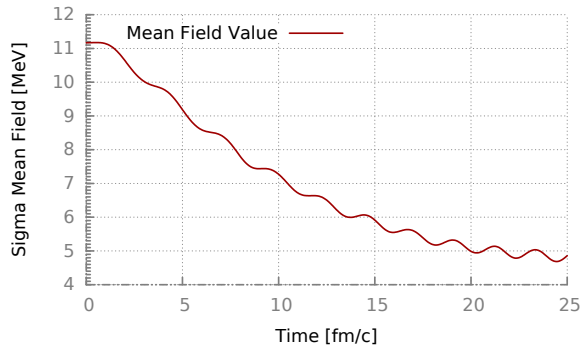

(a) Mean field value $\langle\sigma\rangle$ of the sigma field with respect to time.

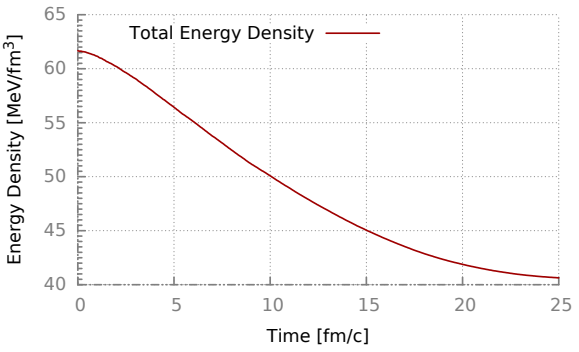

(b) Total energy of the system with respect to the simulation time.

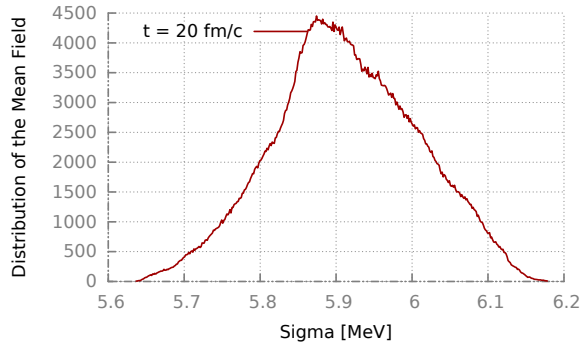

(c) Spatial distribution of the sigma mean field $\langle\sigma(\mathbf{x})\rangle$ at time $t = 20$ fm/c.

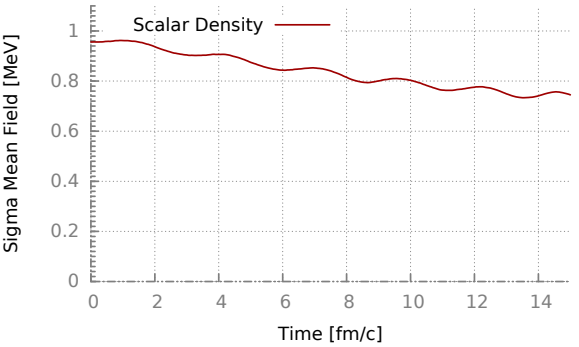

(d) One-loop scalar density $\langle\bar{\psi}\psi\rangle(\mathbf{x})$ with respect to the simulation time

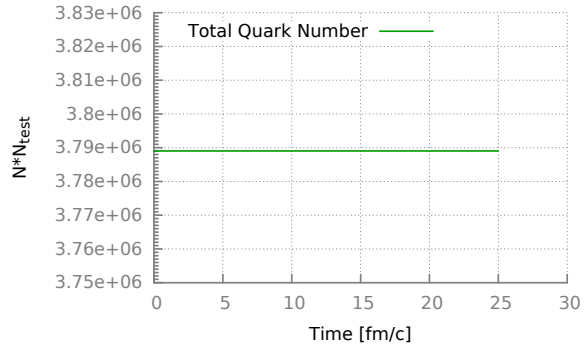

(e) Total quark and anti-quark number of the system. The number is scaled by the number of test-particles N_{test}

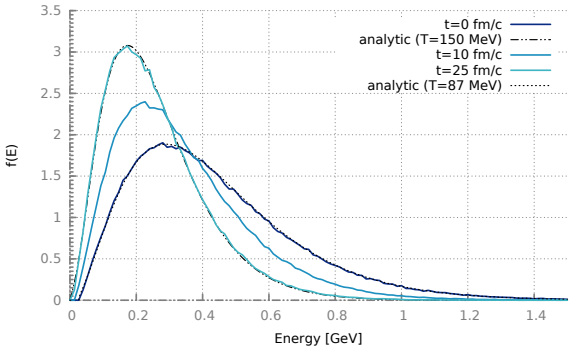

(f) Energy distribution functions of the quarks at different times. The initial and the final distributions are both compared to analytic Boltzmann distributions.

Figure 3.7: Results for the calculation with the heat bath cooling-scenario. The system is initialized in thermal and chemical equilibrium. The quarks are slowly cooled with an external heat bath leading to a decrease of the total system energy.

Chapter 4

Non-Equilibrium Effects

Ignoramus et ignorabimus

Emil Heinrich Du Bois-Reymond

In this chapter various non-equilibrium effects are discussed. The behavior of the linear σ-model is well understood in equilibrium and the basic properties were discussed in chapter 3.1.

The DSLAM model is a numerical implementation of the linear σ-model with the scope of general physical situations, allowing to simulate both systems in or near thermal and chemical equilibrium as well as systems which are far from equilibrium.

The term 'thermal equilibrium' relates to the system state in which the particles' thermal distribution can be described by a single-particle distribution function like the Boltzmann- or Fermi-distribution with a global temperature. For fields, thermal means a stable configuration in which the overall excitation state does not change and all modes are excited according to the equipartition theorem.

Chemical equilibrium describes the state in which the particle density corresponds to the one given by the equilibrium density

$$n_{\mathrm{eq}} = \int \frac{\mathrm{d}^3\mathbf{p}}{(2\pi)^3}\ f(E, m, T)\ . \tag{4.1}$$

The system is in total equilibrium if both the particles are in thermal and chemical equilibrium and the fields are in a configuration in which

$$\frac{\partial\ \Omega_{\mathrm{eq}}\left(\sigma, \left\langle\bar{\psi}\psi\right\rangle\right)}{\partial\sigma} \equiv 0 \tag{4.2}$$

and the overall system-state becomes time independent.

Non-equilibrium effects occur if the system deviates thermally or chemically from its stable state. In both situations, the system dynamics will differ from the discussed equilibrium properties.

In Section 4.1 effects of thermal non-equilibrium will be discussed, in Section 4.2 effects of chemical non-equilibrium will be discussed.

Some non-equilibrium effects have already been discussed in the calculations with a quenched scenario in section 3.3 or with an external heat bath in section 3.3.2. The first implementation of the DSLAM model is lacking chemical processes. As a result the system can not equilibrate effectively. The later chapter 5 describes the extensions of the DSLAM model to allow an effective chemical and thermal equilibration.

4.1 Thermal Non-Equilibrium Effects

Effects of thermal deviation are discussed in this section. In other effective models like hydrodynamics, the medium is assumed to be in or near local thermal equilibrium. This is a assumption which works well in many cases. However, in this section the impact and effect of any deviations of the medium from thermal equilibrium is discussed. To be precise, a comparison between media which can be described by an equilibrium distribution function and media with a different, non-equilibrium distribution function is done.

To calculate the equilibrium behavior of the linear σ-model, the potential Ω for the order parameter $\langle\sigma\rangle$ has to be solved self-consistently for its equilibrium value. One important part of the thermodynamic potential of the σ-field is the one-loop scalar density, which couples the quark density to the field

$$\rho_\sigma \equiv \left\langle \bar{\psi}\psi \right\rangle \equiv g\sigma(\mathbf{r}) \int \mathrm{d}^3\mathbf{p}\ \frac{f\left(\mathbf{r},\mathbf{p}\right) + \tilde{f}\left(\mathbf{r},\mathbf{p}\right)}{E\left(\mathbf{r},\mathbf{p}\right)}\ . \tag{4.3}$$

By employing a test-particle ansatz with a single-particle distribution for the quarks and a zero chemical potential $\mu \to 0$, the scalar density can be factorized in a particle density expectation value and an inverse energy expectation value

$$f\left(\mathbf{r},\mathbf{p}\right) = \sum \delta\left(\mathbf{r_i} - \mathbf{r}\right)\delta\left(\mathbf{p_i} - \mathbf{p}\right)\ , \tag{4.4}$$

$$\left\langle \bar{\psi}\psi \right\rangle \xrightarrow[f\to f_{\mathrm{eq}}]{\mu=0} g\sigma(\mathbf{r})\left\langle n\left(\mathbf{r},T\right)\right\rangle \left\langle \frac{1}{E\left(\mathbf{r},T\right)} \right\rangle\ . \tag{4.5}$$

For the chiral restored phase at $T > T_c$ we can approximate the particle density $n(T)$ and the average energy $E(T)$ with the analytical relations for a massless Fermi gas:

$$\langle n\left(\mathbf{r}, T\right)\rangle = d_q \frac{3\zeta(3)}{4\pi^2} T^3 \ , \tag{4.6}$$

$$\left\langle \frac{1}{E\left(\mathbf{r}, T\right)} \right\rangle = d_q \frac{\pi^2}{18\zeta(3)} T^{-1} \ . \tag{4.7}$$

Both the particle density (4.6) and the inverse energy distribution (4.7) can deviate from equilibrium. Therefore formally they can be described by two different temperatures T_{therm} and T_{chem}. Combining (4.6) and (4.7) results in

$$\langle n\left(\mathbf{r}, T_{\text{chem}}\right)\rangle \cdot \left\langle \frac{1}{E\left(\mathbf{r}, T_{\text{therm}}\right)} \right\rangle = \frac{1}{24} \frac{T_{\text{chem}}^3}{T_{\text{therm}}} \ . \tag{4.8}$$

In this notation we can discuss the behavior of the scalar density $\left\langle \bar{\psi}\psi \right\rangle$ if the temperature is changed with a constant particle density or the other way around.

The result of (4.8) is quite interesting because it shows that the particle density has a much stronger impact on the scalar density $\left\langle \bar{\psi}\psi \right\rangle$ than on the thermal distribution. For full thermal equilibrium with $T_{\text{therm}} = T_{\text{chem}}$ relation (4.8) becomes

$$\left\langle \frac{n\left(\mathbf{r}, T\right)}{E\left(\mathbf{r}, T\right)} \right\rangle = \frac{T^2}{24} \tag{4.9}$$

In Section 3.3.2 a scenario was calculated in which the system was initialized in the hot and chiral-restored phase. The particles were cooled down via coupling to a heat bath and even though the system's total energy was largely reduced, the order parameter $\langle\sigma\rangle$ did not show the expected phase transition to the cold, chiral broken phase. The chiral field moved even further to the chiral restored phase $\langle\sigma\rangle \to 0$ which would be expected for increase of the system temperature.

Equations (4.8) and (4.9) can explain this behavior. In a full equilibrium, $\left\langle \bar{\psi}\psi \right\rangle$ would scale with T^2. Even though the particles showed a thermal distribution over the whole simulation time, the overall system was not in full equilibrium because the particle density could not change. The lack of particle-number changing processes leads to a constant particle number. In terms of equation (4.8) the chemical temperature T_{chem} did not change, so the overall scalar density scaled with

$$\left\langle \bar{\psi}\psi \right\rangle \sim \frac{1}{T} \neq T^2 \ , \tag{4.10}$$

leading to an decrease instead of an increase. This inverse behavior of the scalar density is a non-equilibrium effect and explains why the order parameter moves in the "wrong direction". In contrast the same inverse behavior can be observed if the system is initialized in the cold and

initially chiral broken phase and is heated up by an external heat-bath. If the particle number is constant the chiral field will move towards the direction of the vacuum-expectation value because of the same reason as the chiral density scales differently.

Note that all arguments using the analytic relations (4.8) and (4.9) hold for temperatures above the chiral phase transition, in which the quarks mass can be neglected. The exact scaling of the particle density and the inverse energy can be obtained from numerical calculations, as presented in Figure 4.1 and 4.2.

Both calculations show the effect of the chiral phase transition, in which the change of the quark mass directly leads to a change in the quark density and energies because the chiral fields and quarks are coupled self-consistently. This rapid change of the quark density is crucial for the phase transition, as discussed before.

However, such calculations are not always sufficient to derive the behavior of dynamical systems. Equilibrium calculations show the thermal behavior of a system in comparison to its system temperature if such a system is sufficiently large and has arbitrary large time scales to equilibrate. In such a case discontinuity in the temperature scaling can be observed. For dynamical systems, e.g. quickly expanding fireballs, such an instant change in the particle number, like at the first-order phase transition, is not possible as the annihilation of particles needs time. Such effects will be considered in Section 4.2.

Additionally, the correlation length can diverge at the phase transition [32], increasing the equilibration time arbitrarily. This critical slowing down can prevent the system from equilibrating in short time scales.

Impact of the Thermal Distribution on the Scalar Density

In the previous section the scalar density $\left\langle \bar{\psi}\psi \right\rangle$ was decomposed for an equilibrium one-particle distribution function. We will now investigate the effects of a non-thermal distribution function with their time dependence in an equilibration process. The system is therefore initialized in a thermal non-equilibrium situation and can relax back to thermal equilibrium by elastic quark interaction. The level of equilibration is compared to the value of the one loop scalar density $\left\langle \bar{\psi}\psi \right\rangle$ for full equilibrium.

For this calculation, the linear-σ model is initialized with a non-equilibrium distribution function for the quarks momenta, the Dirac-delta function

$$f\left(\mathbf{r},\mathbf{p}\right) = \sum_{i}^{N(T)} \delta(E_i - E_0(T)) \ . \tag{4.11}$$

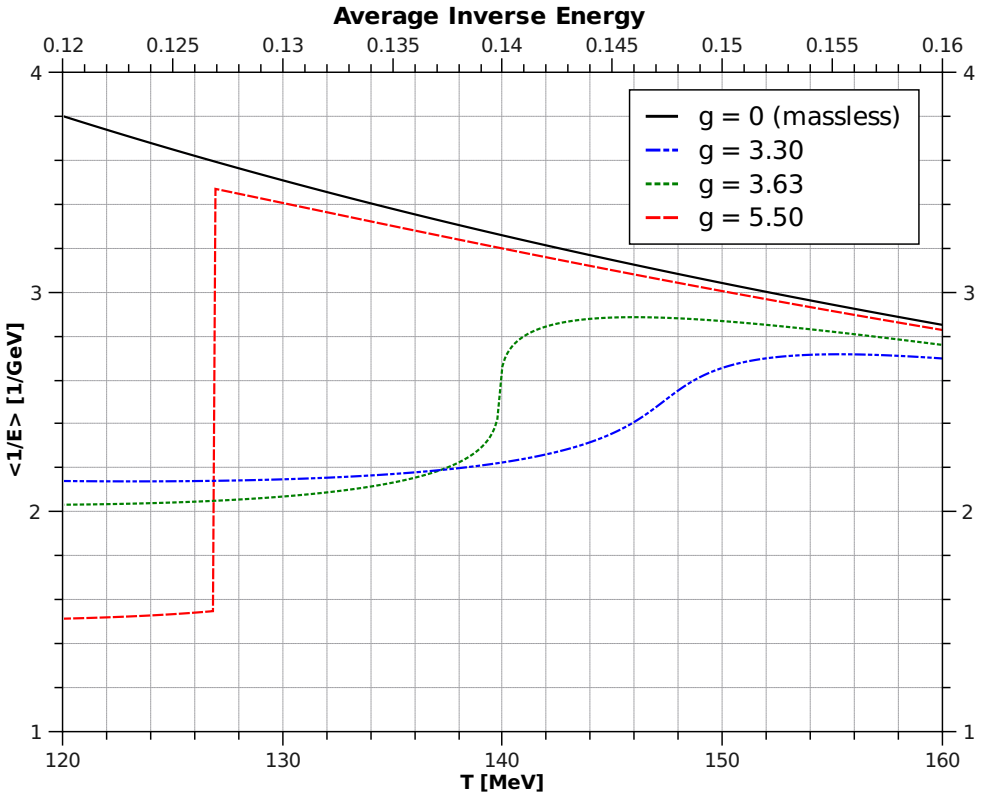

Figure 4.1: Thermal dependency of the inverse energy of quarks $\langle 1/E \rangle(T)$, which is an important part in the one-loop scalar density $\langle \bar{\psi}\psi \rangle$. The quarks behave like massless particles for high temperatures and the inverse energy rises towards the phase transition. The mass changes rapidly at the phase transition, leading to a change of the particle number and the inverse energy. Depending on the order of the phase transition, the change occurs in a jump or in a smooth crossover. At low temperatures the energy is dominated by the rest-mass of the particles, leading to a quasi-constant scaling of the inverse energy.

The energy E_0 is chosen to match the average energy of the system for the thermal Boltzmann distribution, to which the system equilibrates

$$E_0(T) = A_0 \int_M^\infty E \, \sqrt{E^2 - M^2} \, e^{-E/T} \mathrm{d}E \, , \tag{4.12}$$

$$A_0 = \left(\int_M^\infty E \, \sqrt{E^2 - M^2} \, e^{-E/T} \mathrm{d}E \right)^{-1} \, . \tag{4.13}$$

In this calculation the quark-particles equilibrate by elastic interactions. For a quantitative description of the equilibration, a χ-squared test is used, also refereed to as χ^2-test, which compares a distribution function via its frequencies to the expected ones [73]. The χ^2 statistic is given by comparing the observed frequencies O_i with the expected reference frequencies R_i

$$\chi^2 = \sum_i^N \frac{(O_i - R_i)^2}{R_i} \, , \tag{4.14}$$

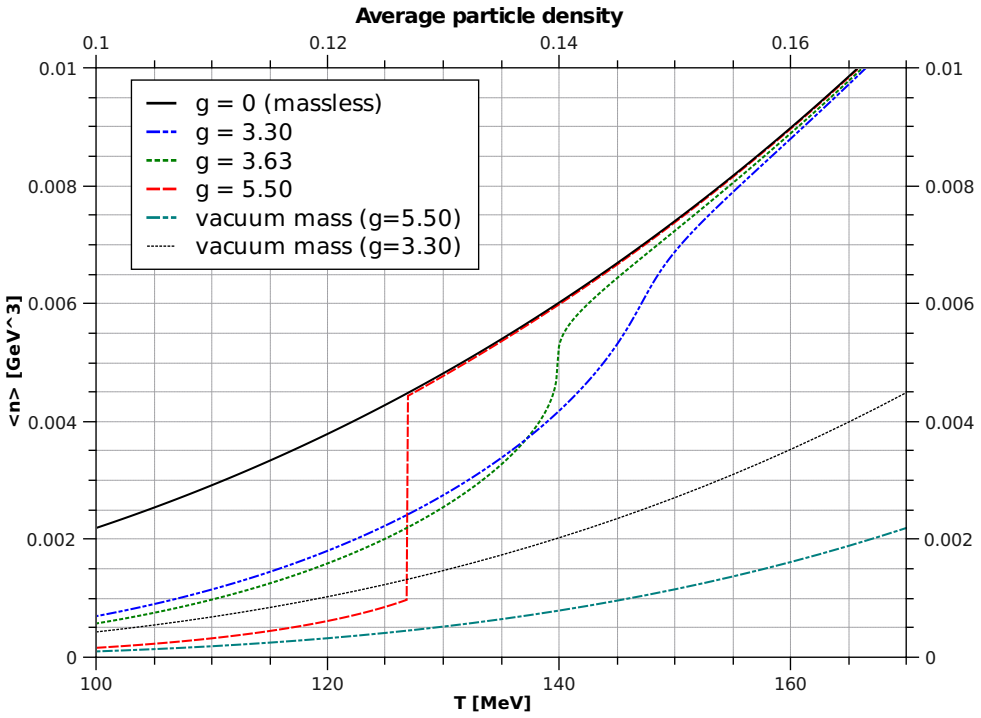

Figure 4.2: Temperature dependence of the average quark density. For high temperatures all three coupling-scenarios approach the analytic solution for massless particles $n \sim T^3$. For low temperatures all three curves approximate the vacuum solution with different masses. In between does the density changes rapidly at the phase transition. The first-order phase transition has a discontinuity in the density function, both second-order transition and crossover show a smooth transition. Furthermore, these curves show the temperature dependence in full equilibrium. Any dynamical simulation will show such a scaling only on very long and slow time scales if the system changes adiabatically.

with total sample size N. For the equilibration test we will choose the Boltzmann distribution for R_i

$$R_i(E_i) = E_i \sqrt{E_i^2 - M^2}\, e^{E_i/T} \ . \tag{4.15}$$

For χ^2 to converge, we have to satisfy both the existence of R as a non-zero number and the physical mass limit

$$R_i(E_i) \in \mathbb{R}_{>0} : \forall E_i \, (E_i > M) \ . \tag{4.16}$$

The χ^2 distribution becomes large if the distribution function and the reference function have no overlap at all. If both functions match perfectly, the χ^2 value will reach zero. This value is a gauge for equilibration in this calculation, its absolute values are not important. The system is considered equilibrated if $\chi^2 \ll 1$ and does not change anymore.

Figures 4.3a and 4.3b show the results of these thermalization calculations. Both systems are initialized with the Dirac-δ distribution. Quarks can interact via constant and isotropic cross sections. The interaction rate is chosen to allow a thermalization for both systems within 30 fm/c.

Figure 4.3a shows the calculation in the chiral restored phase at $T = 150$ MeV, Figure 4.3b shows the same calculation in the chiral broken phase at $T = 100$ MeV. The coupling constant was chosen to be $g = 3.63$. In both figures the scalar density $\left\langle \bar{\psi}\psi \right\rangle$ changes within the thermalization process. The particle number, the total energy and the system volume stays constant, only the change of the total distribution function leads to a change in $\left\langle \bar{\psi}\psi \right\rangle$. Quantitatively, the value $\left\langle \bar{\psi}\psi \right\rangle_{t=0}$ for the initial Dirac-δ distribution is lower compared to an initial f_{eq} and $\left\langle \bar{\psi}\psi \right\rangle$ raises with the level of thermalization. The behavior is very similar for calculations in the chiral restored phase in comparison to calculations in the chiral broken phase:

$$\begin{aligned} \left\langle \bar{\psi}\psi \right\rangle_{f=f_\delta} &= 0.65 \text{ for } T_i = 100 \text{ MeV} \ , \\ \left\langle \bar{\psi}\psi \right\rangle_{f=f_\delta} &= 0.7 \text{ for } T_i = 150 \text{ MeV} \ . \end{aligned} \tag{4.17}$$

In summary the scalar density changes by a factor $(1/0.65 - 1/0.7 \approx 1.4 - 1.5)$ just by the change of the thermal distribution while keeping the particle number constant. The overall impact of the thermal distribution on the scalar density is not as big as a change in temperature or particle number but it is not negligible in dynamical situations in which the distribution function can deviate from equilibrium.

Figure 4.4 shows the phase diagram of the linear σ-model in which the equilibrium quark-distribution is replaced by the Dirac-δ distribution. The particle density is chosen to be the same density as for the Fermi distribution but the momenta of the particles are chosen according to the peaked Dirac distribution. The rest of the calculation is kept the same as in the usual linear σ-model. The temperature dependence in Figure 4.4 differs remarkably from the equilibrium phase diagram (see Figure 2.2). The temperatures of the phase transition are shifted to higher temperatures by about 20 MeV. However the strongest effect is the change of the transition type. The first-order phase transition with $g = 5.5$ is still of first-order, the other two cases $g = 3.63$ and $g = 3.3$ show both a crossover transition with very shallow slopes. The second-order phase transition for $g = 3.63$ is completely lost, and one has to expect that this kind of phase transition is very sensitive to the distribution function and in general will not be visible for non-equilibrium scenarios like quickly expanding systems.

4.2 Chemical Non-Equilibrium Effects

In the previous section the impact of a deviation from thermal equilibrium on the scalar density $\left\langle \bar{\psi}\psi \right\rangle$ and the phase diagram of the linear σ-model was examined. The scope of this section will be to investigate deviations from chemical equilibrium, or i.e. deviations from the equilibrium particle density for a given temperature.

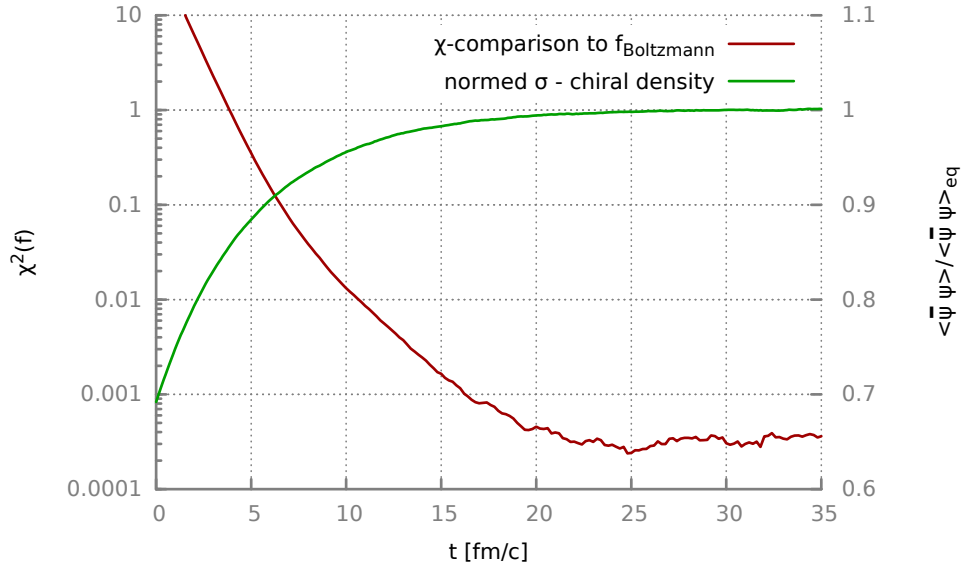

(a) Calculation for a system in the chiral restored phase with $T = 150$ MeV, 530000 particles and $g = 3.63$.

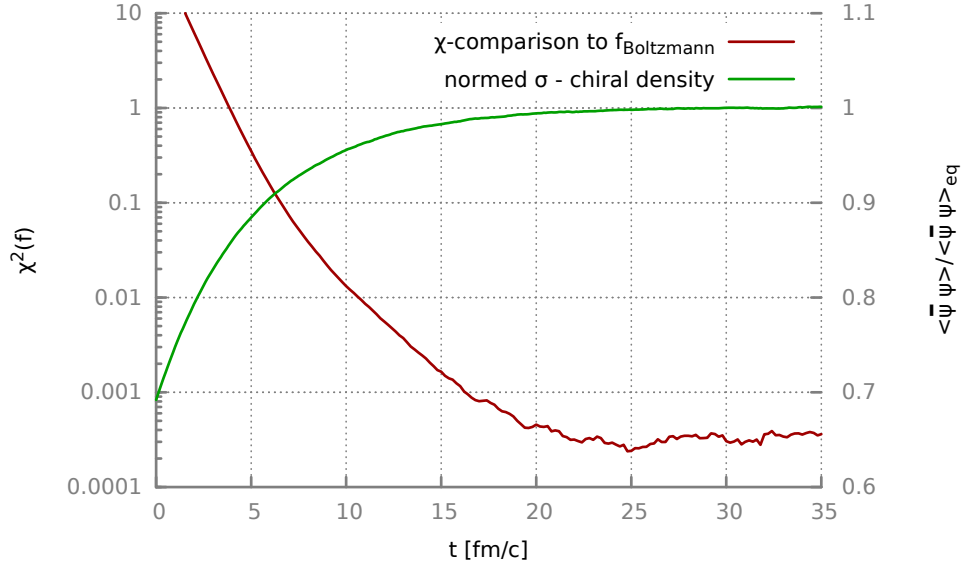

(b) Calculation for a system in the chiral restored phase with $T = 190$ MeV, 230000 particles and $g = 3.63$.

Figure 4.3: Equilibration of two systems initialized with a non-equilibrium distribution, the Dirac distribution $\delta(E - E_0)$. By employing elastic collision the system can equilibrate towards the thermal Boltzmann distribution. The plots show the degree of thermalization with the help of the χ^2 value (left scale), which is $\chi^2 \to 0$ for equilibrated systems. The right scale shows the scalar density $\langle\bar{\psi}\psi\rangle$ which is normed to the equilibrium value for this system. Therefore $\langle\bar{\psi}\psi\rangle \to 1$ in thermal equilibrium. The total particle number is conserved.

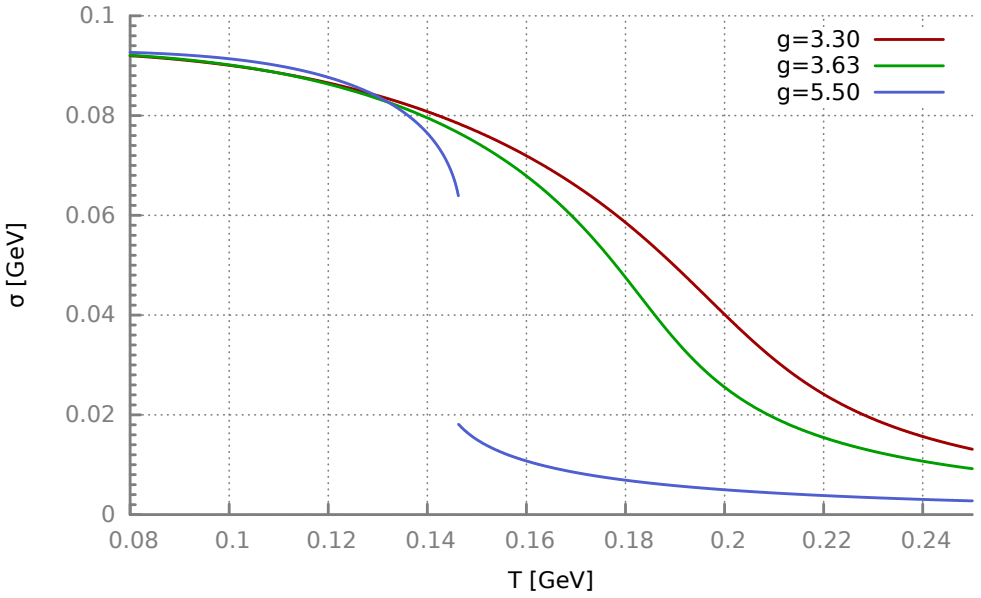

Figure 4.4: Phase-diagram for the linear σ-model with a Dirac-distribution as the thermal distribution functions for the quarks. The particle density is chosen to be the same as for the Fermi-distribution. The change of the thermal distribution leads to a quantitative change in the phase transitions. All critical temperatures are shifted up to higher temperatures and the order of the phase transition is changed. The first-order transition is not changed, but the second order phase transition becomes a crossover and the slope of the crossover transition with $g = 3.3$ becomes even more flat.

In a fully equilibrated medium, both thermally and chemically, a single temperature T and the chemical potential μ describe the entire system characteristics for the energy, momentum, mass and density distributions.

The particle density for a massless gas is given by

$$n(T) = \int_0^\infty \mathrm{d}E \; E^2 e^{-E/T} = 2T^3 N_d \; , \tag{4.18}$$

with the degeneracy factor N_d. For massless fermions, the equilibrium density differs by a factor

$$n(T) = \frac{3}{2} T^3 N_d \zeta(3) \; . \tag{4.19}$$

For massive particles one finds

$$n(T) = \int_m^\infty \mathrm{d}\left(E \; E \cdot \sqrt{E^2 - m^2}\right) e^{-E/T} = N_d \cdot m^2 \cdot T \cdot K_2\left(\frac{m}{T}\right) \; , \tag{4.20}$$

with the modified Bessel-function of second kind K_2.

The numerical solution of the particle density with temperature dependent masses is shown in Figure 4.2.

In Section 4.1 the effect of a constant particle density has already been discussed. A simple model is now used to discuss the impact of a non-equilibrium particle density. The idea is to simulate a system which expands slowly and adiabatically. The current state of the model does not include chemical processes, therefore an effective cooling by expansion is not possible. As a workaround, a simple relation between the system volume and temperature is assumed. This model assumption will not exactly reproduce the quantitative behavior of the linear σ-model, but will allow an effective and qualitative statement about the system behavior.

The total particle number is constant without particle production and annihilation, leading to the density to volume scaling relation

$$n(t) \cdot V(t) = n_0 \cdot V_0 \tag{4.21}$$

An adiabatic expansion is simulated, so the used thermodynamic relation is

$$T(t)V(t)^{\gamma-1} = T_0 V_0^{\gamma-1} \ . \tag{4.22}$$

For the adiabatic exponent the relation for an ideal gas is assumed,

$$\gamma = 5/3 \ , \tag{4.23}$$

which is a very strong assumption but does not compromise the idea of the calculation. The overall scaling relation for the particle density in comparison to the system temperature becomes

$$n(T) = n_0 \left(\frac{T}{T_0}\right)^{3/2} \ . \tag{4.24}$$

To compare the system behavior with the equilibrium model, the simulation is set up at a given temperature and initialized in full equilibrium. At this given temperature the simulated system behaves exactly as the equilibrium model. Employing the density scaling (4.24), the system behavior is calculated for different temperatures by expanding or compressing the box.

For the coupling $g = 3.3$ with a crossover phase transition this initial temperature is set to $T_i = 155$ MeV, for $g = 3.63$ with a the second-order phase transition $T_i = 150$ MeV and for $g = 5.5$ with the first-order phase transition the initial temperature is $T_i = 135$ MeV.

Figure 4.5a and 4.5b show the results of these calculations. In the previous calculations a phase transition could not be observed if the particle temperature was changed in a box calculation in which the particle number and density was kept constant. In this scenario the particle number is still constant but the particle density is changed by a volume change. Figure 4.5a shows a comparison between the equilibrium model and the expansion scenario. Despite the constant particle number, the order parameter shows a phase transition and even the type of phase

transition (first-order, second-order or crossover) is preserved. Surprisingly, the temperature of the phase transition is shifted in all three scenarios to about 20 MeV lower temperatures. The exact amount of this shift depends heavily on the density scaling (4.24) and the initial condition.

The interesting point in this scenario is the seeming restoration of the phase transition behavior. Seemingly, because this kind of phase transition is not a proper phase transition in terms of equilibrium physics. The total particle number is kept constant due to the lack of chemical processes. Figure 4.2 shows the equilibrium behavior of the particle density at the chiral phase transition. A rapid change of the density can be observed at and near T_c. This change is a result of the self-consistent coupling between particles and the chiral fields which is not given in this scenario. The effect of this phase transition-like behavior could be called pseudo phase transition and is a non-equilibrium effect caused by the non-thermal particle density.

The scenario in this section is not directly applicable to a heavy-ion collision because the system in this scenario performed an adiabatic expansion and could thermally equilibrate and the mean field σ-value was able to relax to a stable value. However, this scenario still gives important hints for an expanding system like a fireball in a heavy-ion collision. A rapid expansion will at some point leads to a decoupling of chemical processes, causing an effective freeze-out of chemical processes. Additionally, the timescale for chemical equilibration is typically very large $\tau_{\text{ch}} \sim 200$ fm/c [74, 75] and therefore larger than the scale of the fireball in a heavy-ion collision. From a theoretical point of view a rough estimation can be derived for the collision rate in the system. The collision rate within a particle-cell is proportional to the number of possible collision partners

$$R_{\text{coll}} \sim N_{\text{cell}} \left(N_{\text{cell}} - 1\right) \approx N_{\text{cell}}^2 \ . \tag{4.25}$$

For a linear expanding system the following scaling for the number of particle per cell can be estimated by

$$N_{\text{cell}} = V_{\text{cell}} \cdot \rho_{\text{cell}} = V_{\text{cell}} \frac{N_0}{V_{\text{system}}} = \frac{V_{\text{cell}} \cdot N_0}{\left(L_0 + \Delta L \cdot t\right)^3} \ . \tag{4.26}$$

Combing the two equations leads to a scaling of the collision rate

$$R_{\text{coll}} \sim \frac{1}{1 + \frac{L_0}{\Delta L} t} \ . \tag{4.27}$$

The collision rate within a system with an initial radius of 1 fm and the same expansion rate would drop to 1.5% of the initial rate after 1 fm/c.

These circumstances indicate that a fast expanding system will run out of chemical equilibrium at some point in time, stopping chemical processes and leading to a particle density different to the system's temperature. Any kind of phase transition seen at that or a later point in the evolution will probably show effects of these deviation from chemical equilibrium, changing properties like the temperature or the order of the chiral phase transition. This is important because the

latent energy of the phase transition will lead to a reheating of the medium [52, 76], such an effect depends on the properties of the phase transition. Furthermore, if T_c depends on the expansion and the density of the system, parameter like the initial system size and density are also important for the T_c in such a non-equilibrium expansion scenario.

4.3 Summary

In this part the dynamics and effects of non-equilibrium deviations have been discussed. Non-equilibrium is a broad concept and in this chapter the deviations from thermal and chemical equilibrium of the particles in the linear σ-model have been investigated.

Non-equilibrium deviations occur if a thermal system undergoes a rapid change of state, for example in a rapid expansion or in presence of an external field, or if the system evolution already starts in a situation far from equilibrium, for example in a heavy-ion collision.

Thermal off-equilibrium occurs if the particle's distribution function $f(\mathbf{p})$ differs from the Boltzmann or Fermi-distribution. Effects for thermal deviations have been discussed in Section 4.1. Any deviation from the equilibrium distribution lowers the scalar density $\left\langle \bar{\psi}\psi \right\rangle$, as shown in Figure 4.3a and 4.3b, leading to different stability points in the equations of motion. Overall, thermal deviations do not only change the temperature of the phase transition to higher temperatures, but can also change the order of the phase transition, as shown in the phase diagram of the order parameter for a non-equilibrium particle distribution function in Figure 4.4.

In Section 4.2 effects of deviations from chemical equilibrium have been discussed. The focus was on deviations from the equilibrium particle density, which always occurs if the system evolves out of an equilibrium configuration and the particle number is kept constant. This can happen if these processes are suppressed or the particle production time scales are larger than the evolution timescales. In such a case the system can evolve through a pseudo-phase transition in which the temperatures of the phase transition are shifted to lower temperatures, as shown in Figure 4.5a and 4.5b.

It has been shown that properties of the chiral phase transition of the linear σ-model can be understood in terms of equilibrium calculations. Nevertheless, any deviations from equilibrium can drastically change the dynamics of this phase transition and systems far from equilibrium can be compared hardly to the phase-diagram for thermal and chemical equilibrium. Interestingly, deviations can both increase or decrease the temperature and change the order of the phase transition. Such findings complicate the discrimination of the type of phase transition in a highly dynamic system like in a heavy-ion collision.

All discussed scenarios in this section are "artificial" setups, explicit forbidding reactions or adiabatic expansions. Chemical or thermal equilibrium can not be reached in these scenarios

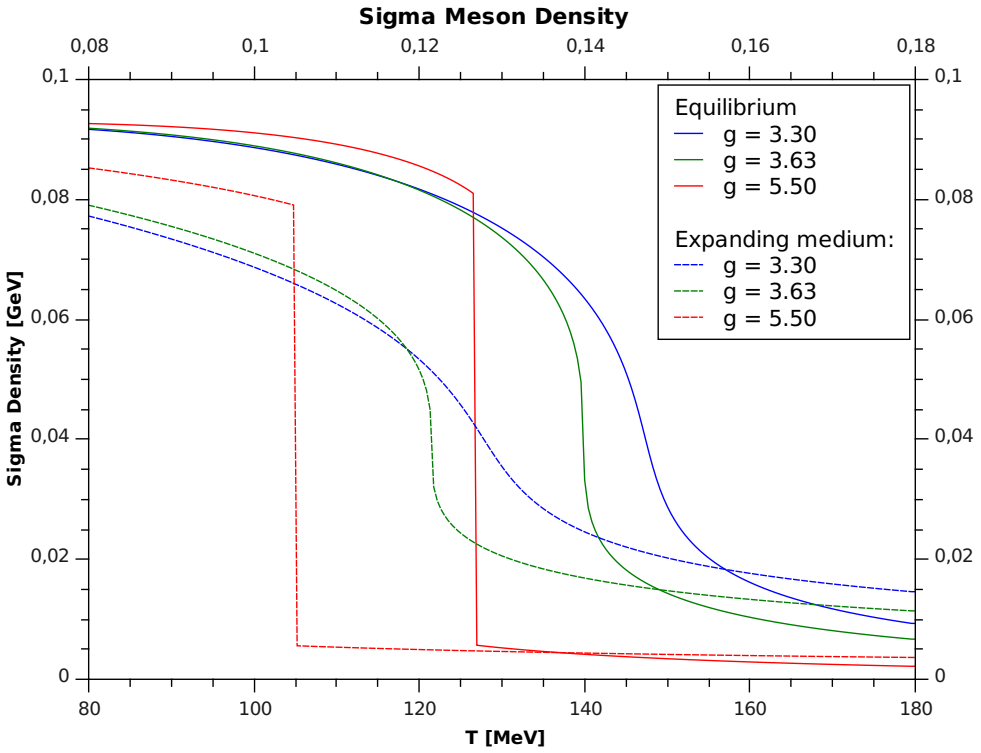

(a) Temperature dependence of the order parameter $\langle\sigma\rangle$.

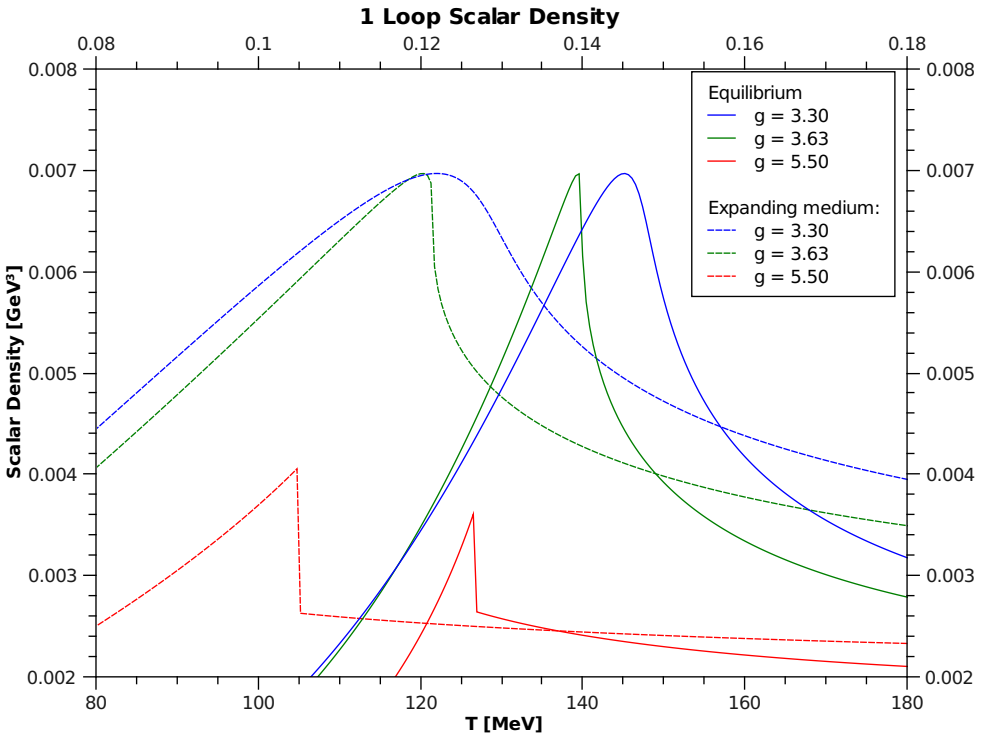

(b) Temperature dependence of the one-loop scalar density $\langle\bar{\psi}\psi\rangle$.

Figure 4.5: Comparison of the temperature behavior of the linear σ-model for a simulation in full thermal and chemical equilibrium (solid line) and for a simulation in which the particle density deviates from equilibrium (dashed line). The total particle number is constant in this non-equilibrium scenario, the density changes by an expansion of the system. The order of the phase transition for the different couplings g are the same in comparison to the equilibrium scenario but the temperature T_c of the phase transition is shifted to lower temperatures.

which do not allow a full and reliable discussion of non-equilibrium reactions. Therefore the DSLAM model will be extended with chemical processes in the next chapter to allow a more realistic simulation for fully dynamic systems.

Chapter 5

Extension of the DSLAM Model

> Wir müssen wissen und wir werden wissen!
>
> David Hilbert

The DSLAM model (**D**ynamical **S**imulation of a **L**inear sigm**A** **M**odel) has been introduced in Chapter 2.2. All interactions are restricted to elastic interactions between particles, potential interactions between fields and a mean field Yukawa-like coupling between particles and fields. Chemical processes are not implemented, leading to a constant particle number, independent of the system's initial conditions.

Ignoring particle-number changing processes can prevent global thermalization, as shown in Section 3.3 or change the system dynamics, as discussed in Section 4.2.

The model is extended in this section with annihilation and pair-production processes, allowing both chemical and thermal equilibration between fields and particles.

Particle production and annihilation is motivated by the coupling term between the chiral fields and fermionic quarks in the interaction-part of the linear σ-model's Lagrangian

$$\mathcal{L}_{\text{int}} = -\bar{\psi}\left[g\left(\sigma + i\gamma_5 \boldsymbol{\pi}\cdot\boldsymbol{\tau}\right)\right]\psi \ , \tag{5.1}$$

which describes a Yukawa-like interaction. In terms of Feynman diagrams this coupling can be interpreted as inelastic processes, which are

particle annihilation

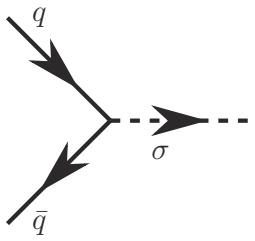

and particle pair production

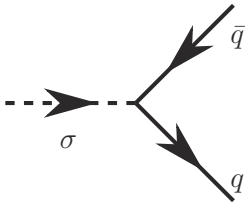

The annihilation of a quark and an anti-quark generates an unstable σ particle, which can decay again to a quark-anti-quark pair.

Such kind of interaction terms for particle production are widely used in effective theories [77–79]. In case of the DSLAM model, particles and fields are approximated to classical, spinless particles and scalar fields, which changes the type of involved fields in the interaction Lagrangian to

$$\mathcal{L}_{int} = g\sigma\phi^*\phi \ , \tag{5.2}$$

while the physical motivation stays the same. The idea of the interaction between fields and particles is discussed in Chapter 7, introducing the particle-field method which is used to numerically implement the interactions between quarks and the sigma field. This chapter discusses the physical properties of these kind of interactions.

Particle annihilation is implemented similarly to the numeric of elastic scattering. For an annihilation process a quark q and an anti-quark $\bar{q}$ have to be in the same cell with volume ΔV. The interaction probability is given by employing a constant and isotropic cross section

$$\Pr\left(\bar{q}q \to \sigma\right) = \hat{\sigma}_{\bar{q}q\to\sigma}\ v_{\text{rel}}\ \frac{\Delta t}{\Delta V N_{\text{test}}} \ , \tag{5.3}$$

with

$$v_{\text{rel}} = \frac{s}{2E_1E_2} \qquad s = \left(p_\mu^1 + p_\mu^2\right)^2 \ . \tag{5.4}$$

The annihilation process is the inverse of the decay process $\sigma \to \bar{q}q$ which describes the decay of an unstable σ-particle. The cross section $\hat{\sigma}_{\bar{q}q\to\sigma}$ is therefore chosen to be the Breit-Wigner cross section [80, 81] which depends on the production threshold of the σ-particle, its mass m_σ and the width Γ of this particle [80]

$$\hat{\sigma}_{\bar{q}q\to\sigma}(s) = \frac{\Gamma^2}{\left(\sqrt{s} - m_\sigma\right)^2 + \left(\frac{1}{2}\Gamma\right)^2} \ , \tag{5.5}$$

with

$$\Gamma = \frac{g^2}{8\pi m_\sigma}\sqrt{1-\left(\frac{2m_q}{m_\sigma}\right)^2} \ . \tag{5.6}$$

The decay width of an unstable scalar particle can be derived from the interaction Lagrangian (5.2) and can be found in Appendix D.4.

The quark mass is given by

$$m_q^2 = g^2\left(\sigma^2 + \boldsymbol{\pi}^2\right) \ . \tag{5.7}$$

The mass of the sigma meson, m_σ, can be calculated in equilibrium from the thermodynamic potential via

$$m_\sigma^2 = \frac{\partial^2\Omega}{\partial\sigma^2} \tag{5.8}$$

with σ at its equilibrium value. The DSLAM model is a dynamic simulation with scope on non-equilibrium calculations. A global temperature does not always exist in non-equilibrium situations, which would be needed to derive the equilibrium mass of the sigma. Nevertheless the mean field value of $\langle\sigma\rangle$ is always given and can be used to derive a mass. Therefore the thermodynamic relation in (5.8) $T \to m_\sigma$ is changed by using $\langle\sigma\rangle \to m_\sigma$. This is done by inverting the calculation

$$\langle\sigma\rangle(T) \text{ from } \frac{\partial\Omega(T)}{\partial\sigma} \equiv 0 \quad \text{to} \quad T_\sigma(\langle\sigma\rangle) \ . \tag{5.9}$$

This temperature T_σ can be seen as a local, coarse grained, effective temperature, which is derived from the mean field of the system. Overall, this step is a model assumption, because an effective temperature could be derived in other ways, as well. An alternative would be the derivation from local thermal modes on the field. An advantage of this method is that T_σ is in principle completely independent from the quark temperature and can be calculated for every numerical cell. Figure 5.1 shows the calculation for the relation $\langle\sigma\rangle \to T_\sigma$ and the employed numerical parameterization of this plot. The details of the parameterization can be found in the chapter on the numerical implementation in Section 8.8.

By using the relation $T_\sigma\left(\langle\sigma\rangle\right)$, a relation for $m_\sigma\left(\langle\sigma\rangle\right)$ can be numerically calculated. Before this is done, the dynamics of m_σ should be considered. For the coupling $g = 3.3$ and $g = 3.63$ the order parameter is always defined; for $g = 5.5$ the thermal behavior of the order parameter shows a discontinuity. Furthermore, this implies that m_σ is bijective for $\sigma \in [0, 93 \text{ MeV}]$ for $g = 3.3$ and $g = 3.63$ but not for $g = 5.5$. To get a feeling for the behavior of the σ-mass, the mass can be calculated in the complete $T - \sigma$ plane and not only at $\sigma = \sigma_{eq}$. Figure 5.2a shows the behavior of the mass in the crossover scenario, the equilibrium mass is always positive defined. Figure 5.2b shows the same calculation for the second-order phase transition scenario. The mass becomes 0 at the phase transition and the equilibrium line touches the red-colored region which indicates a tachyonic configuration, however the mass is always $m_\sigma \geq 0$. A different situation occurs

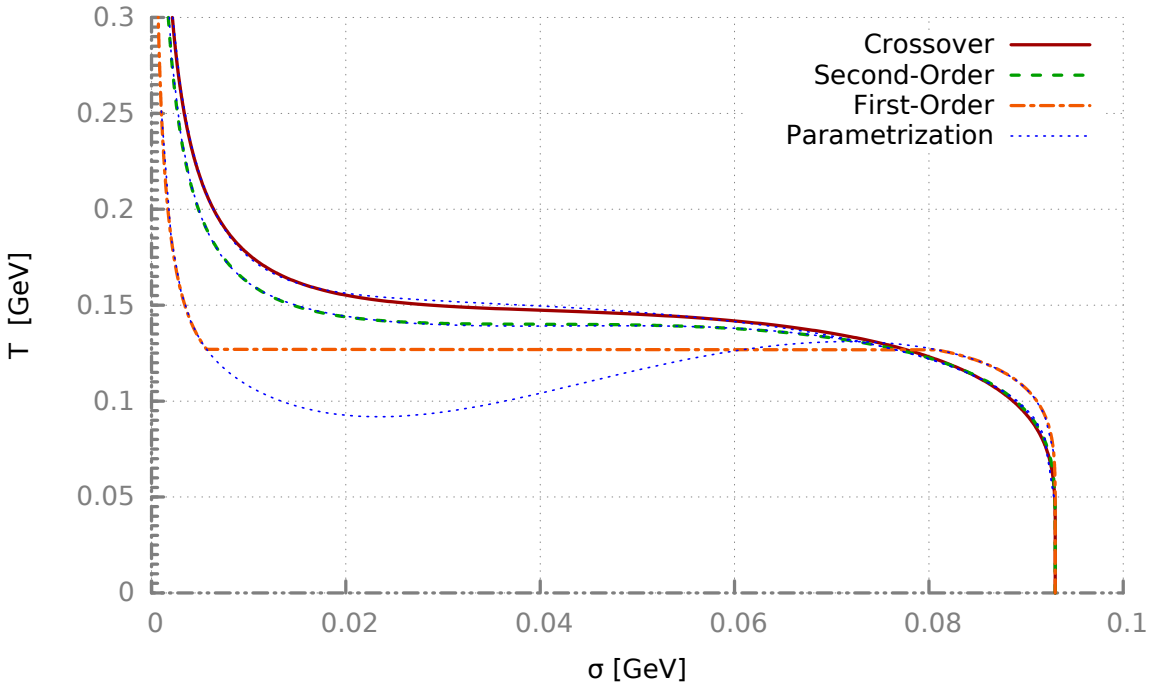

Figure 5.1: The inverse phase-diagram of the mean field $\langle\sigma\rangle$ (colored lines), which is used to dynamically derive a temperature from the current value of the mean field. A numerical implementation has been done with a parameterized version of this plot, which is indicated by the blue, dotted lines. The phase-diagram with the first-order phase transition has a discontinuity at $T_c = 126$ MeV, leading to a region of constant temperature over a wide range for $\langle\sigma\rangle$.

in the first-order phase transition, as shown in Figure 5.2c. In this case the mass $m_\sigma\left(T, \langle\sigma\rangle\right)$ becomes a piece-wise defined function which is divided by a region of negative, tachyonic mass with $m_\sigma^2 < 0$. There is no configuration in which the mass stays positive at the phase transition. So the non-physical region can not be avoided. This is a problem when a parameterization for $m_\sigma(\langle\sigma\rangle)$ should be calculated.

Figure 5.3 shows the parameterization for the mass at a given σ-value. This parameterization is used to derive m_σ in a non-equilibrium configuration in which the fields' and particles' temperature diverge. Such a numerical calculation can easily be performed for the crossover and second-order phase transition. For the first-order phase transition the tachyonic parts have to be considered. Within the regions which are defined by the equilibrium phase-diagram, there is $m_\sigma > 0$ for all $\langle\sigma\rangle$. In contrast, σ-configurations between the phases are not defined. This range is given for $g = 5.5$ by

$$\sigma_{\text{non-therm}} = \left(\sigma\left(T_c^-\right), \sigma\left(T_c^+\right)\right) \approx (7.5 \text{ MeV}, 75 \text{ MeV}) \ . \tag{5.10}$$

Values within this region are not given by the phase-diagram and are indicated by the line of constant temperature in Figure 5.1. Furthermore, the squared mass becomes negative in this region $m_\sigma^2 < 0$. It is not clear how this scenario should be treated in the linear σ-model at this

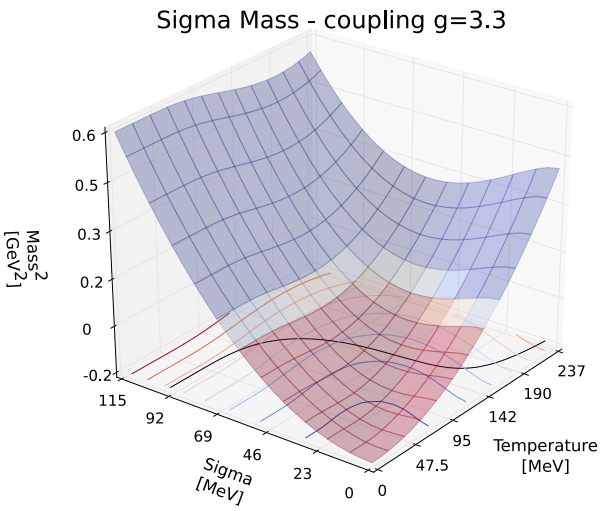

(a) Crossover transition with $g = 3.3$

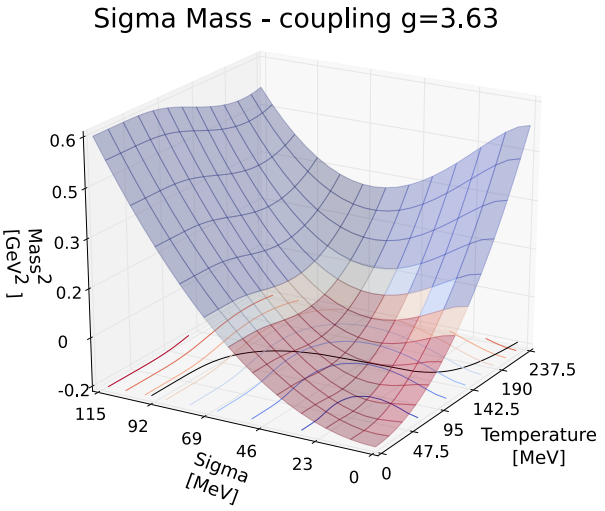

(b) Second-order transition with $g = 3.63$

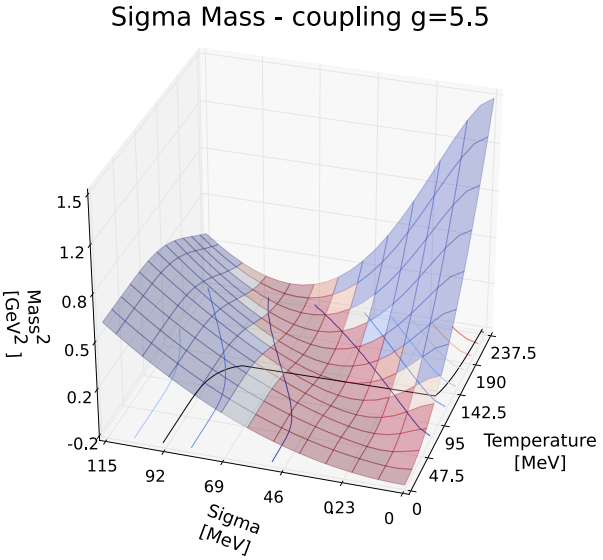

(c) First-order transition with $g = 5.5$.

Figure 5.2: m_σ^2 for different coupling strengths, temperatures and mean field configurations. Blue regions indicate $m_\sigma^2 > 0$, red colored regions indicate negative and tachyonic mass configurations with $m_\sigma^2 < 0$. Black lines indicate the equilibrium configurations in the linear σ-model.

level. Tachyonic particles are a known phenomena in scalar theories [82]. In the DSLAM model one assumes $m_\sigma \equiv 0$ in this region, leading to an effective suppression of $\bar{q}q \leftrightarrow \sigma$ interactions.

Employing a Breit-Wigner cross section and the decay-width for the sigma mesons (see (7.90)), the annihilation probability for quark-anti-quark production in a cell can be calculated. This probability is sampled using Monte-Carlo techniques and in case of an interaction the energy

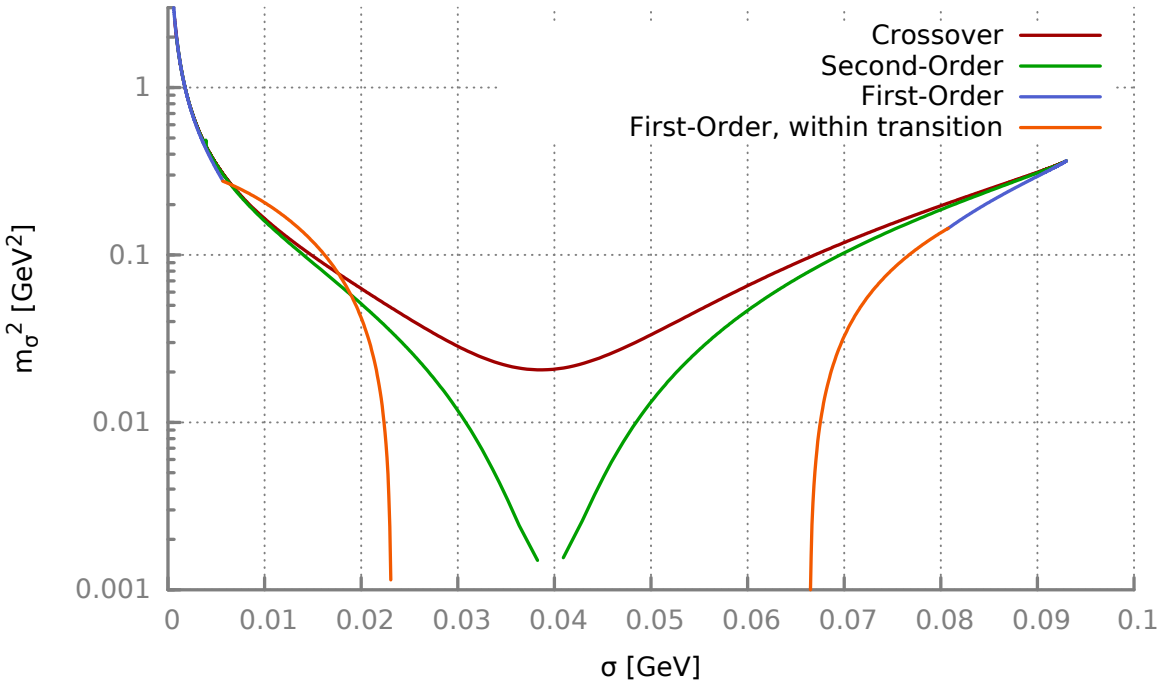

Figure 5.3: Calculation for the relationship $\langle\sigma\rangle \rightarrow m_\sigma^2$. The mass is always positive defined for the crossover transition. For the second-order phase transition the mass shorty reaches zero at the phase transition. In case of the first-order phase transition the physical region is very small (blue line). The mass-parameterization can be extended by deriving m_σ^2 with the temperature of the phase transition ($T_c \approx 126$ MeV) and by using an analytic continuation for σ (instead of the equilibrium σ_{eq}). As a result the mass-relation shows a kink at the region where the $\sigma - T$ combination differs from the equilibrium configuration.

and momentum of the particle pair will be transferred to the sigma field using the particle-field method as described in Section 7.4.4.

To implement the decay process $\sigma \rightarrow \bar{q}q$, some additional physical modeling has to be done. The DSLAM model does not directly implement σ-particles, but instead a scalar classical field is used to describe the field-configuration. Such a field has a single value at every point on the grid and does not have any particle-like properties. However a particle density has to be derived to sample discrete decay-events which can generate quark pairs.

The basic idea is to derive a particle distribution function $f_\sigma(\mathbf{x}, \mathbf{p})$ for σ particles at every grid point. This is done by assuming thermal local equilibrium at every grid point and sampling particles from f_σ which then can be used to calculate decay probabilities. As an equilibrium distribution, the massive, isotropic Boltzmann distribution has been chosen for f_σ. The distribution function can now be fully described by its temperature T and its mass. The sigma particles should be allowed to have a different occupation number in comparison to its temperature, allowing a different n_σ than given by the equilibrium distribution. Therefore the following ansatz has been chosen: The temperature of the distribution is given by the inverse phase diagram for $\langle\sigma\rangle \rightarrow T$.

The same is done for the mass $\langle\sigma\rangle \to m_\sigma$. For the particle density a second value is used, the energy density of the field. This ansatz allows to derive both a temperature and particle density from the scalar fields properties σ and $\dot{\sigma}$. Depending on the temperature of the field, different cases have to be discussed.

f_σ is chosen to be the massive Boltzmann distribution

$$f_\sigma(\mathbf{p}) = d_g 4\pi E \cdot |\mathbf{p}|\, e^{-E/T} \ . \tag{5.11}$$

The equilibrium density is given by

$$n_\sigma = d_g \cdot m^2 \cdot T \cdot K_2\left(\frac{m}{T}\right) \ , \tag{5.12}$$

with the modified Bessel function of the second kind K_2. Therefore equilibrium energy density becomes:

$$\langle\epsilon\rangle = \int \mathrm{d}E\ E^2 \cdot |\mathbf{p}|\, e^{-E/T} = m^2 \cdot T\left[mK_1(m/T) + 3TK_2\left(m/T\right)\right] \tag{5.13}$$

with the known relation $6T^4 = 3nT$ in the limit for $m \to 0$ .The energy density (5.13) is plugged into (5.12) to derive a local equilibrium particle density for a given energy density $n(\epsilon(T))$. Equation (5.13) is rewritten

$$\frac{\left(\langle\epsilon\rangle - m^3 \cdot T \cdot K_1\left(m/T\right)\right)}{3m^2\ T^2} = K_2(m/T) \ , \tag{5.14}$$

which is plugged into (5.12)

$$n_\sigma(\langle\epsilon\rangle) = \frac{\langle\epsilon\rangle - m^3\ T\ K_1(m/T)}{3T} \tag{5.15}$$

with $\langle\epsilon\rangle/3T$ in the limit for $m \to 0$.

A special case is the vacuum $T_\sigma \to 0$, or in case of non-equilibrium system-configurations for $\sigma \geq \sigma_{\mathrm{vac}} = 93$ MeV, in which the σ-particles are assumed to have no thermal energy and only have rest-mass only. In this case the particle density becomes

$$n_\sigma \to \frac{\langle\epsilon\rangle}{m_\sigma} \quad \text{for } T \to 0 \ . \tag{5.16}$$

With these parameterization and approximations the local distribution function f_σ can be determined for every grid cell of the σ mean field. Using T and m_σ, a single particle can be sampled from f_σ and its decay probability (5.6) can be calculated. Instead of performing a Monte-Carlo sampling of the decay probability with many potential decay-particles, only one particle is sampled per cell and time-step and its decay probability is weighted with the local density n_σ

$$P(\sigma \to \bar{q}q) \sim \Gamma \cdot n_\sigma \ . \tag{5.17}$$

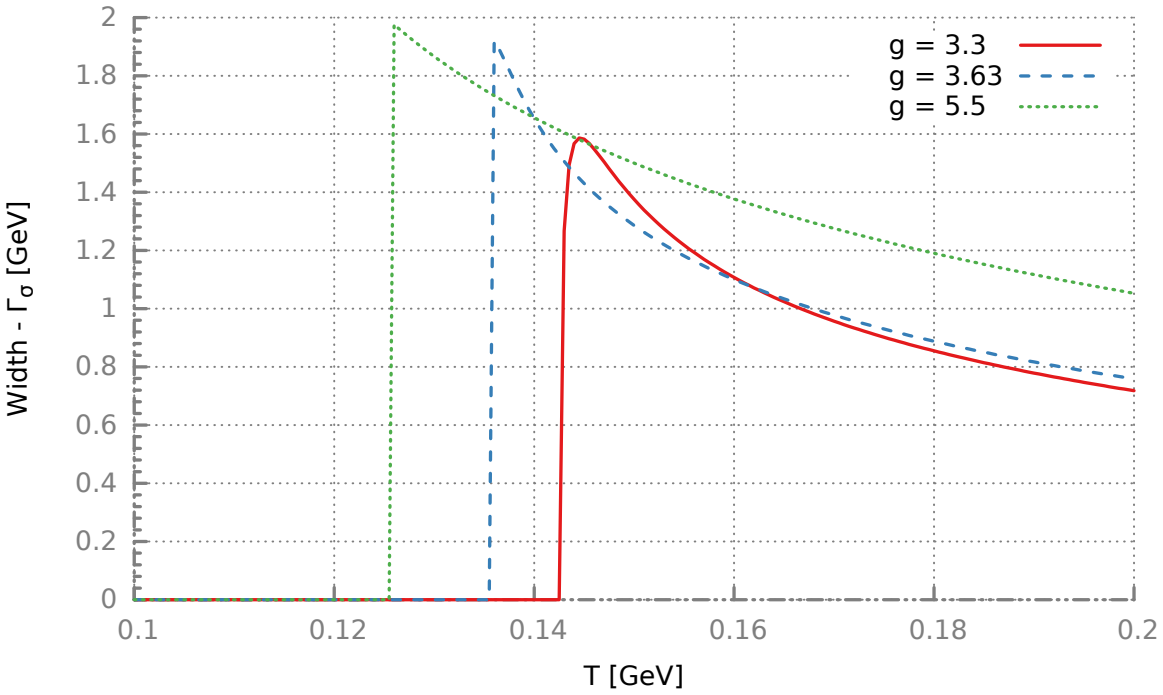

Figure 5.4: Width of the σ-meson, which is used in the Breit-Wigner cross section. The width is calculated from the scalar σ decay-channel (5.6). Below the phase transition in the chiral broken phase, the σ can not decay anymore to quarks because the energy is below the production threshold $m_\sigma < 2m_q$.

This is a valid approximation for the exponential decay probability if $P(\sigma \to \bar{q}q) \cdot \Delta t \ll 1$.

Thermalization Processes and Implementation Considerations

In this paragraph, the DSLAM model was extended with chemical processes between particles and the mean field $\sigma \leftrightarrow \bar{q}q$. The scope of this extension is to implement an effective mechanism which allows both damping of field-excitations and the generation of dynamic fluctuations on the field. Additionally, both particles and fields should be able to equilibrate with this mechanism, leading to the same temperature of the fields and the particles as well as the equilibrium particle density. This implies for an equilibrium state equal rates for both processes

$$\langle R_{\sigma \to \bar{q}q} \rangle_{\mathrm{eq}} = \langle R_{\bar{q}q \to \sigma} \rangle_{\mathrm{eq}}, \tag{5.18}$$

keeping the particle number constant on average and the same average energy transfer per process

$$\langle E_{\sigma \to \bar{q}q} \rangle_{\mathrm{eq}} = \langle E_{\bar{q}q \to \sigma} \rangle_{\mathrm{eq}}, \tag{5.19}$$

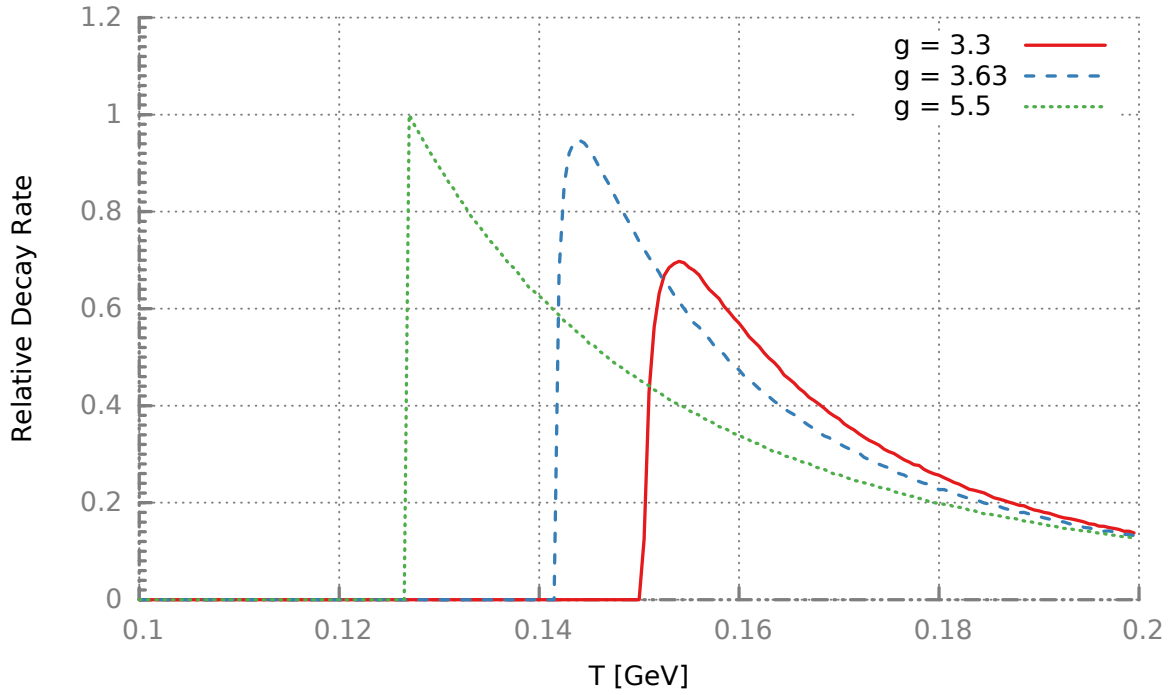

Figure 5.5: Relative reaction rates for the Breit-Wigner cross section, including relativistic effects of the changing m_σ. The rates are normed to the highest rate, which is given by $g = 5.5$.

which keeps the temperature constant for both systems. From the physical point of view, this is guaranteed by using a self-consistent coupling between particles and fields with the decay-width (5.6) and annihilation cross section (5.5), leading to microscopic detailed balance.

From the numerical point of view, this point is very critical because it means a high demand of precision for the parameterization $\langle\sigma\rangle \to T_\sigma$ and $\langle\sigma\rangle \to m_\sigma$ and an accurate sampling of f_σ.

An imbalance of reaction rates would force the system to run out of chemical equilibrium. The same is true if the average energy transfers per process are not correct, because the particle density is derived from the σ-field's energy density. An artificial lowering of the energy density directly implies a lower particle density n_σ, leading again to a runaway from the chemical equilibrium. The importance of global energy conservation can not be stressed enough at this point.

The performance of this method for equilibrium systems is shown in the Section 7.4.4 of the particle field method, in which a thermal box is initialized with the annihilation and decay processes described in these Sections.

The DSLAM model is now extended with chemical processes, allowing an effective thermalization of both fields and particles. This method is now applied to several calculations in the next chapters.

Chapter 6

Calculations with Chemical Processes

> Let us calculate, without further ado, to see who is right. Calculemus!
>
> Gottfried Wilhelm Leibniz

6.1 Thermal Quench with Chemical Processes

In Section 3.3 calculations for a thermal quench are shown. A system is initialized in thermal and chemical equilibrium for the fields and quarks. In a second step, the quarks are reinitialized at a different temperature, leading to a different energy distribution and density of the quarks which induced a global non-equilibrium situations. The results in Section 3.3 showed that the system can not evolve to an equilibrium state if no particle production and annihilation processes are included in the model.

In Chapter 5 the extension of the DSLAM simulation with chemical processes was discussed. This chapter performs the same calculation with a quench of the particles, the equilibration behavior and the impact of the production and annihilation processes is investigated. Due to the implementation of the processes $\sigma \leftrightarrow \bar{\psi}\psi$ the system should be able to equilibrate both locally and globally.

Two scenarios are shown in this section. The first is a scenario, in which only a small temperature quench in the chiral restored phase is performed, keeping the total system in the chiral restored phase. In the second scenario a stronger temperature quench is performed which drives the system through the chiral phase transition.

6.1.1 Small Temperature Quench

The system is initialized in an isotropic and periodic box. Quarks are sampled at an initial temperature of $T = 140$ MeV, the σ-field was initialized at a temperature of $T = 180$ MeV. This kind of quench should result in a final system state in which the system stays in the chiral-restored phase after thermalization.

Figure 6.1 shows the results of the calculation. The system was initialized with the following parameters:

Parameter	System Value
T_σ	180 MeV
$T_{\bar{q}q}$	140 MeV
V_{system}	1 fm^3
coupling g	3.3
N_{test}	$2 \cdot 10^6$
Δt	0.002fm/c
σ_{elastic}	15 mbarn
$\sigma_{\text{inelastic}}$	$\rightarrow$ Breit-Wigner
heat bath	disabled

The calculation was performed with the coupling for a crossover phase transition $g = 3.3$, however no qualitative difference between the different coupling strength was observed. The pair production and annihilation processes drive the system to thermal and chemical equilibrium. The initial temperature of the σ-field and the quarks differed by 40 MeV, after 20 fm/c the system shows a thermal phase in which the quarks and the fields have the same temperature, as displayed in Figure 6.1c and 6.1e. The total quark number drops rapidly after the simulation starts in Chapter 6.1a because the field was initiated without thermal fluctuations. Figure 6.1b shows how the rates for annihilation and pair production converge after 10 fm/c and start to fluctuate around the same mean value. Figure 6.1d illustrates the shift of energy between quarks and fields. The energy of the quarks drops because of the initial particle annihilation but increases again after the potential energy of the field is transformed to new particles after equilibration. The field's energy raises initially by the added energy from the quark-annihilation but relaxes after equilibration. Figure 6.1d shows the direct correlation between the energy of the σ-field and the quarks. Overall, the total verys well conserved, see Figure 6.1f . Figure 6.1e show the quarks distribution functions. The transformation of the field's potential energy leads to an increase in the particles temperature. This temperature increase of about 3 MeV is not very large because the field's potential energy is much smaller compared to the energy of the particles. However, both fields and particles are not exactly in equilibrium, because the particle number does not correspond to the equilibrium value for the final temperature. In Figure 6.1a one can see that

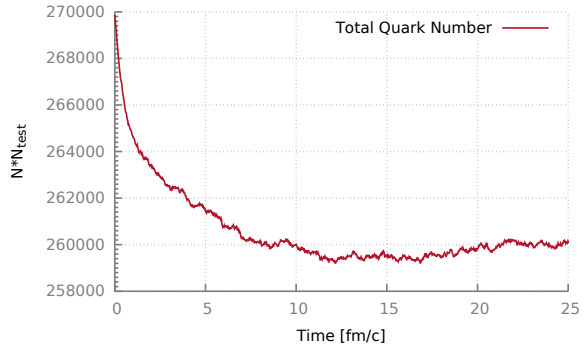

(a) Total number of quarks in the system.

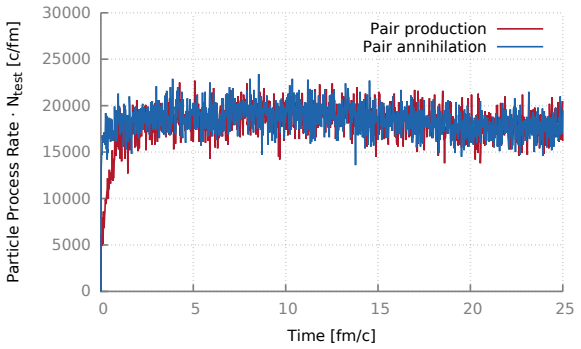

(b) Reaction rate for pair-production and pair-annihilation.

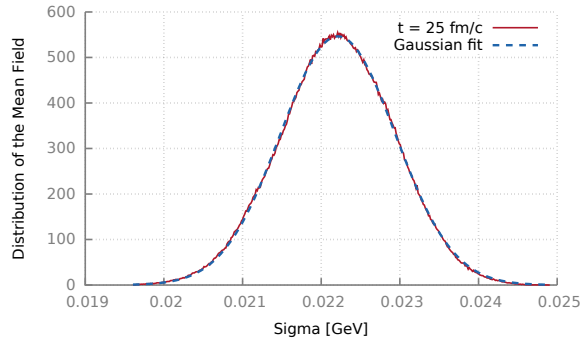

(c) Spatial distribution of the sigma mean field $\langle\sigma(\mathbf{x})\rangle$ after thermalization time $t = 25$ fm/c.

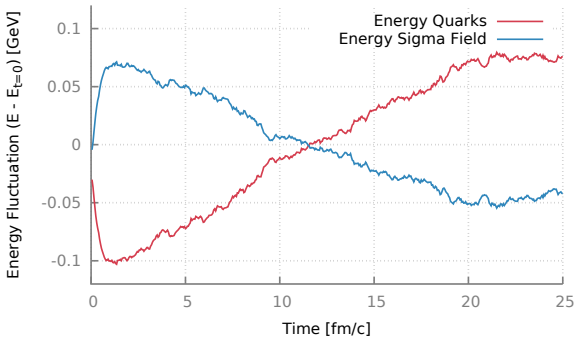

(d) Deviation from the initial energy for the quarks and the energy of the field, calculated with $E(t) - \langle E(t=0)\rangle$.

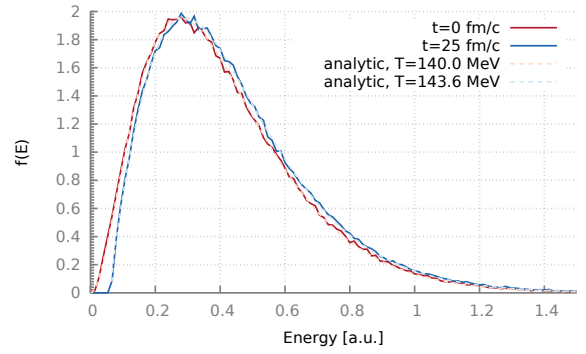

(e) Distribution of the quarks at the beginning of the system and after global thermalization.

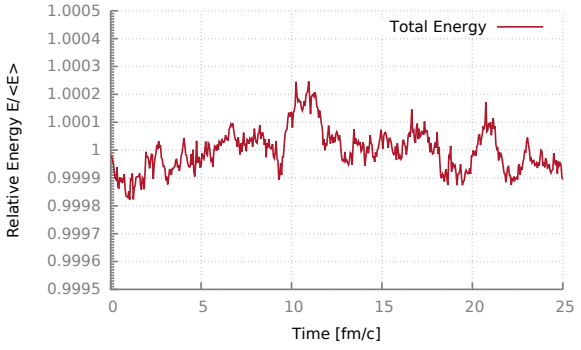

(f) Relative fluctuations of the system's total energy $E(t)/\langle E(t=0)\rangle$.

Figure 6.1: Results for a calculation with the quenched-scenario. Particles and fields can interact and their interaction rates converge after some time, leading the same global temperature. The temperature of the quarks is given by the Boltzmann-distribution, the temperature field is given by the distribution of the field modes, see eq. (7.80).

the particle number is still rising slowly and the mean-value of the σ-field is not exactly at the equilibrium position known from the phase diagram. This final approach takes a long time in this example because the difference in the sigma potential is very tiny at those temperatures, leading to a very weak driving force on the field.

Overall, the system shows a global equilibration. The process $\bar{\psi}\psi \rightarrow \sigma$ creates local and thermal fluctuations on the σ-field. The decay process $\sigma \rightarrow \bar{\psi}\psi$ leads to an effective damping of these fluctuations. Both processes together can drive the system to equilibrium.

6.1.2 Large Temperature Quench

The setup of this calculation is the same as the previous one, with the difference that the temperature of the quarks is far below the temperature of the chiral phase transition, which will drive the initially hot σ-field through the phase-transition, as well.

Figure 6.2f shows results of the calculation. The system was initialized with the following parameters:

Parameter	System Value
T_σ	180 MeV
$T_{\bar{q}q}$	80 MeV
V_{system}	1 fm^3
coupling g	3.3
N_{test}	$2 \cdot 10^6$
Δt	0.002fm/c
σ_{elastic}	15 mbarn
$\sigma_{\text{inelastic}}$	$\rightarrow$ Breit-Wigner
heat bath	disabled

Figure 6.2a to 6.2f display individual observables of the simulation. Figure 6.2e shows the evolution of the σ-mean field. The field starts in the chiral restored phase around $\langle\sigma\rangle \approx 10$ MeV and slowly moves to higher values, which is expected by lower quark density. While moving, the field produces quark anti-quark pairs and gets damped in this process. Figure 6.2b shows the increasing production rate, which rises up to the chiral phase transition, as expected by the Breit-Wigner cross section (see Figures 5.4 and 5.5). The particle number in Figure 6.2a rises as the field moves towards the phase transition. Near and at the transition the process $\sigma \leftrightarrow \bar{q}q$ becomes suppressed and the production and annihilation rates drop because of the sigma mass being below the decay threshold $m_\sigma < 2m_q$. The field becomes undamped, moves faster and oscillates around a new average value. No change in the system behavior can be seen after 10 fm/c, the field shows thermal spatial fluctuations (Fig. 6.2c) but its global value still oscillates undamped as already observed in the first calculations for a simple quench in Section 3.3.

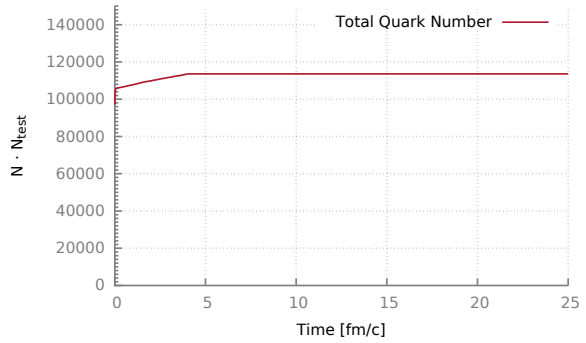

(a) Total number of quarks in the system.

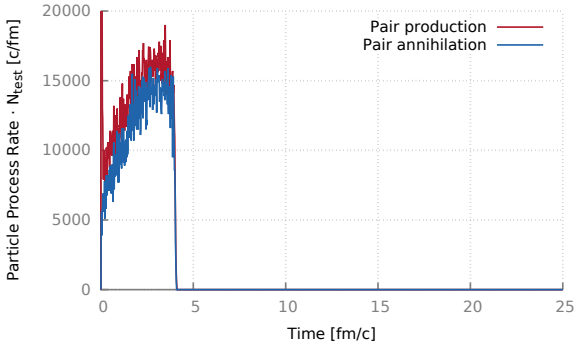

(b) Reaction rate for pair-production and pair-annihilation.

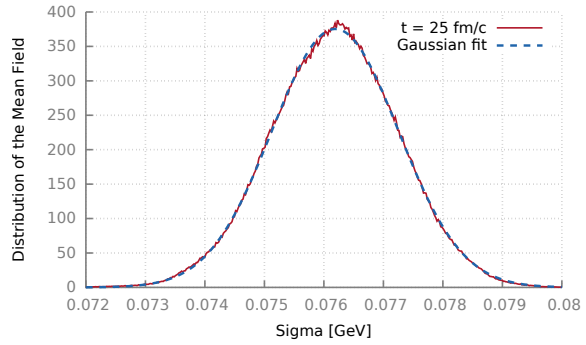

(c) Spatial distribution of the sigma mean field $\langle\sigma(\mathbf{x})\rangle$ after thermalization time $t = 25$ fm/c.

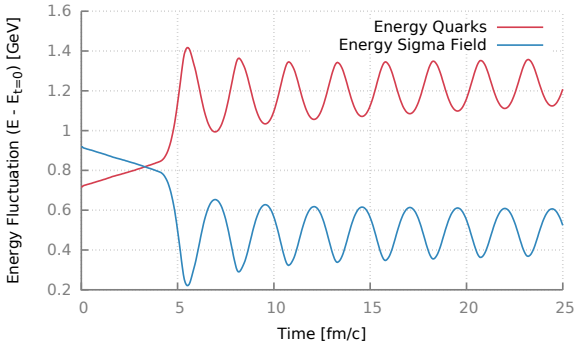

(d) Deviation from the initial energy for the quarks and the energy of the field, calculated with $E(t) - \langle E(t=0)\rangle$.

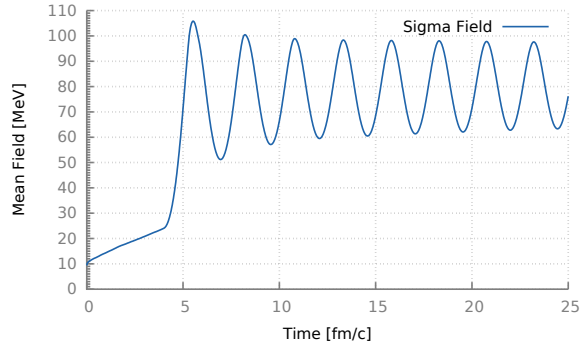

(e) Volume averaged value of the σ-mean field.

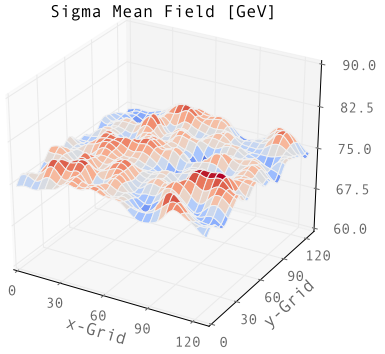

(f) Spatial distribution of the σ-field at $t = 25$ fm/c.

Figure 6.2: Results for a calculation with the quenched-scenario from the initially hot phase to the cold and chiral broken phase. Fields and particles can interact above T_c and the global shift of the σ-field is damped by particle production. At and below T_c field and particles decouple because the σ-particle can not decay anymore. The system becomes undamped and falls in a coherent oscillation.

6.2 Expansion of a Hot Matter Droplet

Previous calculations have been done with model systems in thermal and periodic boxes, which simulate a very large and isotropic system. Such calculations are useful to investigate the basic properties of a model like its thermal and equilibration behavior.

For the next calculations a more complex example is chosen: the expansion of a droplet of hot matter. Such a scenario can be seen as a simple model for a heavy-ion collision, in which two colliding nuclei form a fireball of hot, "exploding" matter.

As an initial condition for this example, the simulation is initialized with a spatial dependent temperature profile for both the quarks and the field. The temperature profile is motivated by a Wood-Saxon like distribution function [83]

$$T(\mathbf{x}) = T_0 \left(1 + \exp\left(\frac{|\mathbf{x}| - R_0}{\alpha}\right)\right)^{-1} , \tag{6.1}$$

with the radius parameter $R_0 = 0.45$ fm and the surface thickness $\alpha = 0.1$ fm. Such a parameterization will result in an effective thickness of around 0.9 fm, however a larger coupling g will increase the effective radius because the chiral phase transition takes place at lower temperatures which are located at the outer region of the blob.

The total system size was chosen to be 5 fm for all dimensions.

All previous simulations were set up to have periodic boundary conditions, simulating an effective microcanonical ensemble. In this case, the system should not be isotropic or periodic in space, the matter droplet should sit in the middle of an "empty" space and should be able to expand arbitrarily. Therefore new boundary conditions are implemented.

Quarks which reach a certain distance from the center of the initial droplet are removed from the system. The distance cutoff is chosen to be $r_c = 2.75$ fm from the center.

The boundary conditions for the fields are a bit tricky, because a simple cutoff is not possible. The best solution would be the implementation of the so-called absorbing boundary conditions (ABC), which perfectly absorb every wave traveling through the boundary, effectively absorbing all its energy [84]. Unfortunately, such boundary conditions are very hard to implement and are computational expensive, especially in three dimensions and to have a good performance their formulation needs to be non-local in time [85]. Still, they have been successfully applied for physical systems like the 3D Schrödinger equation [86].

To keep computational cost reasonable, the boundary conditions are therefore kept periodic, but the outer region of the box are additionally damped with a dissipative term. The σ-field feels

an effective friction $\sim \dot{\sigma}$ for any wave passing the cutoff radius $|\mathbf{x}| > r_c = 2.75$ fm, leading to a strong damping of the waves.

The total energy in this system is not conserved any more and any energy passing the boundary will be damped or removed from the system, preventing an interference with the rest of the system.

In Subsection 6.2.1 calculations with this scenario without the chemical processes $\sigma \leftrightarrow \bar{q}q$ and only mean-field interactions have been performed with the DSLAM model. In Subsection 6.2.2 the same calculations are performed with the full DSLAM model employing chemical processes and isotropic and elastic interactions between quarks. For all three couplings a calculation has been performed. For a consistent comparison between all calculations, the same initial conditions have been chosen for all cases:

for all simulations

Parameter	System Value
T_{initial}	175 MeV
V_{system}	$(6 \text{ fm})^3$
coupling g	$3.3, 3.63, 5.5$
N_{test}	$1 \cdot 10^5$
Δt	0.002 fm/c
r_{quarks}	0.05 fm
t_{run}	20 fm/c

with chemical processes

Parameter	System Value
σ_{elastic}	10 mbarn
$\sigma_{\text{inelastic}}$	Breit-Wigner
$V_{\text{interaction}}$	0.1 fm^3

Graphical plots of the initial conditions for the σ-field and the quarks for the different couplings g are shown in Figure 6.3. The qualitative shape of the σ-field shows a chiral-restored phase in the middle of the box with a sharp crossover to cooler, outer regions. The quark-distribution shows a smooth shape with a sharp peak in the chiral-restored region. This peak is explained by the smaller mass of the quarks in this region, strongly increasing the quark-density.

6.2.1 Expansion Scenario without Chemical Processes

Calculations of hot, exploding matter droplets within chiral models have already been performed in previous studies. They have found the induction and amplification of oscillations in the chiral fields for rapid expansion processes [87] or the formation of shell-like structures [88] which can be explained by kinematic effects [89].

Figure 6.4 shows the time evolution for a system with a crossover transition for $g = 3.3$, Figure 6.5 the evolution for a system with second-order phase transition for $g = 3.63$ and in Figure 6.6 the same calculation is shown for a system with a first-order phase transition. Figure 6.7 and 6.8

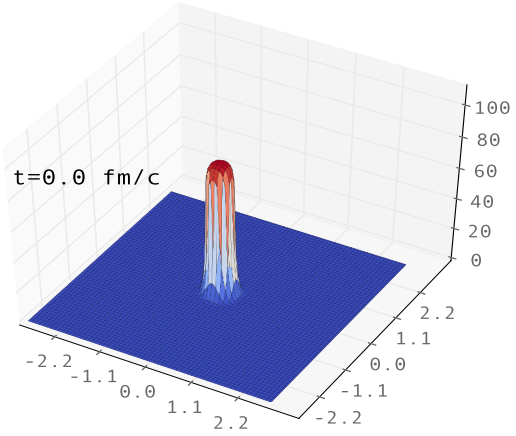

(a) Initial σ-field for $g = 3.3$

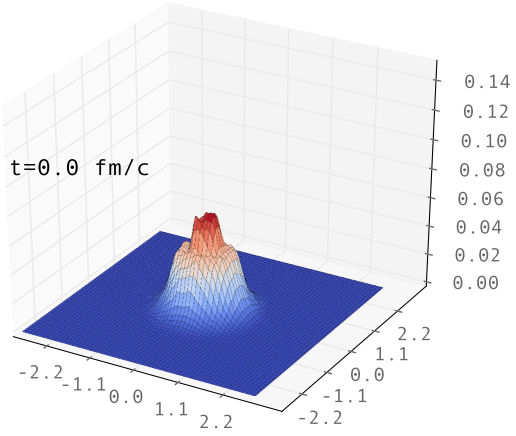

(b) Initial quark distribution for $g = 3.3$

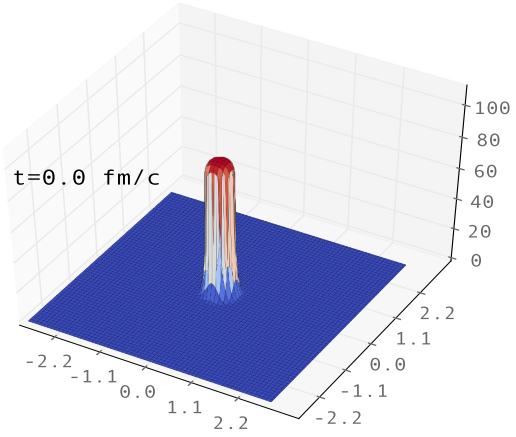

(c) Initial σ-field for $g = 3.63$

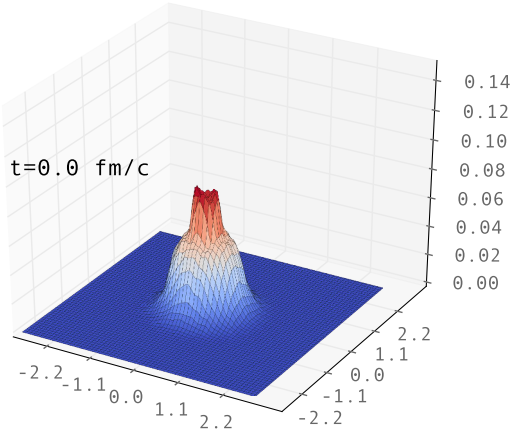

(d) Initial quark distribution for $g = 3.63$

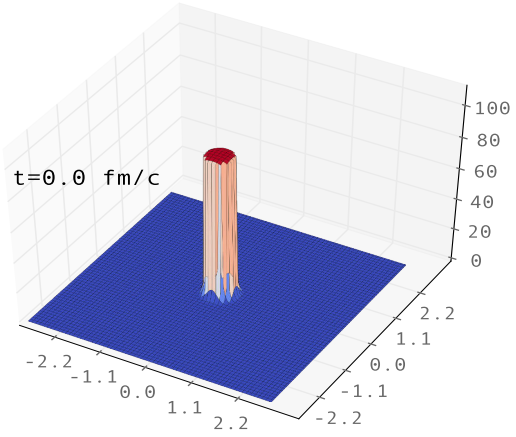

(e) Initial σ-field for $g = 5.5$

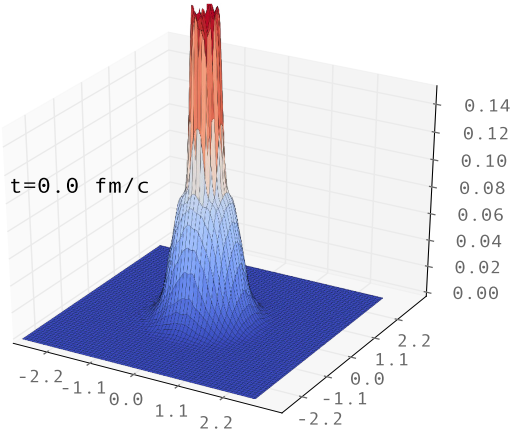

(f) Initial quark distribution for $g = 5.5$

Figure 6.3: Initial conditions of the hot matter-droplet scenario for different coupling strengths. The x- and y-axis show the spatial distance from the origin in fm/c. The z-axis of the σ-plots show the deviation from the vacuum expectation value $\langle\sigma\rangle - \sigma_0$ in MeV. The quark densities are given in $1/\text{fm}^3$.

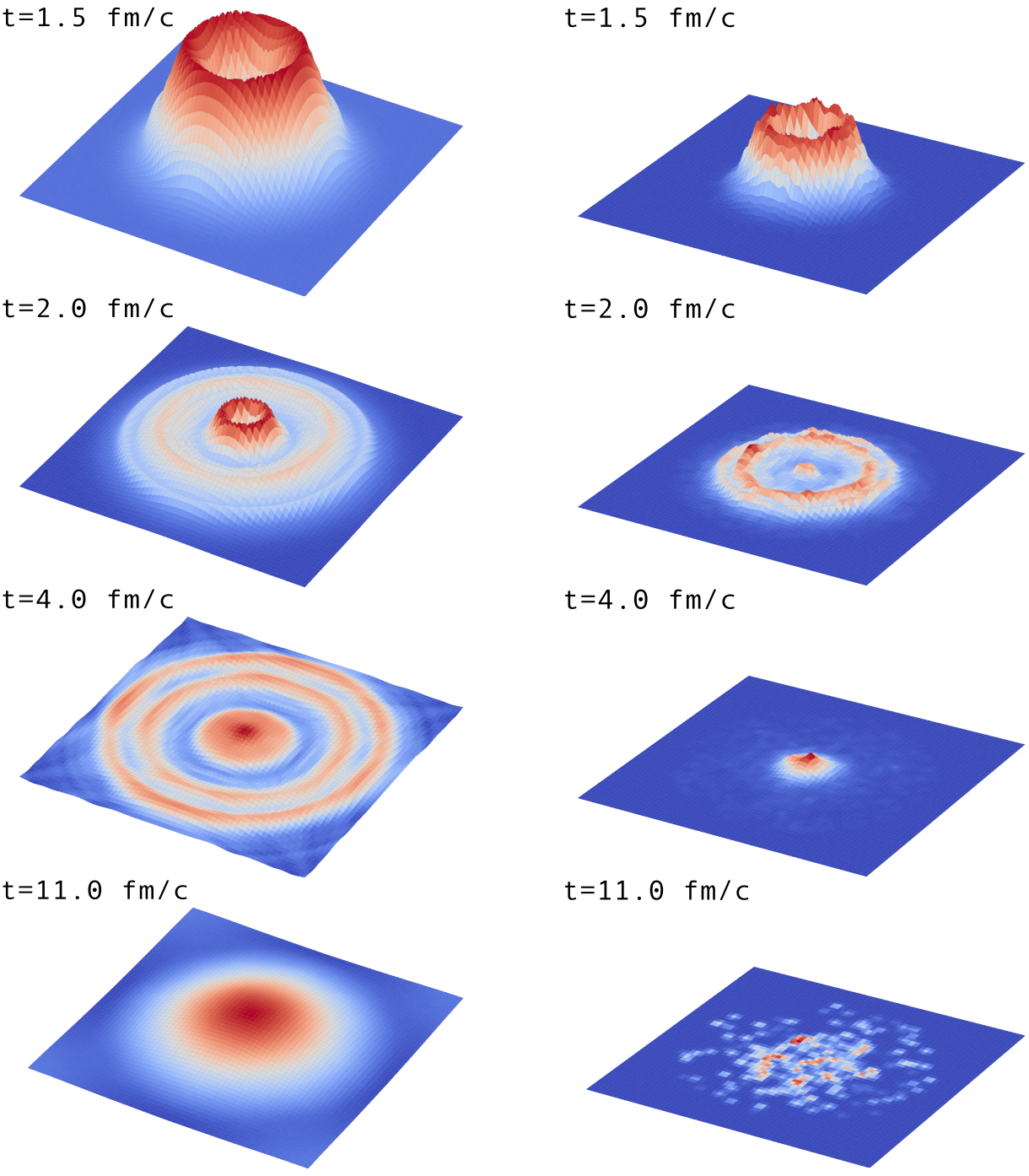

(a) Spatial distribution of the σ-field, cut in the center of the z-plane.

(b) Spatial distribution of the quark density, cut in the center of the z-plane.

Figure 6.4: Time evolution of the hot matter-droplet scenario for $g = 3.3$ with a crossover phase transition and no chemical interactions. **Left:** Deviation of the σ-field from its vacuum value $\langle\sigma_{\text{vac}}\rangle - \langle\sigma\rangle$. **Right:** Total quark density. The scale is the same as in Figure 6.3.

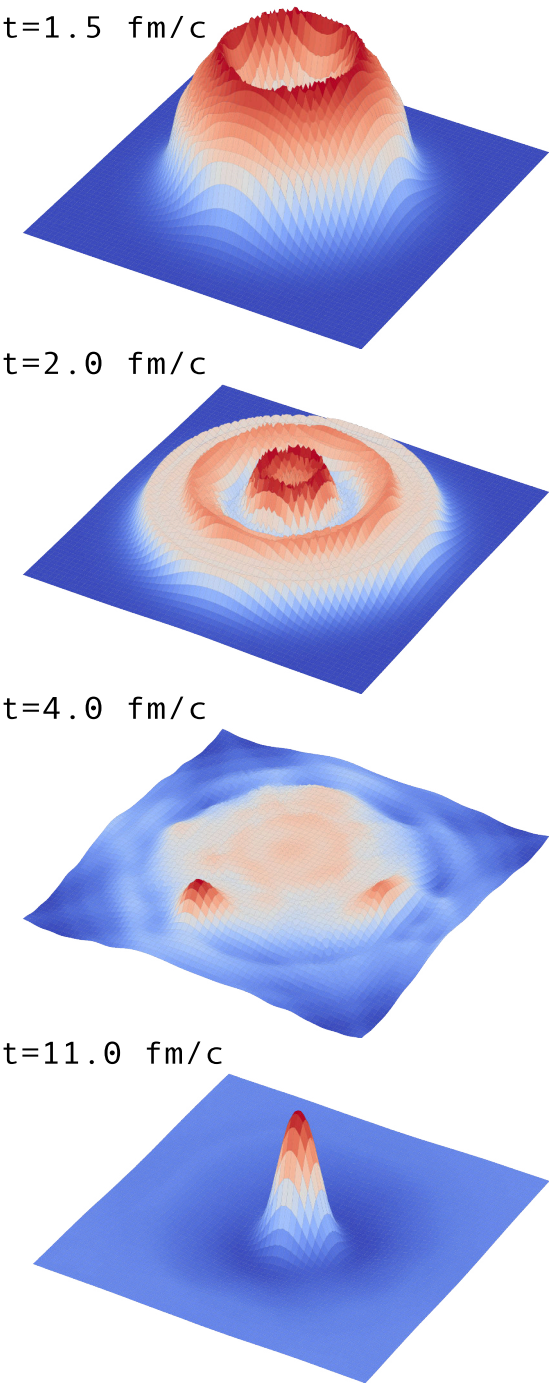

(a) Spatial distribution of the σ-field, cut in the center of the z-plane.

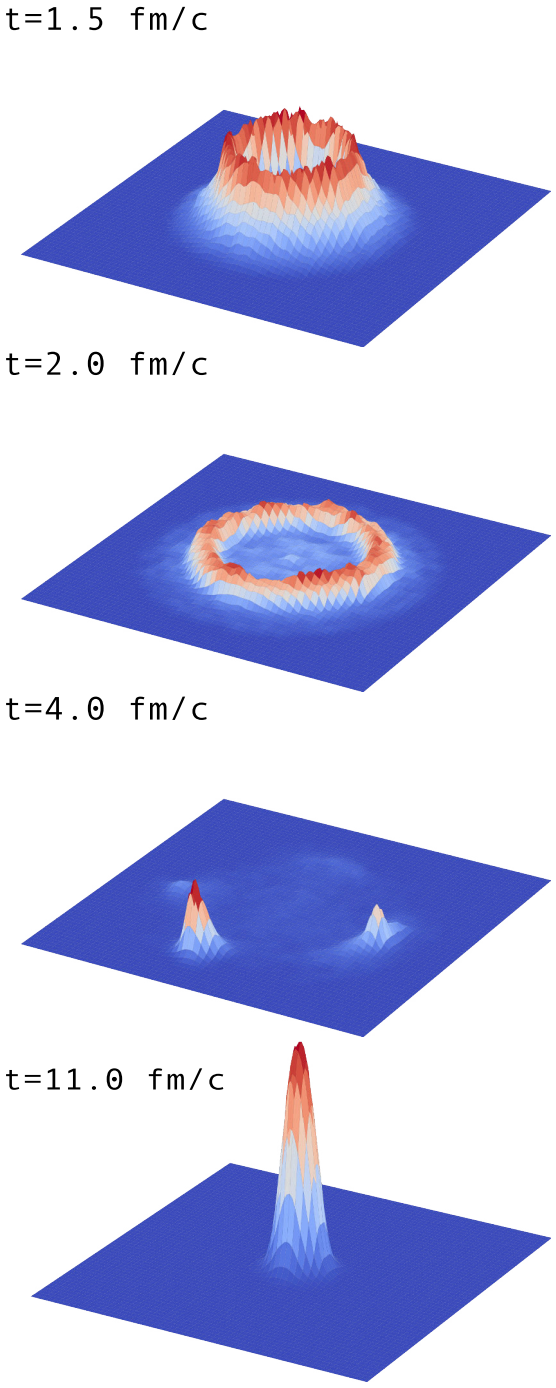

(b) Spatial distribution of the quark density, cut in the center of the z-plane.

Figure 6.5: Time evolution of the hot matter-droplet scenario for $g = 3.63$ with a second-order phase transition and no chemical interactions. **Left:** Deviation of the σ-field from its vacuum value $\langle\sigma_{\text{vac}}\rangle - \langle\sigma\rangle$. **Right:** Total quark density. The scale is the same as in Figure 6.3.

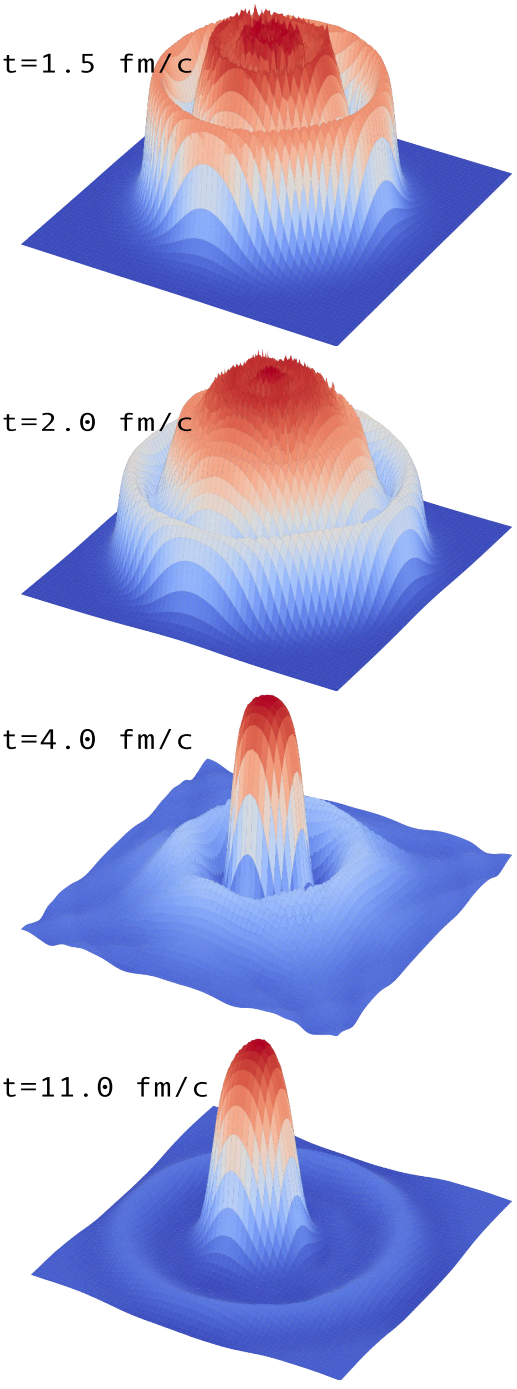

(a) Spatial distribution of the σ-field, cut in the center of the z-plane.

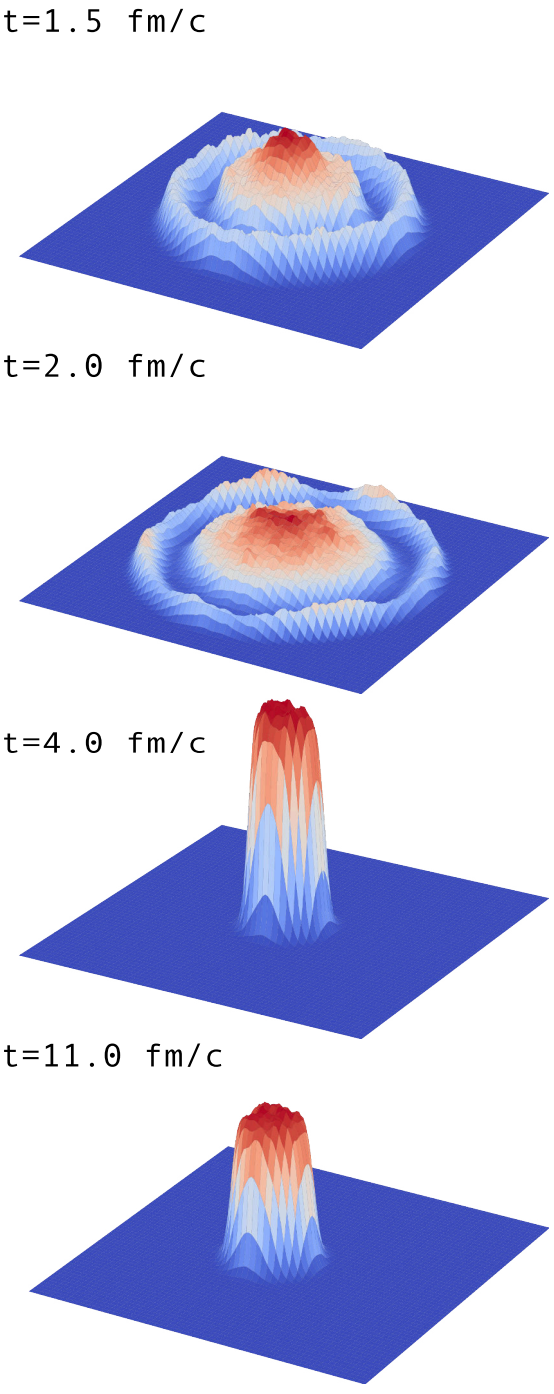

(b) Spatial distribution of the quark density, cut in the center of the z-plane.

Figure 6.6: Time evolution of the hot matter-droplet scenario for $g = 5.5$ with a first-order phase transition and no chemical interactions. **Left:** Deviation of the σ-field from its vacuum value $\langle\sigma_{\text{vac}}\rangle - \langle\sigma\rangle$. **Right:** Total quark density. The scale is the same as in Figure 6.3.

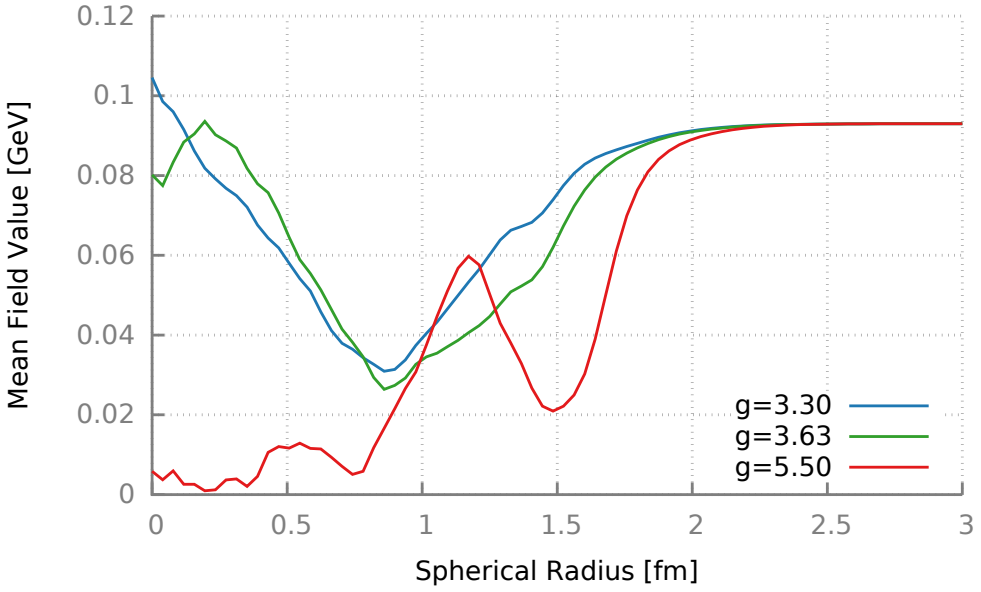

Figure 6.7: Spatial distribution of the σ-field for the simulation time $t = 1.5$ fm/c. The formation of shell-like structures is already observable.

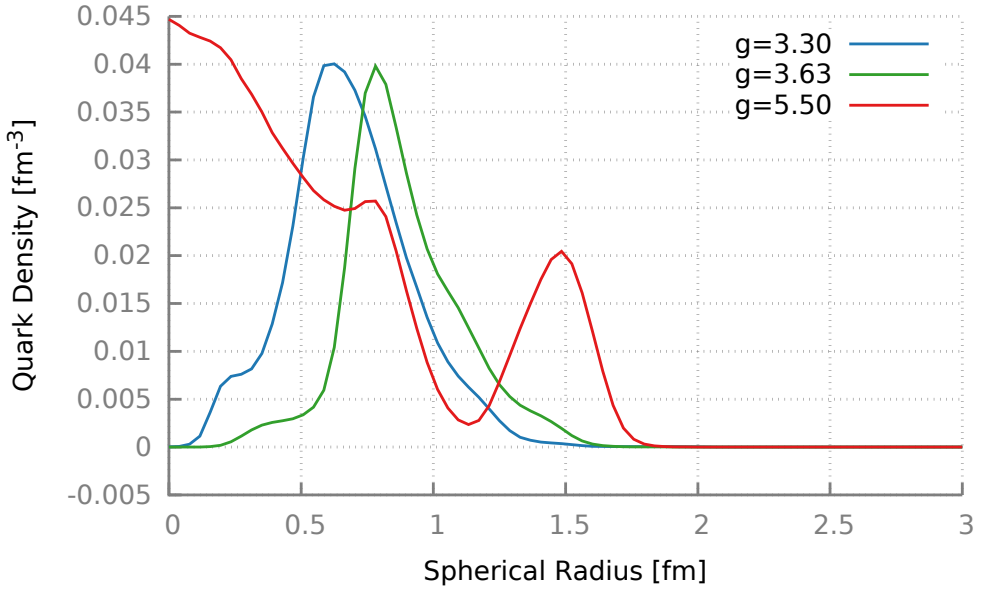

Figure 6.8: Spatial distribution of the quark density in the matter-droplet after a simulation time of $t = 1.5$ fm/c. The density distribution correlates with the distribution of the field because the quarks are accelerated by the field's gradient $\nabla_{\mathbf{x}}\sigma(\mathbf{x})$.

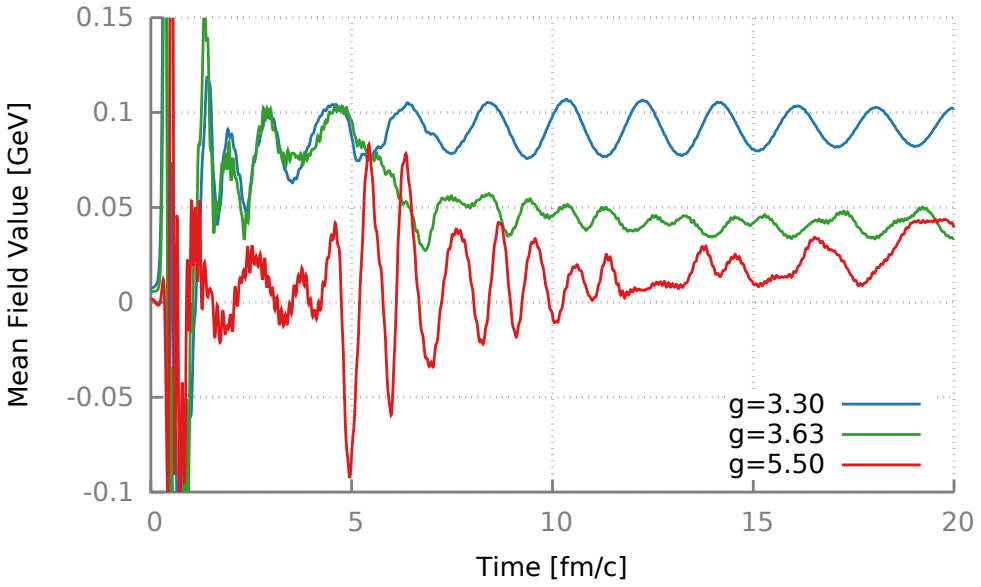

Figure 6.9: Mean field σ value of the grid-cell in the center of the matter droplet. The simulation with $g = 3.3$ evolves towards a vacuum solution, but the mean field keeps on oscillating. For $g = 3.63$ and $g = 5.5$ the system evolves to a meta-stable state. Strong gradients drive the field to a very fast oscillation in the beginning.

display the radial value of the σ-field and the total quark density at the time $t = 1.5$ fm/c. All three scenarios show the formation of shell-like structures in which the quarks are transported out of the system. The time evolution of the system for all three couplings are quite similar, the field starts a fast oscillation in the center of the matter-droplet and with time the field radiates energy via long wavelength oscillations which run out of the system. The higher the coupling, the higher the fluctuations and oscillations. Figure 6.9 shows the value of the numerical σ grid-cell at the center of the matter droplet. The initial oscillations are very strong and become damped after a few fm/c. Furthermore, another interesting observation can be made. For $g = 3.3$ the system evolves and finally oscillates around its vacuum expectation value. The quark density goes to zero as all quarks have left the system. In contrast, for $g = 3.63$ and $g = 5.5$ the mean-field stays in an intermediate state between the chiral restored and chiral broken state, the quark densities show the formation of a stable blob of quark matter, which stays stable for a very long time. In our simulation these drops were stable with lifespans > 50 fm/c. These quark-drops persist of relative cold quarks which can not escape the chiral potential because their kinetic energy is lower than their vacuum mass, implying a bound state in the chiral potential and therefore an effective condensation of quark-matter.

An investigation of the particle number and the quark distribution function in the stable-matter droplet is given in the next sub-section.

6.2.2 Expansion Scenario with Chemical Processes

In the previous section the calculations for the rapid expansion of the hot matter droplet are discussed. The σ-field shows a rapid oscillation in the beginning of the expansion and loses energy mainly by radiating long wavelength oscillations which propagate out of the system. Without any interaction processes the system stays nearly isotropic, only small spatial fluctuations of the quark-density lead to small deviations in the symmetry.

Additionally, for larger couplings the system can fall into a meta-stable state in which cold quarks are trapped in a potential-well of the chiral field which has a long lifetime.

In this section the same calculations are performed, employing the same initial conditions but with the extension of chemical processes $\sigma \leftrightarrow \bar{q}q$ from the full DSLAM model. These processes should lead to additional particle production whenever the σ-field shows strong fluctuation and particle annihilation in areas of high quark density, inducing additional fluctuations on the field.

Figure 6.10, 6.11 and 6.12 show the time evolution of the σ-field and the total quark density for the hot-blob scenario with chemical interactions and different couplings. All calculations are in analogy to the calculations in the previous Subection 6.2.1 and can be compared directly. There are a couple of qualitative differences between the calculations with and without chemical processes. For all three different couplings the types of fluctuations are very different. The systems without chemical processes showed strong global fluctuations, leading to shell-like structures with a fast oscillation of the chiral field at the origin of the matter droplet. The fluctuations are much less present in the calculations with chemical processes. The decay process $\sigma \rightarrow \bar{q}q$ damps such strong fluctuations by removing kinetic energy from the field. In contrast, the process $\bar{q}q \rightarrow \sigma$ creates strong local fluctuations on the field, increasing with a stronger coupling constant g. Additionally, all calculations without chemical processes stayed quasi symmetric through their time evolution while the calculations with chemical processes show a breaking of this symmetry after a very short time. This symmetry is broken by strong and spatial dependent fluctuations of the quark density and the field-distribution and by a collective drift of both particles and the field disturbance. Such a drift is surprising but is explained by the conservation of energy and momenta in the interactions between fields and particles. The σ-field can emit particles, generating a momentum-kick in the opposite direction of the particles, leading to a random-walk phenomena of the droplet. These outcomes are remarkable because no direct random processes are involved in the numerical simulation, which would create these fluctuations. All stochastic and fluctuating processes are the result of microscopic interaction kernels and cross-sections which are sampled via Monte-Carlo methods.

By comparing the calculations with chemical processes with different couplings g, qualitative differences are visible, as well. The fluctuations in the field and particle density increase for stronger couplings. For a coupling of $g = 5.5$ the quark density forms small regions with higher

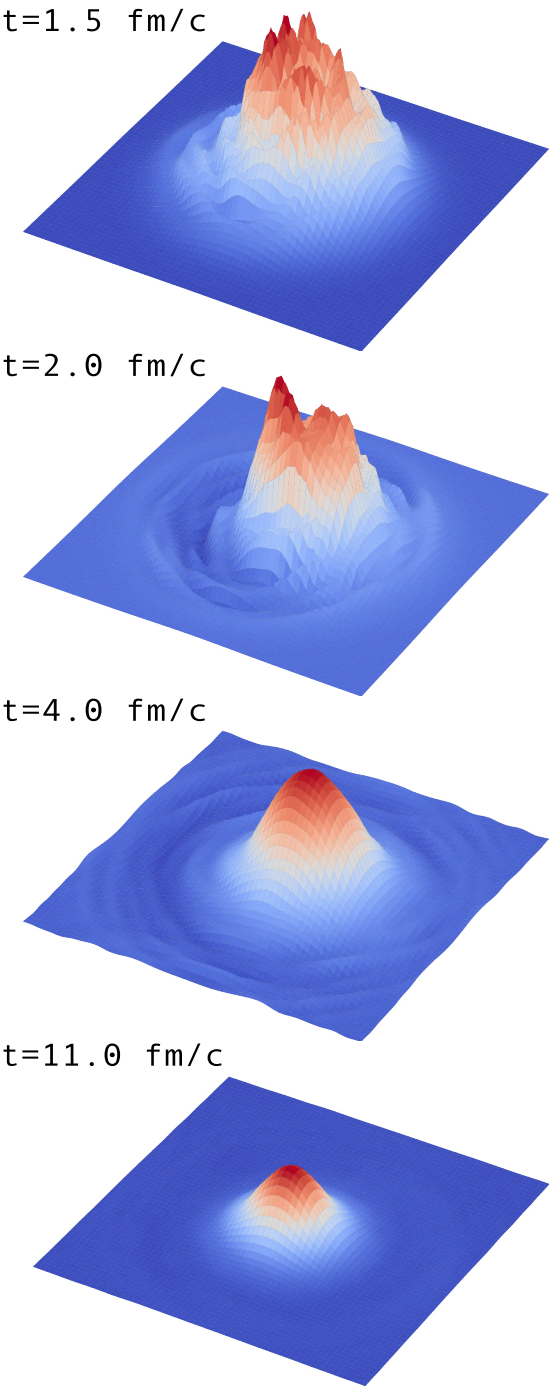

(a) Spatial distribution of the σ-field, cut in the center of the z-plane.

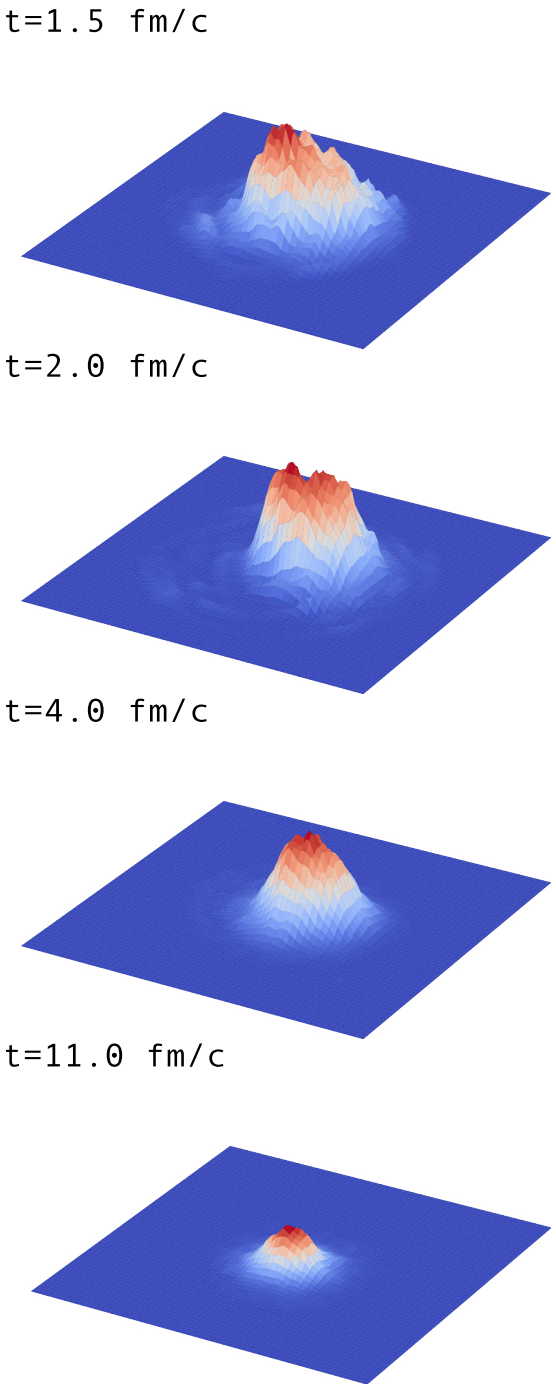

(b) Spatial distribution of the quark density, cut in the center of the z-plane.

Figure 6.10: Time evolution of the hot matter-droplet scenario for $g = 3.3$ with a crossover transition and chemical processes $\bar{q}q \leftrightarrow \sigma$. **Left:** Deviation of the σ-field from its vacuum value $\langle\sigma_{\text{vac}}\rangle - \langle\sigma\rangle$. **Right:** Total quark density. The scale is the same as in Figure 6.3.

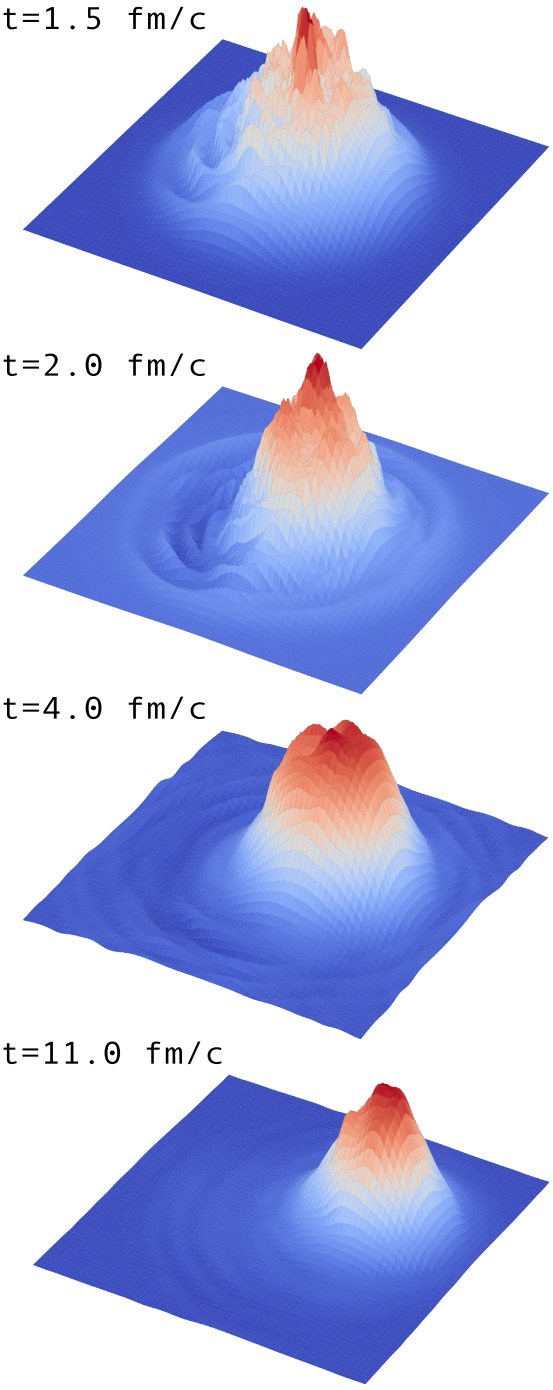

(a) Spatial distribution of the σ-field, cut in the center of the z-plane.

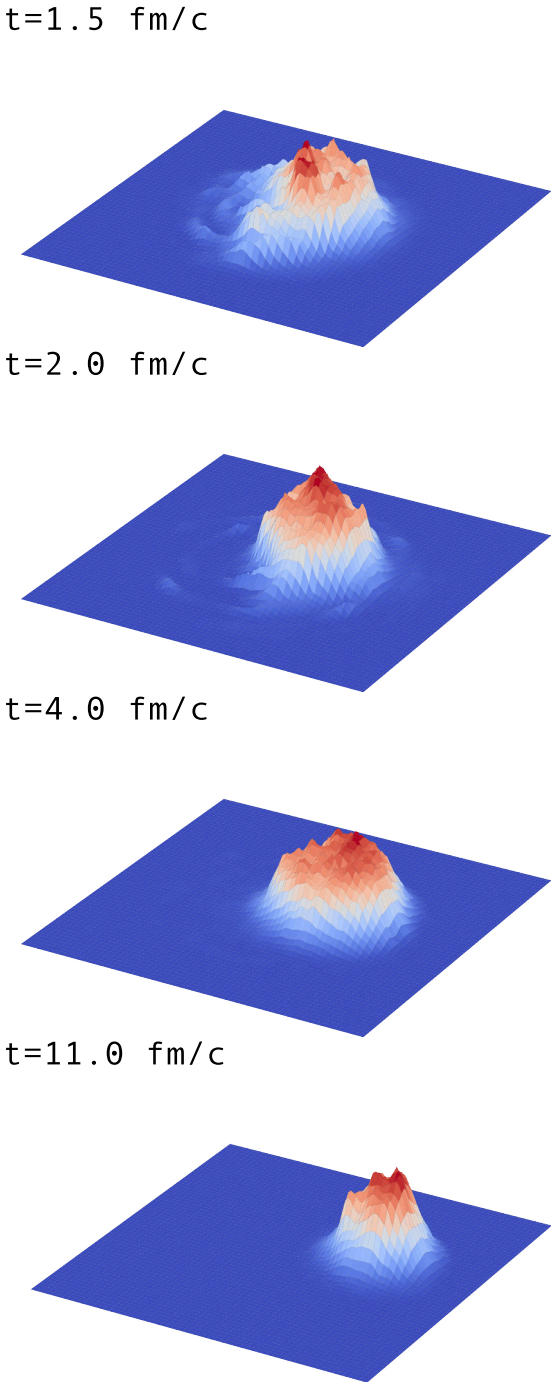

(b) Spatial distribution of the quark density, cut in the center of the z-plane.

Figure 6.11: Time evolution of the hot matter-droplet scenario for $g = 3.63$ with a second-order phase transition and chemical processes $\bar{q}q \leftrightarrow \sigma$. **Left:** Deviation of the σ-field from its vacuum value $\langle\sigma_{\text{vac}}\rangle - \langle\sigma\rangle$. **Right:** Total quark density. The scale is the same as in Figure 6.3.

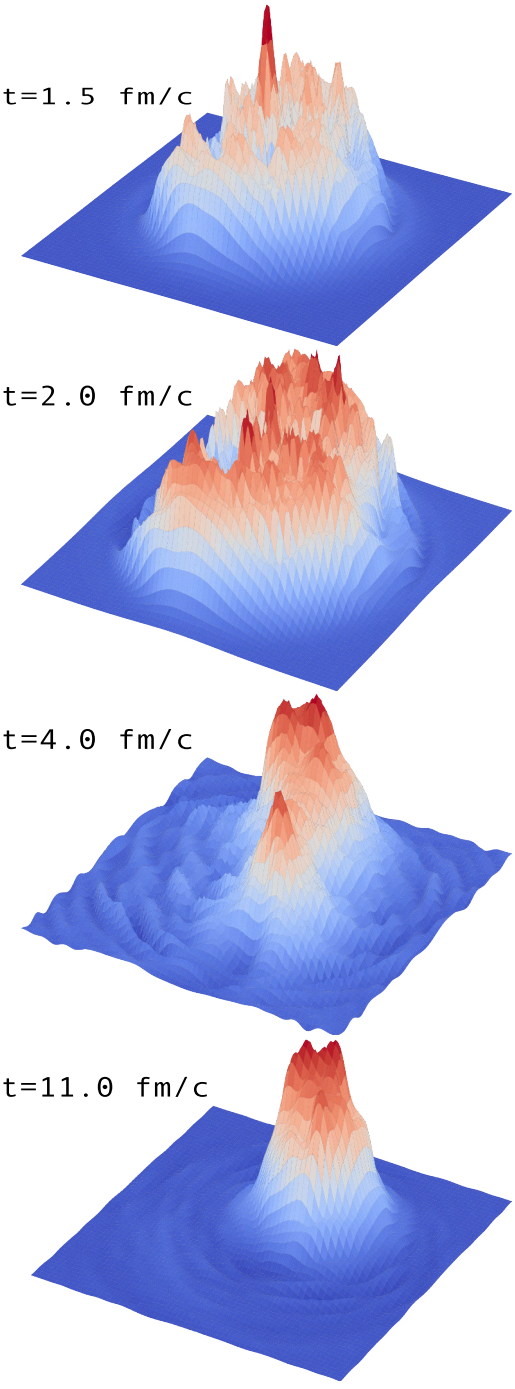

(a) Spatial distribution of the σ-field, cut in the center of the z-plane.

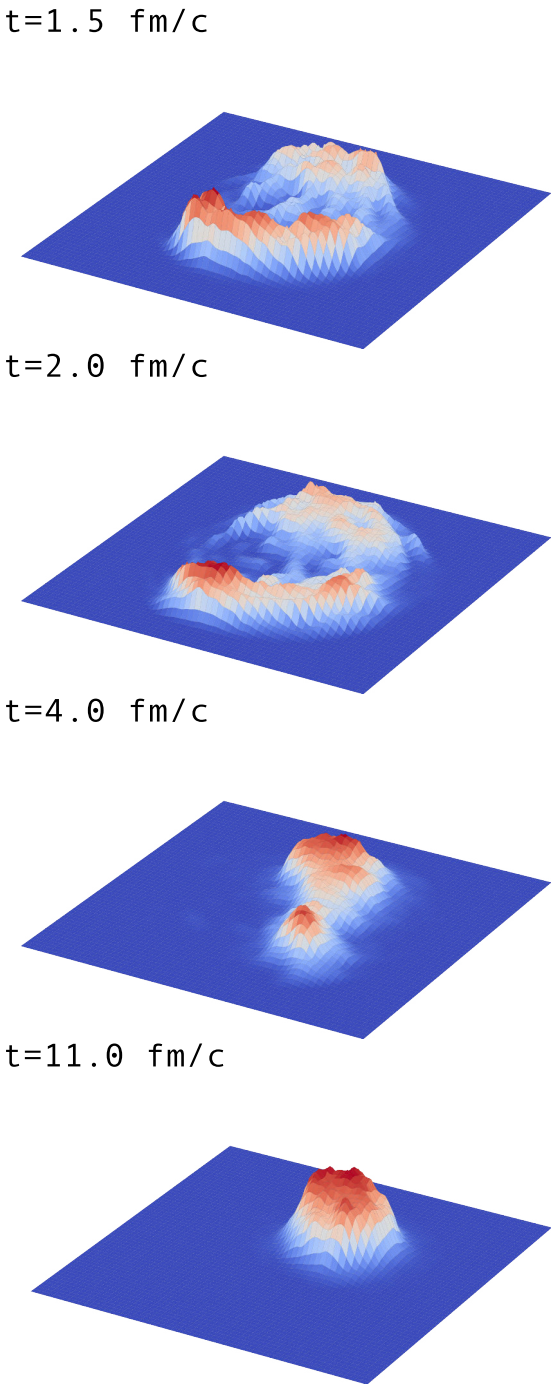

(b) Spatial distribution of the quark density, cut in the center of the z-plane.

Figure 6.12: Time evolution of the hot matter-droplet scenario for $g = 5.5$ with a first-order phase transition and chemical processes $\bar{q}q \leftrightarrow \sigma$. **Left:** Deviation of the σ-field from its vacuum value $\langle\sigma_{\text{vac}}\rangle - \langle\sigma\rangle$. **Right:** Total quark density. The scale is the same as in Figure 6.3.

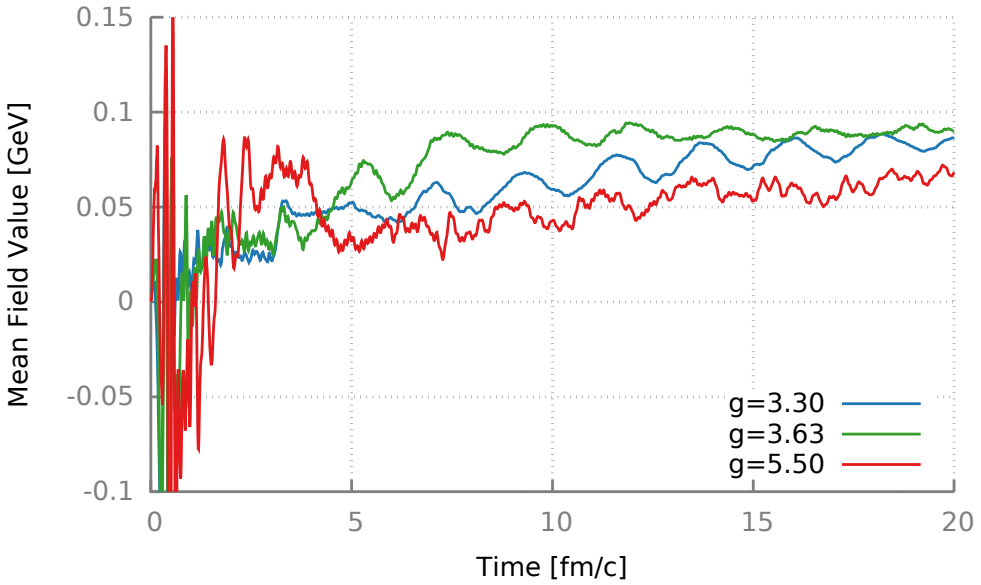

Figure 6.13: Mean field σ value of the grid-cell in the center of the matter droplet. For all couplings the system tends to the vacuum equilibrium value, a lower couplings show lower fluctuations.

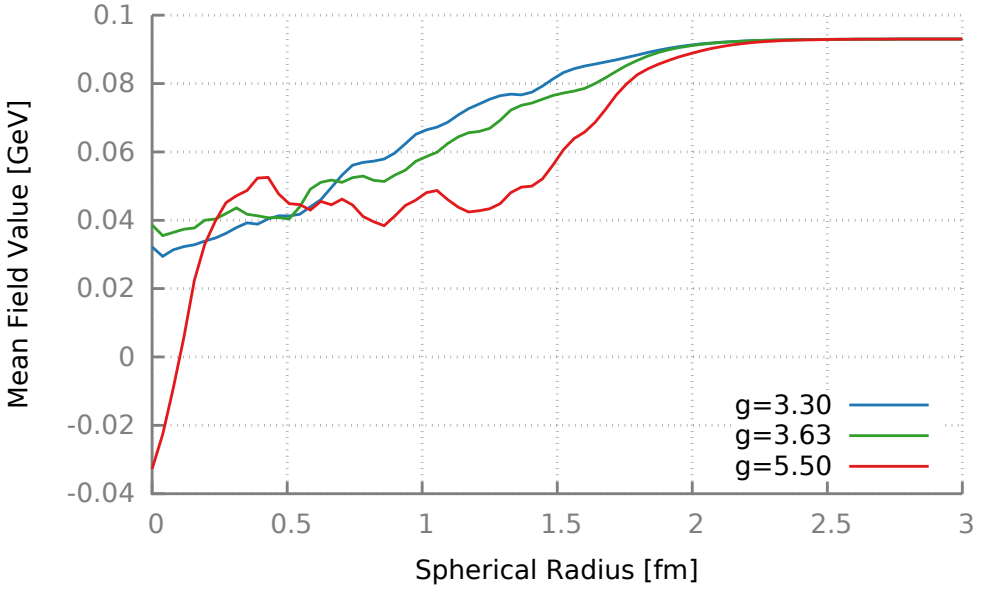

Figure 6.14: Spatial distribution of the σ-field for the simulation time $t = 1.5$ fm/c. Even though the field can show strong local fluctuations from the interactions with the quarks, the overall spatial distribution shows a much smoother transition as in the simulation without chemical processes. Due to the damping by the $\sigma \to \bar{q}q$ process shows less global oscillations.

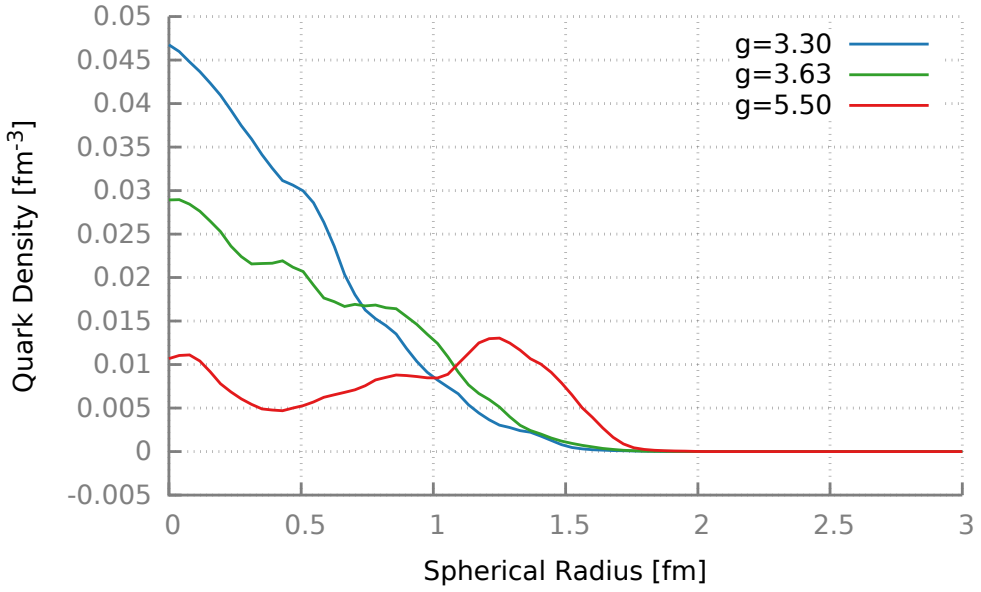

Figure 6.15: Spatial distribution of the quark density in the matter-droplet after a simulation time of $t = 1.5$ fm/c. The simulation without chemical processes showed a strong shell-like structure, which is smoothed out in the simulations with chemical processes because σ-decay processes damp strong oscillations of the field.

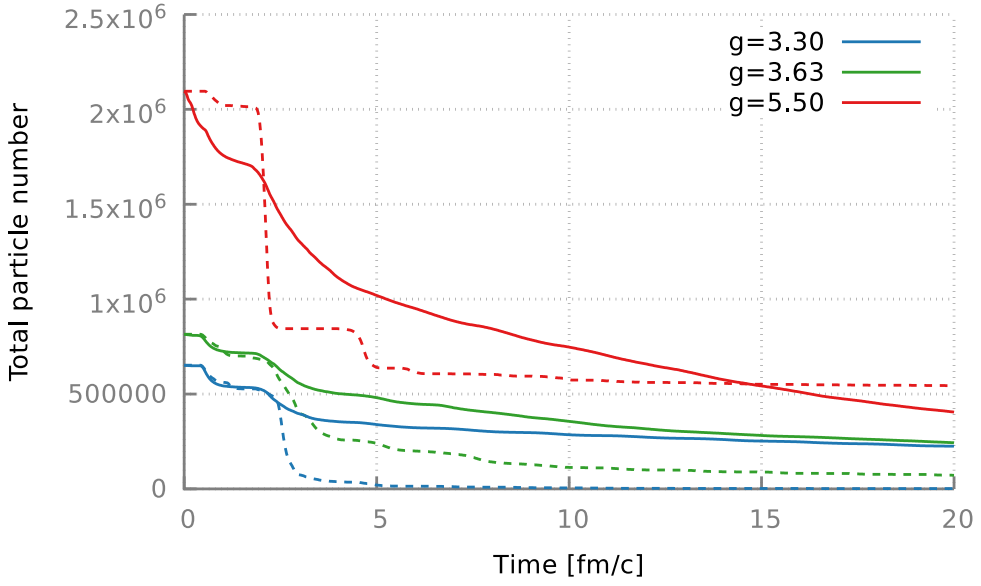

Figure 6.16: Total quark number on the matter-droplet scenario. Solid lines show the simulation runs with chemical processes, the dashed line the simulations without the $\sigma \leftrightarrow \bar{q}q$ process. Tn the scenario without chemical processes the droplet radiates most of the quarks in shell-like structures, as reflected in the quark-number plateaus which drop suddenly. Due do condensation processes can the system form meta-stable states in which cold quarks are trapped in a chiral potential-well, which can be observed in the stable, non-zero quark number for $g = 5.5$ over long times. The behavior is completely different in case of the calculation which chemical processes, in with the systems lose quarks in a steady and continuous process, the formation of quark-number plateaus is washed out.

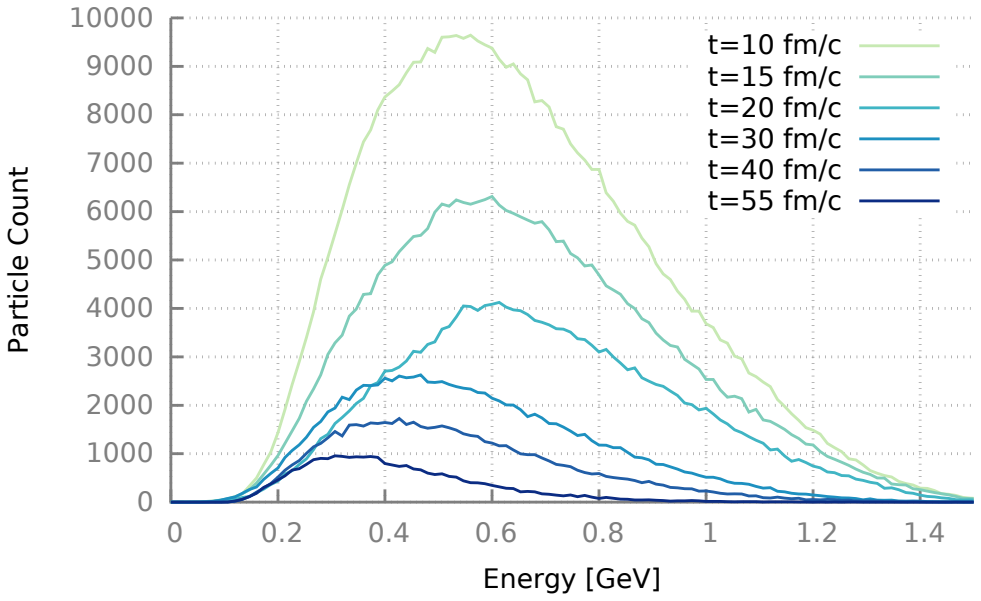

Figure 6.17: Energy distribution functions of the quarks in the simulation for the matter-droplet scenario with $g = 5.5$ and chemical processes. After 10 fm/c most of the initial particles have left the system and the remaining particles have formed a condensed drop of cold quarks, which are trapped in a chiral-potential well. One can see a non-thermal distribution function in the beginning, which slowly thermalized due to elastic interactions. However, mainly high-energy quarks can leave the potential well, leading to both a slow evaporation of the drop and to an effective cooling of the remaining particles.

densities, which merge with time. These observations are consistent with calculations of the linear σ-model with a hydrodynamic background [51, 52, 64], in which the authors find the strongest fluctuations for a medium with a first-order phase transition. Classical theories of phase transitions predict the strongest fluctuations at and near the phase transition for second-order transitions. Calculations presented in this section have the strongest fluctuations for the coupling with the first-order phase transition. At first, this scenario can not be directly compared to a phase transition. A phase transition is a phenomena described by equilibrium physics for very large systems which evolve in the adiabatic limit on large time scales. Fluctuations are a phenomena which needs time and is created by interactions of the thermal medium. Most important, the correlation length is often largely enhanced at the phase transition, which is no problem for systems which are much larger than this correlation length. The scenario of the hot-matter droplet is quite the opposite. The system size is in the order of the interaction length and therefore its correlation length. The quark matter expands rapidly and its dynamic creates strong non-equilibrium distributions and the total lifespan of the system is at most in the order of the equilibration timescale. Additionally, a rapid expansion leads to a highly non-isotropic system with gradients and parts of the system separates to regions with very different densities and temperatures. All these circumstances do not allow a consistent description of the system in terms of an equilibrium phase transition, especially not if the quarks are described by particles

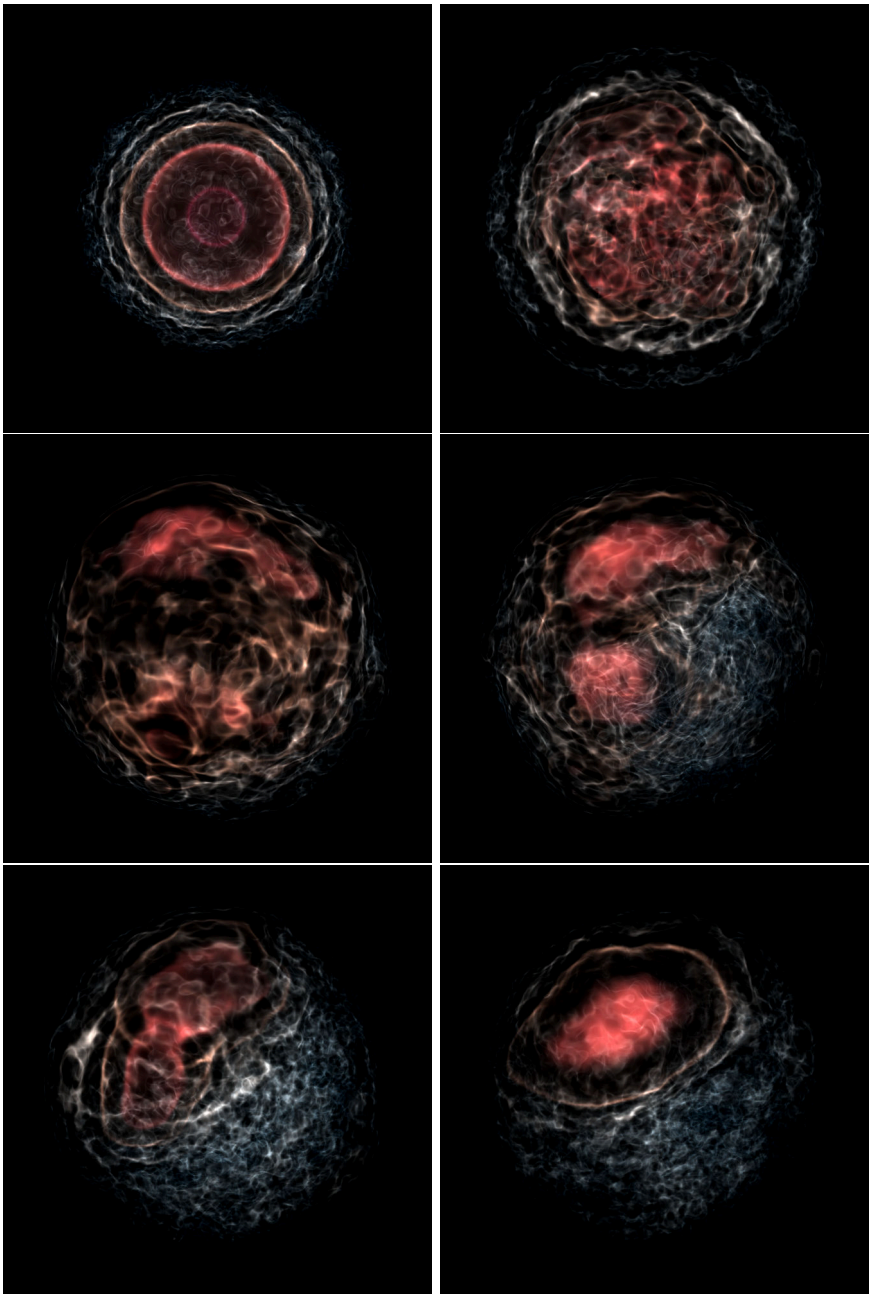

Figure 6.18: Volumetric 3D rendering of the quark density for the hot matter droplet scenario with a coupling of $g = 5.5$, a first-order transition and chemical processes. The time progresses for 1 fm/c for every image. Regions with high particle densities are colored red, the scale is constant over all images. Visualization was created using the yt-toolkit [90].

with non-equilibrium distributions and not by a fast equilibrating medium. Any deviation from equilibrium descriptions have a strong impact on the thermal properties of the medium, as shown in Section 4.1.

Considering the systems dynamics in terms of its transport properties would be a more adequate approach to the characteristics of the systems behavior. The strong fluctuations only occur if the chemical processes $\sigma \leftrightarrow \bar{q}q$ are present, their microscopic interaction kernels are derived from a Breit-Wigner cross-section. Calculations in Chapter 5 (see Figure 5.4 and 5.5) have shown a direct relation between the average cross-section and the coupling g, which in first order scales with $\sim g^2$, leading to a higher interaction rate between fields and particles. This already implies more fluctuations for the calculations with the coupling $g = 5.5$ and quite similar fluctuations for $g = 3.3$ and $g = 3.63$, even though these different couplings would show very different kind of phase transitions in a thermal system. Furthermore, two other aspects play an important role in the comparison of the different calculations. The coupling has a direct impact on the mass of the quarks. A higher coupling leads to a larger vacuum mass and a lower mass in the chiral restored phase. This implies both a larger particle number at the same temperature for a higher coupling and a larger potential energy for the chiral fields. The second aspect has its origin in the phase diagram. Higher couplings lead to a lower T_c in the linear σ-model, which strongly changes the dynamics of the chemical interactions as they are only possible above the mass threshold, meaning above T_c. For lower T_c, in comparison to other couplings, the quarks and the fields have more time to stay in the chiral restored phase, more time to interact with each other and therefore more time to build up fluctuations via these interactions. This already implies stronger fluctuations, regardless of the type of phase transition, which would be given by the corresponding coupling. A fair comparison between the scenarios is not given by comparing the system at different temperatures. Better approaches could be a comparison with same energies or same particle number.

The impact of the stronger coupling on the quark dynamics has already been show in the previous section. Formations of meta-stable drops of quarks could be observed, especially $g = 5.5$. This behavior can be seen in this calculations, too. For $g = 5.5$ with chemical reactions the system even shows something like bubble formation. Figure 6.18 shows a volumetric 3D rendering of the quark density which projects the full three dimensional density, while Figure 6.12 is only a 2D cut of the grid. The 3D figure shows strong density fluctuations and visualizes how small areas of high quark-density start to merge into larger areas, having some similarity to the condensation of water drops in steam. The mechanism of this condensation is the energetic favorable configuration for the σ-field. Interestingly, the condensation progresses and the σ-field looses energy by radiating wave excitations. The process seems to stop after 10 fm/c by forming a stable drop. In difference to the calculations in the previous section this drop is not stable at all. Figure 6.16 shows the total quark number of the system, showing a steady decrease of quarks in the system, indicating some kind of particle evaporation from the drop. This evaporation seems to be quite slow and

calculations have shown a lifespan up to 50 fm/c before the drop bursts. Figure 6.17 displays the distribution function of the quarks with their time dependence after a condensation drop has been formed. The figure shows a decline of the quark number with time and mainly particles with high energies leave the system. This is reasonable because high energetic particles can leave the potential well, leading to a collective cooling of the remaining medium.

The calculations in this section have shown the very interesting complexity of such a simple initial condition like an expanding matter droplet. The chemical reactions between particles have a very strong impact on the system behavior and dramatically change both fluctuations and medium propagation within the expansion. However, a characteristic signature which allows a event-by-event discrimination between the different kind of couplings and phase transitions in this scenario has not been found, at least not for calculations with the crossover coupling $g = 3.3$ and the second-order transition coupling $g = 3.63$. Such a discrimination could be possible in a statistical investigation of the angular distribution of the quarks which are emitted from the fluctuating chiral field.

6.3 Large Scale Systems

All calculations in this chapter up to Figure 6.18 are done for systems with a fireball which has an initial diameter of roughly $d \approx 1$ fm. In comparison to a heavy-ion such a system is very small. Both lead and gold nuclei have a diameter of around $d_{\text{au}} \approx 14$ fm, resulting in a volume two orders of magnitude larger than in this scenario. Therefore quantified predictions for a heavy-ion collision can not be derived from these calculations. Both the number of involved quarks and the energy density in the system could lead to different phenomena. Additionally, a much larger spatial and time scale could change the behavior at the phase transition because the system has potentially more time to evolve and form structures in the particle densities.

However, a fully realistic simulation of a heavy-ion collision was not the scope of this chapter but to show how interactions between fields and particles lead to a qualitatively very different behavior. Additionally, as these types of calculations are new, this chapter should be seen as a proof-of concept and a basic investigation to understand the properties and interaction phenomena.

The choice of system-size was not motivated by the numerical capabilities of the DSLAM model which is able to handle larger scales. Nevertheless, one has to keep in mind that larger systems are harder to control numerically and to start with small, not so violent systems is a good idea.

Several calcualtions are still work-in-progress while this was written and will be presented in a later publication. These calculations show the same scenario as in this chapter but with much larger system sizes. As an outlook, first results are presented here. The system volume was

chosen $V = (36\text{ fm})^3$ and the hot matter droplet has an initial diameter of $d \approx 14$ fm, roughly corresponding to a gold nuclei. The temperature was again chosen to be $T = 175$ MeV and the couplings remain at $g = 3.3$, $g = 3.63$ and $g = 5.5$. To increase the numerical precision and to avoid numerical problems the grid-size was increased to $N_{\text{grid}} = 192^3$ and the time step was reduced to $\Delta t = 0.001\text{fm/c}$. The interaction volume was slightly increased to $V_{\text{interaction}} = (0.4\text{ fm})^3$. The total particle number was around 5 million particles with a test-particle multiplicator of 200. All other parameters have been kept unaltered.

Figure 6.19 and 6.20 show the result for a calculation with a large expanding matter droplet. Both figures compare the same calculations with and without chemical interactions and different couplings, $g = 3.3$ with a cross-over transition in Figure 6.19 and $g = 5.5$ in Figure 6.20.

The calculations without chemical interactions do not change very much in comparison to the smaller systems. The overall symmetry of the system stays effectively intact and known structures like the shell-structures and cold quark droplets are still present.

The picture changes a bit for calculations with chemical interactions, especially for larger couplings like $g = 5.5$. After a short expansion phase the matter droplet starts to form strong and non-isotropic structures in the quark density due to the annihilation and creation process. In Figure 6.19 first structures are already present at $t \approx 1\text{fm/c}$. These structures blur while the matter expands.

In Figure 6.20 these structures are much stronger and much finer. The reason is the strong coupling between the field and particles, leading to fast annihilation and strong damping of the field by σ-decay. While expanding, the fluctuations on the σ-field become stronger. Around $t = 5\text{fm/c}$ the annihilation-rate of the quarks is negligible because of the low particle density due to expansion. The σ-decay becomes the dominating effect, leading to a strong damping of the field and to a quasi-freeze out of the field leading to some kind of local bubble-formation. The resulting field distribution stays stable for several 10fm/c local bubbles converge slowly to a big drop. This final drop contains the already known cold quarks which were not able to escape the kinetic potential.

In the calculations for larger system a qualitatively difference between the couplings can be seen in the time evolution. While calculations for $g = 3.3$ and $g = 3.63$ behave similar, calculations for $g = 5.5$ show a very different behavior: the quark matter forms bubbles and freezes out in a relative long-living structure. One of the remaining questions is if this formation can be observed in experiment. A possible approach will be an investigation of the angular distribution of the emitted particles, which could be mapped to an angular distribution of measured particle multiplicity. This is subject to an upcoming publication.

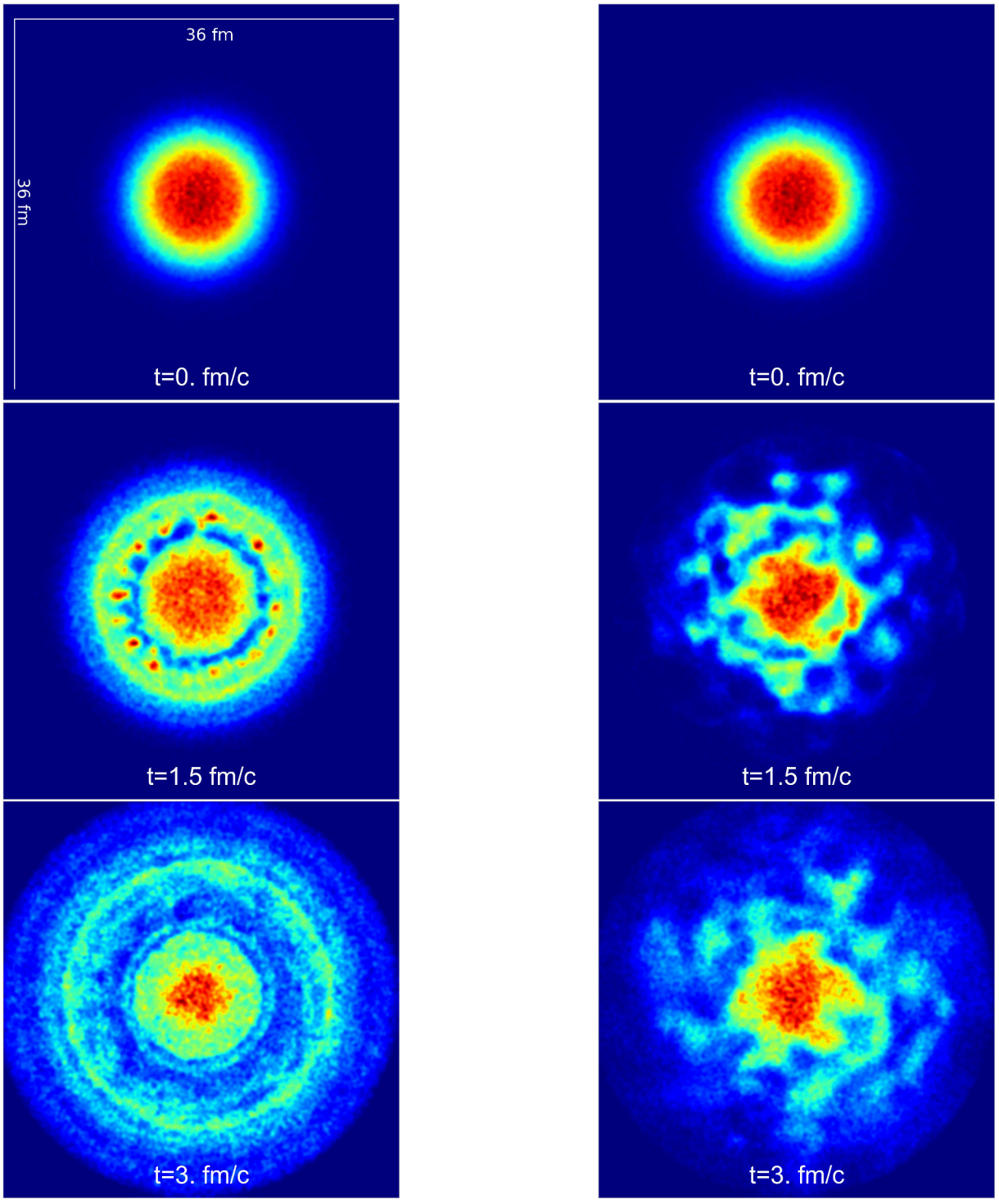

Figure 6.19: Evolution of the quark density for a large hot matter droplet scenario with $g = 3.3$. The initial size of the droplet has an diameter of around $d \approx 14$ fm which corresponds to the size of a gold nuclei, the total size of the system is $V = (36 \text{ fm})^3$. **Left:** Simulation without chemical interactions **Right:** simulation with chemical interactions. Chemical interactions lead to formation of non-isotropic structures but the overall expansion of the system is not strongly altered.

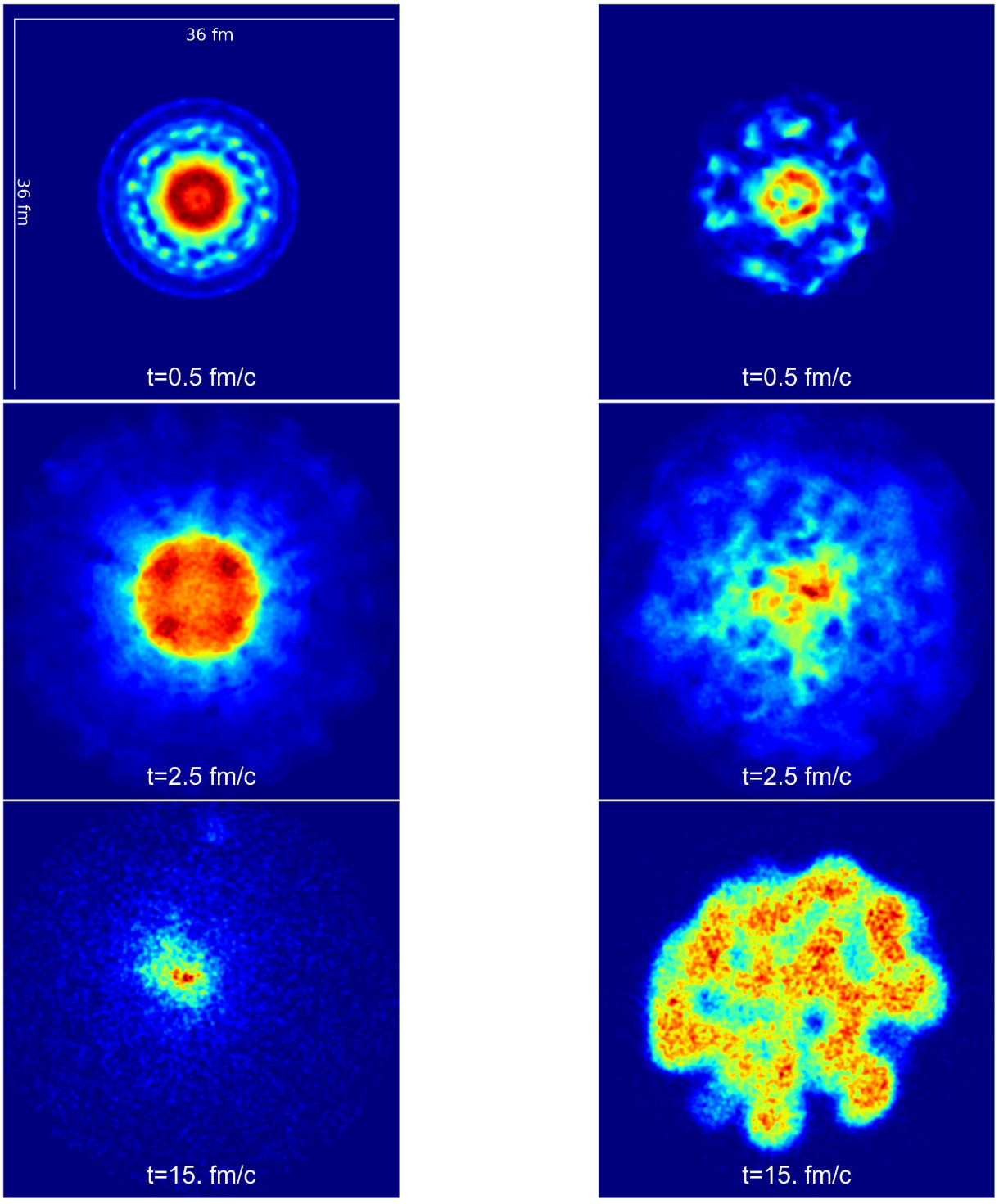

Figure 6.20: Quark density for a large hot matter droplet scenario with $g = 5.5$. The initial size of the droplet has an diameter of around $d \approx 14$ fm which corresponds to the size of a gold nuclei, the total size of the system is $V = (36\text{ fm})^3$. **Left:** Simulation without chemical interactions **Right:** simulation with chemical interactions. Chemical interactions lead to a generation of strong and detailed structures. After 5fm/c the expansion of the system is stopped by the strong damping of the field, leading to the formation of local bubbles.

Chapter 7

Particle-Wave Interaction Method

> Creativity is intelligence having fun.
>
> Albert Einstein

This chapter discusses a new method which allows a numerical treatment of noncontinuous interactions between fields and particles, called the particle-field method. The chapter starts with a historical introduction of the wave-particle duality, which gave the basic idea for the particle-field method. In Section 7.2 existing approaches for interaction between fields and particles and their drawbacks are discussed. This discussion includes the Vlasov-equation, interactions in Fourier-space and the Langevin-equation. Section 7.3 introduces the ideas and concepts of the particle-field method. In Section 7.4 several examples and simple scenarios are presented which implement the particle-field method with increasing levels of complexity and demonstrate the possible applications of this method. The last Section 7.5 considers several general properties of the method.

7.1 Wave-Particle Duality

The wave-particle duality is one of the fundamental aspects of modern quantum physics. The discussion about waves and particles has not been started with quantum physics, but already with the first attempts to find a physical and mathematical theory for light.

Christiaan Huygens, one of the pioneer founders of the optical theory, investigated and advocated the wave theory of light. Light is described by propagating wave fronts, light sources emit spherical waves. In contrast, Isaac Newton proposed 1704 in his 'Opticks' the corpuscular theory of light in which light is described by particles. Reflection of light is the simple scattering of particles on the surface of objects.

In 1801 Thomas Young started experiments with light interference, a phenomena which could only be explained with a wave theory of light. The later very famous double-slit experiment became one of the standard experiments in quantum physics. Other physical experiments and phenomena like diffraction, polarization, medium dependent propagation velocities and the discovery of electromagnetic waves made the wave theory of light popular.

In the beginning of the 20th century Max Planck discovered his famous radiation law, which solved the problem of the correct description of energy density of black-body radiation. He introduced a discrete factor, the Planck constant h, in which energy is quantized in a system. Albert Einstein published his work on the photoelectric effect in 1905. While most physical effects of light are described by a wave theory, the energy of light shows a discrete property. In the described experiment, electrons can be emitted from a metal plate by a beam of light. The wave theory postulated the rate of emitted electrons to be a product of the wave frequency and amplitude. However, the experiment showed a threshold for the light's frequency. Frequencies lower than this threshold do not tear out electrons, independent of the wave's amplitude. Einstein postulated the quantum nature of light, coming in energy packets proportional to its frequency. Additionally to its wave-properties, light consists of a finite and integer number of energy quanta, which explain the discrete energy portions observed in the experiments. This dual description of light was later summarized under the name photon. Both works of Planck and Einstein were honored with a Nobel price.

15 years later Louis de Broglie postulated a wave nature for massive particles, like electrons. This hypothesis was first heavily discussed in the community but three years later in 1927 Clinton Davisson and Lester Germer showed the diffraction of electrons in crystals. The final and most important experiment was the double-slit experiment with electron in 1961 by Claus Jönsson. The experiment showed the interference of single electrons with themselves, its explanation is the wave nature of microscopic particles by interactions on scales of the de-Broglie wavelength. This relation holds even for mesoscopic objects like atoms or even carbon molecules like C_{60} fullerenes [91].

The wave-particle duality has lead to a long discussion concerning the interpretation of this not intuitive principle. Today, quantum particles are accepted to have both a wave-like and particle-like nature at the same time. Their actual behavior depends on the physical context. Systems which classically have wave-like phenomena can show quantized and particle-like behavior, as well.

7.2 Physical Motivation

The objective of this part of this work is to develop a method which allows the interaction between particles and fields. The original motivation for this approach was given by the DSLAM

model, in which the chiral σ-field must be able to exchange energy and momentum with a particle ensemble to equilibrate chemically and thermally on an intermediate timescale of a few fm/c. This exchange has to be noncontinuous to allow an effective interpretation in terms of particle creation and annihilation. In the following sections different approaches and existing techniques for interactions between particles and fields are discussed. Possible drawbacks are explained and the need for an alternative method is given.

7.2.1 Vlasov-Equation Approach

The classical Boltzmann-equation is used to describe the transport and interactions of particles in the dilute-gas limit [92]. The description is given by a continuous distribution function. Their time dependence is propagated by a set of integro-differential equations

$$\mathbf{v} \cdot \frac{\partial f}{\partial \mathbf{x}} + \frac{\mathbf{F}}{m} \cdot \frac{\partial f}{\partial \mathbf{v}} + \frac{\partial f}{\partial t} = I_{\text{Coll}} \ . \tag{7.1}$$

The first term in (7.1) describes the general propagation of a particle, which moves along in space with its velocity. The second term describes the change of momentum by an external force. The term ∂_t considers the time dependence of the system. The collision integral I_{Coll} describes the change of the distribution function by interactions between the particles

$$I_{\text{Coll}} = \int_{\mathbf{v}_1} \int_{\mathbf{\Omega}} \left(f' f_1' - f f_1 \right) \sigma \left(\mathbf{\Omega} \right) \left| \mathbf{v}_1 - \mathbf{v}_2 \right| \, \mathrm{d}\mathbf{\Omega} \, \mathrm{d}^3\mathbf{v}_1 \ . \tag{7.2}$$

with the phase-space distribution Ω and $\sigma\left(\mathbf{\Omega}\right)$ is the differential cross section. Equation (7.2) is a non-linear integro-differential equation and has in general no analytic solutions. Usual approaches to solve the Boltzmann equations use a stochastic approach with Monte-Carlo methods, like BAMPS with test-particles [93], or simplified models with a linearization of the equation [94].

To describe charged particles in a plasma, Anatoly Vlasov used the collisionless Boltzmann equation with $I_{\text{Coll}} = 0$ and coupled the particles to field potentials [72, 95, 96], resulting in the famous (relativistic) Vlasov-equation:

$$\frac{\partial f}{\partial t} + \frac{\mathbf{p}}{E} \cdot \frac{\partial f}{\partial \mathbf{x}} + \mathbf{F}(\mathbf{x}, \mathbf{p}, t) \cdot \frac{\partial f}{\partial \mathbf{p}} = 0 \tag{7.3}$$

with the on-shell dispersion relation, $E = \sqrt{m^2 + \mathbf{p}^2}$.

In case of the linear σ-model with constituent quarks, particles and fields are coupled via the Yukawa interaction $\sigma\bar{\psi}\psi$. The implementation in the DSLAM model is realized by employing a mean-field approximation for the σ and and the effective mass for the particles $m_{\text{eff}}^2 \sim \mathbf{\Phi}^2$,

leading to an effective field-dependent dispersion relation

$$E(\mathbf{x}) = \sqrt{p^2 + g^2 \mathbf{\Phi}^2}\,. \tag{7.4}$$

$E(\mathbf{x})$ can be seen as a potential and with

$$\mathbf{F}(\mathbf{x}) = -\nabla_{\mathbf{x}} U(\mathbf{x}) \tag{7.5}$$

the field and the particle phase-space distribution function $f(\mathbf{x}, \mathbf{p}, t)$ become coupled. With a test-particle ansatz, which generates a distribution function from a sum of classical point particles,

$$f(\mathbf{x}, \mathbf{p}, t) \to \sum_n \delta(\mathbf{x} - \mathbf{x}_n(t))\, \delta(\mathbf{p} - \mathbf{p}_n(t)) \ , \tag{7.6}$$

every particle feels a force induced by the gradient of the mean field in the effective mass

$$\dot{\mathbf{p}}_n(t) = -\nabla_{\mathbf{x}} E(\mathbf{x}_n(t), \mathbf{p}_n(t), t) \ . \tag{7.7}$$

Such a mean-field coupling accelerates particles along the field-gradients. In the σ-model the field is coupled to the particles with the chiral density $\langle \bar{\psi}\psi \rangle$, giving a feedback from the particles to the field. However, particles at the same point in space feel the same force in (7.7). In an isotropic system, particle momenta can not be thermalize on a short time scale. For field modes, such a mean-field coupling cannot thermalized the system either, as it leads to reversible dynamics. It can thermalize when employing interactions by higher-order loops [97, 98] or by coupling the mean-field to particles with collision kernels. Still, such a coupling would thermalize only on large time scales much larger than the interaction timescale of the particles. Additionally, the interactions within the Vlasov equations are very soft and do not include inelastic processes like particle production and annihilation. Nevertheless these processes play an important role in the linear σ-model, leading to a shift in thermodynamic properties without particle number changing processes, and in dynamical calculations the chiral phase transition is lost if the field can not dissipate energy by particle production upon a temperature change. The problem has been discussed in Chapter 4.

7.2.2 Interactions in Fourier Space

One of the big challenges of statistical physics is the vast amount of degrees of freedom. To describe a volume of gas with classical mechanics, one has to solve $6N$ degrees of freedom with the total number of gas particles N. If these particles can interact, the number of coupled equations raises exponentially. The Boltzmann equation, which can be regarded as an approximation reduces the degrees of freedom to an analytic distribution function with 3 spatial, 3 momentum and a time dimension. A collision-less Boltzmann equation can be solved quite easily. However,

even only for two-particle interactions in a dense gas, the calculation complexity rises again dramatically. To solve a Boltzmann collision integral, at least 6 dimensions have to be solved (3+3 in the momentum space). If spatial dependency is taken into account often 9 dimensions have to be integrated numerically. Numerical computational complexity and memory consumption raise with the dimensional discretization N_g with complexity N_g^9. Even for modern computers this is far from practical use. The full representation of a single-particle distribution in three spatial, three momentum and and a single time step (which corresponds to the Markov approximation) with a quite coarse discretization of $N_g = 64$ already consumes 512 Gigabytes, which is 64 times more than the typical memory of a current desktop computer.

A common approach to approximate quantum field systems is to assume spatial isotropy and reduce the phase-space distribution of the physical problem to functions in momentum space. This ansatz has been very successful and answered many questions regarding non-equilibrium phenomena and thermalization [99–101]. In case of spatial symmetry, calculations can be performed in Fourier space. This holds if the calculation is within small volume cells in which spatial symmetry can be assumed.

Additionally, in quantum field theory interactions and their propagators are well defined in momentum space, leading to transition probabilities for single Fourier modes in terms of scattering-matrix elements,

$$S_{fi} = \langle \mathbf{p}_1' \mathbf{p}_2' \ldots | S | \, \mathbf{p}_1 \mathbf{p}_2 \ldots \rangle \, . \tag{7.8}$$

These probabilities can be treated perturbatively, like in quantum electrodynamics (QED). In numerical simulations, such dynamics can be applied to a classical field, and the impact on the system by changing single Fourier modes is easily calculated through the sum of the modes' energies. This method works well for systems in momentum space with the assumption of spatial isotropy. In the case of spatial anisotropy or if the system propagation is done in position space and only the interactions are performed in momentum space, then this method implies a violation of causality. The change of a single mode in momentum space changes the field distribution instantaneously in position space over the whole volume, which is illustrated in Figure 7.1, resulting in superluminal signal propagation. Additionally, the system will show strong long-range correlations. These physical artifacts render this method unsuitable for simulations which rely on position-space calculations.

7.2.3 Langevin Method

The Langevin or Ito-Langevin equation [102] is a stochastic differential equation, used to describe systems with two different scales. The "macroscopic" long-range and slow-timescale part is described by deterministic equations of motion. Additionally, it is coupled to the "microscopic" small scales, which are described by short-ranged fast random processes. Originally, this equation

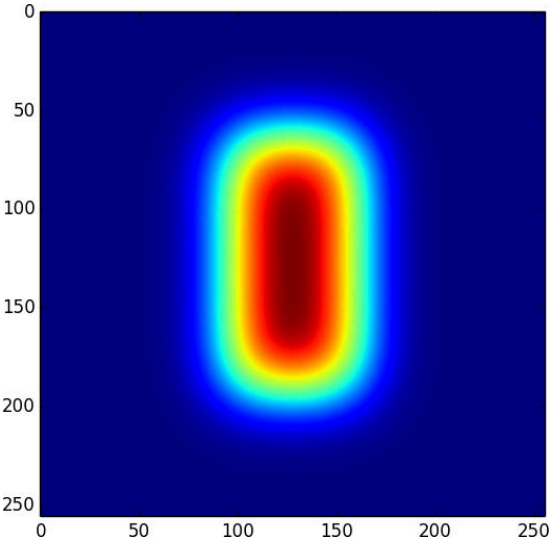

(a) Initial field distribution

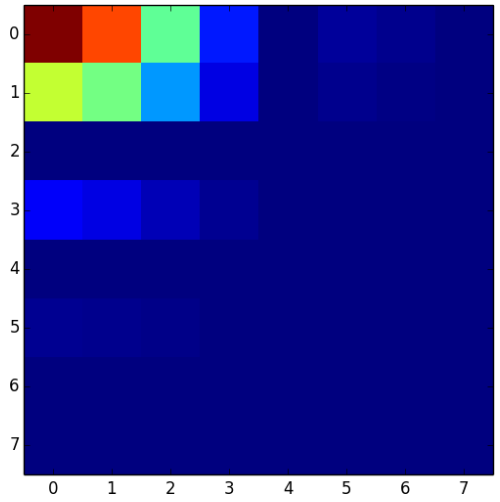

(b) Initial Fourier spectrum

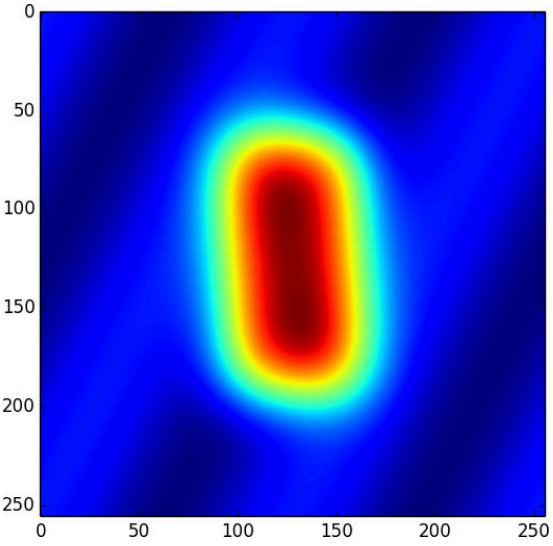

(c) Modified field distribution

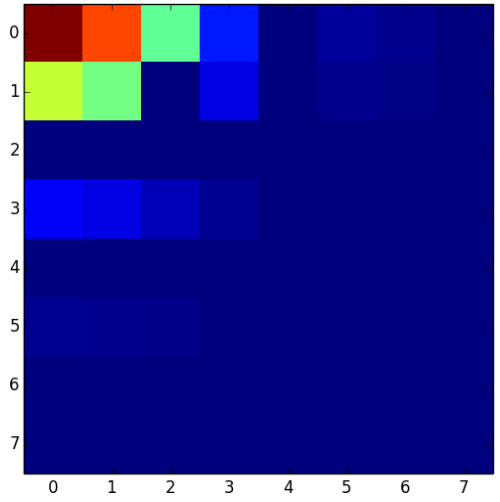

(d) Modified Fourier spectrum.

Figure 7.1: Change of an given field distribution by changing a single Fourier-mode within an interaction process. The difference between the two Fourier spectrums in Fig 7.1b and Fig. 7.1d is the mode with $\mathbf{k} = (2, 1)$ which set to zero in this example. The change of a single mode in momentum space leads to a change of the field distribution over the whole system volume.

was developed to describe the stochastic drift of a heavy particle in an infinite heat bath of light, thermal particles. The original Langevin equation reads

$$m\ddot{x}(t) = -\gamma\dot{x}(t) + F_{\text{ext}}(x,t) + \xi(t) \tag{7.9}$$

with an external force F_{ext}, the linear damping coefficient γ, and a stochastic force ξ. The random noise of this fluctuating force is often assumed and simply characterized by Gaussian white noise and leads to an average energy flux from and into the bulk system, while the damping is the dissipative average part with the back reaction of the medium to the energy-momentum exchange neglected.

The development was inspired by Brown, who observed pollen under a microscope, drifting by the noise of the water bath. Later on, this equation was applied to statistical physics, solid state physics, electro-technical systems, complex systems with many degrees of freedom and complex quantum systems. Another approach is even used in the modeling of wind turbulences for wind turbines [103] or in finance to model stock market fluctuations [104].

In nuclear physics, the Langevin Equation has been applied on top of the Boltzmann equation to include fluctuations in the system [105–108]. By dividing dynamics of a scalar quantum field in a hard and a soft part, a stochastic description of the system can be employed which resembles a Langevin equation [109]. The Langevin equation can be used to investigate fluctuations in the linear σ-model [110] or with similar methods to investigate disoriented chiral condensates [111]. Using the influence formalism, classical equations for the $O(N)$ modeled at presence of a heat-bath can be derived, when a stochastic interpretation is employed [112]. In [51, 52, 64] the Langevin equation has then been employed to phenomenologically model a stochastic coupling of a hydrodynamic particle bath and a classical field within a linear σ-model. This coupling allows an effective thermalization of the mean field. However, a Markovian and Gaussian approximation of the Langevin-equation can lead to problems if simple dissipation within the Langevin equation is interpreted in terms of particle production [113].

The Langevin equation has some drawbacks, however. The dissipation of the equation (7.9) due to the friction term, $\gamma\ \mathrm{d}\phi(t)/\mathrm{d}t$ is a continuous process. This is a natural assumption for continuous systems like fields or waves and a reasonable approximation for systems with a clear separation of scales, like in the classical example of a heavy particle in a bath of light ones. However, many processes are discrete and occur as single events. The same problem holds for the random force, ξ, which acts continuously and changes its value with every time step in numerical implementations. Because of the random nature of this process, the exact amount of exchanged energy can only be controlled in a statistical manner, and the back reaction at the bulk medium is neglected. In most implementations, the random force $\xi(t)$ is modeled by Gaussian white noise without a memory kernel,

$$\langle \xi(t) \rangle = 0\ , \tag{7.10}$$

$$\langle \xi(t)\ \xi(t') \rangle = \kappa \delta(t - t')\ . \tag{7.11}$$

Using a more sophisticated ansatz with memory kernel, the random force can be extended to a non-Markovian stochastic process with colored noise [114].

Before we discuss the relation between momentum and energy dissipation within a Langevin equation, we have to define them for a field ϕ. For a general Klein-Gordon equation,

$$\partial_\mu \partial^\mu \phi + m^2 \phi + \frac{\partial U}{\partial \phi} = 0\ , \tag{7.12}$$

the following conserved quantities can be defined [115, 116]:

$$\begin{aligned} E &= \int_V \mathrm{d}^3x\, \epsilon(\mathbf{x}) \\ &= \int_V \mathrm{d}^3x\, \left[\frac{1}{2}\dot{\phi}^2 + \frac{1}{2}\left(\vec{\nabla}\phi\right)^2 + U(\phi) \right], \end{aligned} \tag{7.13}$$

$$\mathbf{P} = \int_V \mathrm{d}^3x\, \mathbf{\Pi}(\mathbf{x}) = \int_V \mathrm{d}^3x\, \dot{\phi}\vec{\nabla}\phi, \tag{7.14}$$

$$\mathbf{A} = \int_V d^3x \left[\mathbf{x} \left(\frac{1}{2}\dot{\phi}^2 + \frac{1}{2}\vec{\nabla}\phi^2 + U(\phi)\dot{\phi} \right) + t\dot{\phi}\vec{\nabla}\phi \right] \tag{7.15}$$

where E denotes the total field energy, $\mathbf{P}$ is the total momentum and $\mathbf{A}$ the angular momentum. For any positive-definite potential U, the following relation holds

$$|\mathbf{P}| \leq E. \tag{7.16}$$

The dissipative part of the Langevin equation for the field $\gamma\partial_t\phi$ damps both the energy (7.13) and the momentum (7.14). For a potential-free wave equation with damping,

$$\partial_t^2 \phi(t,x) + \gamma\dot{\phi}(t,x) = \nabla^2\phi(t,x)\ , \tag{7.17}$$

the ratio of $P(t)/E(t)$ is non-linear in time (see Fig. 7.2), because both quantities are non-linear operators while $\dot{\phi}$ is linear. This results in different damping rates for E and P. This behavior complicates any attempt to couple particles and fields through inelastic interactions within an effective model.

Another problem arises with the continuous nature of the dissipative term in the Langevin equation. For a continuous process quantities like energy transfer can be calculated by integrating over a time interval but an amount of interaction by counting events cannot be defined. In contrast, singular events like particle pair-production can be counted, and rates are defined in a statistical manner. This becomes a problem when one tries to couple a scalar field theory to an ensemble of particles with interactions given by pair production and annihilation. Energy loss of the scalar field leads to energy gain in the particle ensemble and vice versa. Such an ansatz

is used in the famous and successful cosmological inflation model [117], in which particles are created by the energy loss of the oscillating scalar field, Φ. Particle production is described by rate equations, which are derived from the field equations of motion. Trying to simulate such a process with finite ensembles of particles leads to different problems. The energy loss within a time step Δt can be calculated from the fields and mapped to a certain number of created particles. The minimum amount of needed energy is always the rest mass of the particles

$$\min\left[E\left(\bar{\psi}\psi\right)\right] = 2m_{\psi} \tag{7.18}$$

The energy of a discrete number of created particles will however never match exactly with the continuous loss rate. Additionally, the physical process of pair production will depend on the simulation time-step size, and for $\Delta t \to 0$ a mapping between the continuous dissipation and the non-continuous particle creation will not be possible anymore. Another problem is the fact that the random force $\xi(t)$ changes its value at every point in time, both for white and colored noise. Trying to couple this behavior to pair production and annihilation leads to the same problem as the microscopic processes will depend on the time step.

In summary, the Langevin equation is a very good choice for an effective description of a system with two interacting scales. However, a microscopic modeling of the interaction processes is complicated by the continuous nature of the Langevin process. In the next section we will present how to potentially solve these problems by a non-continuous approach.

7.3 Particle-Field Interaction

In the previous section, the current methods for interactions between scalar fields and particles have been discussed. In this section, a new approach is discussed, which allows discrete interactions between fields and particle. This methods splits up in two sub-methods. The first is a numerical technique which changes the shape and the properties of a scalar field in a way, in which it looks like a discrete interaction has taken place. In summary this method changes the energy and momentum density of a small sub-volume of a field. These energy and momentum change can have arbitrary values wihtin physical limits.

The second part of the method describes how this discrete change of energy and momentum can be physically derived and described by microscopic interactions. A probability distribution for interactions will be discussed, which allows a simulation with Monte-Carlo methods.

Several examples and consistency checks will be given and the mathematical properties of this theory are discussed. This includes calculations for a harmonic oscillator, which is damped by discrete dissipation. Two other calculations cover the discrete Langevin equation in a harmonic oscillator and a one-dimensional scalar field. The last calculation is already the predecessor of

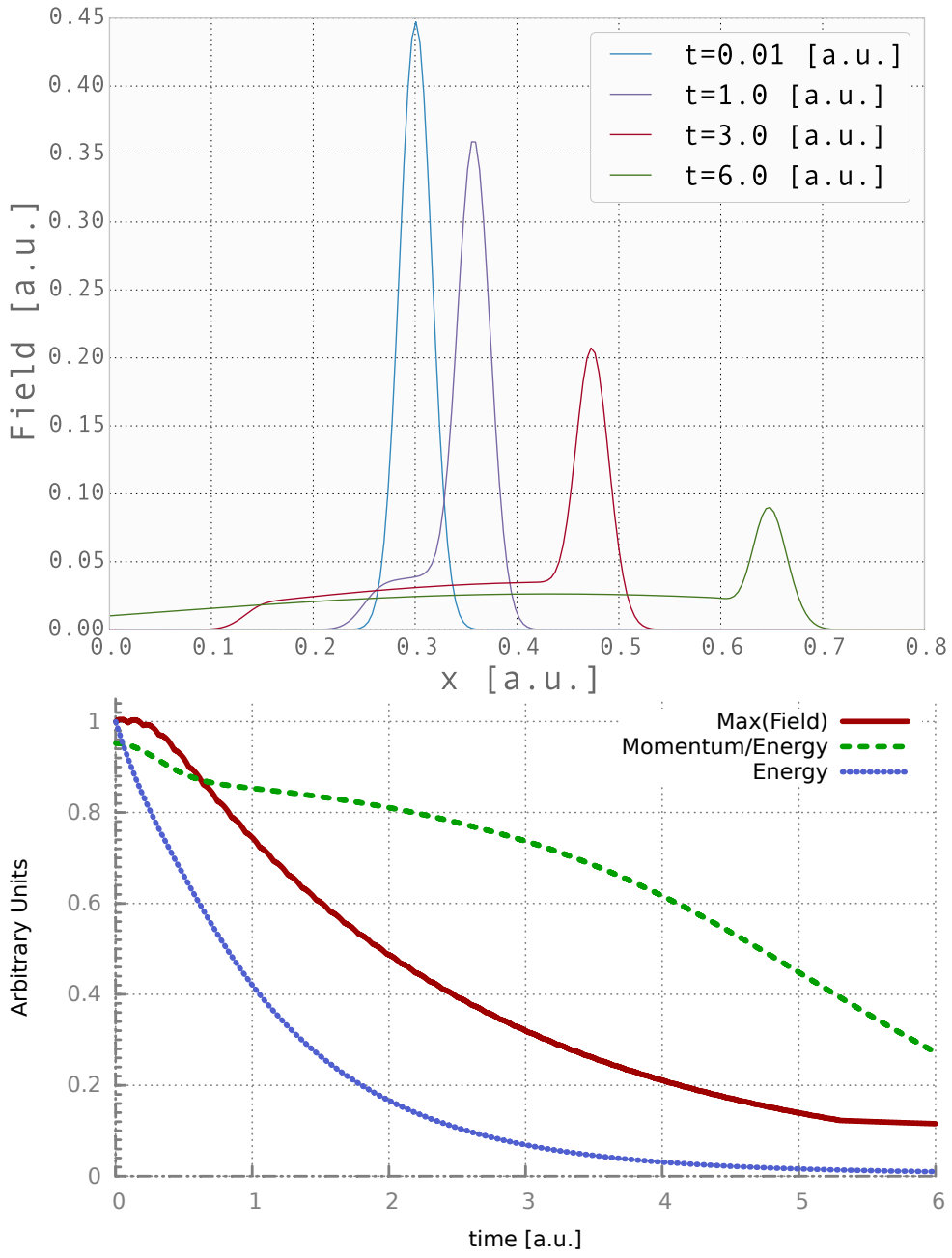

Figure 7.2: Top: Simulation of a 1D damped wave equation with a traveling Gaussian wave packet. **Bottom**: Relative plots of the maximal amplitude, the systems total energy, and the ratio of total momentum to total energy. Both energy and momentum are damped but with different rates, resulting in a non-linear relation even though the damping term $\dot{\phi}$ is linear. The non-linearity rises due the non-linear relation of the energy.

the DSLAM model, in which a three-dimensional scalar field is coupled to a particle ensemble. Both parts of the system can exchange energy by inelastic interactions like particle production and annihilation.

7.3.1 Discrete energy and momentum transfers from and to a field

Particles and fields are described in a very different manner. While scalar fields define a single quantity as function of time and position in continuous space (or discrete space on a grid), particles are characterized by their position and momentum. For particles, this sums up to three position coordinates, the energy and three-momentum values at every point in time. Fields are described by continuous functions or N^3 values on a three-dimensional N-sized grid for the field $\phi(\mathbf{x}, t)$ and its time derivative, $\dot{\phi}(\mathbf{x}, t)$.

To allow consistent interactions between particles and fields, the following features have to be fulfilled and are discussed in the following. Interactions have to be

- discrete in time, their time of impact must be given by a physical process
- take place at a given spatial point, the point of the physical interaction
- take place in a spatially limited volume
- energy and momentum transfer should be exactly definable
- both damping and excitations should be possible
- time and strength of the interaction should be derivable from physical processes

Discrete in time. For this point, a weak assumption is made: The interactions acting on the field ϕ can be seen as perturbations which keep the original equations of motion of the field intact. This can be motivated from the Boltzmann equation for particles as well as from the Langevin equation. Both approaches describe the physical propagation by a set of differential equations and interactions are given by interaction kernels.

$$\mathbf{v} \cdot \frac{\partial f}{\partial \mathbf{x}} + \frac{\mathbf{F}}{m} \cdot \frac{\partial f}{\partial \mathbf{v}} + \frac{\partial f}{\partial t} = I_{\text{Coll}} \tag{7.19}$$

The left handed side of equation (7.19) describe the propagation of particles given by their momenta and external forces. The collision term I_{Coll} describes the interaction between particles. E.g. in the parton cascade BAMPS [93] the collision term is interpreted stochastically. Particles are propagated via the interaction-free equations of motion most of the time and at some t_{int} they scatter. The only constraint is the mean free path being larger than the typical numerical size of an interaction cell [118].

The same interpretation will be taken here, a field ϕ is propagated via its undisturbed equations of motion EOM_0

$$\phi(t) \xrightarrow{\mathrm{EOM}_0} \phi(t + \Delta t). \tag{7.20}$$

At some interaction time t_i the field changes additionally by an interaction term,

$$\phi(t_i) = \phi_0(t_i) + \delta\phi \ . \tag{7.21}$$

Afterwards, the disturbed field is propagated with the general equation of motion. Overall interactions are interpreted as short events in time, neither do they occur continuously nor are they stretched over a longer time interval.

Interaction point and limited volume. As particle interactions take place at a defined position, the same should apply to the field interactions. However the interaction can not be constrained to a single interaction point in space for numerical and mathematical reasons if the interaction should be discrete. In fact, the interaction by the Langevin noise term ξ is point like in space but it acts as a point like force, not as a point like change in the field. A point like change of the field lead to a discontinuity which would break both numerical implementations as well as the equations of motion. Additionally, the term $\nabla_x \phi$ becomes undefined in such a case. Therefore the interaction must be located in a small volume around an interaction point. Nevertheless, an interaction volume implies a small break of Lorentz-invariance, so this volume should be small and be motivated as a smearing in space-time. A limited volume is also needed to quantize a well-defined amount of energy.

Exact energy and momentum transfer. If an interaction is derived from particle creation and annihilation, we have an exact amount of energy and momentum that is transferred between particles and fields, which is given by the particles energy and momentum

$$E = \sqrt{(\mathbf{p}_1 + \mathbf{p}_2)^2} \ , \tag{7.22}$$

$$\mathbf{P} = \left(\mathbf{p}^1 + \mathbf{p}^2\right) \ . \tag{7.23}$$

To obey energy-momentum conservation, this energy transfer must be exact at every interaction to keep the sum of the field- and particle energy constant at all times.

Derivation from physical processes By modeling the interaction with discrete events, two quantities are characteristic for such an interaction event have to be defined: when does the interaction take place and how strong it is? In case of the Langevin equation, these two quantities collapsed to a single transfer rate. In the discrete case, these two quantities have to be derived somehow. We will see that this can be accomplished by describing the interaction process by a physical model. In case of particle creation and annihilation, it is defined by a microscopic

cross-section. An example is given in the implementation of the DSLAM model, which uses a Yukawa-like interaction between quarks and an unstable scalar particle, see Chapter 5.

To link the very different description of particles and fields, common mathematical and physical properties have to be found. The most simple approach is to use energy and momentum. For particles, energy and momentum are directly given by their momentum four-vector. For a field we can employ the already discussed relations (7.13) and (7.14):

$$\begin{aligned} E &= \int_V \mathrm{d}^3x\, \epsilon(\mathbf{x}) \\ &= \int_V \mathrm{d}^3x\, \left[\frac{1}{2}\dot{\phi}^2 + \frac{1}{2}\left(\vec{\nabla}\phi\right)^2 + U(\phi)\right], \\ \mathbf{P} &= \int_V \mathrm{d}^3x\, \mathbf{\Pi}(\mathbf{x}) = \int_V \mathrm{d}^3x\, \dot{\phi}\vec{\nabla}\phi, \end{aligned}$$

A discrete interaction now maps to a discrete change of energy and momentum at a given position x and time t_k. The field $\phi(\mathbf{x}, t_k)$ is propagated with its undisturbed equations of motion and changed due to an interaction by a kick $\delta\phi(\mathbf{x}, t_k)$ which changes the energy and momentum by the desired amount ΔE and $\Delta\mathbf{P}$. This leads to relations of four coupled non-linear equations,

$$\Delta E(t_k) = E\left[\phi(\mathbf{x}, t_k) + \delta\phi(\mathbf{x}, t_k)\right] - E\left[\phi(\mathbf{x}, t_k)\right], \tag{7.24}$$

$$\Delta\mathbf{P}(t_k) = \mathbf{P}\left[\phi(\mathbf{x}, t_k) + \delta\phi(\mathbf{x}, t_k)\right] - \mathbf{P}\left[\phi(\mathbf{x}, t_k)\right]. \tag{7.25}$$

For $\Delta E > 0$ energy will be added to the field around $\mathbf{x}$, for $\Delta E < 0$ energy will be dissipated from the field. In general no unique and analytic solution exists for (7.24) and (7.25). In the next section a possible approach to solve these two equations is discussed.

7.3.2 Parameterization of interactions

Without further constraints, equation (7.24) and (7.25) have either no solutions or infinitely many. The problem is the fact that (7.24) and (7.25) reduce equations with many degrees of freedom to four scalar values, E and $\mathbf{P}$. A classical field on a numerical grid has as many degrees of freedom as it has grid points, in general $\sim N^d$, in the continuous case the number of degrees are continuous and non-countable. Even if the system rests in a box and has a high-frequency cutoff, the general statement is

$$N_{\mathrm{DOF}}\left(\phi, \dot{\phi}\right) \gg 4 \tag{7.26}$$

The first approach to this problem was an algorithm, which assumes an initial random perturbation and evolves dynamically by progressively minimize the energy and momentum difference in the equations with the constrain to minimize the needed strength of the disturbance, as well. For flat fields or fields with weak waves on it, the algorithm showed nice “interaction bumps”. In general

however, it was not numerically stable, had no guaranteed convergence and had problems with strongly asymmetric fields. Additionally, this solution was not very elegant as it left no control over the interaction space and lacked of a physical motivation.

To tackle these problems, the degrees of freedom of the numerical problem have to be reduced to a controllable system. The trick is to introduce an interaction parameterization which has a smooth spatially profile, is spatial limited and has exact four parameters, which can be mapped to momentum and energy properties.

In Appendix A different possible parameterization are discussed. To summarize this appendix chapter, the numerical parametrization for $\delta\phi(\mathbf{x}, t_k)$ has to be as smooth as possible. A natural choice would be the use of a single point like excitation on the grid. This is ineffective for two reasons: point like excitations are unsteady points on a numerical grid and lead to numerical artifacts like the Gibbs-phenomena, artificial exciting high frequencies and violating energy conservation.

A useful and robust parametrization is a three dimensional, moving Gaussian wave packet,

$$\delta\phi(\mathbf{x}, \mathbf{v}) = A_0 \prod_i^3 \exp\left[-\frac{(x_i - v_i\tilde{t})^2}{2\sigma_i^2}\right]\Bigg|_{\tilde{t}\to 0}. \tag{7.27}$$

The variables $\mathbf{v}$ define the direction and velocity of the Gaussian wave packet and A_0 the strength of the interaction. The three position arguments x_i are fixed by the interaction position. The time-parameter $\tilde{t}$ is needed to define and calculate the derivatives for the energy and momentum in (7.13) and (7.14),

$$\partial_t \delta\phi \overset{t\to 0}{=} -A_0 \prod_i^3 \left[\left(\frac{c v_i x_i}{\sigma_i^2}\right) \exp\left(\frac{(x_i)^2}{2\sigma_i^2}\right)\right] \tag{7.28}$$

$$\partial_{x_i} \delta\phi \overset{t\to 0}{=} -A_0 \frac{x_i}{\sigma_i^2} \prod_i^3 \left[\exp\left(\frac{(x_i)^2}{2\sigma_i^2}\right)\right] \tag{7.29}$$

The three widths of the Gaussian σ_i are free parameters, and can be fixed to a single spherical radius by $\sigma_x = \sigma_y = \sigma_z = \sigma$. It determines the interaction volume and should be chosen to fit the system scale. It has an impact on the minimal scale of possible modes in the system, as we will see in Section 7.4.3.

With this parametrization, a wave packet is added to the field after an interaction. Figure 7.3 shows an example of a field kick, which is parameterized with this Gaussian parametrization. The field gets a small "bump" at the interaction point.

To find A_0 and $\mathbf{v}$ in the parameterization (7.27), which solve (7.24) and (7.25) for a given ΔE and $\Delta\mathbf{P}$, the four coupled and non-linear equations have to be solved with a numerical equation solver. ΔE and $\Delta\mathbf{P}$ are given by the physical interaction, the derivation of these quantities will

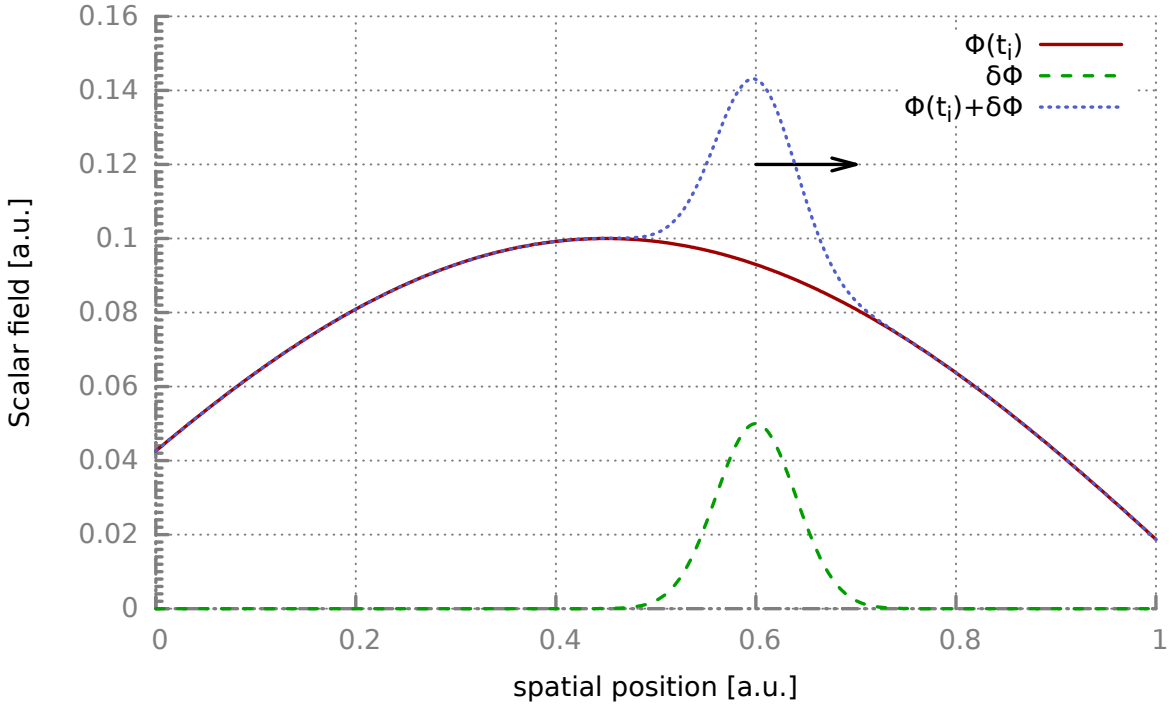

Figure 7.3: Visualization of the interaction principle, as described in (7.27). The energy of the initial field $\phi(t)$ is changed by a parameterized field variation $\delta\phi$. The resulting field $\phi(t) + \delta\phi$ is increased by a given energy ΔE and momentum $\Delta\mathbf{P}$. The traveling direction of the Gaussian is depending on the momentum.

be explained in various examples in the next chapters. A simple visualization of this principle is given in Figure 7.3, which shows the local modification of the field by a Gaussian.

An important implementation issue for finding A_0 and $\mathbf{v}$ is the energy dependence of the field and which part of the energy-contributions are dominating. The general definition of the energy (7.13) is again

$$E = \int_V \mathrm{d}^3x\, \epsilon(\mathbf{x}) = \int_V \mathrm{d}^3x\, \left[\frac{1}{2}\dot{\phi}^2 + \frac{1}{2}\left(\vec{\nabla}\phi\right)^2 + U(\phi)\right], \tag{7.30}$$

Depending on the system dynamics, the dominant part of the equation can differ. In case of a damped harmonic oscillator, the potential energy $U(\phi)$ is as import as the kinetic energy of the system's energy; therefore it is favorable to change the potential energy in case of an interaction. In case of the linear σ-model, the change of the potential energy is quite weak in comparison to chagne of the kinetic parts of the field for a small disturbance. If the σ field is equilibrated and shows thermal noise, most of the energy is stored in the kinetic parts of the energy:

$$\frac{1}{2}(\dot{\phi})^2 + \frac{1}{2}(\nabla\phi)^2 \gg U(\phi)\ . \tag{7.31}$$

In such a case a more appropriate interaction-parametrization would change mainly the kinetic energy of the system and not the potential energy. This becomes even more important if the

interaction should also remove energy from the system. If the parametrization would change the potential energy, adding of energy would always be possible. In contrast, removing energy would be impossible in most of the time, if the field holds most of its energy as kinetic energy, not potential energy.

A possible Gaussian parametrization in three dimensions, which changes mainly the kinetic energy of the system could have exactly the same form as (7.27) but keeps ϕ untouched and adds all its energy to $\dot{\phi}$. This has a very nice side effect: adding of energy does not generates an immediate Gaussian wave packet, which appears "out of the blue" on the field, but rather creates a kick which evolves the interaction bump with time. In this case, the wave equation stays continuous in space and additionally in time.

Removing of energy works according to the same principle, just the other way around. Energy is taken from the field by reducing the kinetic part of the field $\dot{\phi}$ by damping it with the Gaussian ansatz.

Finally, the parameterization (7.27) should be seen as a classical approximation which is valid for small velocities. The parameterization is not Lorentz invariant, resulting in spatial extent which does not depend on the velocity. This has an interesting effect, in case of a 3D system, the maximal momentum to energy ratio which can be generated with (7.27) is $\max\left\{\frac{P}{E}\right\} = 1/2$. The parameterization can be extended with a Lorentz boost, for example along the x-direction for $\mathbf{v} = (v_x, 0, 0)$

$$\begin{aligned}\delta\phi(\mathbf{x}, t) =& A_0 \exp\left(-\frac{\gamma^2 \left(x - v_x t\right)^2}{2\sigma^2}\right) \\ & \times \exp\left(-\frac{y^2 + z^2}{2\sigma^2}\right)\end{aligned} \tag{7.32}$$

The Lorentz-boost leads to a disc shaped deformation of the initially spherical Gaussian. With the boost, the momentum to energy ratio of (7.32) has the correct relativistic limit

$$\lim_{v \to 1} \left\{\frac{P}{E}\right\} = 1 \ . \tag{7.33}$$

At $v = 0.3$ both solutions differ by a factor of about 18%, for small velocities they are nearly the same, and (7.27) can be used as a safe approximation.

Calculations for the momentum to energy ratio of the two parameterizations (7.27) and (7.32) are given in Appendix A.

7.3.3 Modeling of energy transfers

In the previous section, the mathematical framework for energy and momentum transfer has been discussed. To apply this method to physical systems, additional modeling has to be done. The above method describes how to transfer a given amount of energy ΔE and momentum $\Delta\mathbf{P}$ to or from a scalar field at a given interaction point $\mathbf{x}$ and time t_i. To realize this method in a numerical simulation like a transport or Monte-Carlo simulation, appropriate values for ΔE, $\Delta\mathbf{P}$, $\mathbf{x}$ and t_i have to be defined. Motivated by the stochastic interpretation of interaction cross-sections, a probability distribution for energy and momentum exchanges which has to be derived according to the physical problem can be defined

$$P\left(\Delta E, \Delta\mathbf{P}, \Delta t\right) \ . \tag{7.34}$$

In Section 7.4 we will give various examples, calculations and results for such a modeling. In general the probability distribution (7.34) can have a memory kernel and can depend on the whole history with $P\left(\Delta E, \Delta\mathbf{P}, t\right)$, but we will use the Markov approximation in which only the current system state is important for future events, and (7.34) depends on the time-step size, Δt, only.

7.4 Examples And Model Calculations

The particle-field interaction method described in the previous sections is a general and abstract method to transfer energy and momentum from and to a system. This framework is not sufficient to fully describe the interactions of a system. As discussed in section 7.3.3, physical derivations for ΔE and $\Delta\mathbf{P}$ have to be found in terms of a probability distribution function $P\left(\Delta E, \Delta\mathbf{P}, \Delta t\right)$. In the next section, several examples will be given and their properties are investigated. These examples are well known and understood systems like the harmonic oscillator with different couplings or the Langevin equation. Classical approaches will be compared to interactions given by the particle-field method and should give an insight and feeling about the principles of the method and its capabilities.

7.4.1 Discretely damped 0-D harmonic oscillator

As the most simple test system, we choose the classical one-dimensional oscillator with damping,

$$\frac{\mathrm{d}^2x}{\mathrm{d}t^2} + \gamma\omega_0\frac{\mathrm{d}x}{\mathrm{d}t} + \omega_0^2 x = 0 \tag{7.35}$$

The frictional part $\gamma\frac{\mathrm{d}x}{\mathrm{d}t}$ dissipates energy from the system in a continuous process. We want to model the same system to have a discrete, noncontinuous damping and within an ensemble average both systems should behave the same.

Casting eq. 7.35 to an Hamilton equation leads to an equation with an explicit time dependence:

$$H = \frac{p^2}{2m}\ \mathrm{e}^{-\gamma t} + \frac{1}{2}m\omega_0^2 x^2\ \mathrm{e}^{-\gamma t} \tag{7.36}$$

Typically there are three types of solutions to equation (7.35), under-damped, critical-damped and over-damped. All three solutions show their dissipation via an exponential damping function $\sim \exp(-\gamma_{\mathrm{eff}} \cdot t)$ with $\gamma_{\mathrm{eff}} = \gamma_{\mathrm{eff}}(\omega_0, \gamma)$ as an effective damping parameter.

Motivation for a noncontinuous damping In classical mechanics, the harmonic oscillator is continuous both in space and momentum. Its energy levels are on a continuum and so are any dissipative processes. Quantum mechanics changed this behavior fundamentally with the introduction of quantization. The quantum energy levels became discrete with a lower limit:

$$E_n = \hbar\omega\,(n + 1/2)\ , \tag{7.37}$$

$$n = \frac{E_n}{\hbar\omega} - \frac{1}{2}\ , \tag{7.38}$$

so for $n \gg 1$:

$$n \sim E\ . \tag{7.39}$$

Within this ansatz the damping of a quantum oscillator becomes highly non-trivial, because the energy can now only jump between the energy niveaus $E_n - E_{n+1} = \Delta E$. In theory this has been a long unsolved problem and was most of the time solved by coupling quantum oscillators to heat-baths or stochastic-classical systems which absorbs the exchanged energy [119–122]. The idea of discrete energy jumps in the oscillator was the motivation for this first example calculation.

Energy of a classical harmonic oscillator In the following the properties of a classical, damped harmonic oscillator are discussed. The equation of motion is

$$\frac{\mathrm{d}x(t)^2}{\mathrm{d}t^2} + \omega_0^2\ x(t) + 2\gamma\frac{\mathrm{d}x(t)}{\mathrm{d}t} = 0\ . \tag{7.40}$$

Depending on the damping coefficient γ, the following solutions exist:

$$\gamma > \omega_0, \text{ over-damping}: \quad x(t) = C_0 \exp(\gamma_+ t) + C_1 \exp(\gamma_- t) \ , \tag{7.41}$$

$$\gamma = \omega_0, \text{ critical-damping}: x(t) = (C_0 + tC_1) \exp(-\omega_0 t) \ , \tag{7.42}$$

$$\gamma < \omega_0, \text{ under-damping}: \ x(t) = \exp(-\gamma t) C \sin(w_d t + \varphi) \ , \tag{7.43}$$

$$w_d = w_0 \sqrt{1 - \gamma^2} \ . \tag{7.44}$$

To compare against the quantum oscillator, the energy for the classical oscillator is calculated. The over-damped and critically damped oscillators both show an exponential decay when higher order terms are ignored:

$$E_{\text{kin}}^{(\gamma > \omega_0)} \approx \bar{E}_0 \ \mathrm{e}^{-\bar{\gamma} t} \ , \tag{7.45}$$

$$E_{\text{kin}}^{(\gamma = \omega_0)} \approx \bar{E}_0 \ \mathrm{e}^{-\omega_0 t} \ . \tag{7.46}$$

A more interesting case is the under-damped one

$$E_{\text{kin}}^{(\gamma < \omega_0)} = \frac{C^2}{2} \mathrm{e}^{-2\gamma t} \left[\omega_d \cos(\omega_d t + \varphi) - \ \gamma \sin(\omega_d t + \varphi) \right]^2 \ . \tag{7.47}$$

The energy of the under-damped oscillator shows an exponential decay with cosine and sine terms. These terms lead to a modulation of the dissipation because the oscillator only looses energy when it is moving. However, on average, on long timescales or for weak coupling, the energy loss scales roughly as an exponential:

$$E_{\text{kin}}^{(\gamma < 1)} \approx \bar{E}_0 \mathrm{e}^{-\gamma \omega_0 t} \tag{7.48}$$

In all three cases of the damping, the energy loss of a harmonic oscillator can be approximated by a simple exponential decay.

Modeling Of The Discrete Energy Loss

In Section 7.3.3 the description of the interaction was discussed in terms of a probability distribution function $P(\Delta E, \Delta \mathbf{P}, \Delta t)$. In this section the energy loss distribution function for the discrete damped oscillator will be derived.

To model a discrete damping for the harmonic oscillator with linear damping $\gamma \dot{x}$, a deterministic formalism which removes a given quantum of energy at fixed times out of the system could be introduced. However a more natural choice is a probabilistic ansatz, which models the system's initial total energy E_0 as a sum of small energy quanta $\overline{\Delta E}$:

$$E_0 = N_0 \cdot \overline{\Delta E} \ . \tag{7.49}$$

N_0 is the initial number of energy quanta and can also be called "steppiness" because it defines in which energy steps the system can be damped. The energy of the system can be damped by changing the energy quanta $N(t)$

$$E(t) = N(t) \cdot \overline{\Delta E} \ . \tag{7.50}$$

This change of $N(t)$ has to be modeled and mapped to the equations of motion. We now explain how to find an interaction probability function like (7.34) for this system. In this example, we can assume a two-state interaction: for a given Δt, the oscillator can lose a quantum of energy $\overline{\Delta E}$, or it can be left undisturbed. For $\Delta t \ll 1$ we can neglect multiple decays; additionally we assume a Markov process, so the oscillator only depends on its current state and has no 'memory'. Using these constraints, the interaction probability function $P\left(\Delta E, \Delta t\right)$ without memory-kernel can be described as:

$$P\left(\Delta E, \Delta t\right) = \Pr_{\text{loss}}(\Delta t)\delta(\Delta E - \overline{\Delta E}) + \Pr_{0}(\Delta t)\delta(\Delta E) \tag{7.51}$$

with $\Pr_{\text{loss}}$ being the probability to lose an energy quantum ΔE in the time interval Δt. $\Pr_0$ is the probability for the system to stay unchanged. Both probabilities are related by the norm of the probability distribution

$$\int P\left(\Delta E, \Delta t\right) \mathrm{d}\Delta E = \Pr_{\text{loss}}(\Delta t) + \Pr_{0}(\Delta t) = 1 \tag{7.52}$$

To find the probability for the oscillator to lose a certain amount of energy, we assume that every energy quantum $\overline{\Delta E}$ can decay independently. The definition for the exponential decay is

$$\frac{\mathrm{d}N(t)}{\mathrm{d}t} = -\gamma N(t) \tag{7.53}$$

with each decay event having a constant and independent decay probability in a time step $\mathrm{d}t$ of $\Pr = \gamma \mathrm{d}t$. With $\mathrm{d}t \to \Delta t$ and $\Delta t \ll 1$ we can write

$$\Delta N(t) = -\gamma \Delta t N(t) \tag{7.54}$$

However, we want to calculate the probability of a single energy quantum to decay. The number of energy quanta is given by (7.50)

$$N(t) = E(t)/\overline{\Delta E} \tag{7.55}$$

which increases the number of energy quanta if $\overline{\Delta E}$ decreased.

The total probability of a decay of a single quantum in a system of many quanta is in first-order approximation the sum of all single-probabilities

$$\Pr_{\text{loss}}\left(\Delta E\right) = \gamma \cdot \Delta t \cdot N(t) = \gamma \cdot \Delta t \ \frac{E(t)}{\overline{\Delta E}} \ . \tag{7.56}$$

For $N_0 \to \infty$ or $\Delta E \to 0$ this is the definition of the exponential decay law, while a finite N_0 will give a discrete exponential decay for a finite ensemble. For the total probability distribution function $P(\Delta E, \Delta t)$ we obtain

$$\begin{aligned} P(\Delta E, \Delta t) = \delta(\Delta E - \overline{\Delta E}) \left(\gamma \cdot \Delta t \frac{E(t)}{\overline{\Delta E}} \right) , \\ + \delta(\Delta E) \left(1 - \gamma \cdot \Delta t \frac{E(t)}{\overline{\Delta E}} \right) . \end{aligned} \tag{7.57}$$

Simulating $P(\Delta E, \Delta t)$ will give the same average energy loss scaling for $E(t)$ as the original harmonic oscillator with continuous damping.

In a numerical realization, the oscillator is propagated with the free equation of motion,

$$\frac{\mathrm{d}^2 x}{\mathrm{d}t^2} + \omega_0^2 x = 0. \tag{7.58}$$

This equation of motion conserves the total energy. To simulate damping, at every time step the decay probability density $P(\Delta E)$ is sampled using Monte-Carlo techniques. In case of a decay, the oscillator will lose the given amount ΔE by employing the method described in Section 7.3.1. In case of a oscillator, only the energy equation (7.24) has to be solved. The change δx on $x(t)$ becomes a simple shift of the oscillator,

$$x_t \to x_t + \delta x. \tag{7.59}$$

For a harmonic potential, this can be done analytically by solving

$$\begin{aligned} \overline{\Delta E} &= E(x_{t+1}) - E(x_t) \\ &= \frac{1}{2} \left[\omega_0^2 x_{t+1}^2 + \dot{x}_{t+1}^2 - \omega_0^2 x_t^2 - \dot{x}_t^2 \right] . \end{aligned} \tag{7.60}$$

The derivatives are approximated by the first-order difference discretization and with $\mathrm{d}t \to \Delta t$:

$$\dot{x}_{t+1} = \frac{x_{t+1} - x_t}{\Delta t} , \tag{7.61}$$

$$\overline{\Delta E} = \frac{1}{2\Delta t^2} (x_{t+1} - x_n)^2 - \frac{1}{2} \dot{x}_t^2 - \frac{1}{2} \omega_0^2 x_t^2 + \frac{1}{2} \omega_0^2 x_{t+1}^2 . \tag{7.62}$$

Solving (7.60) for x_{t+1} results in

$$\frac{x_t \pm \Delta t \sqrt{2\overline{\Delta E} + 2\overline{\Delta E} \Delta t^2 \omega_0^2 + \left(\Delta t^2 \omega_0^2 + 1 \right) \dot{x}_t^2 + \Delta t^2 \omega^4 x_t^2}}{1 + \Delta t^2 \omega_0^2} . \tag{7.63}$$

By neglecting higher order terms of order $\mathcal{O}\left(\omega^2 \Delta t^2\right)$ and higher results in the simple first-order approximation

$$x_{t+1} = x_t \pm \Delta t \sqrt{2\overline{\Delta E} + \dot{x}_t^2} \tag{7.64}$$

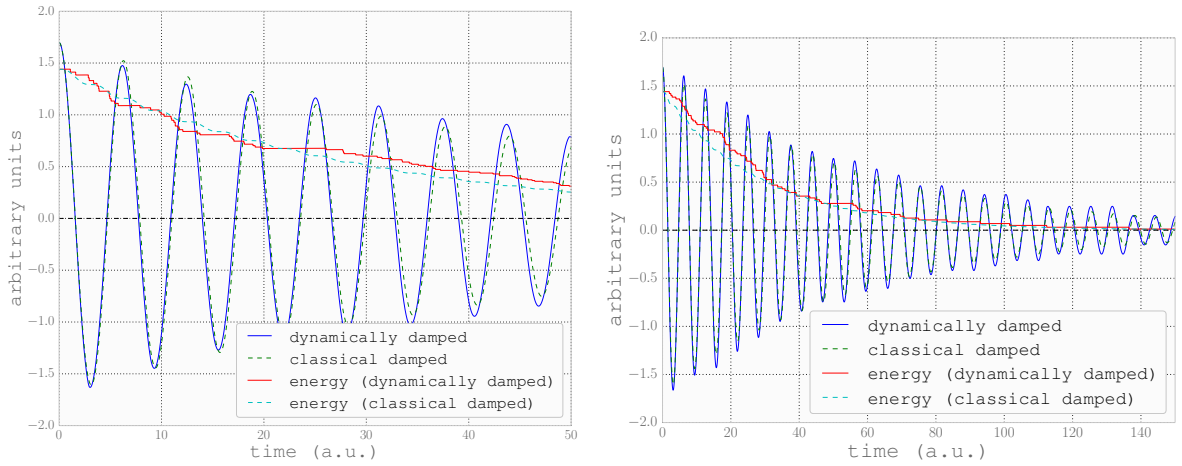

Figure 7.4: Simulation of discrete damped harmonic oscillators. The number of simulated particles / energy excitations is $N = 150$. With every decay of a particle, the oscillator loses a bit of energy, leading to damping of its motion. The discrete and continuous version have the same ensemble average. In a single run statistical deviation occurs.

This can be seen as an addition to the undisturbed equations of motion. With $\overline{\Delta E} \to 0$ equation (7.64) becomes the usual, first order Euler propagation for a differential equation: $x_{t+1} = x_t + \Delta t \cdot \dot{x}_t$. The additional term $\overline{\Delta E}$ is the change of the system given by the interaction-kick, changing the total system's energy with exactly this amount of energy. The sign $\pm$ in front of the square root is determined by the direction of $\dot{x}_t$, a kick with $\overline{\Delta E} > 0$ should always point in the direction of the current velocity $\dot{x}_t$. Note that $\overline{\Delta E}$ can always be positive while it can only be negative if

$$\dot{x}_t^2 \geq 2 \left| \overline{\Delta E} \right| \tag{7.65}$$

to have a real solution for the propagation equation. Even if there would be enough potential energy to fulfill this equation, a larger change of x_{t+1} would induce a larger kinetic energy than it should be dissipated from the system.

With these equations, a simple harmonic oscillator with discrete damping can be implemented. Two example calculations are shown in Figure 7.4, where a oscillator is simulated with 150 possible energy steps $\Delta E / E_0 = 150$. Every time such an energy mode decays, the energy is taken out of the system. In the limit of $\Delta E \to 0$, the the oscillator is damped continuously, again. On average, the continuously damped and the discretely damped oscillator have the same ensemble average. However, due to statistical fluctuations, both the amplitude and the phase can differ from time to time. In terms of Monte-Carlo simulations, this is highly intentionally.

7.4.2 Oscillator coupled to Langevin Equation

In the previous section, a harmonic oscillator was dynamically damped by a discrete dissipation. In a second benchmark, we extend the damped harmonic oscillator by a coupling to a heat bath via a Langevin equation, similar to [120]. The Langevin equation is a stochastic equation, which was motivated to describe a heavy particle in a thermal path of very small particles. By many, random kicks, the particle performs a random walk in the medium, later called Brownian motion (after the botanist Robert Brown). This calculation is done for a scalar oscillator as well as for a one-dimensional harmonic field. For the classical and zero-dimensional case, the equations of motion reads [92, 123]

$$\frac{\mathrm{d}^2}{\mathrm{d}t^2}x(t) + \gamma\frac{\mathrm{d}}{\mathrm{d}t}x(t) + x(t) = \kappa\xi(t) \ , \tag{7.66}$$

where $\xi(t)$ is defined as Gaussian white noise with $\langle\xi(t)\xi(t')\rangle = \delta(t-t')$. Using the equipartition theorem and the fluctuation-dissipation theorem [124], we can fix the strength of the stochastic force in the equilibrium case as

$$\kappa = \sqrt{2\gamma T}. \tag{7.67}$$

This relation is also known from Einstein's work on Brownian motion, connecting the stochastic drift of particles with the kinetic properties [125].

The equation of motion (7.66) describes a damped harmonic oscillator, driven by a Gaussian-distributed random force $\xi(t)$, which can increase or decrease the energy of the system by 'kicking' the oscillator. On average, the oscillator will show a Gaussian position distribution and by using the Fokker-Planck equation one can derive the equilibrium distribution for the energy, which is a Boltzmann distribution

$$f(E) \propto \exp(-E/T). \tag{7.68}$$

To simulate the oscillator with the Langevin dynamics within our proposed method, we propagate the system with the interaction-free equation of motion,

$$\frac{\mathrm{d}^2}{\mathrm{d}t^2}x(t) + x(t) = 0, \tag{7.69}$$

and model the discrete interactions again as small kicks to have the same statistical averages as the initial equation of motion (7.66). A representation for the stochastic force $\kappa\xi(t)$ in terms of energy changes can be found by using the relation

$$\frac{dE}{dt} = \dot{x}(t)\cdot F(t) = \dot{x}(t)\cdot\kappa\cdot\xi(t) \ , \tag{7.70}$$

which becomes in the discrete case with $\mathrm{d}t \to \Delta t$ and $t \to t_n$

$$\Delta E = \dot{x}(t)\cdot\Delta t\cdot\kappa\cdot\tilde{\xi}(t_n). \tag{7.71}$$

The stochastic force $\tilde{\xi}(t)$ is still a Gaussian white noise with a normally distributed random number ξ_n in each time step t_n

$$\tilde{\xi}(t_n) = \frac{\xi_n}{\sqrt{\Delta t}} \ . \tag{7.72}$$

The factor $\sqrt{\Delta t}^{-1}$ is needed to fix the norm of the uncorrelated white noise via

$$\langle \xi_n \xi_m \rangle = \frac{\delta_{mn}}{\Delta t}. \tag{7.73}$$

The total interaction probability distribution function $P\left(\Delta E, \Delta t\right)$ is now composed of four single probabilities: the probability of no interaction in a time interval Pr_0, the damping of the oscillator by the process $\gamma \dot{x}(t)$ with the probability $\mathrm{Pr}_{\mathrm{loss}}$, as discussed in the previous section, and the two cases where the energy of the system is changed by the stochastic force $\tilde{\xi}(t)$: we can see in (7.71) that depending on the signs of ξ and $\dot{x}(t)$ a random kick can add energy to a system or dissipate energy from it. Both processes are symmetric in general and from this symmetry one gets $\langle \Delta E \rangle = 0$ in equilibrium. However $\langle \Delta E^2 \rangle > 0$ always holds.

The probability $\mathrm{Pr}_{\mathrm{loss}}$ has already been discussed in the previous section 7.4.1 and follows the same systeamics here. The loss and gain terms induced by the stochastic force are given by (7.71), due to their symmetry they are both subsumed in a single probability density term. The sum of all terms for the interaction probability distribution is

$$\begin{aligned} P(\Delta E, \Delta t) &= \delta\left(\Delta E - \dot{x}(t) \cdot \Delta t \cdot \kappa \cdot \xi(t)\right) \\ &+ \delta(\Delta E - \overline{\Delta E}) \left(\frac{\gamma \cdot \Delta t}{\overline{\Delta E}} E(t) \right) + \underset{0}{\mathrm{Pr}} \ \delta(\Delta E). \end{aligned} \tag{7.74}$$

The no-interaction probability Pr_0 is again found by normalizing with $\int P(\Delta E, \Delta t) \mathrm{d}\Delta E \equiv 1$. Equation (7.74) looks quite complicated, but the single terms can be easily interpreted and simulated. The last term is the contribution for no interaction to happen at all. The second last term describes the probability for a system to lose a given amount of energy $\overline{\Delta E}$ due to the friction, just like in our first example. The first term describes the process of gaining energy from the stochastic force. To sample the gain- and loss-terms by the random kicks in the probability density, one can simply sample a random kick ξ_n and calculate the given energy difference from (7.71) which is propagated back to the system. As we simulate a single degree of freedom, the already known relation for changing the energy (7.64) can be used.

In this example we describe the dissipative process with discrete decay steps while the energy fluctuations given by $\xi(t)$ can have continuous values. Even though this seems contradictory, it has two reasons: we wanted to stay as close as possible to the original system, the Langevin equation, which has continuous interactions. The second reason is we wanted to introduce continuous values for ΔE at this point because in the last example of this Section particles and fields exchange energy by discrete particle annihilation and creation processes. The motivation is

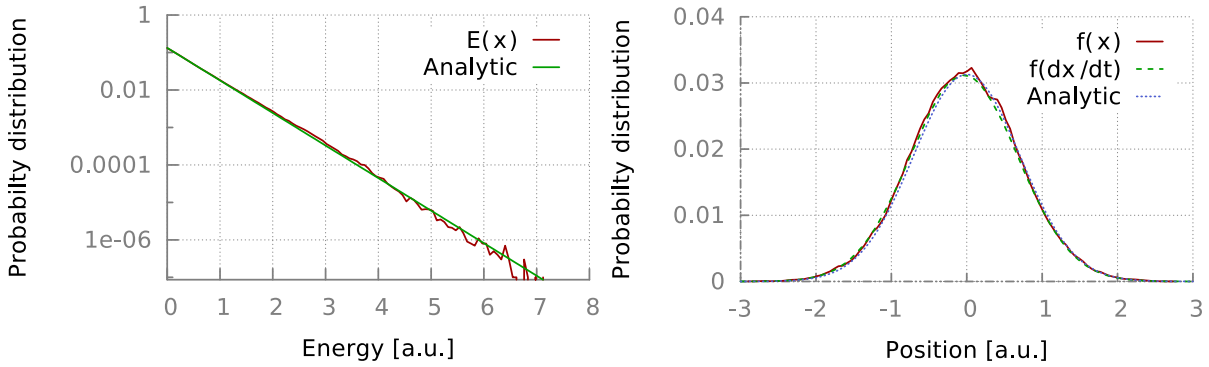

Figure 7.5: Simulation of a harmonic oscillator, coupled to a heat bath via a Langevin equation. The random force and the damping is implemented with the non-continuous energy-transfer method. The plot shows the distribution function of the energy, the position distribution and the velocity distribution for a temperature of $T = 0.5$ a.u. and 10^8 calculation steps and a corresponding energy-step size. Both plots coincide with the expected analytical result, which is $\exp(-E/T)$ for the energy distribution (left) and $1/\left(\sqrt{2\pi T}\right)\exp\left(-m\omega_0^2 x^2/2T\right)$ for the spatial distribution (right).

the DSLAM model in which chemical processes between quarks and the σ-field are discrete in time, their energy and momentum spectrum is continuous.

Figure 7.5 shows the position and velocity distribution of the harmonic oscillator, which is a Gaussian. The width of the distribution depends on the temperature in the fluctuation-dissipation relation (7.67) and scales with $\sqrt{T}$. The energy distribution shows an exponential tail $\exp(-E/T)$with the same temperature. The numerical calculation was performed with our method, which works differently than the usual Langevin equation, however all results are in good agreement due to the consistent description of the energy exchange rates.

7.4.3 One-Dimensional Scalar Field coupled to Langevin Equation

The previous calculations have been employed with a single degree of freedom. In the next example, the 0D system (7.35) is extended to a $1+1$-dimensional field. The single degree of freedom $x(t)$ is now replaced by a scalar field $\phi(x,t)$ with the equation of motion of a potential-free wave equation with a stochastic force and damping:

$$\left(\frac{\partial^2}{\partial t^2} - \frac{\partial^2}{\partial x^2}\right)\phi(x,t) \quad + \gamma\frac{\partial}{\partial t}\phi(x,t) + \phi(x,t) = \kappa\xi(x,t)\ . \tag{7.75}$$

The stochastic force is the $(1+1)$-dimensional extension of the Gaussian white noise

$$\langle \xi(x,t)\xi(x',t')\rangle = \delta(x-x')\delta(t-t')\ . \tag{7.76}$$

The stochastic process (7.75) is simulated as a reference system. In comparison, in our simulation the field $\phi(x,t)$ is propagated with the disturbance free equations of motion. The stochastic force and damping are simulated analogously to in the $(0+1)$-dimensional example. Because of the additional dimension of the system, we could model a momentum exchange ΔP, as given in (7.34). We neglect this term because the original Langevin-equation does not model this term either. However, the last example in this chapter will address this issue.

Since this system is one-dimensional, the simple analytic relation (7.64) can not be used anymore because the interaction point becomes an interaction volume with a finite spatial extent. We have used a one-dimensional form of the Gaussian parameterization (7.27). For each point of the system an interaction probability is sampled with (7.74). In case of an interaction, the center of the Gaussian interaction parameterization is located at the interaction point and the change of the field $\phi(\mathbf{x},t)+\delta\phi(\mathbf{x})$ is solved by using equation (7.24) with the help of a numerical solver. For every interaction at some point $\mathbf{x}$ the neighbor cells of the interaction point are changed as well. The reason is the spatial extension of the Gaussian parameterization leading to a smeared interaction region or volume. This holds both for adding energy as well as removing energy from the system.

As shown in Figure 7.3, this will result in a field given by a superposition of small interaction bumps. In the equilibrium state, the field distribution will show spatial fluctuations, distributed among the field's modes. Overall the equilibrium state behaves very similar to the oscillator case but with a spatial extent in one-dimension and therefore more dynamics. The same holds true for the interaction probability distribution density which is the spatial extended version of (7.74):

$$\begin{aligned} P(x,\Delta E,\Delta t) &= \delta\left(\Delta E - \dot{\phi}(x,t)\cdot\Delta t\cdot\kappa\cdot\xi(x,t)\right) \\ &+\delta(\Delta E-\overline{\Delta E})\left(\frac{\gamma\cdot\Delta t}{\overline{\Delta E}}E(x,t)\right)+\Pr_0\ \delta(\Delta E)\ . \end{aligned} \tag{7.77}$$

A very interesting observable is the power spectrum of the field

$$S(\mathbf{k}) = \lim_{t\to\infty}\frac{1}{2t}\int_{-t}^{t}\mathrm{d}t\,|\mathcal{F}[\phi(x,t)](\mathbf{k})|^2 \tag{7.78}$$

with the spatial Fourier transformation $\mathcal{F}$

$$\mathcal{F}[f(\mathbf{x})](\mathbf{k}) = \int_{-\infty}^{\infty} f(\mathbf{x})\cdot e^{i\mathbf{x}\cdot\mathbf{k}}\mathrm{d}^3\mathbf{x}\ . \tag{7.79}$$

In case of the classical Langevin equation, the expected distribution of the power spectrum can be calculated. A damped field coupled to a white-noise process is expected to show Brownian noise, as it effectively integrates the white noise over time [126]. The resulting field has an average

spectrum in form of a power with the temperature as the mode amplitude [124, 127]

$$S(k) = \frac{T}{k^2} \ . \tag{7.80}$$

Figure 7.6 shows the expected spatial spectrum for the classical Langevin equation (7.75) and for the simulation with our proposed method. For large and small momenta k, deviations occur due to finite-system effects, in the intermediate region the spectrum shows a very good agreement with (7.80). At some point the small wavelengths with large k are suddenly strongly suppressed.

The explanation for this behavior is the fact that we use a finite-volume excitation in the parameterization (7.27). In a classical Langevin equation, the point-like stochastic force ξ has a constant spectrum $S_\xi(k) \sim c$, allowing to excite any modes. Within our method, the energy is changed in a small but finite-size sub-volume. The smallest excitable mode in the system has therefore the same scale as the interaction volume. Employing the Gaussian parameterization (7.27), this scale is the width σ. The resulting mode cutoff can be calculated evaluating the spectrum of the parameterization (7.27), here for our 1-dimensional example:

$$|\mathcal{F}[\delta\phi(x,t)](k)|^2 \sim \exp\left(-k^2 \cdot \sigma^2/2\right) \approx \begin{cases} 1 & \text{for } k \ll \sigma \\ 0 & \text{for } k \gg \sigma \end{cases} \tag{7.81}$$

At the scale $k^2\sigma^2 \approx 1$ the Gaussian shape leads to a soft cutoff which suppresses all higher modes. We therefore define a soft-cutoff scale at

$$k_{\text{Cutoff}} \equiv \frac{\sqrt{2}}{\sigma} \ . \tag{7.82}$$

These results show that our method is capable of simulating a thermal system with Langevin dynamics with controlled systematic numerical errors.

7.4.4 Particle Ensemble coupled to Scalar Field

In this section we use the proposed method to couple an ensemble of particles to a scalar field in a (3+1)-dimensional simulation. The simulated system is a microcanonical box with a scalar field, particles and anti-particles. Particles can perform two-body elastic collisions, the field is propagated via a wave equation, like in the sections before. Additionally, field and particles can interact by microscopic particle annihilation and creation processes. This system is motivated by the DSLAM model. However, the calculations can be seen from a generic view in which an anharmonic field theory is coupled to a particle ensemble to give a more complex example system.

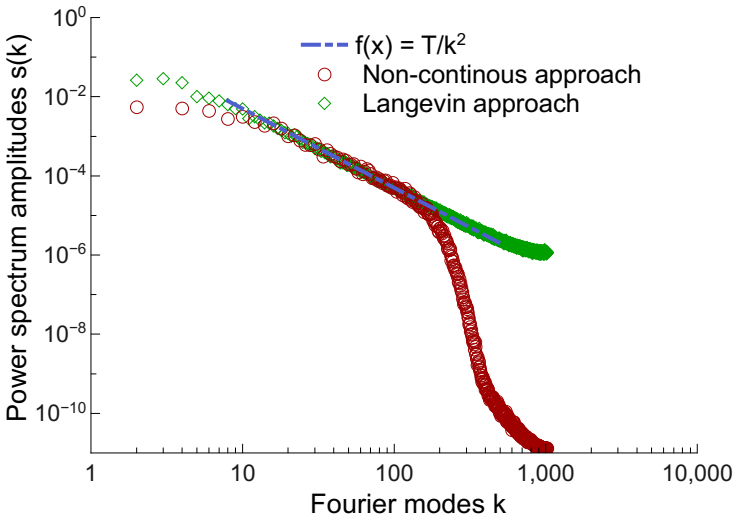

Figure 7.6: Time averaged power-spectrum of the one-dimensional wave equation $\phi(x,t)$. The spectrum is calculated according to (7.78). The system is a one-dimensional harmonic oscillator, coupled to a Langevin equation with a continuous and a non-continuous ansatz. The dashed, blue line shows the theoretical solution of the system T/k^2, the red circles the non-continuous approach and the green diamonds show the classical Langevin equation as a reference. All three curves are in very good agreement in the intermediate region and show the same system temperature, which was chosen to $T = 0.5$ a.u. Both Fourier plots are averaged over 100 snapshots of the same run. Simulated was a grid with 1024 points. At large wavelengths, both systems deviate due to finite system size effects. At small wavelengths the non-continuous methods has an interesting cut-off due to the finite-size of the interaction region in comparison to the point-like interactions of the classical Langevin method.

The equations of motion for the σ field are

$$\left(\frac{\partial^2}{\partial t^2} - \nabla_{\mathbf{x}}^2\right)\sigma(\mathbf{x},t) = -\lambda^2\left(\sigma^2(\mathbf{x},t) - \nu^2\right)\sigma(\mathbf{x},t) + f_\pi m_\pi^2 + g\sigma(\mathbf{x},t)\cdot\left\langle\bar{\psi}\psi\right\rangle(\mathbf{x},t)\ . \tag{7.83}$$

with the couplings strengths for the chiral potential $\lambda^2 = 20$, the explicit symmetry breaking term $f_\pi m_\pi^2$ and a mean-field potential between the field and the particles with the coupling g. Besides the mean field and potential interactions, a particle q and an anti-particle $\bar{q}$ can annihilate to a field quantum. The underlying process is the Yukawa coupling

$$\mathcal{L}_{\text{int}} = g\bar{\sigma}\phi^*\phi \tag{7.84}$$

which can create a sigma particle by pair annihilation,

$$\bar{q} + q \to \sigma, \tag{7.85}$$

or destroy it in the inverse decay process,

$$\sigma \to \bar{q} + q \,. \tag{7.86}$$

Feynman diagrams of both processes are

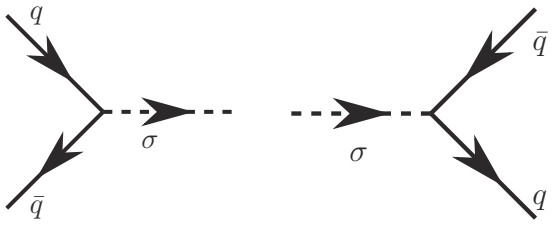

A complete discussion of the linear σ-model is given in Chapter 2.

Interaction between particles and the field is modeled in several steps. The quark annihilation process is calculated with a microscopic cross section, the generated particle is treated as an unstable particle resonance, the σ particle. The created sigma particle is not propagated or added to the system as a real particle but its energy and momentum is transferred to the scalar field, keeping the system's total energy and momentum conserved. In the inverse process, field excitations in the scalar field are treated as energy excitations. These excitations are modeled as unstable particles which can decay and create an particle-anti-particle pair again.

In the following the details of this modeling and the algorithm are explained in detail. We start with the implementation of the particle-annihilation process.

The interaction probability of the two incoming particles for the process $\bar{q}q \to \sigma$ is calculated microscopically. In our simulation it is modeled with a constant, isotropic cross-section $\hat{\sigma}_{\bar{q}q\to\sigma}$ respecting all kinematic constraints. For Monte-Carlo sampling, we use the stochastic interpretation of the cross section [93] for a set of particles in a cell

$$\Pr\left(\bar{q}q \to \sigma\right) = \hat{\sigma}_{\bar{q}q\to\sigma}\ v_{\mathrm{rel}} \frac{\Delta t}{\Delta V N_{\mathrm{test}}}\ , \tag{7.87}$$

with

$$v_{\mathrm{rel}} = \frac{s}{2E_1E_2}\ , \tag{7.88}$$

and the Mandelstam variable s

$$s = \left(p_\mu^1 + p_\mu^2\right)^2\ . \tag{7.89}$$

We have chosen the Breit-Wigner cross section [80, 81]

$$\sigma_{\bar{q}q\to\sigma}(s) = \frac{\bar{\sigma}\ \Gamma^2}{\left(\sqrt{s} - m_\sigma\right)^2 + \left(\frac{1}{2}\Gamma\right)^2} \tag{7.90}$$

with a constant factor $\bar{\sigma}$ and the mass of the created unstable particle m_σ. The Breit-Wigner cross section is discussed in Chapter 5.

When an interaction occurs, the net-energy and -momentum transfer is calculated with

$$\Delta E = \sqrt{s} \qquad \Delta \mathbf{P} = (\mathbf{p}_1 + \mathbf{p}_2)\,. \tag{7.91}$$

At the particles' interaction point the particles are removed from the ensemble and their net-energy and -momentum is transferred to the field ϕ at this point, keeping the total energy and the total momentum conserved. This transfer is done by changing the field energy and momentum at the interaction point of the particles using our proposed method. The energy and momentum difference equations (7.24) and (7.25) are solved for the interaction-time step with a numerical solver. The field $\phi(\mathbf{x}, t)$ is changed by employing the 3D Gaussian parameterization $\delta\phi(\mathbf{x})$ (7.27). By changing the amplitude as well as the direction of motion of the Gaussian, both the energy and momentum can be changed within the interaction volume such that the numerical solver can transfer ΔE and $\mathbf{\Delta P}$ to the field. Figure 7.3 shows a simplified version of this process in which small Gaussian blobs over a small volume generate small energy excitations on the field ϕ

To obtain thermal and chemical equilibration, the inverse process has to be implemented according to the principle of detailed balance. In kinetic theory detailed balance is described by reversing a process in time and having the same probability for it. For example the s-channel scattering of two particles of species A to particles of species B

$$A_1 + A_2 \to B_1 + B_2 \tag{7.92}$$

should have the same probability as the inverse process B going to A. In terms of quantum-field theory the scattering matrix elements must be symmetrical

$$|M_{AB}|^2 \equiv |M_{BA}|^2 \ . \tag{7.93}$$

Note that this does not include kinematic limits which can always forbid various processes and channels. In terms of field theory, detailed balance can be guaranteed if all self-energies and polarization functions are generated from a given set of so called closed or vacuum diagrams by using a formalism like the 2PI generating functionals [37] and by the unitary of the S-matrix [128].

We have already discussed the method for particle annihilation. The inverse process, particle production, has to be derived differently, because the field has no initial particles which we could use for Monte-Carlo sampling. Instead, we only have the scalar field ϕ and its properties like energy and momentum from which we have to derive particle-like properties. This step is again subject to the underlying physical model. For every point at the field, we assume the field excitations to consist of unstable particles which can decay to stable particles with $\sigma \to \bar{q}q$. In

case of a decay, the field ϕ loses the amount of energy at the interaction point, leading to an effective damping of the field. This decay process is modeled in two steps. First we have to assume a distribution function $f_\sigma(\mathbf{x}, \mathbf{p}, t)$ for σ particles at every possible interaction point. The properties of $f_\sigma(\mathbf{x}, \mathbf{p}, t)$ have to be derived from the field properties at every point in space which is done by assuming local equilibrium via coarse graining within a field cell. To be consistent with detailed balance, the equilibrium distribution for f_σ must have the same temperature as the particle's distributions, f_q and $f_{\bar{q}}$. In the linear σ model, the potential and therefore the equilibrium-mean field has a thermodynamical temperature dependence, which maps a mean-field value for every temperature $T \to \langle\phi\rangle(T)$. By inverting this relation $\langle\phi\rangle(T) \to T$, we can calculate the effective temperature of the field at every point of the field.

The next needed quantity is the particle density

$$n_\sigma\left(\mathbf{x}, t\right) = \int \frac{\mathrm{d}^3\mathbf{p}}{(2\pi)^3}\; f_\sigma\left(\mathbf{x}, \mathbf{p}, t\right) \;. \tag{7.94}$$

Depending on the underlying distribution function f_σ a relation between the particle and energy density has to be found

$$n_\sigma\left(\mathbf{x}, t\right) \to n_\sigma\left(\mathbf{x}, t, \epsilon\left(\mathbf{x}\right)\right) \;. \tag{7.95}$$

The energy density ϵ is fixed by assuming the same energy density for the distribution function and the field

$$\epsilon = T^{00} = \int \frac{\mathrm{d}^3\mathbf{p}}{(2\pi)^3}\; E\; f_\sigma(\mathbf{x}, \mathbf{p}, t) \equiv E\left(\sigma(\mathbf{x}), \dot{\sigma}(\mathbf{x})\right) \;. \tag{7.96}$$

The chosen distribution function and particle density has to be consistent with the annihilation process. Additionally, usually the local cell is not at rest. So we boost the distribution function f_σ relativistically with the boost-velocity $\mathbf{v} = \mathbf{p}/E$. The field energy E and $\mathbf{p}$ contained in the cell around $\mathbf{x}$ are determined according to (7.13).

In our calculations we have used the Boltzmann distribution for the particles q, anti-particles $\bar{q}$ and the σ-particles

$$f(\mathbf{p}, \vec{v}) = \exp\left(-\frac{1}{T}\mathbf{u}\cdot\mathbf{p}\right) = \exp\left(-\frac{\gamma}{T}(E - \vec{v}\cdot\mathbf{p})\right) \;, \tag{7.97}$$

but the local energy-relation (7.96) can easily be extended to other distributions like the Bose-Einstein distribution. After calculating a distribution function, σ particles are sampled from f_σ with Monte-Carlo methods. For every sampled particle the decay probability is calculated. In the center of of momentum frame of the particle, the decay probability is given by

$$\Gamma_\sigma = \frac{g^2}{8\pi m_\sigma}\sqrt{1 - \frac{4m_q^2}{m_\sigma^2}} \;, \tag{7.98}$$

with Γ_σ consistent to (7.90). Note that Γ_σ is valid only in the rest frame of the decaying particle. To calculate Γ in the laboratory-frame it has to be boosted

$$\Gamma_{\text{boosted}} = \frac{\Gamma}{\gamma} = \Gamma \frac{m}{E} = \Gamma \sqrt{1 - \frac{\mathbf{p}^2}{E^2}}. \tag{7.99}$$

This boost has to be applied in (7.90), too. In case of the linear σ-model, the particle's mass m can have a temperature dependence $m(T)$ which suppresses interactions at the phase transition, as seen in Figure 5.4 and 5.5.

If a σ-particle decays, the energy and momentum of the particle is calculated as

$$\Delta E = E_\sigma, \quad \Delta \mathbf{P} = \mathbf{P}_\sigma \ . \tag{7.100}$$

The resulting amount of energy and momentum is removed again from the field around the interaction point with the help of the four energy and momentum difference equations (7.24) and (7.25) and the Gaussian parameterization (7.27). Again, this parameterization leads to a small interaction volume from which the energy is dissipated.

To come back to our notation of an interaction probability distribution, we use the above discussed concepts to formulate an interaction probability density per numerical cell

$$\begin{aligned} &P\left(\Delta E, \Delta \mathbf{P}, \Delta t\right) = \\ &\sum_{i,j}^{N_{\text{cell}}} \delta\left(\Delta E - \sqrt{s}\right) \delta\left(\Delta \mathbf{P} - \left(\mathbf{p}_i + \mathbf{p}_j\right)\right) \frac{\hat{\sigma}_{\bar{q}q \to \sigma} v_{\text{rel}}(s) \Delta t}{\Delta V N_{\text{test}}} \\ &+ \delta\left(\Delta E - E_\sigma\right) \delta\left(\Delta \mathbf{P} - \mathbf{P}_\sigma\right) \frac{\Gamma_\sigma(m_\sigma)\ n_\sigma(\phi(\mathbf{x}), t) \Delta t}{\Delta V} \\ &+ \Pr_0 \delta\left(\Delta E\right) \delta\left(\Delta \mathbf{P}\right) \end{aligned} \tag{7.101}$$

with the sum over all particles N_{cell} in a cell.

By implementing this algorithm, one has to be careful to really fulfill the discussed implications given by detailed balance. Besides the correct physical implementation, the numerical implementation has to be stable and very precise. First, the average interaction rates of particle creation and annihilation has to be the same for any temperature, leading to no change of net-particle number.

$$R_{\bar{q}q \to \sigma} = R_{\sigma \to \bar{q}q} \ , \tag{7.102}$$

Secondly, the average energy exchange per process has to be the same for both processes

$$\langle E_{\bar{q}q \to \sigma} \rangle = \langle E_{\sigma \to \bar{q}q} \rangle \ . \tag{7.103}$$

Finally, the spectra of both processes have to be the same.

Violating one of these conditions would lead to an unstable system. While the transition rates can fluctuate and differ at a given time, their average has to be the same, otherwise the particle number would drift out of equilibrium If the transaction rates are the same but the average energy transfer for both processes differ, the system will as well run out of equilibrium. Obviously, the energy equipartition theorem is violated, if net-energy is constantly transferred from one system part (for example the fields) to another part (the particles). Additionally, with the proposed method for the particle density (7.95) a lower energy density in the fields leads to a lower calculated particle density, which again results in lower particle decay, which amplifies the problem.

7.4.4.1 Numerical Calculations

To test the described method for numerical stability and physical correctness, several numerical calculations have been performed. The main goal is the test of energy, momentum and particle number conservation, as well as numerical and physical stability, which is done by simulating a microcanonical ensemble. The setup was a finite-size and cubic box with periodic boundary condition, to simulate a large thermal system. Periodic boundary conditions conserve momentum and energy at the system boundaries. The used model is already the DSLAM implementation linear σ-model, however the results discussion is general for other field theories and the numerical and mathematical properties of the particle-field method can be extended to other three-dimensional simulations. The linear σ-model has a temperature dependent mass, but in the scenario of thermal and chemical equilibrium this feature of the σ-model can be neglected because the mass stays constant over the simulation run time. As initial conditions, all particles and fields have been initialized at a given temperature (numerical details are given in Section 8.5.1). Without the particle-field interactions, the results would be the same as the equilibrium calculations in Chapter 3 and the system would stay more or less constant. All units of time, rates, system size and temperature will be kept in arbitrary unis (a.u.) instead of physical unity (like fm, GeV, ...). Furthermore, the exact physical unity and properties of the system are not necessary to discuss energy conservation and stability of the system and simulation.

The number of test-particles is set to approximate $N_{\text{test}} = 3 \cdot 10^6$, the numerical time steps are set to $\Delta t = 0.002$ a.u., the numerical grid-size of the fields is $N_\sigma = 128^3$ with $\Delta V = \left(\frac{6 \text{ fm}}{128}\right)^3$, the simulation run time is 300 a.u., which corresponds to 150000 time steps. The interaction volume of the Gaussian parametrization is 32^3 grid points, which is about 1.5% of the system volume.

7.4.4.2 Results

Figures 7.7 to 7.14 and show the results of the described simulation. Over the whole simulation time, the total energy and momentum stays constant, while the particle number and the scalar

mean field show thermal fluctuations around a stable mean value. Figures 7.8 shows the total particle number, Figure 7.7 the mean field. Field and particles are coupled via the chemical processes (7.85) and (7.86) and exchange energy and momentum, leading to fluctuations in both local energy densities and their total energy. Figure 7.9 represents the scalar field distribution, showing a stable Gaussian distribution. For a thermal field this is the expected result, similar to the Langevin result (7.67). The width of the Gaussian shows small thermal fluctuations over time, and the mean value drifts according to (7.7).

This is a remarkable result, because our scalar field shows the distribution of a thermal field which is in general produced by coupling the field to a Langevin like process. A classical field, coupled to a Gaussian noise, would show an equipartition of energy of $k_B T$ for every mode. However, integrating over all modes leads to the famous classical ultraviolet catastrophe. In our case, the field shows a slightly different distribution of energy on the modes as shown in Figure 7.11. For large wavelengths, the modes have an equipartition of energy, for small wavelengths the modes are strongly suppressed by the soft cutoff. This cutoff is due to the same mechanism as discussed in (7.82) and (7.81). The finite size of the interaction volume leads to a smeared distribution of energy which is transferred to different modes. However, no modes which are much smaller than the interaction volume can be excited. The shape of the interaction parameterization (7.27) is directly reflected in the spectrum of the kinetic energy, as can be seen by the analytic line in the Figure. The effective width of the interaction σ_{eff} in Figure 7.11 is given by

$$\sigma_{\text{eff}} = \sqrt{\sigma_x^2 + \sigma_y^2 + \sigma_z^2}. \tag{7.104}$$

This soft cutoff is the first interesting feature of the proposed method. The second aspect is that while classical Langevin models need a stochastic force for thermalization, the proposed method does not need a non-deterministic random source. We use the particle bath and physically motivated, microscopic interactions while having full control over the interaction rate as well as the energy and momentum exchange. See Figure 7.10 for a plot, showing an initially vanishing scalar field with some field excitations generated by particle interactions. These particle-annihilation processes increase the field's energy, and large field modes are created. After some time, these modes overlap and the field will start to shows a random, Gaussian distribution. Figure 7.9 shows the expected Gaussian distribution [129] after the field has thermalized. The distribution function of the particles show a thermal Boltzmann distribution $f_q(E) \sim \exp(-E/T)$ as seen in Figure 7.12. The temperature of the particles is the same as the one of the thermal field fluctuations.

The maximal observed deviation of the total energy was in the order of magnitude of about 10^{-3}. A discussion of the numerical errors is given in Subsection 7.5.5. Source for numerical errors is the partial differential equations solver and the particle-field method, which employs a large

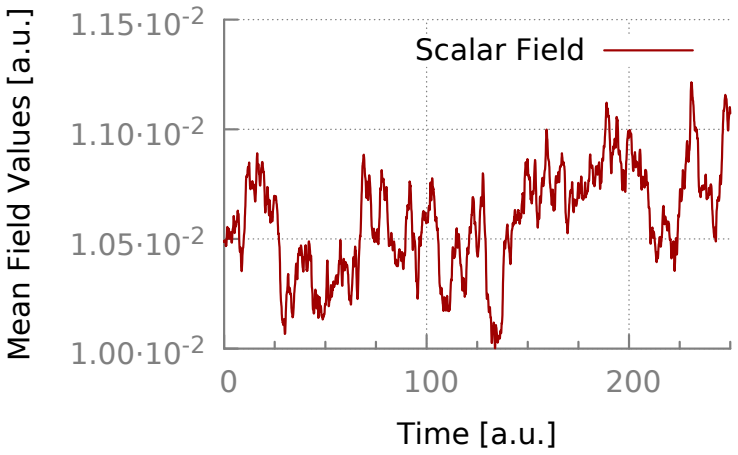

Figure 7.7: Plot of the volume-averaged value of the scalar field. Kinetic excitations on the field can decay to particles and particles can annihilate to excitations of the field leading to both local and global fluctuations of the scalar field and the particle densities.

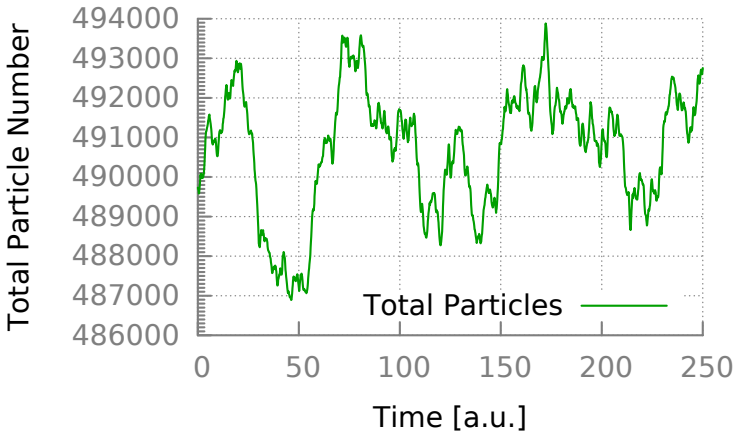

Figure 7.8: Total particle number in the thermal-box simulation. Particles can annihilate, their momentum and energy is transferred to the scalar field in form of scalar-field excitations. Because of the dynamic nature of this process, the total particle number fluctuates around the average thermal value.

amount of calculations on the field, each generating an unavoidable numerical error. The same holds true for the momentum conservation.

Figure 7.15 is not part of the equilibrium-box calculation but shows a sketch of a single interaction, both for adding and removing energy from the field. The center of all images is the interaction point with the Gaussian distributed interaction volume around it. In case of an interaction with only energy transfer and no momentum transfer, the energy distribution in the interaction volume becomes spherically symmetric. With a net-momentum transfer, the distribution is asymmetric and peaked in the moving direction of the momentum.

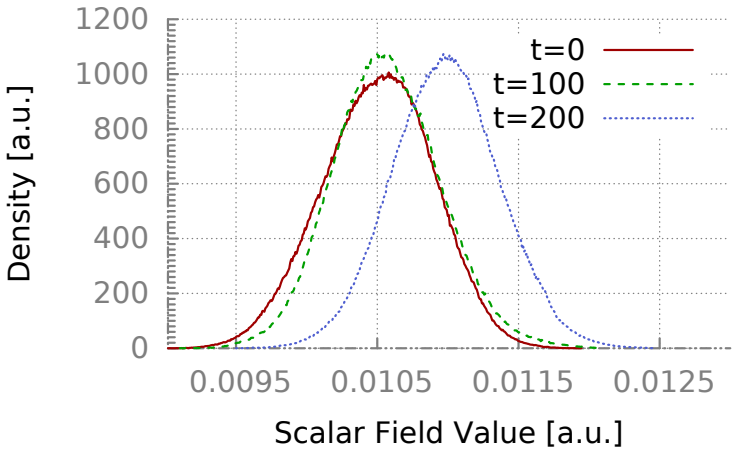

Figure 7.9: Distribution of the scalar field values. The field shows the expected thermal Gaussian noise/fluctuations. The mean of the Gaussian can drift slowly with time as plotted in Figure 7.7. Particle annihilation increases the local fluctuations of the scalar field, and particle production damps them by dissipating energy from the interaction region.

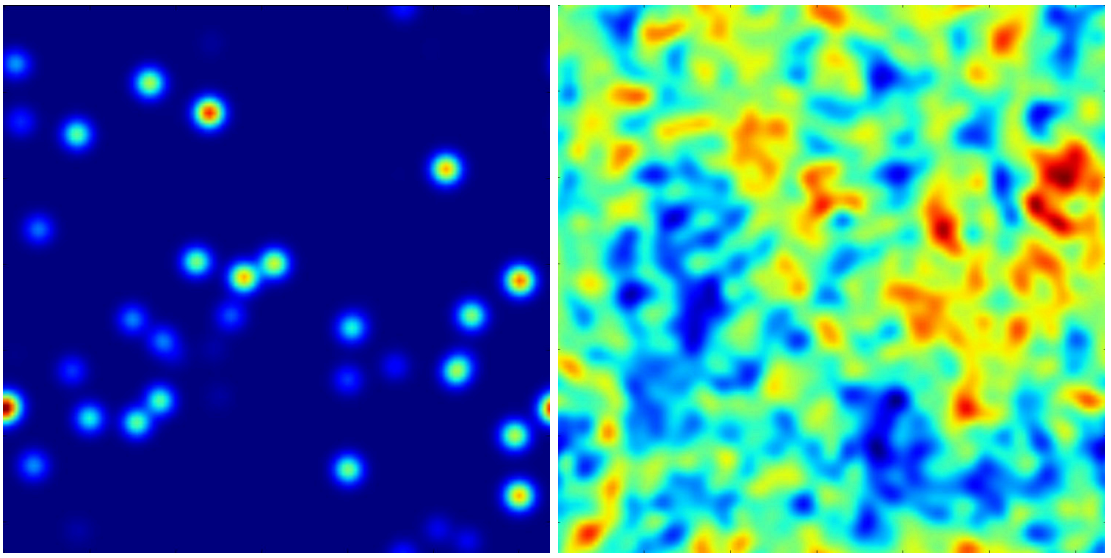

Figure 7.10: Plot of the scalar field in an $x - y$ plane cut at different times in the simulation. The simulation starts with a uniform scalar field without any excited modes. Due to particle creation and annihilation, field fluctuations are created dynamically within the simulation. The color coding shows the value of the scalar field. **Left:** Some particles have annihilated and have created small, local excitations of the scalar field in form of moving, Gaussian shaped blobs. **Right:** The same simulation after the creation and annihilation rate have equalized. The field shows Gaussian fluctuations due to the overlap of many modes, which have been generated by particle annihilation. Particle-field interactions induce mode excitations of the scalar fields, leading to local fluctuations. The spatial width of the fluctuations scales with the interaction volume given by the width of the Gaussian parameterization (7.27) and the height and strength of the fluctuation scales with the system temperature T.

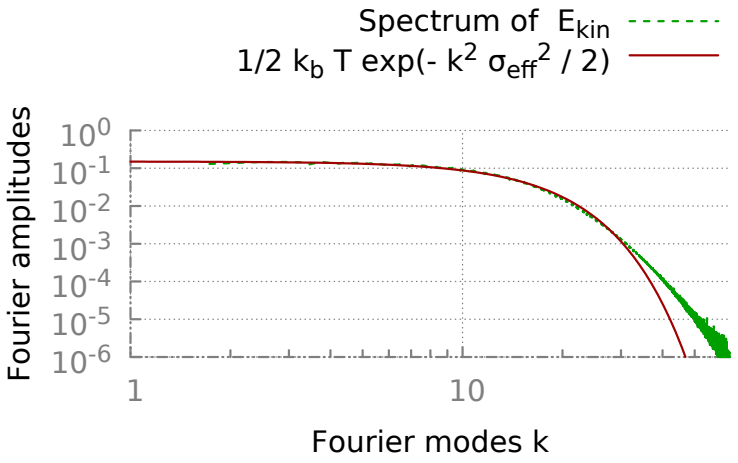

Figure 7.11: Spectrum of the field's kinetic energy $\dot{\sigma}^2/2$. While the thermal spectrum of a classical field has an average energy of kT for every mode due to the equipartition theorem, with $T = 0.15$a.u., the simulated field has an evenly distributed energy per mode only for large wavelengths, like in the classical case. For small wavelengths, the spectrum is suppressed by a soft cut-off. This cut-off is defined by the spatial extent of the interactions on the field. The deviation from the analytical result at higher modes can be explained by the non-linear potential in the field equations of motion.

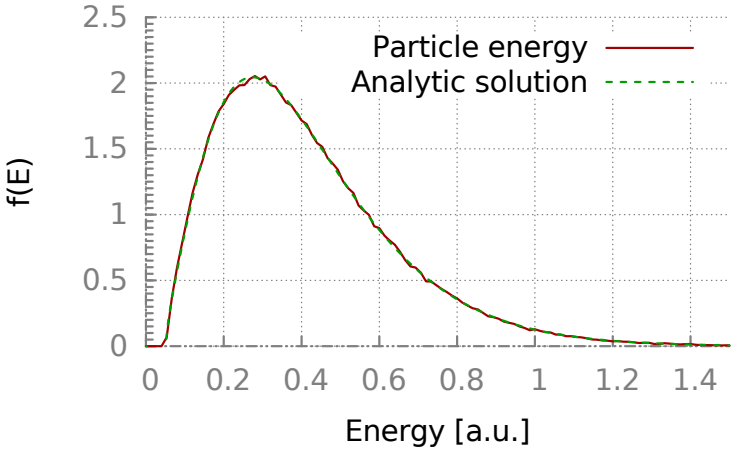

Figure 7.12: Distribution function of the particle energies showing a thermal Boltzmann distribution $f_q(E) \sim \exp(-E/T)$. By microscopic interactions particles and field can exchange energy and momentum and equilibrate to the same temperature $T = 0.15$ a.u. by annihilation and creation processes.

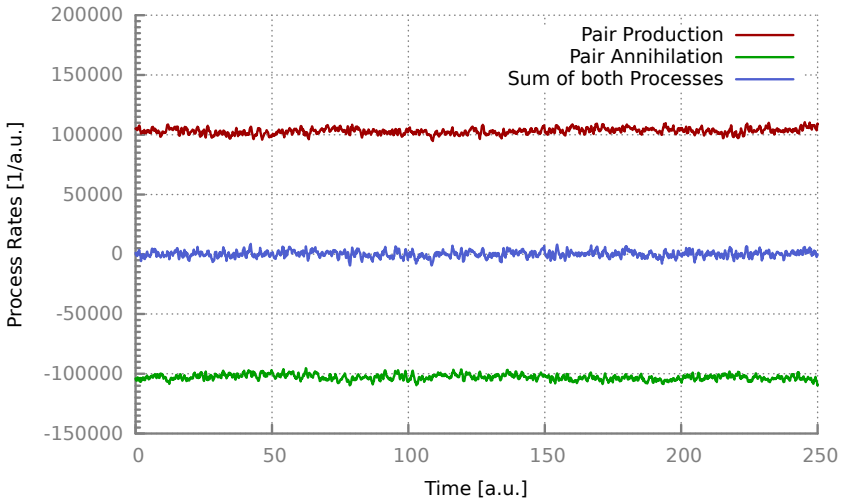

Figure 7.13: Volume integrated rates for the processes $\sigma \to \bar{\psi}\psi$ (pair production) and $\bar{\psi}\psi \to \sigma$ (pair annihilation). Both processes are independent of each other but due to detailed balance both rates are equal on average. Chemical equilibrium is therefore guaranteed. To keep thermal equilibrium, the average energy distribution of both processes has to be the same (not shown in this plot).

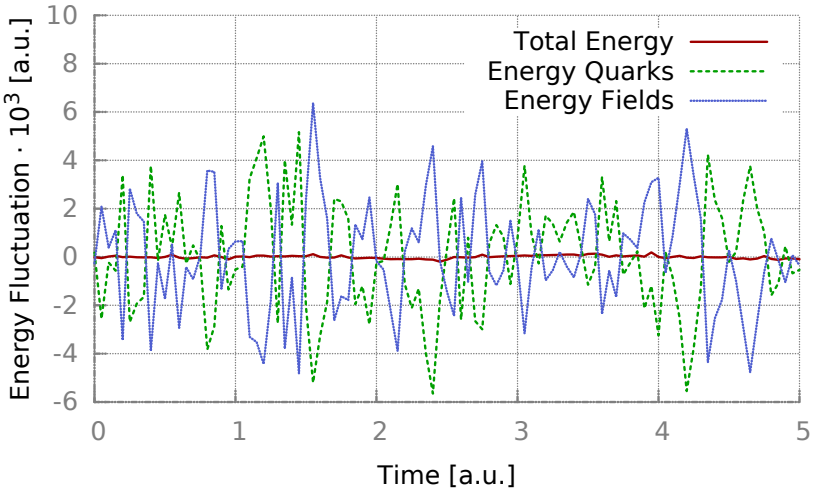

Figure 7.14: Energy fluctuations of the scalar field and the particles, $E(t) - \langle E \rangle$. Field and particles exchange energy by particle production and annihilation processes. While the total energy of the system is conserved and shows only numerical fluctuations, the energy of the components show thermal fluctuations, which are anti-correlated due to total-energy conservation. The relative fluctuations of the field's energy is $\sim 10^{-2}$, of the quarks $\sim 10^{-3}$. The total energy fluctuates on a scale of $|\Delta E|/\langle E \rangle \lesssim 5 \cdot 10^{-5}$. A more in depth discussion of numerical errors can be found in Section 7.5.5.

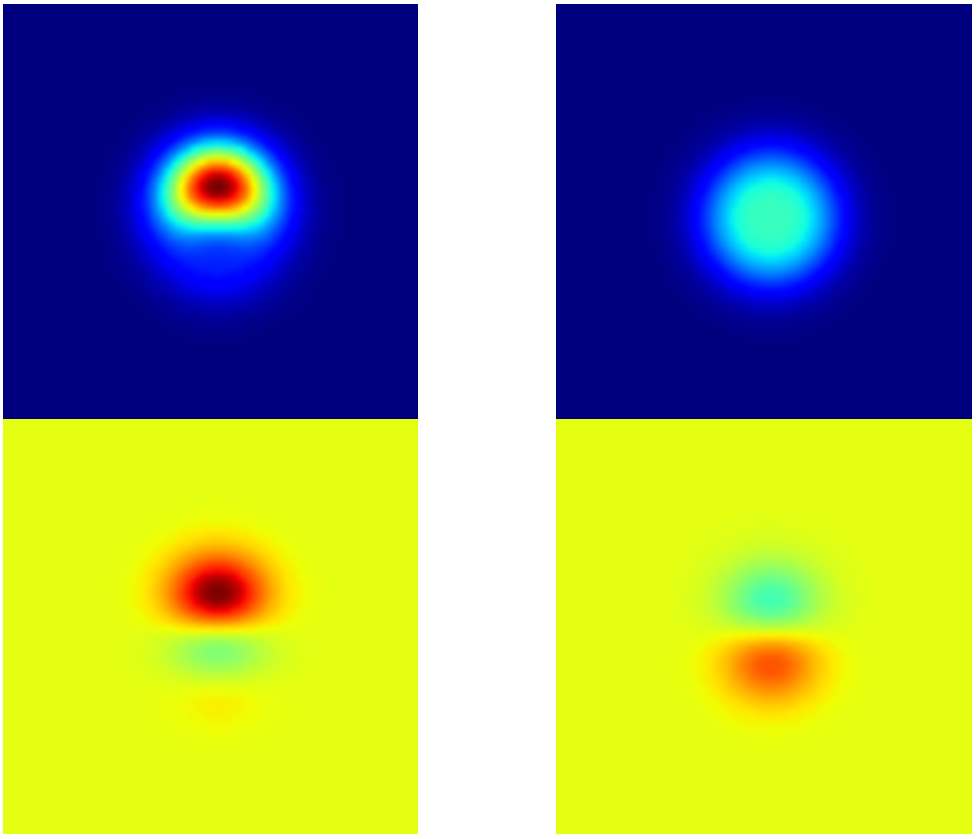

Figure 7.15: Energy and momentum transfer from particles to a scalar field. The pictures on the top show the energy density in the $x-y$ plane, the images at the bottom show the momentum in the $x-y$ plane. **Left:** The Gaussian has a strong momentum pointing in upwards direction. **Right:** The Gaussian has no net-momentum and only adds energy to the scalar filed. In both pictures, the added Gaussian to the scalar field has a spherically symmetric shape (not shown in the pictures), the resulting energy and momentum density is only symmetric if no momentum is transferred. In case of a net momentum, the energy and momentum density show a peak in the direction of motion.

7.5 Additional properties of the field-particle method

The particle field method is a general method to exchange energy between different systems, for example particles and fields. The exact implementation of the interaction properties is given by the underlying physical models. However some general physical properties are given by the mathematical structures of the framework. Additional information about the numerical properties of different interaction parameterizations are given in Appendix A.

7.5.1 Field Self-Interactions

In the previous sections, the discrete interaction between scalar fields and a heat bath or particles have been discussed. These interactions were interpreted as energy and momentum exchanges, leading to discrete perturbations in addition to the field equations of motion. Thereby the field was treated to behave like a local ensemble of particles, for example $f_\sigma(\mathbf{x}, \mathbf{p}, t)$ in case of the σ-field. These particles were used to calculate interaction probabilities between external particles, like quarks, and the σ-field

$$\bar{q}q \leftrightarrow \sigma \ . \tag{7.105}$$

A possible next step would be the extension to describe elastic and inelastic interactions within the same particle species, like in the σ-field, for example

$$\sigma_1 + \sigma_2 \rightarrow \sigma_3 + \sigma_4 \quad \text{or} \quad \sigma_1 + \sigma_2 \rightarrow \sigma_3 + \sigma_4 + \sigma_5 \ . \tag{7.106}$$

However, such a process, even if it would exist in perturbation theory, can not be employed with the particle-field method. The reason is energy and momentum conservation within an interaction cell. The particle-field method interprets interaction in terms of energy and momentum differences ΔE and $\Delta \mathbf{P}$. For any interaction between the same particle species at a local interaction point, both the total energy and total momentum is unchanged:

$$\Delta E = E_{t_i+\Delta t} - E_{t_i} = 0 \tag{7.107}$$

$$\Delta \mathbf{P} = \sum_i \mathbf{p}_i = 0 \tag{7.108}$$

This result is perfectly fine with the interpretation of a scalar field being a sum of coherent and strongly correlated particles. Any interaction between the particles of the same species should be described by the equation of motion.

7.5.2 Field-Field Interaction

The particle-field method was motivated and introduced with the scope of interactions between a field and an ensemble of particles. The implementation for the damping process $\sigma \to \bar{q}q$ can be used to extend this method for interactions between different fields. In case of the linear σ-model, the interaction between the σ-field and the pionic field $\boldsymbol{\pi}$ are given by the interaction potential

$$\mathcal{L}_{\sigma,\boldsymbol{\pi}} = \frac{\lambda^2}{2}\sigma^2\boldsymbol{\pi}^2 \ . \tag{7.109}$$

The general equation of motion describe this interaction in the mean-field approach. Additional, interactions in terms of discrete interaction processes like

$$\sigma \leftrightarrow \pi\pi \tag{7.110}$$

can be described and implemented with the particle-field method to implement additional processes which generate non-deterministic field distributions and additional thermal modes on the fields. The implementation would be the same as described in Section 7.4.4. Particle distributions f_σ and $f_{\boldsymbol{\pi}}$ are derived at a possible interaction point from the local field's properties. These distribution function are used to calculate microscopic interaction probabilities, realizations of these interactions are calculated using Monte-Carlo techniques. For every interaction, the energy and momentum exchange is calculated and is fed back to the fields using the described methods. An interaction is then described by a discrete energy and momentum transfer from one field to another field while the total energy and momentum stays constant.

7.5.3 Influence of Test-Particles and the Interaction Volume

The test-particle ansatz was used in this work to solve the Vlasov- and Boltzmann-equation. An analytic distribution function is discretized by a finite number of test-particles which represent a statistical ensemble of the original distribution function. Additionally, by rescaling the particle number with an artificial multiplier N_{test}, which linearly scales the number of particles. The total energy of the system is independent of the test-particles, which rescales the energy per particle with this factor. Every particle is propagated with its physical mass, energy and momentum m, E and $\mathbf{P}$, however energy and momentum are rescaled within collisions and energy-momentum exchanges:

$$\hat{E}_i = \frac{E_i}{N_{\text{test}}} \tag{7.111}$$

A higher N_{test} leads to a lower exchanged energy for two particles in a collision. The same holds for particle creation and annihilation. For physical particles, the needed energy for pair production $\bar{q}q$ is at least

$$\min\left(E_{\bar{q}q}\right) = 2m_q \tag{7.112}$$

With test particles, this energy threshold is rescaled:

$$\min\left(E_{\bar{q}q}\right) = \frac{2m_q}{N_{\text{test}}} \tag{7.113}$$

In the particle-field method, this test-particle scaling has a notable impact. Both the total energy and momentum of every particle is scaled with N_{test}, see (7.111). This changes the absolute values for the energy and momentum transferred from and to the field. The ratio of the energy to momentum stays constant

$$\frac{\hat{E}_i}{\hat{P}_i} = \frac{E_i}{P_i} \ , \tag{7.114}$$

which leads to a relative scaling of the Gaussian parametrization, but its shape and movement is not altered.

However, the minimal pair-production threshold has an impact on the system dynamics. With (7.113) being the smallest energy the wave equation can dissipate, N_{test} has a direct impact as a cut of energy dissipation. A small number of the test-particle multiplier could lead to a loss of damping of a field if the fluctuations and energy density on the field is too weak to create a particle pair. On the other hand, a very large number in the test-particle multiplier repatriates the system back to a continuous damping, like in the Langevin-equation.

The second important parameter for the particle production threshold is the interaction volume which is given by the width of the Gaussian parametrization $\sigma_{\mathbf{x}}$. A larger width leads to a larger interaction volume and therefore includes a larger volume of the field in the interaction. The larger this volume the more energy can be dissipated from the field. The maximum amount of energy which can be dissipated in a single interaction is given by

$$\max\left(\Delta E\right) = \int_V \mathrm{d}\mathbf{x}\ \epsilon(\mathbf{x}) \prod_i \exp\left[-\frac{\left(\mathbf{x}-\mathbf{x}_{\text{int}}\right)^2}{2\sigma_i^2}\right] \ . \tag{7.115}$$

With the simple approximation of a constant energy density $\epsilon(\mathbf{x}) = \epsilon$ and for a spherical Gaussian $\sigma_i = \sigma$, equation (7.115) becomes

$$\begin{aligned} \max\left(\Delta E\right) &= 4\pi\epsilon \int_V \mathrm{d}r\ r^2\ \exp\left(-\frac{r^2}{2\sigma}\right) \\ &= (2\pi)^{3/2}\,\epsilon\,\sigma^3 \ . \end{aligned} \tag{7.116}$$

The maximal possible energy which can be dissipated by an interaction scales linearly with the volume. By comparing (7.113) with (7.116) the threshold energy density ϵ_{min}, at which the field has enough energy to create particle-pairs, can be derived as

$$\epsilon_{\text{min}} = \frac{1}{\sqrt{2}\ \pi^{3/2}}\ \frac{m_q}{\sigma^3 N_{\text{test}}} \ . \tag{7.117}$$

A higher test-particle number and a larger interaction volume decreases the lowest energy density at which the field starts to be damped and dissipated. This behavior is not a numerical artifact but consistent with the test-particle ansatz and the discrete damping. The more massive and energetic the particle pairs become, the more energy is needed to create them. This leads to a more "steplike" damping, as it was shown in the example of the discretely damped harmonic oscillator.

7.5.4 No-Momentum-Approximation

The particle-field method allows to transfer arbitrary amounts of energy and momentum to and from fields, described by the four parameters ΔE and $\Delta \mathbf{P}$. The numerical implementation leads to a system of four coupled, non-linear equations which have to be solved consistently. As an approximation to reduce the numerical complexity, the energy-momentum transfer can be approximated to have zero momentum exchange

$$\Delta E = \Delta E \qquad \Delta \mathbf{P} = 0 \; . \tag{7.118}$$

The full problem for the energy-momentum equations (7.24) and (7.25) reduces to the single scalar and non-linear equation for the energy (7.24). This reduces the computational costs dramatically because a completely different set of solvers can be used, the number of equations to solve reduce and some additional numerical optimizations can be used. A numerical optimization, which can be employed with this approximation is discussed in the Section 8.7.

This zero-momentum approximation is applicable, in cases where a net-momentum transfer is not important for the system dynamics or the dynamics is described by a large superposition with a zero net-transfer of momentum. Typical examples are the simulation of a Langevin-like equation, in which momentum transfers are not considered or a thermal medium in rest.

However, this approximation still allows full controllable and discrete interactions with energy conservation.

7.5.5 Numerical Errors

Interactions between particles and fields employ a relative large number of numerical operations on the fields. In this subsection a rough estimation of the numerical errors is given.

Modern computer systems represent floating point numbers by using the IEEE Standard for Floating-Point Arithmetic (IEEE 754). Employing double-precision 64-bit precision, all numbers are represented in the form

$$x = m \cdot 2^e \tag{7.119}$$

with a 11 bit precision for the exponent e and a 52 bit precision for the mantissa m. While a double-precision number is defined over a very large range (from $2.23 \cdot 10^{-308}$ to $1.8 \cdot 10^{308}$), the precision within numerical operations is much smaller than implied by the precision of the exponent. For typical arithmetic operations like $\pm$ and $\times$, the expected error per operation due round off effects is in the order of magnitude

$$\epsilon = 2^{-53} \approx 5.7 \cdot 10^{-16} \ . \tag{7.120}$$

An interaction between a particle pair and the scalar field affects a grid region of $N = 40^3 = 64 \cdot 10^3$ grid points, leading to a numerical error of about $6 \cdot 10^{-12}$. This numerical error is still four orders of magnitude smaller than the error given by the non-linear solver, which finds its solution with a precision of about $\approx 10^{-8}$. The presented test-calculations simulated roughly 10^7 collisions, corresponding to 20 times the number of particles. For a rough estimation, we assume the numerical errors in each simulation run to have a random total and maximal error of

$$\epsilon_{\max} = 10^{-8} \cdot \sqrt{40^4 \cdot 10^7} \approx 10^{-3} \tag{7.121}$$

Numerical calculations have shown a relative precision of about 10^{-5}, see for example Figure 7.14.

Note that beside the errors given through round-off effects, the partial differential equation solver can generate numerical noise when employing strong gradients, differing from the exact solution of the equations of motion. These mathematical errors can exceed the numerical errors in non-equilibrium scenarios. The used solving scheme in DSLAM is the Leap-Frog solver, whose properties are explained in Section 8.3.2. This solving scheme conserves energy over a period of several time steps and has a numerical solving precision of Δt^2. A more detailed discussion on numerical errors can be found in [130, 131].

Chapter 8

Numerical Implementation-Details of the DSLAM Model

> Essentially, all models are wrong, but some are useful.
>
> George Edward Pelham Box

This chapter describes the numerical realization and implementation of the DSLAM model (**Dy**namical **S**imulation of a **L**inear **S**igm**A** **M**odel). The main focus does not lie on the physical properties of the underlying linear σ-model but on the numerical methods and algorithms which have been employed as well the used programming techniques and software packages.

This chapter is organized as follows: Section 8.1 explains the basic architecture and used software libraries. Numerical details on the single components of the simulation are described in Section 8.2.

8.1 Software Architecture and Programming Techniques

The DSLAM model was written with help of different programming languages and employs several external libraries.

Python was chosen as the primary developing language `https://www.python.org/` because of its clean syntax and very fast developing cycles. It is an interpreted language, which is in general not as performant as a compiled language like C, but employing the correct techniques, it can be used for efficient numerical calculations. Many recent projects within high performance computing (HPC) are realized using Python [132, 133]

For numerical processing within Python, the Numpy library [134] was used, which offers a set of highly efficient data arrays for real and complex numbers and offers optimized numerical operations on them like matrix and statistical operations.

Special mathematical functions, non-linear equation solvers and root finder have been used from the SciPy library [135]. These have been used for solving the self-consistent initial conditions of the linear σ-model.

Most of the code for initialization, interfacing, analysis and memory management was written in Python, however some performance critical parts have been written in plain C with OpenMP extensions. Such parts included particle propagation, particle interactions and particle-field interactions and calculations of field gradients. Interfacing between C-Code and Python was established with the Cython library [136], code written in C was compiled with the GNU compiler collection (GCC).

For spatial Gaussian filtering of the quark density Fourier transformations are heavily used in DSLAM. The highly optimized Fast-Fourier library FFTW3 and PyFFTW3 libraries [137] and its Python interface was used for calculating transformations and inverse-transformations.

The C part of the code uses the GNU Scientific Library (GSL) [138] for fast access to numerical methods like the root solving and optimization routines in the routines for field-particle interactions. Non-linear equation solving was done with the Powell Hybrid algorithm [139].

Monte-Carlo simulations need a large number of high quality random numbers. This includes a long period, uniformly distributed, lack of correlation, high dimensionality and should pass statistical tests. A robust and well suited random number generator is the Mersenne twister [140] with a period of $(2^{19937} - 1)$. The actual implementation was the SIMD optimized version [141] with a much higher throughput on modern CPUs. However, for a new project I would choose the newer WELL generators [142] because of their smaller CPU cache footprint, faster code and its preferable statistical properties.

Online and offline data plots are generated with the Matplotlib library [143]. Plots found in publications of this thesis are generated mainly by Gnuplot [144].

8.2 Numerical Implementation Details

8.2.1 High-Level View

The DSLAM model is a numerical simulation which solves the equations of motion of an ensemble of quarks q, anti-quarks $\bar{q}$, the σ-field and a π-field. The model has no memory, only the current

state of the system is saved, which are the physical properties of the particles, the fields and their first derivatives.

Particles are represented as test particles. All particles have nine arguments: three position and three momentum coordinates, mass and their particle/antiparticle properties. Other quantities like the energy is calculated dynamically from the nine given properties. The particle masses are not constant but are dynamically determined from the mean field $\langle\sigma\rangle$. These dynamic masses are recalculated in every time step.

Fields are characterized by their scalar value represented on a grid. Typically the grid was chosen to be cubic with grid sizes of $N = 128$, $N = 192$ or $N = 256$. Most calculations have been done with grid sizes less than 200^3 because of the memory foot-print of large grids. A multiple of 2 for N has been chosen for numerical reasons, mainly because of the efficiency of the Fast-Fourier transform for such configurations. Every field is represented by two three-dimensional grids, one holding the current scalar value at every grid-edge and one field for representing the field derivative.

At every time step, particles are propagated with their collision free equations of motion including forces and gradients given by the scalar fields. Particles are therefore softly accelerated in this calculation step.

In a second step the fields are propagated according to their equations of motion. The mean field interactions given by the potentials are included as well as the potential given by the quark scalar densities.

After performing the mean field interactions, the quarks are scattered according to their elastic collision routines and their interactions with a heat bath. Then particles can annihilate and create field excitations, and in the last step field excitations can generate new particles by energy-momentum dissipation. Destroyed particles are cleaned up, newly created particles are added to the system.

In a last step the particle masses given by the Yukawa interaction and the quark scalar density is recalculated.

Different analysis steps are done on demand after the last process of a single calculation step.

8.2.2 Particle Representation and Propagation

The DSLAM model treats both fields and particles. In the linear σ-model, particles are represented by fermionic spinors $\bar{\phi}$ and ϕ. In a classical ansatz, these spinors are approximated by single-state distribution functions

$$\psi, \bar{\psi} \rightarrow f_q(\mathbf{x}, \mathbf{p}, t), f_{\bar{q}}(\mathbf{x}, \mathbf{p}, t) \ , \tag{8.1}$$

which describes the whole system as a sum of independent particle states, ignoring Pauli-blocking or other quantum mechanical properties. Another approximation is the negligence of memory-kernels. This so called Markov approximation reduces the distribution to a "current state" by neglecting all memory effects in the system evolution. In general, a quantum system has a complex dependency on its own history

$$\frac{\mathrm{d}f(\mathbf{x},\mathbf{p},t)}{\mathrm{d}t} = \int_{-\infty}^{t} k(t')I\left(f(\mathbf{x},\mathbf{p},t'),\mathcal{L},t'\right)\mathrm{d}t' \ , \tag{8.2}$$

where $k(t')$ is the memory kernel of the system and I a general interaction kernel which defines the system dynamics and interaction. In the case the system evolution depends only on its current state with $k(t') = \delta(t-t')$, the history of the distribution function can be neglected

$$f(\mathbf{x},\mathbf{p},t) \to f(\mathbf{x},\mathbf{p}) \ , \tag{8.3}$$

and the distribution function is reduced to a 6-dimensional object.

The numerical representation of the distribution function is done with the test particle method [70, 71], where the continuous distribution function is represented by a large but finite number of δ-distributions. Every set of δ-distributions carries the physical properties of a classical particle with an on-shell dispersion-relation

$$f(\mathbf{x},\mathbf{p}) = \frac{1}{N_{\mathrm{test}}}\sum_{i}^{N_{\mathrm{test}}} \delta^3(\mathbf{x}-\mathbf{x}_i)\delta^3(\mathbf{p}-\mathbf{p}_i) \ . \tag{8.4}$$

To propagate the distribution function, the Vlasov equation is employed. It was originally proposed to describe charged particles in plasmas

$$\left[\partial_t + \frac{\mathbf{p}}{E(\mathbf{x},\mathbf{p})}\cdot\nabla_{\mathbf{x}} - \nabla_{\mathbf{x}}E(\mathbf{x},\mathbf{p})\nabla_{\mathbf{p}}\right] f(\mathbf{x},\mathbf{p}) = 0 \tag{8.5}$$

which describes the time evolution of the particle distribution function. All calculations are done with given initial conditions, these systems are consistent propagated according to their equations of motion. No explicit time dependence is given, for example by time-dependent potentials or other external effects. An explicit time dependence of external potentials are not treated in the DSLAM model. Any time dependence of the Boltzmann-Vlasov equation is only given by the systems internal interactions and propagation. Later on, the right hand side of (8.5) will get an extra interaction term $I(t)$, which describes the hard interactions between quarks and fields and with an external heat bath.

The second term of (8.5) describes the trivial particles propagation given by their momentum, without any further interactions this term propagates the particle on straight lines according to

their velocity. The last term changes the particle momenta due to their mean-field forces.

$$\left(-\nabla_{\mathbf{x}} E(\mathbf{x},\mathbf{p})\nabla_{\mathbf{p}}\right) f(\mathbf{x},\mathbf{p}) \ . \tag{8.6}$$

Formally these forces are given by the gradients of the particles energy $\nabla_{\mathbf{x}} E$ which is puzzling in the first moment. All particles are coupled via the Yukawa-interaction term in the Lagrangian (2.1),

$$\mathcal{L}_{\text{int}} = \bar{\psi}\left(-g\left(\sigma + i\gamma_5 \boldsymbol{\tau}\cdot\boldsymbol{\pi}\right)\right)\psi \ , \tag{8.7}$$

This coupling leads to a dispersion relation by a space-dependent effective mass which is dependent on the mean-field

$$m_{i\psi}^2 = g^2\left(\sigma^2(\mathbf{x}_i) + \boldsymbol{\pi}^2(\mathbf{x}_i)\right) \tag{8.8}$$

, and the effective energy reads

$$E_i = \sqrt{\mathbf{p}_i^2 + g^2\left(\sigma^2(\mathbf{x}_i) + \boldsymbol{\pi}^2(\mathbf{x}_i)\right)} \ . \tag{8.9}$$

Any gradients in σ and $\boldsymbol{\pi}$ induce a local mean field force on the particles, given by

$$F = -\nabla_{\mathbf{x}}\,\mathcal{U} = -\nabla_{\mathbf{x}} E(\sigma,\boldsymbol{\pi}) \ . \tag{8.10}$$

In the DSLAM model, particles are represented by the quadruple $p_i = (p_x, p_y, p_z, m_i)$. Their position is updated via the first-order Euler propagation, which can be derived by plugging the test-particle ansatz (8.3) in the Vlasov-equation (8.5), leading to the known relations

$$\dot{\mathbf{x}}_i = \frac{\mathbf{p}_i}{E_i} \ , \qquad \dot{\mathbf{p}}_i = \mathbf{F}(\mathbf{x}_i) = -\vec{\nabla} E(x_i) \tag{8.11}$$

which becomes in first-order approximation

$$\mathbf{x}_i(t+\Delta t) = \mathbf{x}_i(t) + \Delta t \cdot \frac{\mathbf{p}_i(t)}{E_i} \ , \tag{8.12}$$

$$\begin{aligned} \mathbf{p}_i(t+\Delta t) &= \mathbf{p}_i(t) - \Delta t \nabla_{\mathbf{x}} E(\mathbf{x}_i) \\ &= \mathbf{p}_i(t) - g^2 \Delta t \frac{\nabla_{\mathbf{x}}\left(\sigma(\mathbf{x}_i) + \boldsymbol{\pi}(\mathbf{x}_i)\right)}{E(\mathbf{x}_i)} \ . \end{aligned} \tag{8.13}$$

g is the coupling strength of the Yukawa interaction. After each complete propagation step of the fields and particles, the particle mass is recalculated with (8.8).

8.3 Particle Interactions

In the original Vlasov equation (8.5), particles do not scatter on each other. They are only influenced by the mean field forces of the σ and $\boldsymbol{\pi}$ fields. In the DSLAM model additional

dynamics is added by including binary collisions between the particles. The collision integral in the Boltzmann equation for binary collisions is

$$\left.\frac{\partial f}{\partial t}\right|_{\text{coll}} = \int_{\mathbf{v}_1}\int_{\Omega'} \left(f' f_1' - f f_1'\right) v_{\text{rel}}\, \sigma(\mathbf{\Omega}')\, \mathrm{d}\Omega'\, \mathrm{d}^3\mathbf{v}_1 \tag{8.14}$$

with the a cross section $\sigma(\mathbf{\Omega}')$. In the DSLAM model, the cross section is approximated with an isotropic and constant cross section

$$\frac{\partial \sigma(\mathbf{\Omega}')}{\partial \Omega'} = \mathbf{0}\ . \tag{8.15}$$

To simulate particle interactions, the volume of the simulation is divided in an even spaced, cubic grid with cell size ΔV. Within every grid cell, all particles can interact with each other. The size ΔV has to be consistent with the mean-free path of the particle and their interactions. The mean-free path scales with the density and cross section via

$$\lambda_{\text{mfp}} = \frac{1}{n\sigma}\ , \tag{8.16}$$

the cell size has to be smaller than the mean-free path to avoid artifacts by the particle-in-cell method [145]

$$\lambda_{\text{mfp}} \gg \sqrt[3]{\Delta V}\ . \tag{8.17}$$

Within a cell, every particle pair can interact with the stochastic interaction probability [93]

$$P = v_{\text{rel}} \frac{\sigma}{N_{\text{test}}} \frac{\Delta t}{\Delta V}\ , \tag{8.18}$$

where v_{rel} is a kinematic factor. The derivation and explanation can be found in Appendix D.1.

Interaction probabilities given by (8.18) are sampled using Monte-Carlo techniques. In case of an interaction event, particles are collided head-on-head in the center of momentum frame. The boost $\boldsymbol{\beta}$ is given by the two colliding particles

$$\boldsymbol{\beta} = \frac{\mathbf{p}_1 + \mathbf{p}_2}{E_1 + E_2}\ . \tag{8.19}$$

In this system the total momentum vanishes:

$$\mathbf{p}_1' + \mathbf{p}_2' = 0\ . \tag{8.20}$$

In case of an isotropic and constant cross section, the interaction is sampled uniformly on a sphere, the scattered momenta $\mathbf{p}_3'$ and $\mathbf{p}_4'$ are rotated and calculated in spherical coordinates:

$$\begin{aligned} \alpha &\in [0 \dots 2\pi] \\ \cos\theta &= [-1 \dots 1] \\ \sin\theta &= \sqrt{1-\cos^2\theta} \end{aligned} \tag{8.21}$$

$$\mathbf{p}_3' = |\mathbf{p}_1'| \begin{pmatrix} \sin\theta\cos\alpha \\ \sin\theta\sin\alpha \\ \cos\theta \end{pmatrix} \qquad \mathbf{p}_4' = -\mathbf{p}_3' \ , \tag{8.22}$$

$$\begin{aligned} E_1' &= \sqrt{\mathbf{p}_1'^2 + m_1} \ , \\ E_2' &= \sqrt{\mathbf{p}_1'^2 + m_2} \ . \end{aligned} \tag{8.23}$$

After calculating $\mathbf{p}_3'$ and $\mathbf{p}_4'$, the momenta are boosted back to the lab frame and are used in the further simulation.

8.3.1 Virtual Heat Bath Method

The DSLAM model is a microcanonical simulation of a particle and field ensemble. All equations of motion, mean field interactions, elastic particle collisions and particle production and annihilation processes conserve energy and momentum. To simulate a thermal box which can change its temperature, the simulation has to be extended to allow canonical simulations, thus allowing a thermal exchange of energy while conserving the particle number in this canonical process. In total however, the particle number can change due to internal annihilation and pair-production processes. A canonical process can be implemented with a heat reservoir.

The most simple ansatz would be the implementation of reservoir walls. Whenever particles reach the wall, they are replaced by thermal particles from the reservoir. This ansatz has some major drawbacks. The rate of energy exchange is directly proportional to the particle density and the number of particles touching the wall. Additionally, in a coupled medium artificial correlations will be generated. This can be visualized by a temperature change of the system. The system will cool down near the walls and will build up a temperature gradient, see figure 8.1. Conversely, if the medium has physical correlation through interactions, these correlations get suddenly washed out near the reservoir walls because of the newly generated, uncorrelated particles.

A workaround is a heat bath, which is implemented by virtual particles. This kind of heat bath can be described as a second, infinitely large particle reservoir which exists in addition to the physical particles. These two particle species can interact via microscopic interactions. However, the second particle species is not directly simulated but thermal particles are sampled according

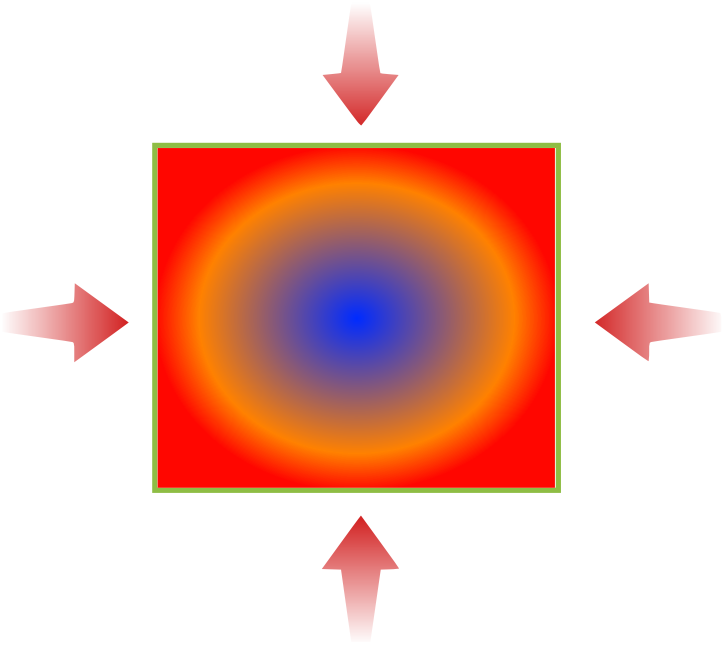

Figure 8.1: Visualization of a small system embedded in a thermal heat bath, which is realized by reservoir walls which emit thermal particles back into the system when a physical particle leaves the system through the walls. This type of heat bath creates inhomogeneities and artificial correlations by building up a temperature gradient for a system with a strongly coupled medium.

to an equilibrium Boltzmann distribution function on demand if energy should be exchanged with the heat bath, therefore the name virtual heat bath.

For every particle in a cell, a potential interaction partner is sampled from an equilibrium-distribution function $f(\mathbf{p}, T)_{\text{bath}}$. The temperature of the distribution function is a parameter of the heat bath. Employing a microscopic collision kernel, the interaction probability can be calculated. If an interaction happens, the particle and the virtual heat bath particle interact and exchange energy and momentum. The amount of exchange energy can be positive or negative and depends on the collision kinematics. After some time the distribution function of the system will align with the thermal distribution function.

In case of the DSLAM model, the thermal heat bath distribution function was chosen to be the Boltzmann distribution, which is the thermal equilibrium distribution for the quarks if the system can equilibrate via elastic interactions

$$f(\mathbf{p}, T)_{\text{bath}} = \exp\left(-\frac{E}{T}\right) \ . \tag{8.24}$$

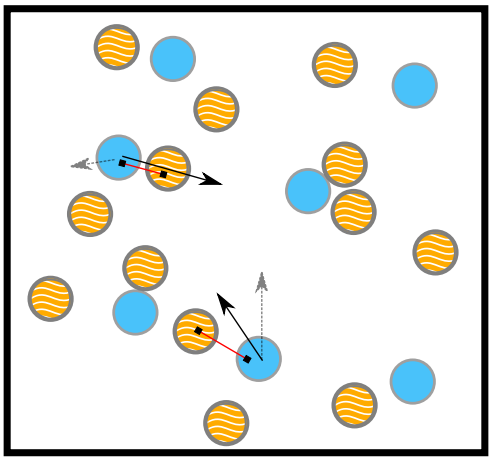

Figure 8.2: Visualization of the virtual heat bath method. Physical particles (yellow) can interact with virtual particles of the heat bath (blue). Virtual particles are not propagated but are according to a thermal distribution function for every possible interaction partner. Interaction probabilities are calculated using microscopic cross sections. In case of an interaction, particles and virtual particles exchange energy and momentum. Within the time evolution the distribution function of the physical particles will converge to the equilibrium distribution of the heat bath.

The total particle density of the heat bath particles scales with the third power of the temperature, increasing the effective reaction rate with the heath bath

$$\int \mathrm{d}E \; f(\mathbf{p}, T)_{\mathrm{bath}} = n_{\mathrm{bath}} \; . \tag{8.25}$$

For every particle in a cell, a virtual partner particle is sampled from (8.24) and for every pair the interaction probability is calculated. For an isotropic cross section σ_{bath} is analogous to the one of elastic scatterings (8.18) and reads

$$P_{\mathrm{bath}} = \frac{s \cdot \sigma_{\mathrm{bath}}(T)}{E_1 E_{\mathrm{bath}}} \frac{\Delta t}{\Delta^3 x} \tag{8.26}$$

where E_1 is the energy of the physical particle, E_{bath} the energy of the thermal particle and s as the Mandelstam variable.

With a constant cross section $\sigma_{\mathrm{bath}}(T) = \sigma_{\mathrm{bath}}$ the interaction rate between the heat bath and the physical particles scales with the particle number and the density of the heat bath n_{bath}, which itself depends on the bath temperature.

In case the temperature of the heat bath should change within a simulation but the interaction rates should be kept constant, the cross section should be chosen temperature dependent as well. For

$$\sigma_{\mathrm{bath}}(T) = \frac{\hat{\sigma}_{\mathrm{bath}}}{2T^3} \tag{8.27}$$

the interaction rate stays with the heat bath and the particles independent of the temperature.

Figure 8.2 shows a visualization of the principle of the virtual heat bath. The method of a virtual-particle bath mimics a canonical heat bath. By sampling virtual particles from the heat bath, the exchanged amount energy between particles and "real" particles has a stochastic character. This method has several advantages. Spatial anisotropies are not generated, any energy exchange between particles and the heat bath is distributed evenly across all particles. Additionally, a fine grained control over the heat bath is given by the two parameters temperature T and the heat bath cross section σ_{bath}. The ratio of the system- and heat bath temperature measures the hardness of the interactions

$$r_{\text{bath}} = \frac{T_{\text{bath}}}{T_{\text{medium}}} \tag{8.28}$$

and gives the average energy exchange between the two reservoirs. The cross section σ_{bath} determines the time in which the system equilibrates because it is proportional to the reaction rate between the particles and the heat bath while. The heat bath method is used in the DSLAM model to control the temperature of a thermal box. It is both used to keep the system at a constant temperature and to change the system temperature, for example to drive the system from a hot phase through the chiral-phase transition to a cold phase. All energy which is released in the phase transition can be absorbed by the heat bath. Calculations with the virtual heat bath method are used in Section 3.2.1 in which a particle ensemble thermalizes with the heat bath, see Figure 3.4 and 3.5.

8.3.2 Fields

in the DSLAM model all fields are described by scalar fields. Both the σ-field and the $\boldsymbol{\phi}$-fields are characterized by three-dimensional representations on a cubic numerical grid. Every grid point represents the mean field value in the given cell $\langle \sigma(\mathbf{x}, t) \rangle$, the same applies to their fist-order derivatives $\langle \dot{\sigma}(\mathbf{x}, t) \rangle$. These representations include the physical mean field approximation of the quantum-fields

$$\sigma(\mathbf{x}, t) \to \langle \sigma(\mathbf{x}, t) \rangle \ , \qquad \boldsymbol{\pi}(\mathbf{x}, t)_i \to \langle \boldsymbol{\pi}(\mathbf{x}, t)_i \rangle \tag{8.29}$$

and the spin-saturation approximation;

$$\boldsymbol{\pi}(\mathbf{x}, t) \to n_\pi \langle \pi(\mathbf{x}, t) \rangle \tag{8.30}$$

which treat the three pion-fields as a single evenly distributed field ensemble.

Within these approximations, all fields are treated and propagated like classical fields, higher-order loop corrections and self-energies are neglected in the equations of motion. The mean field

equations of motion are

$$\begin{aligned}\left(\frac{\partial^2}{\partial t^2}-\nabla_{\mathbf{x}}^2\right)\sigma(\mathbf{x},t) &= -\left[\frac{\partial U(\sigma,\vec{\pi})}{\partial\sigma}+g\langle\bar{\psi}\psi\rangle\right]\sigma(\mathbf{x},t)+f_\pi m_\pi^2\ ,\\ \left(\frac{\partial^2}{\partial t^2}-\nabla_{\mathbf{x}}^2\right)\pi(\mathbf{x},t) &= -\left[\frac{\partial U(\sigma,\vec{\pi})}{\partial\pi}+g\langle\bar{\psi}i\gamma_5\psi\rangle\right]\pi(\mathbf{x},t)\ .\end{aligned} \tag{8.31}$$

Equations (8.31) are partial-differential equations (PDE) which have to be solved numerically. This can be done with potentially any PDE-solver. Robust choices for a broad range of numerical problems are the Runge-Kutta method and the leap-frog method. The Runge-Kutta method is a class of numerical solvers for differential equations but the most applied method is the classical Runge-Kutta method which uses an explicit fourth-order solving system for arbitrary differential equations [146]. This method can be used for implicit solving schemes as well [147]. The Runge-Kutta is a high-precision solver with small numerical error but as a drawback it does not guarantee systematic energy conservation and has a relatively high implementation complexity.

In numerical studies with the Klein-Gordon equation, solving schemes which conserve energy seem to be favorable in comparison to systems with smaller solving error but energy conservation-violation [148, 149]. While the integration error may change the actual system propagation, energy conservation seems to keep overall system dynamics stable.

An algorithm which conserves energy with carefully chosen approximations of derivatives by finite differences is the leapfrog algorithm [150] and has a propagation error scaling with $\epsilon\sim\mathcal{O}\left(\Delta t^2\right)$ and a global energy conservation within a given bound for equations of motion with a conservative potential.

The leap-frog algorithm is derived by Taylor-expanding an integration step

$$\mathbf{x}(t+\Delta t)=\mathbf{x}(t)+\frac{\mathrm{d}\mathbf{x}(t)}{\mathrm{d}t}\Delta t+\frac{\mathrm{d}^2\mathbf{x}(t)}{\mathrm{d}t^2}\frac{\Delta t^2}{2!}+\frac{\mathrm{d}^3\mathbf{x}(t)}{dt^3}\frac{\Delta t^3}{3!}+\mathcal{O}\left(\Delta t^4\right)\ . \tag{8.32}$$

Using $\dot{\mathbf{x}}=\mathbf{v}$ and Newtons law to express the second derivative with a Force, the above equation can be written in a physical form

$$\mathbf{x}(t+\Delta t)=\mathbf{x}(t)+\mathbf{v}(t)\Delta t+\frac{\mathbf{a}(t)}{2}\Delta t^2+\frac{\mathrm{d}^3\mathbf{x}(t)}{dt^3}\frac{\Delta t^3}{3!}+\mathcal{O}\left(\Delta t^3\right)\ . \tag{8.33}$$

Summing $\mathbf{x}(t+\Delta t)$ with the same expression for $\mathbf{x}(t-\Delta t)$ and solving for $\mathbf{x}(t+\Delta t)$, the Δt^3 term cancels and one gets the Leap-frog propagation equation

$$\mathbf{x}(t+\Delta t)=2\ \mathbf{x}(t)-\mathbf{x}(t-\Delta t)+\frac{\mathbf{a}(t)}{2}\Delta t^2+\mathcal{O}\left(\Delta t^4\right)\ . \tag{8.34}$$

Equation (8.34) can already be used for the propagation of the wave equations, the propagation error is of order $\mathcal{O}\left(\Delta t^2\right)$, and the total energy is conserved.

However for an implementation within the DSLAM model this equation is not directly applicable because the particle-field method would violate energy and momentum conservation. The leap-frog method conserves energy by interleaving multiple time steps within the physical context. In the particle-field method the field is locally changed to simulate the energy and momentum transfer between particles and fields. A direct local change of $\phi(\mathbf{x}, t)$ and $\phi(\mathbf{x}, t - \Delta t)$ induces a numerical error proportional to $\delta\phi(\mathbf{x}, t)$ and violates energy conservation. A solution would be to change the explicit solving mechanism of the Leap-Frog algorithm with the explicit method of the energy-momentum-change of the particle-field method to a combined implicit method, in which both $\phi(\mathbf{x}, t + \Delta t)$, $\phi(\mathbf{x}, t)$ and ΔE and $\Delta \mathbf{P}$ is changed at the same time.

Another and more simplistic approach is to expand (8.34) to include the velocity, which then can be changed by interactions. Equation (8.34) can be expanded to include velocities by using the relation

$$\phi(t + \Delta t) - \phi(t) = \dot{\phi}\left(t + \frac{1}{2}\Delta t\right)\Delta t \ . \tag{8.35}$$

By interweaving the different time steps again, the following relation is an equivalent solving method to (8.34):

$$\begin{aligned} \phi(t + \Delta t) &= \phi(t) + \dot{\phi}(t)\Delta t + a(t)\ \frac{\Delta t^2}{2}\ , \\ \dot{\phi}(t + \Delta t) &= \dot{\phi}(t) + \frac{\Delta t}{2}\left[a(t) + a(t + \Delta t)\right]\ . \end{aligned} \tag{8.36}$$

This is the leap-frog method which is implemented in the DSLAM model. Interesting is the propagation of the velocity, which is a linear combination of the current and future time step. For computation it can be favorable to reverse the calculation order of ϕ and $\dot{\phi}$. This can be done by the transformation $(t + \Delta t) \to t$ and $t \to (t - \Delta t)$ and calculating the velocity before the new field configuration. However in this approach the Euler propagation has to be used for the first and initial time step of the system

$$\phi_{t+1} = \phi_t + F(\phi_t)\Delta t \ . \tag{8.37}$$

Overall the velocity-based Leap-frog algorithm conserves the total energy for all potential and spatial-derivative based forces of the field. For all interactions between particles and fields the energy violation is of the order $\mathcal{O}\left(\Delta t^2\right)$. On average, these errors can cancel. In case the Euler-method is used, the overall numerical energy conservation violation would scale with $\mathcal{O}\left(\Delta t\right)$.

All forces acting on the fields are summarized in $F(\phi_t)$, they are given by the potential terms in (8.31). $f_\pi m_\pi^2$ is a constant source term which has no spatial dependencies. The potential term

$$\frac{\partial U(\sigma,\vec{\pi})}{\partial\sigma} = \lambda^2\sigma(\mathbf{x},t)\left(\sigma^2(\mathbf{x},t)+\boldsymbol{\pi}^2(\mathbf{x},t)-\nu^2\right) \tag{8.38}$$

is space dependent but carries no gradient terms. The spatial derivative in (8.31) are approximated by second order finite differences on the numerical grid with grid-size Δx,

$$\nabla_x^2\sigma(\mathbf{x},t) \approx \frac{\sigma(\mathbf{x}+\Delta x\cdot\mathbf{e}_x,t)-\sigma(\mathbf{x}-\Delta x\cdot\mathbf{e}_x,t)}{2\Delta x}\,. \tag{8.39}$$

The last undiscussed term in (8.31) is the one-loop quark scalar (and pseudo-scalar) density

$$\rho_\sigma \equiv \left\langle\bar{\psi}\psi\right\rangle_\sigma(\mathbf{x}) \equiv g\sigma(\mathbf{x})\int \mathrm{d}E\ \frac{f(\mathbf{x},\mathbf{p})+\tilde{f}(\mathbf{x},\mathbf{p})}{E\,(\mathbf{x})} \tag{8.40}$$

and the pseudo-scalar density

$$\rho_{\boldsymbol{\pi}} \equiv \left\langle\bar{\psi}\psi\right\rangle_{\boldsymbol{\pi}}(\mathbf{x}) \equiv g\boldsymbol{\pi}(\mathbf{x})\int \mathrm{d}E\ \frac{f(\mathbf{x},\mathbf{p})+\tilde{f}(\mathbf{x},\mathbf{p})}{E\,(\mathbf{x})}\,. \tag{8.41}$$

$f(\mathbf{x},\mathbf{p})$ is represented with test particles, so the scalar density becomes

$$\left\langle\bar{\psi}\psi\right\rangle_\sigma(\mathbf{x}) \equiv g\sigma(\mathbf{x})\sum_i^N \frac{\delta(p_i-p)\delta(x_i-i)}{\sqrt{p_i^2+g^2(\sigma^2+\pi^2)}}\,, \tag{8.42}$$

$$\left\langle\bar{\psi}\psi\right\rangle_\pi(\mathbf{x}) \equiv g\pi(\mathbf{x})\sum_i^N \frac{\delta(p_i-p)\delta(x_i-i)}{\sqrt{p_i^2+g^2(\sigma^2+\pi^2)}}\,. \tag{8.43}$$

In (8.43) spin saturation was assumed $\vec{\pi}\to 3\langle\pi\rangle$. These densities act like a potential for the σ and $\boldsymbol{\pi}$ fields in the equations of motion. In fact, they are an essential part for the chiral phase transition. By representing the quark distribution function $f(\mathbf{x},\mathbf{p})$ with test particles, the scalar densities can be rewritten in terms of a sum over delta-distributions:

$$\left\langle\bar{\psi}\psi\right\rangle_\sigma(\mathbf{x}) = g\sigma(\mathbf{x})\sum_i^N \frac{\delta(\mathbf{x}_i-\mathbf{x})}{\sqrt{p_i^2+g^2(\sigma^2+\pi^2)}} \tag{8.44}$$

$$\left\langle\bar{\psi}\psi\right\rangle_{\boldsymbol{\pi}}(\mathbf{x}) = g\pi(\mathbf{x})\sum_i^N \frac{\delta(\mathbf{x}_i-\mathbf{x})}{\sqrt{p_i^2+g^2(\sigma^2+\pi^2)}} \tag{8.45}$$

Equations (8.43) and (8.45) could be implemented numerically but would lead to numerical instabilities in the partial differential equation solvers because their spatial distribution has a Dirac-delta character and would lead to point like sources in the chiral field potentials. Even in thermal and chemical equilibrium, the system would become unstable due to numerical noise. To

avoid this problem, the scalar and pseudo-scalar density must by smoothed. This can be done by a convolution with a Gaussian kernel

$$\left\langle\left\langle\bar{\psi}\psi\right\rangle(\mathbf{x})\right\rangle = \frac{N_0}{\sqrt{2\pi}^3\sigma_x\sigma_y\sigma_z}\int_V \mathrm{d}u^3\left\langle\bar{\psi}\psi\right\rangle(\mathbf{x}-\mathbf{u})\exp\left(-\frac{u_x^2}{2\sigma_x^2}-\frac{u_y^2}{2\sigma_y^2}-\frac{u_z^2}{2\sigma_z^2}\right) . \tag{8.46}$$

Beside the positive effect on the numerics, this smearing can be interpreted as the uncertainty principle of the quarks. The delta-functions in (8.42) and (8.43) represents the center of the position distribution, the exact position of the particle is smeared out. The width of this smearing can be either set as a free parameter or can be motivated by physical properties like estimated quark-radii given by the uncertainty principle within the proton.

Equation (8.46) smears the scalar density over a small volume defined by σ_x, σ_y and σ_z. For a numerical implementation of (8.46), the volume of the 3D Gaussian has to be smaller than the system volume $\prod_i^3\sigma_i \ll V$ to avoid artifacts. N_0 takes into account cut-off effects of the Gaussian if some parts of the convolution are cut off due the finite system volume. For sufficiently large systems $N_0 \approx 1$, for smaller systems one has to chose $N_0 > 1$ because (8.46) must preserve the integral measure of (8.42)

$$\int_V \mathrm{d}x^3\left\langle\left\langle\bar{\psi}\psi\right\rangle(\mathbf{x})\right\rangle = \int_V \mathrm{d}x^3\left(\left\langle\left\langle\bar{\psi}\psi\right\rangle(\mathbf{x})\right\rangle * G(\mathbf{u})\right) . \tag{8.47}$$

In (8.46) a parameter N_0 was introduced. In general, this parameter has to be $N_0 = 1$ to fulfill (8.46). However, this is only guaranteed if the width of the Gaussian kernel is much smaller than the size of the system $\sigma_i \ll L_i$ or

$$G(\mathbf{r}=\mathbf{L}) \approx 0 \tag{8.48}$$

for the size of the system $\mathbf{L}$. If this is not the case, N_0 must be chosen to correct for any cut-off effects which occur through the convolution and by the numerical restriction of $\mathbf{L}_{\text{system}} < \infty$:

$$\frac{1}{N_0} = \int_{V_{\text{system}}} \mathrm{d}x^3\frac{G(\mathbf{x})}{\sqrt{2\pi\boldsymbol{\sigma}^2}^3} . \tag{8.49}$$

For sufficiently large systems this correction factor equals unity $N_0 \approx 1$, for smaller systems this factor will differ from unity.

The Gaussian smearing has to be calculated in every time step, therefore an efficient implementation should be chosen. A possibility is to replace the convolution in position space with a multiplication in Fourier-space and by Fourier transforming $\mathcal{F}$ both functions, multiply and applying the inverse transformation $\mathcal{F}^{-1}$ afterwards:

$$\int_V \mathrm{d}u^3 f(\mathbf{x}-\mathbf{u})\cdot g(\mathbf{u}) = \mathcal{F}^{-1}\left\{\mathcal{F}\left\{f\right\}\cdot\mathcal{F}\left\{g\right\}\right\} \tag{8.50}$$

An implementation in 3D position space would have a calculation complexity of $\mathcal{O}(N^6)$, a general implementation in Fourier-space reduces the complexity to $\mathcal{O}(N^2)$ and if a Fast-Fourier-Transform (FFT) is used, it is reduced down to $\mathcal{O}(N \log N)$. For further optimization, the Gaussian convolution kernel can be pre-calculated in Fourier space $\mathcal{F}\{G(\mathbf{u})\}$ because it stays constant over whole simulation. The largest computational complexity of the Gaussian kernel is not the Fourier transform but the actual calculation of the kernel because the calculation of exponential values is very CPU intensive.

By pre-calculating the Gaussian kernel, one has to take care of the kernel's symmetries

$$G(u_i) = G(-u_i) \text{ for } u_i = \{u_x, u_y, u_z\} \ . \tag{8.51}$$

8.4 Particle-Field Interactions

In this section the numerical implementation of the numerical particle-field interactions is explained.

As discussed in Section 7.4.4, interactions between particles and fields can be described by microscopic processes. In this section the implementation of the DSLAM model within the scope of the linear σ-model is discussed. The physical description and derivation of the processes are done in Chapter 5, references are given whenever a physical variable is used.

For both particle annihilation and pair-production, energy and momentum transfer-probabilities have been derived

$$\begin{aligned} &\Delta E(\sigma(\mathbf{x},\mathbf{p}), f(\mathbf{x},\mathbf{p}), \Delta t) \\ &\Delta \mathbf{P}(\sigma(\mathbf{x},\mathbf{p}), f(\mathbf{x},\mathbf{p}), \Delta t) \end{aligned} \tag{8.52}$$

In this section the actual numerical implementation is discussed if such a ΔE and ΔP has to be applied to the system.

8.4.1 Particle Annihilation

Quarks and anti-quarks can annihilate by an interaction cross section like the Breit-Wigner cross section, see equations (5.5) and (5.6). In case of an annihilation process, the net energy and momentum transfer is calculated for the pair of test-particles

$$\Delta E = \left(\sqrt{m_1^2 + \mathbf{p}_1^2} + \sqrt{m_2^2 + \mathbf{p}_2^2}\right), \qquad \Delta \mathbf{P} = \sum_i^3 \frac{p_{1,i} + p_{2,i}}{N_{\text{test}}} \ . \tag{8.53}$$

The position of the interaction is given by that of the two particles

$$\mathbf{x}_{\text{int}} = \frac{\mathbf{x}_1 + \mathbf{x}_2}{2} \ , \tag{8.54}$$

the arithmetic can be seen as an simple approximation for the interaction point but is needed to define an exact interaction point on the numerical grid if the grid-spacing of the fields is smaller than the particles' collision-cell-spacing. The particles' interaction point is interpolated to the nearest position on the field-grid and within the interaction region the same amount of energy and momentum from (8.53) should be deposited by the interaction region. For this calculation the initial energy of the undisturbed field is needed with

$$E_0 = E(\phi(\mathbf{x},t)) = \frac{1}{2}\left(\dot{\phi}^2(\mathbf{x},t) + \left(\nabla_{\mathbf{x}}\phi(\mathbf{x},t)\right)^2\right) + U\left(\phi(\mathbf{x},t)\right) \ , \tag{8.55}$$

the time derivative is approximated with a first order finite difference, the spatial difference is approximated with the first order central step method

$$\nabla_x \phi(\mathbf{x}) \approx \frac{\phi(\mathbf{x}+\Delta x) - \phi(\mathbf{x}-\Delta x)}{2\Delta x} \ . \tag{8.56}$$

In a first step only the energy difference equation is solved with a numerical solver

$$\Delta E(t_k) = E\left[\phi(\mathbf{x},t_k) + \delta\phi(\mathbf{x},t_k)\right] - E\left[\phi(\mathbf{x},t_k)\right] \ , \tag{8.57}$$

the velocity of the Gaussian parametrization is set to zero $\mathbf{v} \equiv 0$. This intermediate step is not needed but leads to a better and more robust numerical convergence.

$$\Delta E\left(A_0\right) = E(\phi(\mathbf{x},t) + \text{sgn}(\xi)\cdot\delta\phi(A_0, \mathbf{v}=0, \mathbf{x}, t)) - E_0 \ . \tag{8.58}$$

$\delta\phi$ is described by a Gaussian parametrization

$$\delta\phi(\mathbf{x},\mathbf{v}) = A_0 \prod_i^3 \exp\left(-\frac{(x_i - v_i\tilde{t})^2}{2\sigma_i^2}\right)\Bigg|_{\tilde{t}\to 0} \quad \xrightarrow{\mathbf{v}\to 0} \quad A_0 \prod_i^3 \exp\left(-\frac{x_i^2}{2\sigma_i^2}\right) \ , \tag{8.59}$$

the random number $\text{sgn}(\xi)$ is either positive $+1$ or negative -1 and is used to randomly chose a direction in which the energy excitation should be placed on the field. If the parametrization would only add energy to a positive direction, the field would get an average kick, leading to an global oscillation of the field. In terms of Fourier-transformation $\text{sgn}(\xi)$ randomly changes the phase of Fourier modes in the positive or negative direction.

After finding a solution for (8.58), both energy and momentum equations are solved simultaneously with

$$\Delta E(t_k) = E\left[\phi(\mathbf{x}, t_k) + \delta\phi(\mathbf{x}, A_0, \mathbf{v}, t_k)\right] - E\left[\phi(\mathbf{x}, t_k)\right], \tag{8.60}$$

$$\Delta \mathbf{P}(t_k) = \mathbf{P}\left[\phi(\mathbf{x}, t_k) + \delta\phi(\mathbf{x}, A_0, \mathbf{v}, t_k)\right] - \mathbf{P}\left[\phi(\mathbf{x}, t_k)\right]. \tag{8.61}$$

The equations are solved with respect to A_0 and $\mathbf{v}$ for the given ΔE and $\Delta \mathbf{P}$ and the final parametrization is added to the field

$$\phi(\mathbf{x}, t_{\text{int}} + \Delta t) = \phi(\mathbf{x}, t) + \delta\phi(A, \mathbf{v}, \mathbf{x}) \ . \tag{8.62}$$

After a successful transfer of energy and momentum to the field, the annihilated particle pair is removed from the system.

In case the numerical solving algorithm can not find a solution for the annihilation process or it does not converge in a given number of iterations, the single annihilation process is canceled and the particles are left unchanged. This should happen only in rare cases and can be reduced by regarding the mathematical limits for $\Delta E/|\Delta \mathbf{P}|$. These limits are discussed in the Appendix A.4 and A.5.

8.4.2 Pair Production

The probability for a particle-pair annihilation process is given by a microscopic cross-section and the properties of the involved particles'. Such a process removes particles from the particle ensemble and adds that amount of energy and momentum to the field, creating excitations and fluctuations on the fields. In the inverse process, the pair production, removes energy and momentum from the field which effectively damps its fluctuations and creates new particles in the particle reservoir. The probability of this process can not be derived directly from the particles' properties because scalar fields have no particle-like properties.

In Chapter 5 and Section 7.4.4 the motivation and basic steps have been discussed. In the numerical implementation of the DSLAM model, the employed calculation steps are discussed now for the decay process of σ-field excitations

$$\sigma \rightarrow \bar{q}q \ . \tag{8.63}$$

For every point on the numerical field's ϕ-grid

$$(n_x, n_y, n_z) \tag{8.64}$$

the mean field value of the field, its derivative, its energy and momentum has to be calculated

$$\begin{aligned} \langle \phi \left(n_x, n_y, n_z\right) \rangle \ , \\ \langle \dot{\phi} \left(n_x, n_y, n_z\right) \rangle \ , \\ E\left(n_x, n_y, n_z, \phi, \dot{\phi}\right) \ , \\ \mathbf{P}\left(n_x, n_y, n_z, \phi, \dot{\phi}\right) \ . \end{aligned} \tag{8.65}$$

The energy and momentum are calculated accordingly to equation (7.13) and (7.14). The field values can be taken directly from the numerical grid values with

$$\langle \phi \left(n_x, n_y, n_z\right) \rangle = \phi \left(n_x, n_y, n_z\right) \tag{8.66}$$

or the mean field values can be extracted by a Gaussian convolution of the actual numerical values in analogy to the Gaussian smearing of the quark density in (8.46). In case of an interaction the field ϕ is not only changed at the interaction point $p\left(n_x, n_y, n_z\right)$ but also at its neighbor points due the Gaussian parametrization (see eq. (7.27)). Because an interaction changes a sub-volume of the system, this same volume can be used to calculate an average energy, momentum and mean field within this sub-volume. Both method turned out to work equally well, they only differ if the field ϕ has many excitations which are smaller than the size of the interaction volume. In this case the non-convoluted algorithm will show a slightly larger pair-production rate until the high-frequency excitations are damped. In the case of thermal fluctuations, both methods behave equally.

After calculating $\langle \phi \rangle$, $\langle \dot{\phi} \rangle$, E and $\mathbf{p}$ for a field-cell, a distribution function has to be derived from this quantities. By assuming a boosted Boltzmann equation as a thermal distribution

$$f_\sigma(\mathbf{p}) = \exp\left(-\frac{\mathbf{u} \cdot \mathbf{p}}{T}\right) \ , \tag{8.67}$$

with the cell-velocity $\mathbf{v}$ is given by the cells energy and momentum:

$$\vec{v} = \frac{\vec{p}}{E} \qquad \text{and} \qquad \mathbf{u} = \gamma \left(\frac{1}{\vec{v}}\right) \ . \tag{8.68}$$

All free parameter of this distribution function are given by the temperature T and the collective velocity given by the cell $\mathbf{u}$. By integrating the distribution function over all momenta, the particle density of the system is given. However, in the DSLAM model the system should be able to deviate from thermal and chemical equilibrium. For every grid cell local thermal equilibrium has to be assumed, otherwise a local fit with a distribution function would not be possible. Still, the temperature can very strongly over the system volume for a small numerical grid.

In the DSLAM model, the mean field value $\langle\sigma\rangle$ is used to derive the temperature by inverting the thermodynamic relation for the thermal equilibrium value of σ

$$\langle\sigma(T)\rangle \;\rightarrow\; T\left(\langle\sigma\rangle\right) \;. \tag{8.69}$$

This is done by numerically calculating the thermodynamic relation and creating an inverse lookup interpolation, details are given in Section 8.8. The same method is used to derive the temperature dependent mass of the sigma quanta m_σ with

$$m_\sigma = m_\sigma\left(\langle\sigma\rangle\right) \;. \tag{8.70}$$

To calculate a decay probability for field excitations, a sigma-particle density n_σ has to be derived. To allow a deviation between the local ensemble temperature and the local particle density, the density is not derived from the coarse-grained temperature but from the local energy density.

$$n_\sigma(T) = \int \mathrm{d}^3\mathbf{p}\; f_\sigma(\mathbf{p},T) \;, \tag{8.71}$$

the energy density is given by

$$\epsilon_\sigma(T) = \int \mathrm{d}^3\mathbf{p}\; \epsilon(\mathbf{p})\; f_\sigma(\mathbf{p},T) \;. \tag{8.72}$$

For a system with massless particles, these relations would have the form

$$n(T) = 2T^3 \;, \tag{8.73}$$

$$\epsilon(T) = 3T^4 \;, \tag{8.74}$$

which leads to

$$n(\epsilon) = \frac{2\epsilon}{3T_\sigma} \;. \tag{8.75}$$

For massive particles this relation is

$$n(\epsilon) = \frac{\epsilon}{3T_\sigma} - m_\sigma^2 T_\sigma K_1(m_\sigma/T_\sigma) \;, \tag{8.76}$$

with the modified Bessel function of the second kind K_n.

After the parameter T, m_σ, n_σ and $\mathbf{v}$ are determined, a σ particle is sampled from $f_\sigma(\mathbf{p},T)$. The particle-decay probability is given by the already in Chapter 5 and Section 7.4.4 discussed Breit-Wigner cross section

$$\sigma_{\bar{q}q\rightarrow\sigma}(s) = \frac{\bar{\sigma}\;\Gamma^2}{\left(\sqrt{s}-m_\sigma\right)^2 + \left(\frac{1}{2}\Gamma\right)^2} \;. \tag{8.77}$$

The decay event of this particle is sampled with Monte-Carlo techniques

$$\text{decay if } \Gamma \frac{\Delta t}{N_{\text{test}} \Delta V} > \xi \quad \text{with } \xi \in [0,1] \ . \tag{8.78}$$

In case of a decay, the energy and momentum

$$\begin{aligned} E &= \sqrt{m_\sigma^2 + \mathbf{p}_\sigma^2} \ , \\ \mathbf{P} &= \mathbf{p}_\sigma \end{aligned} \tag{8.79}$$

are removed from the field. This is done in analogy to the already discussed method in Section 8.4.1. At the interaction point of the field-excitation decay, the energy density and momentum density has to be reduced accordingly to the values given by (8.79).

Removing energy and momentum from a field can be described in two steps. First, the kinetic energy of the field at the interaction point is reduced. This changes both the energy and momentum. To get the correct energy and momentum at the same time, an additional Gaussian wave packet is added in the second step to the field to correct for the missing or excessive momentum. The Gaussian parametrization for energy removing is therefore

$$\delta\phi(\mathbf{x}, \mathbf{v}) = |\mathbf{v}| \cdot \exp\left(-\frac{\mathbf{x}^2}{2\sigma^2}\right) \ , \tag{8.80}$$

$$\begin{aligned} \delta\dot{\phi}(\mathbf{x}, \mathbf{v}) = \kappa\dot{\phi}(\mathbf{x}) \exp&\left(-\frac{\mathbf{x}^2}{2\sigma^2}\right) \\ &+ |\mathbf{v}| \exp\left(-\frac{(\mathbf{x} - \Delta t\ \mathbf{v})^2}{2\sigma^2}\right) \ . \end{aligned} \tag{8.81}$$

with the width σ of the Gaussian parametrization and the damping coefficient κ. For $\kappa = 0$ the complete energy is removed from the field, for $\kappa = 1$ none of the energy is removed. Note that in (8.81) the parametrization of the Gaussian wave packet is slightly different than in the parametrization for adding energy to a field. In (8.81) κ damps the field and $\mathbf{v}$ is the direction and strength of the "correction" wave packet which is added to the system.

$$\tilde{\mathbf{v}} = \frac{\mathbf{v}}{|\mathbf{v}|} \tag{8.82}$$

However the actual velocity of the wave packet is normed to 1. This has a practical reason: the "correction" wave packet which adds missing momentum removed by κ should interfere with the least possible impact. A wave packet with the maximal physical velocity needs the least packet-"height" to add momentum to the system. In this case $\mathbf{v}$ is not directly associated with the amount of momentum which should be removed from the system but as a correction part in combination with κ.

The four non-linear equations are solved with respect to κ and $\mathbf{v}$. In case of finding a solution, the energy and momentum is removed from the system and the σ-particle is decayed to a particle-pair which is added to the particle-ensemble at the interaction point.

In the rest frame of the σ-particle the particles are created and their momentum is set to

$$\vec{p}_1 = -\vec{p}_2 \ . \tag{8.83}$$

The spatial orientation is sampled isotropically and their momenta are boosted back into the laboratory-frame. More details of the decay kinematics can be found in Appendix D.

8.4.3 Sampling of a boosted Boltzmann equation

The Boltzmann equation describes a gas of relativistic particles within a rest frame, implying the average velocity is zero

$$\sum_i^N p_i(x) = 0 \ . \tag{8.84}$$

Sampling such a distribution is straight forward as described in Appendix B.2. However, if the reference frame has a non-vanishing boost, sampling becomes more complicated.

Sampling a boosted system could be done in two ways: sampling the system at rest and boosting every sampled particle afterwards, or sampling a boosted distribution. The first method gives wrong results [151] because it ignores the boost of the phase space. The sampling of a boosted distribution is based on the method presented in [152] and will be explained in the following. In this work such a boosted distribution is needed to sample particles from a scalar field for the field-particle interactions, see Section 7.4.4 for a example system. The numerical details on these kind of interaction are explained in Section 8.4.

We assume a boosted velocity in z-direction

$$\mathbf{v} = \gamma \begin{pmatrix} 1 \\ 0 \\ 0 \\ v_z \end{pmatrix}, \qquad \gamma = \frac{1}{\sqrt{1 - \left(\frac{\mathbf{v}}{c}\right)^2}} \ . \tag{8.85}$$

The Boltzmann equation is introduced:

$$f(\mathbf{p}) = \exp\left(-\frac{1}{T}\mathbf{u}\cdot\mathbf{p}\right) = \exp\left(-\frac{\gamma}{T}(E - v_z p_z)\right) = \exp\left(-\frac{\gamma}{T}(E - v_z\cos(\theta)|\mathbf{p}|)\right) \ , \tag{8.86}$$

$$f(\mathbf{p}) = e^{-\gamma E/T}\exp\left(\frac{\gamma v_z}{T}\cos(\theta)|\mathbf{p}|\right) \ . \tag{8.87}$$

The last equation is integrated over $\int_{-1}^{1} \mathrm{d}\cos\theta$, and we arrive at the final formula:

$$f(\mathbf{p}, v_z, T) = \frac{4\pi T|\mathbf{p}|}{v_z\gamma} e^{-\gamma E/T} \sinh\left(\frac{\gamma v_z|\mathbf{p}|}{T}\right) \tag{8.88}$$

Equation (8.88) is used to sample an energy for a particle with a given temperature and boost-velocity. After the energy is sampled, a direction θ can be sampled with the above relation

$$f(\theta) = \frac{1}{N_0} \exp\left(-\frac{\gamma v_z}{T}|\mathbf{p}|\cos(\theta)\right) \ , \tag{8.89}$$

with the norm

$$N_0 = \frac{2T \sinh\left(\frac{P v_z \gamma}{T}\right)}{|\mathbf{p}| v_z \gamma} \ . \tag{8.90}$$

Sampling in ϕ is done uniformly as it is not affected by the boost. After sampling the particle, the reference frame should be rotated to the direction the original velocity of the particle, which is done straight forward by a rotation matrix.

Two things are interesting in Equation (8.88): The Lorentz γ changes the temperature of the system by $T^* = T/\gamma$ and the phase space for θ is narrowed by the boost. Figure 8.3 shows three examples of such an boosted distribution. In the limit $v \to 0$ the unboosted Boltzmann distribution is obtained, which is isotropic in θ. For non-vanishing velocities, the distribution starts to peak in forward direction $\theta \to -1$ and more and more particles move in the same direction, which is expected from kinetic considerations.

8.5 Initial Conditions

Several different types of initial conditions are used in the DSLAM model and are used depending on the physical context. Most of the initial conditions are some type of thermal distribution with or without a spatial dependence. Every type is discussed in its own subsection in the following.

8.5.1 Thermal initial conditions

For calculation of physical systems different types of initial conditions have been used. The most simple initial condition was thermal equilibrium with a isotropic σ-mean field. This type of initial conditions solves the thermal initial conditions with a time-independent system state. The equations of motion for the σ-field is

$$\left(\frac{\partial^2}{\partial t^2} - \nabla_{\mathbf{r}}^2\right) \sigma\left(\mathbf{x}, t\right) = \left[\frac{\partial U(\sigma, \boldsymbol{\pi})}{\partial \sigma} + g\left\langle\bar{\psi}\psi\right\rangle\right] \sigma(\mathbf{x}, t) + f_\pi + m_\pi^2 \ . \tag{8.91}$$

For

$$\left(\frac{\partial^2}{\partial t^2} - \nabla^2_{\mathbf{r}})\right) \sigma_0\left(\mathbf{x}, t\right) \equiv \sigma_0 \equiv 0 \quad \text{and} \quad \boldsymbol{\pi} \equiv 0 \ . \tag{8.92}$$

stable solutions can be found by solving the self-consistent equation

$$\left[\lambda^2(\sigma_0 - \nu^2) + g^2 \int \mathrm{d}^3\mathbf{p} \ \frac{f(\mathbf{x},\mathbf{p},t) + \tilde{f}(\mathbf{x},\mathbf{p},t)}{E(\mathbf{x},\mathbf{p},t)}\right] \sigma_0 - f_\pi m_\pi^2 = 0 \tag{8.93}$$

For $\boldsymbol{\pi} \neq 0$ no stable solutions can be found and the system would behave like two coupled, non-linear oscillators which constantly transfers energy from the σ-field to the $\boldsymbol{\pi}$-fields and reverse. Equation (8.93) has to be solved numerically. Depending on the position in the phase diagram the minimum of $U(\sigma)$ can be very wide and flat, especially near the phase transition, so a slow but exact converging method is favorable here. To find a self-consistent σ_0, the quark-distribution is important. For thermal calculations they are described with the Fermi-Dirac distribution

$$f(\mathbf{x},\mathbf{p},\mu,t=0) = \frac{2N_cN_f}{(2\pi)^3} \frac{1}{1+\exp(\frac{E-\mu}{T})} \ . \tag{8.94}$$

For calculations with particle-interactions and scatterings, the relativistic Boltzmann distribution

$$f(\mathbf{x},\mathbf{p},\mu,t=0) = \frac{2N_cN_f}{(2\pi)^3} \exp\left(-\frac{E-\mu}{T}\right) \tag{8.95}$$

was chosen because is describes the thermalized state in the DSLAM model. Quark interactions in the DSLAM model do not include Pauli-blocking terms in the microscopic collision integrals.

In most of the calculations the chemical potential was set to zero, $\mu = 0$, leading to a balanced number of particles and anti-particles. The energy of the particles is given by the dynamical mass given by the σ-field

$$E_\psi(\mathbf{x},\mathbf{p}) = \sqrt{\mathbf{p}^2 + g^2\sigma^2(\mathbf{x})} \ . \tag{8.96}$$

After finding a thermal σ_0, the particle N_q and anti-particle number $N_{\bar{q}}$ can be sampled

$$\begin{aligned} N_q &= N_{\text{test}} \int \mathrm{d}V \int \mathrm{d}^3\mathbf{p} \ f(\mathbf{x},\mathbf{p},\mu,t) \ , \\ N_{\bar{q}} &= N_{\text{test}} \int \mathrm{d}V \int \mathrm{d}^3\mathbf{p} \ f(\mathbf{x},\mathbf{p},-\mu,t) \ . \end{aligned} \tag{8.97}$$

The energy of each particle is sampled according to the employed distribution function using the accept-reject method for the Boltzmann distribution or the Metropolis-Hasting method for the Fermi-distribution function. The position of the particles is sampled isotropically

$$f(\mathbf{x}) = \begin{cases} \frac{1}{V} & \text{if } \mathbf{0} \leq \mathbf{x} \leq \begin{pmatrix} L_x & L_y & L_z \end{pmatrix} \\ 0 & \text{otherwise} \ . \end{cases} \tag{8.98}$$

The same is done for the spatial direction of the particles' momenta in spherical coordinates φ and θ

$$f(\varphi) = \begin{cases} \frac{1}{2\pi} & \text{if } 0 \leq \varphi \leq 2\pi \\ 0 & \text{otherwise} \end{cases} , \tag{8.99}$$

$$f(\theta) = \begin{cases} \frac{1}{\pi} & \text{if } -1 \leq \cos(\theta) \leq 1 \\ 0 & \text{otherwise} \end{cases} . \tag{8.100}$$

To fulfill (8.92), the initial movement of the mean field is set to zero

$$\dot{\sigma} = 0 . \tag{8.101}$$

8.5.2 Initial conditions with a off-equilibrium particle distribution

To examine the behavior of particle thermalization, the system has to be initialized with a non-equilibrium distribution. For the thermalization calculations in Section 3.1 or the discussion of non-equilibrium effects in Section 4.1, a Dirac-delta distribution has been chosen

$$f(\mathbf{x}, \mathbf{p}, t) = \frac{2N_c N_f}{(2\pi)^3} \, n_0 \cdot \delta(E - E_0) . \tag{8.102}$$

All particles have the same energy E_0 but the direction of their momenta is chosen randomly. In this scenario, the particles have a very strong deviation from thermal equilibrium. In the linear σ-model this has an impact on the one-loop scalar density $\left\langle \bar{\psi}\psi \right\rangle$, which changes the equilibrium mean field value σ_0.

The initialization process is the same as described in subsection 8.5.1 with the difference that the distribution function in (8.93) has to be chosen to be the Dirac-distribution. In practice a numerical integration of Dirac-δ distributions is not recommended, so the one-loop scalar density should be integrated by hand

$$\int \mathrm{d}^3\mathbf{p} \, \frac{f + \tilde{f}}{E(\mathbf{x}, \mathbf{p}, t)} = \frac{2N_c N_f}{(2\pi)^3} \, \frac{\bar{n}_0 + n_0}{E_0} . \tag{8.103}$$

The constant n_0 is the density for quarks, $\bar{n}_0$ the density for anti-quarks, which is added to define a physical total particle density for the Dirac-distribution. It can be chosen to fit a physical distribution, like the Boltzmann distribution

$$n_0 \equiv \int \mathrm{d}^3\mathbf{p} \, \exp\left(-\frac{E - \mu}{T}\right) , \tag{8.104}$$

$$\bar{n}_0 \equiv \int \mathrm{d}^3\mathbf{p} \, \exp\left(-\frac{E + \mu}{T}\right) . \tag{8.105}$$

8.5.3 Temperature Quench

Thermal equilibration between fields and particles can be tested with a temperature quench. Fields and particles are initialized consistently at a given initial temperature T_1 using the techniques in subsection 8.5.1. In a second step the particles are re-sampled with a new temperature T_2 while leaving the field properties unchanged. Both the particle density and momenta are resampled with (8.95) and (8.97). The field's and particle's subsystems are in thermal equilibrium, the whole system is in non-equilibrium both thermally and chemically.

8.5.4 Woods-Saxon distribution

As a simple model for a nuclear collision, a thermal Woods-Saxon-like temperature distribution can be employed. The initial state will be a hot "blob" with a temperature gradient starting at some temperature T_0 at the center of the distribution and drops exponentially to vacuum temperature. For every numerical particle- and field-cell at local-thermal distribution is sampled according to the spatial dependent Woods-Saxon temperature. The original Woods-Saxon potential is [83]

$$V(r) = \frac{V + iW}{1 + \exp\left(\frac{r - r_0}{a}\right)} \ . \tag{8.106}$$

Using this motivation, a space dependent and radially symmetric temperature can be formulated

$$T(\mathbf{x}) = T_0 \left(\frac{1 + \exp\left(\frac{-R_0}{\alpha}\right)}{1 + \exp\left(\frac{|\mathbf{x}| - R_0}{\alpha}\right)} \right) \ , \tag{8.107}$$

with R_0 as the width of the distribution and the slope strength α. Typical choices in DSLAM were $R_0 = 0.5$ fm and $\alpha = 0.1$ fm. The constant upper part of the fraction is a correction term to have $T(\mathbf{0}) = T_0$.

Every particle-grid cell is initialized with its own $T(\mathbf{x}_{\text{cell}})$. Every field-grid cell is initialized with its respective $\langle\phi\rangle(T(\mathbf{x}_{\text{cell}}))$. In case the fields should be initialized with thermal fluctuations, the kinetic part $\dot{\phi}$ is initialized globally with T_i and is then cell-wise multiplied with the spatial dependent temperature

$$\dot{\phi}(\mathbf{x}) = \dot{\phi}_0 \cdot T(\mathbf{x}) \ . \tag{8.108}$$

8.6 Thermal fluctuations of the fields

In the previous sections we have discussed how to employ different kinds of thermal initial conditions, for example for the mean field value $\langle\phi\rangle$. Fluctuations and thermal excitations,

however, are given by the fluctuation-dissipation theorem, which has been discussed in Section 7.4.4. The spectrum of fluctuations in Fourier mode is given by

$$S\left|\dot{\phi}(\mathbf{k})\right| = \frac{k_B T}{2} \exp\left(-\frac{1}{2}\,\mathbf{k}^2\sigma^2\right) \ . \tag{8.109}$$

A numerical algorithm to sample the kinetic part of a field with a power spectrum according to (8.109) is given in the Appendix E.

Equation (8.109) is defined in Fourier space and therefore for an isotropic and large system. It is not clear how to sample a field which has a space dependent temperature gradient because the temperature in (8.109) is constant for the system. One could use small sub-volumes and sample these volumes with an average temperature, but as (8.109) is not scale-invariant, this method does not work very well and would create artifacts at the boundaries of these cells. As an intermediate solution, the method as in equation (8.108) can be used. The field is sampled with a global, initial temperature T_0, the kinetic fluctuations in position space are then "damped" with an space dependent temperature distribution $T(\mathbf{x})/T_0$

8.7 Numerical optimizations

Different numerical optimizations are used within the DSLAM model to increase the overall performance. General optimizations like compiler flags, numerical libraries, memory access patterns or cache optimizations are very effective techniques but are of a general scope and are not discussed here. Nevertheless, several very model specific optimizations are employed in the DSLAM model.

Sub-volume calculations Interactions between particles and fields are modeled by a Gaussian parametrization leading to an effective limited interaction volume. Typically, these interaction volumes much smaller than the total volume of the system. To find solutions for the energy- and momentum-manipulation equations (7.24) and (7.25), the parametrization has to be solved in the numerical grid. The Gaussian parametrization is restricted to an effective volume, so the numerical solver can work on this restricted sub-volume. By copying the numerical interaction to a sub-memory and solving the equations on this much smaller system, a strong performance gain can be accomplished. This is most effective of the sub-volume can be stored in the CPU's cache.

Precalculated parameterizations, exponential functions and convolution kernels Many calculations within the simulation are performed every time step and some parts of these calculations stay constant. An example is the Gaussian convolution kernel for the smearing of the quark densities. This kernel and its Fourier transformation can be precalculated and stored in

memory once at the initialization phase of the simulation. The same technique can be used for the Gaussian parametrization of the particle-wave method. In the first step of the particle-annihilation process, only the energy difference for the field manipulation is calculated. The parametrization stays constant and is only scaled by the factor A_0. Instead of recalculating the parametrization in every solver iteration, this static parametrization should be precalculated once. For the momentum changing part of the interaction, this is not possible because the shape of the Gaussian changes by varying the velocity of the wave packet. An optimization for this case is discussed n the next paragraph.

Approximation of the exponential function Finding a suitable configuration of the scalar field within a particle-field interaction, many numerical solver iterations are performed. In every step, a new Gaussian parametrization is calculated, resulting in a huge amount of calls to the exponential function. This function call is very computing intensive and modern CPUs do not have an optimized instruction set for that call. A numerical trick is to optimize the exponential function itself. One has to keep in mind that it is sufficient for the particle-field method to have a parametrization for the field disturbance, which is similar to a Gaussian function, but it is not needed exactly satisfy the Gaussian shape. The only important benchmark is the correctness of the total energy and momentum which the solver tries to find. Therefor a simple approximation of the exponential function can be employed, motivated by the infinite sum definition

$$e^x = \lim_{n\to\infty} \left(1 + \frac{x}{n}\right)^n \quad . \tag{8.110}$$

In practice such a method is never used to obtain an exact result, but can be used for small x with a truncation for $n = 1024$ and $x^{1024} = \left(x^{512}\right)^2 = \left(\left(x^{256}\right)^2\right)^2 = ...$ Within the particle field method, all calculations are done in a scale of GeV with numerical values around $10^{-3} \ll 1$, we can therefore expand the exponential function around 0 with a limited n

$$\exp(x) \approx (1 + x/1024)^{1024} \quad . \tag{8.111}$$

In an efficient numerical implementation of this equation the 10th power would be replaced by an iterative multiplication loop instead of a power function or by an compiler (in case not a special math-compiler is used). Eventhough this approach looks rather tedious, it can speed up the overall simulation by a factor 2-3 without impact on precision.

8.8 Temperature Parametrization

For the particle-field method in the DSLAM model, the temperature of the field has to be derived from the mean field value $\langle\sigma\rangle \to T$. Mathematically this is the inverse function of the mean

field thermodynamic relation $T \to \langle\sigma\rangle$. For every grid-cell, such a temperature derivation has to been performed. The calculation of $\langle\sigma\rangle(T)$ is already quite computational intensive, the inverse function is even worse. Therefore a lookup table or parametrization is favorable.

From the mathematical side the function if $\langle\sigma\rangle(T)$ injective and surjective for the following domains

$$\begin{aligned} T &\in [0 \dots \infty] \ , \\ \langle\sigma\rangle &\in (0, 93 \text{ MeV}] \ . \end{aligned} \tag{8.112}$$

The mean field value to temperature calculation is a very crucial and important part in the DSLAM model because it is a major component in the physical dynamics of the model. It is very important to chose a precise and consistent parametrization for the inverse function because it is crucial to the thermodynamical system stability. If the lookup $\sigma \to T$ does not give the correct values, thermal and chemical equilibration can not be guaranteed because the system dynamics can become inconsistent. Additionally, if the inverse function is not strictly monotonic, the system will become unstable as well. In case of a non-monotonic parametrization, the heat-capacity can become negative at that point, leading to a temperature drift between fields an particles.

In the DSLAM model, a parametrization of the temperature dependence has been chosen with the following functional expansion

$$T(\sigma) = \sum_{n=0}^{4} [a_n(\sigma - x_0)^n] + \frac{b}{\sigma} + e_1 \exp(-\sigma/e_2) + c_1 \log(c_2\sigma + c_3) \ , \tag{8.113}$$

which was found phenomenologically. The exponential and logarithmic terms have been introduced to take into account the asymptotic behavior for $\sigma \to 0$ and $\sigma \to 93$ MeV. For all parametrization x_0 was a good choice.

For all parameterizations, the following boundary conditions are assumed

$$T(\sigma) = \begin{cases} 0 & \text{if } \sigma > 92.6 \text{ MeV} \\ 10 \text{ GeV} & \text{if } \sigma < 0 \end{cases} \tag{8.114}$$

because there is no thermodynamical equivalent for σ outside of the definitions. For high temperatures σ slowly approaches $\sigma \to 0$. However, this happens very slowly and in the DSLAM model with particle creation and annihilation processes, the σ-field becomes strongly damped due particle decay-processes before it can reach physically not defined regions. It is therefore safe to assume a temperature cut-off with $T \to 10$ GeV for $\sigma \to 0$. The same holds for the vacuum case with $T \to 0$.

A plot of the temperature dependence parametrization is given in Figure 8.4.

For different coupling constants g of the linear σ-model, the different parameter have been fitted:

Parametrization for $g = 3.3$ (Cross-Over Transition)

a_0	0.140371	± 0.0015	(1%)
a_1	0.0797545	± 0.042	(52%)
a_2	-0.830246	± 0.76	(91%)
a_3	-289.383	± 14.8	(5%)
a_4	1082.8	± 590	(55%)
b	$7.30668 \cdot 10^{-05}$	$\pm 2.6 \cdot 10^{-05}$	(36%)
e_1	0.109632	± 0.01	(9.4%)
e_1	0.003943	$\pm 9.5 \cdot 10^{-05}$	(2.4%)
c_1	0.00141628	± 0.0022	(154%)
c_2	-9.80346	± 5.6	(57%)
c_3	0.88392	± 0.52	(65%)

Parametrization for $g = 3.63$ (Second-Order Transition)

a_0	0.130497	± 0.0007	(0.5%)
a_1	0.295938	± 0.036	(12.3%)
a_2	-1.71026	± 0.33	(18.9%)
a_3	-297.958	± 9.9	(3.3%)
a_4	1089.32	± 413.4	(38%)
b	0.000148013	$\pm 8 \cdot 10^{-6}$	(5.5%)
e_1	0.074768	± 0.004	(5.4%)
e_2	0.00338549	$\pm 6.5 \cdot 10^{-6}$	(1.9%)
c_1	0.00118907	± 0.0017	(146%)
c_2	-22.6742	± 12	(53%)
c_3	2.06127	± 1.1	(60%)

Parametrization for $g = 5.5$ (First-Order Transition)

$a0$	0.0995044	± 0.0005	(0.5%)
a_1	1.51053	± 0.015	(1%)
a_2	12.0974	± 0.72	(6%)
b	$8.43777 \cdot 10^{-5}$	$\pm 1.9 \cdot 10^{-7}$	(0.2%)
a_3	-758.905	± 5.9	(0.8%)
a_4	5596.65	± 313	(5.6%)
e_1	0.08084	± 0.0004	(0.3%)
e_1	0.00143467	$\pm 6.1 \cdot 10^{-6}$	(0.4%)
c_1	0.0151211	± 0.0004	(2.9%)
c_2	-22.1402	± 0.03	(0.14%)
c_3	2.06474	± 0.004	(0.19%)

Additionally, at the first-order phase transition the mean field value $\langle\sigma\rangle$ jumps from the chiral broken phase into the chiral restored phase with a discontinue jump. In the inverse parametrization, this is covered by setting

$$T = 0.126875 \text{ for } 0.0056676381 \leq \sigma \leq 0.08079643 \tag{8.115}$$

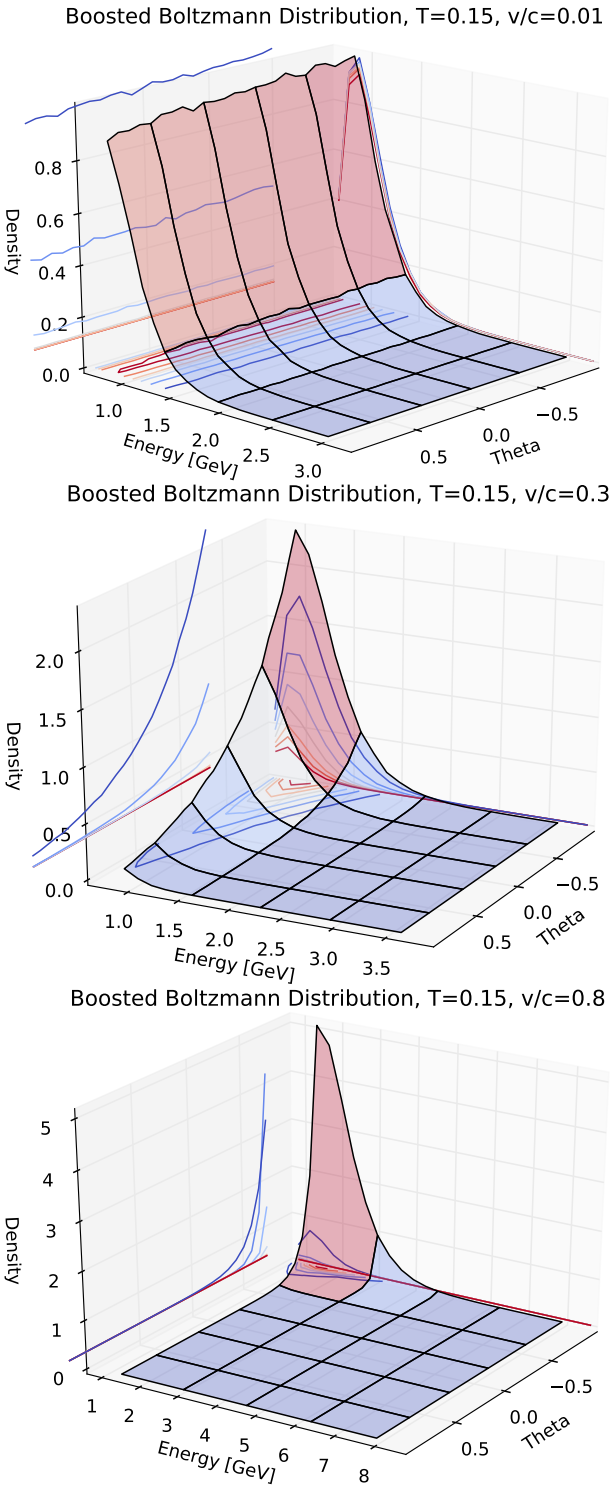

Figure 8.3: Examples of boosted Boltzmann distributions. While the non-boosted distribution (a) is completely uniform in θ and ϕ and only shows the typical $E^2 e^{-E/T}$ dependency, the boosted distributions in (b) and (c) are strongly peaked in forward direction of θ.

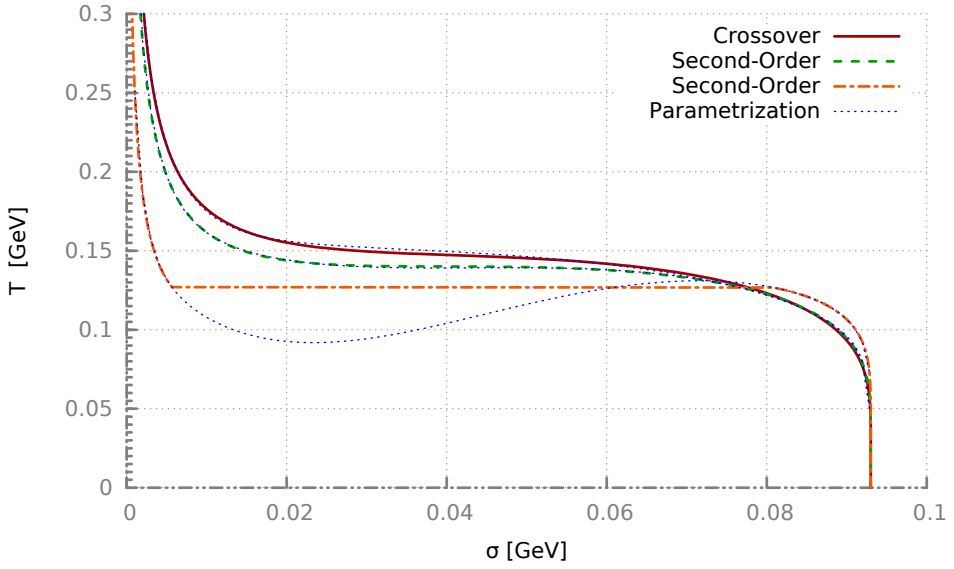

Figure 8.4: Parametrization for the thermodynamic relation $\langle\sigma\rangle \rightarrow T$ for different coupling constants. In case of the first-order phase transition, the region of 0.0057 GeV $\leq \sigma \leq$ 0.0808 GeV is not defined thermodynamically and jumps with a discontinuity, so a constant temperature is assumed.

Chapter 9

Summary and Conclusions

> Wer aufhört, besser zu werden, hat aufgehört, gut zu sein.
>
> Philip Rosenthal

The scope of this thesis was the investigation of non-equilibrium effects at and near the chiral phase transition of QCD matter. A direct approach to quantum chromodynamics is not possible, so an effective model with similar properties and symmetries has been chosen to study thermal and non-thermal properties and to derive qualitative equivalent predictions. The chosen model was the linear σ-model with constituent quarks. This model consists of chiral fields and particles and has no color-confinement but a chiral phase transition with different kinds of phase transitions, depending on the model parameter. To extend existing calculations with thermal approaches, a numerical implementation for the σ-model has been developed in this thesis, the DSLAM model, which employs test particles in a Vlasov equation and classical approximations on a 3D grid for the fields. The resulting model is capable of simulating various types of initial conditions and non-equilibrium effects as no equilibration assumptions are implied on the medium.

The equilibrium properties of the chiral phase transition are already well understood for the linear σ-model and fair for the theory of quantum chromodynamics. The question of the type of phase transition in QCD and its transition temperature is still open. An effective model like the linear σ-model can not fully address these issues as it is still a different model with different properties. However, it can help to clarify the question on possible observables and indicators which allow to derive properties of the chiral phase transition upon signatures in the detectors of modern heavy-ion experiments.

Several aspects of non-equilibrium effects have been examined in this work. A more static approach was the analysis of effects caused by thermal deviation from equilibrium in the quark-distribution function or by deviations from the equilibrium density. In the DSLAM model the quark can acquire arbitrary momenta, resulting in a distribution function different from a equilibrium one like the Fermi distribution. A medium temperature can not be defined in such a case but such deviations change the energy density at which the phase transition would take place in comparison to a fully equilibrated medium. The same can be shown for the order of the phase transition in such a static analysis. Deviations in the distribution function can change the behavior and potential of the σ-field, leading to a different order of the phase transition. An even stronger effect has the density of the quarks, which is given by the total particle number and the scalar chiral density in the model. Any deviations from the equilibrium density have a dramatic effect on the critical temperature of the phase transition. These findings make it hard to derive valid signatures for the σ-model which allow conclusions from observations like final state energies or density distributions as the system reacts very sensitively to initial state deviations and also to any deviations from equilibrium through the whole evolution.

The second approach to non-equilibrium effects was attempted by dynamical simulations with explicit non-equilibrium initial conditions like quenched or rapidly expanding media. These model systems showed the importance of chemical processes, which are needed for an effective thermalization of both thermal modes and even more importantly the particle number. Equilibration time scales heavily depend on the interaction-time scales. Additionally, simulations with expanding matter drops showed that the type and strength of fluctuations mainly depend on the coupling between particles and the field and their reaction rate, and not on the type of phase transition the model shows in an adiabatic equilibrium phase transition. This is a real surprise as a rapid expansion and cooling is something very different from an adiabatic phase transition. Phenomena like critical slowing down was observed indirectly because the reaction rates of the process $\sigma \leftrightarrow \bar{\psi}\psi$ dropped near and at the phase transition. A reduction of the reaction rates increased the correlation length and correlation time-scales. In a calculation of an expanding matter droplet, this "freeze-out" of interactions has only a minor effect because the system does not stay long enough in this region to gain significant effects from it. Another possible approach to observe critical slowing down would be to regard a large and thermal system which is slowly driven near the phase transition by a heat bath. The damping of chemical reactions could lead to a kind of kinetic freeze-out of the fluctuations which increases the correlation and fluctuation lengths of the system.

However, some other interesting aspects have been found with the DSLAM model in the rapid expansion scenarios. The formation of bubbles and strong, local fluctuations have been observed for simulations with a strong coupling between fields and particles. These fluctuations and bubbles would not be visible in a heavy-ion experiment, but their impact on angular distributions of conserved charges could be a possible observable and are subject to further investigations.

In summary, the physical calculations and investigations in this work indicate that non-equilibrium effects have a very strong impact on the properties of the matter in the linear σ-model. Standard thermal approaches and views on the phase diagram of the σ-model are only valid for systems which are very close to thermal and chemical equilibrium. Highly dynamical systems can show a very different behavior to a usual phase transition. However, the importance of the chemical processes $\sigma \leftrightarrow \bar{q}q$ in the σ-model open a possible new approach to this topic as signatures for dynamical systems could relate strongly to the microscopic properties of these interactions.

Upcoming experiments with the CBM detector at the Facility for Antiproton and Ion Research (FAIR) will include extensive studies on the deconfinement and chiral phase transitions. By probing nuclear matter with heavy-ion collision, quark-gluon matter of high energy and very high densities is created. Varying these parameter and observing event-by-event fluctuations will make the CBM experiment a powerful tool in the exploration of the QCD phase diagram.

The used model and implementation includes some strong approximations, and quantum effects have been mainly ignored in this work. The cross-sections for the processes should be extended using quantum calculations, especially for strong couplings at the phase transition, in which the field's mass m_σ becomes tachyonic. A better treatment of the pion sector could increase the realism of the model at low temperatures, as well.

In the process of modeling and implementing the numerics of the σ-model, another interesting topic crystallized in this thesis, the particle-field method. One of the first problems with the model was the lack of interactions between fields and particles, which became a real challenge as there was no general method which allowed collision-like interactions between a classical particle and a classical, multidimensional field.

A good description for both fields and particles turned out to be energy and momentum and after some careful numerical testing it turned out that interactions could be described by the noncontinuous exchange of energy and momentum, borrowing some old ideas from the wave-particle duality of matter. The resulting method was the first which allowed arbitrary interactions at arbitrary timescales between fields and particles, conserving both energy and momentum all the time. Several simple and complex model-systems have been developed and used to test the robustness of the method, and a large part of this thesis was used to investigate this newly developed method. I hope this method is applied to other topics and areas in research in which this generic problem is occurring.

Appendix A

Numerical Properties of Different Interaction Parameterizations

To hold a pen is to be at war.

François-Marie Arouet (Voltaire)

This section is dedicated to the momentum to energy ratio of a particle-wave excitation on a wave equation. The underlying system is a free wave equation

$$\frac{\partial^2 u}{\partial t^2} = c^2 \nabla^2 u \ . \tag{A.1}$$

For simplicity, the wave equation has no potential $V(u) = 0$. This is reasonable for weak potentials or small, energetic excitations which keep most of their energy in the kinetic parts $\dot{u}$ or ∇u.

The energy, the momentum and the ratio of both is calculated for several wave excitations. Because of numerical reasons, all excitations will behave differently and are more or less useful in a numerical implementation.

If the wave equation would have a non-negative potential, all calculations in this chapter are still valid, however they have to be seen as upper limits. For a given energy, a potential lowers the possible momentum of a wave packet. This effect can be approximated with the following equation

$$\frac{P}{E_{\text{free}}} > \frac{P}{E_{\text{free}} + V(\phi)} \ . \tag{A.2}$$

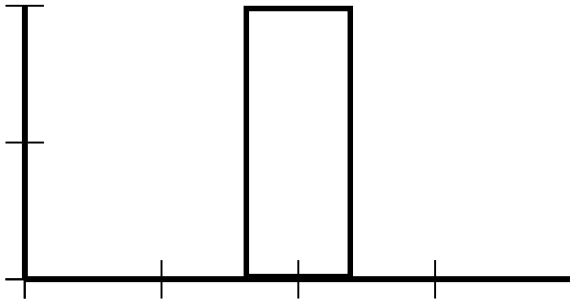

Figure A.1: One-point stencil on a discrete, numerical grid. The excitations moves from left to right.

ϕ	0	0	h	0	0
$\nabla\phi$	0	0	$h/\Delta x$	$-h/\Delta x$	0
$\dot{\phi}$	0	$-hv/\Delta t$	$hv/\Delta t$	0	0
$\nabla\phi \cdot \dot{\phi}$	0	0	$h^2 v/\left(\Delta x\ \Delta t\right)$	0	0

Table A.1: Numerical representation of the one-point stencil and its spatial and time like differences as seen in figure A.1. Both the first order spatial and time difference scheme has been applied. The stencil is normed to a height of 1.

A.1 Energy-Momentum Transfer Ratio for a One-Point Stencil in One Dimension

The maximum momentum to energy ratio for a one-point stencil on a numerical x_i grid is calculated. A one-point stencil can be described as the numerical pendant to the Kronecker-δ. We assume a moving, single grid point excitation, which is moving in one direction with the velocity v. For simplicity a one dimensional system is assumed

$$f(x) = h\delta(x - x_i - v \cdot t) \ . \tag{A.3}$$

The stencil describes a excitation within the wave equation, the velocity v is an initial velocity which defines the momenta of the excitation. The actual movement velocity is determined by the dispersion relation of the wave equation.

The energy and the momentum of the moving one-point stencil are calculated by employing finite differences for the derivatives

$$\nabla\phi(x) \to \frac{f(x + \Delta x) - f(x)}{\Delta x} \ , \tag{A.4}$$

and

$$\frac{\mathrm{d}\phi(x)}{\mathrm{d}t} \to \frac{f(t + \Delta t) - f(t)}{\Delta t} \ . \tag{A.5}$$

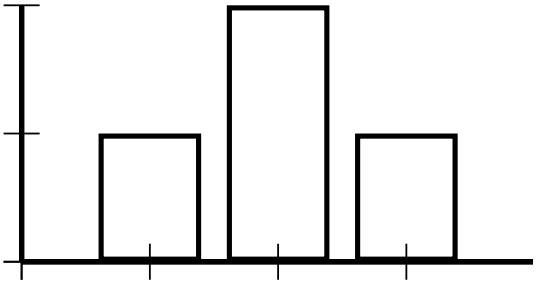

Figure A.2: 3-point stencil on a discrete, numerical grid. The excitations moves from left to right.

The energy and momentum for a one-point stencil is the sum over the energy contributions for every grid point. The single contributions are given in Table A.1. The total energy is

$$E = \sum_i \frac{1}{2}\left(\phi(x_i,t)^2 + (\nabla\phi(x_i,t))^2 + \dot{\phi}(x_i,t)^2\right) = \frac{1}{2}\left(h^2 + \frac{2h^2}{\Delta x^2} + \frac{2h^2v^2}{\Delta t^2}\right) , \tag{A.6}$$

and the total momentum

$$P = \sum_i \nabla\phi(x_i,t)\dot{\phi}(x_i,t) = \frac{h^2 v}{\Delta t \Delta x} . \tag{A.7}$$

Their ratio of momentum to energy is

$$\frac{P}{E} = \frac{2h^2}{\Delta x^2\left(\frac{2h^2v^2}{\Delta x^2} + \frac{2h^2}{\Delta x^2} + h^2\right)} . \tag{A.8}$$

For a general wave equation with velocity $v = c = 1$, we can assume with no loss of generality $\Delta x = \Delta t$:

$$\frac{P}{E} \xrightarrow[v=1]{\Delta x=\Delta t} \frac{2}{\Delta t^2 + 4} \overset{\Delta t \ll 1}{\approx} \frac{1}{2} \tag{A.9}$$

For a one point stencil on a numerical grid, the maximum momentum to energy ratio can not be come larger than 1/2.

A.2 Energy-Momentum Transfer Ratio for a Three-Point Stencil In One Dimension

In this section the maximum momentum to energy ratio is calculated for a three-point stencil. Like in the previous section, the maximum energy to momentum ratio of a three point stencil is calculated. The three-point stencil has two additional, smaller steps on the grid and Table A.2 with all energy and momentum contributions becomes more complex.

ϕ	0	$h/2$	h	$h/2$	0
$\nabla\phi$	0	$h/2\Delta x$	$h/2\Delta x$	$-h/2\Delta x$	$-h/2\Delta x$
$\dot{\phi}$	$-hv/2\Delta t$	$-hv/2\Delta t$	$hv/2\Delta t$	$h/2\Delta t$	0
$\nabla\phi\cdot\dot{\phi}$	0	$h^2v/\left(4\Delta x\ \Delta t\right)$	$h^2v/\left(4\Delta x\ \Delta t\right)$	$h^2v/\left(4\Delta x\ \Delta t\right)$	0

Table A.2: Numerical representation of the 3-point stencil and its spatial and time like differences as seen in figure A.2. Both the first-order spatial and time difference scheme has been applied. The stencil is normed to a height of 1.

The energy and the momentum of the moving 3-point stencil are

$$E = \frac{1}{2}\sum_i \frac{1}{\Delta x}\left(\phi(x_i)^2 + (\nabla\phi(x_i))^2 + \dot{\phi}(x_i)^2\right) = \frac{1}{2}\left(\frac{3h^2}{2} + \frac{h^2}{\Delta x^2} + \frac{2h^2v^2}{\Delta t^2}\right)\ , \tag{A.10}$$

and

$$P = \sum_i \nabla\phi(x_i)\dot{\phi}(x_i) = \frac{3h^2v}{4\Delta t\Delta x}\ . \tag{A.11}$$

Their ratio is:

$$\frac{P}{E} = \frac{3h^2}{2\Delta x^2\left(\frac{2h^2}{\Delta x^2} + \frac{3h^2}{2}\right)} \tag{A.12}$$

For a general wave equation with velocity $v = c = 1$, we can assume without loss of generality $\Delta x = \Delta t$:

$$\frac{P}{E} \xrightarrow[v=1]{\Delta x=\Delta t} \frac{3}{3\Delta t^2 + 4} \overset{\Delta t\ll 1}{\approx} \frac{3}{4} \tag{A.13}$$

As we can see, the three-point stencil has a maximal ratio of 0.75, while the one point-stencil had a ratio of 0.5

The more points the stencil has, the more "smooth" it behaves on the grid. A more smooth function will have its maximal momentum to energy ratio more in the region of 1.

Impact of the finite-difference definition

In the above calculations, the backwards definition of the spatial finite difference has been used

$$\nabla_x f(x) \approx \frac{f(x) - f(x-\Delta x)}{\Delta x}\ . \tag{A.14}$$

If the forward definition would have been used

$$\nabla_x f(x) \approx \frac{f(x+\Delta x) - f(x)}{\Delta x}\ , \tag{A.15}$$

the P/E-ratio for the one-point stencil would become exactly 1. However, if the stencil would then travel in the opposite direction, the ratio would drop again to 1/2. Furthermore, if the center-difference definition would have been used

$$\nabla_x f(x) \approx \frac{f(x+\Delta x) - f(x-\Delta x)}{2\Delta x} \tag{A.16}$$

the ratio would be even worse.

However, the general statement still holds: the more smooth the stencil and the more spatial distributed points exist, the better the momentum-to-energy ratio will become, independently of the finite-difference definition.

Numerical artifacts In the above sections, the use of point like excitations on the grid was discussed. It turned out, that these excitations have a poor momentum-to-energy ratio. This problem becomes even worse, if numerical errors are taken into account. If a non-continuous excitation happens on a numerical grid, most wave equation solvers will generate numerical artifacts. This happens typically if the size of the excitations are in the order of the grid-resolution. The result are unphysical oscillations (Gibbs phenomenon) and high-frequency problems (Nyquist error). Figure A.3 shows two examples of those numerical artifacts. The artifacts are strongly suppressed for smooth excitations, in general they are suppressed with the order of their differentiability, similar to the convergence theorem of Fourier series.

The numerical noise, like in figure A.3, turns the one-point and 3-point stencil method useless for practical applications. The noise increases heavily the derivative terms, which increases the energy. In contrast, the momentum is canceled and the momentum to energy ratio is driven close to zero. So even if an initial excitation can be added very precisely to the numerical grid, it will evolve to noise after some time. F Therefore in the next section a very smooth function will be investigated, the Gaussian function.

A.3 Energy-Momentum Transfer Ratio for a One-Dimensional Gaussian

For simplicity, we assume a vanishing potential

$$V(\phi) = 0 \ . \tag{A.17}$$

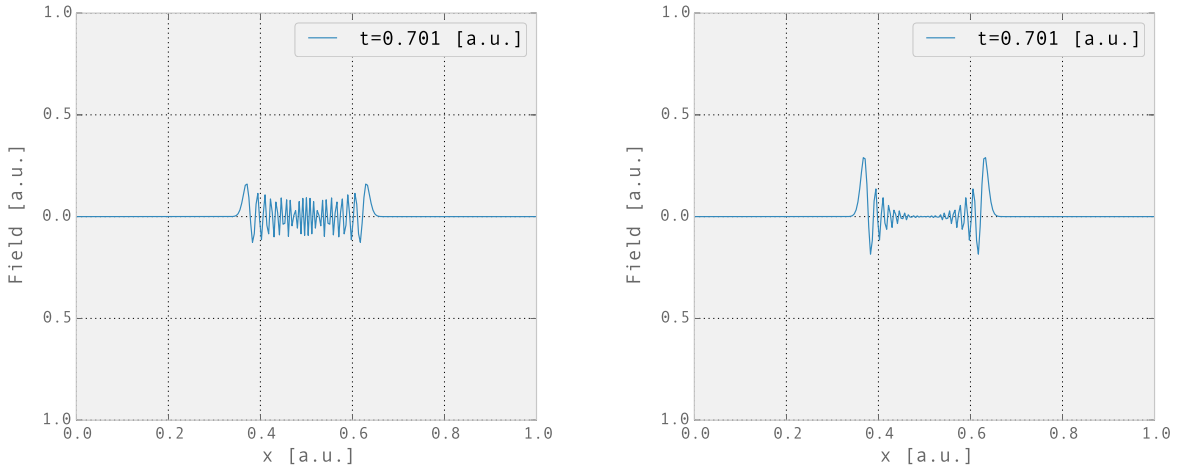

Figure A.3: Comparison of point-like excitations on the numerical grid. **Left:** the grid was excited on a single grid point (one-point stencil). **Right:** the grid was excited on three grid points (3-point stencils). Both excitations create numerical artifacts, however the disturbance with the single grid point is much stronger than the three-point excitation. The smoother the initial excitation, the less numerical artifacts are generated by the partial differential equation solver.

This is a reasonable approximation for small excitations or fast moving excitations where $\nabla\phi^2 \gg \phi^2$ or $\dot{\phi}^2 \gg \phi^2$.

$$\phi(\mathbf{x}, t) = \exp\left(\frac{-(x - vt)^2}{2\sigma^2}\right) \tag{A.18}$$

$$E = \frac{1}{2}\int \mathrm{d}x \ \left[\dot{\phi}^2(x, t = 0) + (\nabla\phi(x))^2\right] \tag{A.19}$$

$$P = \int \mathrm{d}x \ \left[\dot{\phi}(x, t = 0) \cdot \nabla_i\phi(x)\right] \tag{A.20}$$

For $v \to 1$, the momentum ratio is exactly 1 at every point in space:

$$\frac{P(x)}{E(x)} = 1 \tag{A.21}$$

For a 1D Gaussian, the wave packet can be directly interpreted as a particle excitation with the properties:

$$P \leq E \tag{A.22}$$

Because of the smoothness of the Gaussian, we have no discretization effects. For a Gaussian on a discrete grid, a small amount of discretization errors will occur, if the number of field elements is too small.

A.4 Energy-Momentum Transfer Ratio for a Non-Relativistic 3D Gaussian

In the previous section, the transfer for a moving Gaussian in one dimension was calculated. This is a reasonable approximation for a fast wave, a weak potential or a small but string excitation, which kinetic energy is dominant. $max(P/E)$ was 1. This calculation is extended to three dimensions now.

$$\phi(\mathbf{x},t) = \exp\left(\frac{-\left(x-v_x t\right)^2}{2\sigma_x^2}\right)\exp\left(\frac{-\left(y-v_y t\right)^2}{2\sigma_y^2}\right)\exp\left(\frac{-\left(z-v_z t\right)^2}{2\sigma_z^2}\right) \tag{A.23}$$

$$\dot{\phi}(\mathbf{x}) = \partial_t \phi(\mathbf{x},t)|_{t\to 0} \tag{A.24}$$

$$\nabla_i \phi(\mathbf{x}) = \partial_t \phi(\mathbf{x},t)|_{t\to 0} \tag{A.25}$$

$$E = \int_V \mathrm{d}x^3 \frac{1}{2}\left(\dot{\phi}^2(\mathbf{x}) + \left[\sum_i^3 \nabla_i \phi(\mathbf{x})\right]^2\right) \tag{A.26}$$

$$P_i = \int_V \mathrm{d}x^3 \left(\phi(x)\cdot\nabla_i\phi(\mathbf{x})\right) \tag{A.27}$$

For simplicity, the velocity is assumed along the x-axis

$$\vec{v} = v_x \cdot \vec{e}_x \ . \tag{A.28}$$

For $\sigma_i^2 > 0$

$$\frac{P}{E} = \frac{2v_x\sigma_y^2\sigma_z^2}{\left(1+v_x^2\right)\sigma_y^2\sigma_z^2 + \sigma_x^2\left(\sigma_y^2+\sigma_z^2\right)} \ . \tag{A.29}$$

Equation (A.29) gives the momentum to energy ratio for a three dimensional Gaussian wave packet with a given velocity v_x. However, this will not be the final equation because we already know that wave excitations travel with $|v| = 1$. Let us check for the maximum of equation A.29 with respect to the velocity.

We assume a spherical wave packet

$$\sigma_x \equiv \sigma_y \equiv \sigma_z \equiv 1 \ . \tag{A.30}$$

Equation (A.29) becomes

$$\frac{2v_x}{3+v_x^2} \ . \tag{A.31}$$

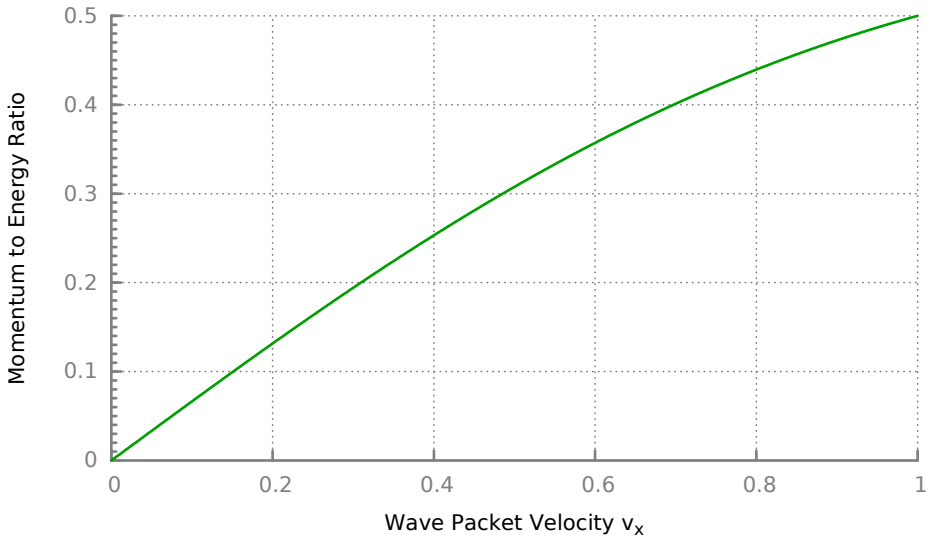

Figure A.4: Ratio of the momentum to energy transfer of a 3D spherical Gaussian for a given velocity.

Figure A.4 shows equation (A.30) with respect to the velocity. The ratio seems to have a maximum at $\pm\sqrt{2}$ of ≈ 0.7. However, this is a numerical artifact. An excitation with $v > 1$ would generate two Gaussian waves, one in forward direction with $v = 1$ and another in backwards direction with $v = -1$. For a physical wave equation, the following limit is obtained

$$\max\left(\frac{P}{E}\right) \overset{\mathbf{v}\to 1}{=} \frac{1}{2} \ . \tag{A.32}$$

This is an interesting result. For any spherical Gaussian wave packet (and in fact for any other spherical object), only 50% of the transferred energy can be in form of momentum. This seems puzzling but can be easily explained by the fact that $\dot{\phi}, \nabla_x\phi, \nabla_y\phi$ and $\nabla_z\phi$ contribute to the energy but only $\dot{\phi}$ and $\nabla_x\phi$ contribute to the momentum.

Let us now take a look at an elliptical Gaussian by starting with equation (A.29) and defining

$$\sigma_y = \sigma_z \equiv a\sigma_x \ . \tag{A.33}$$

$$\frac{P}{E} = \frac{2a^2 v_x \sigma_x^2}{2a\sigma_x^2 + a^2(1+v_x^2)\sigma_x^2} \overset{\mathbf{v}\to 1}{=} \frac{a}{1+a} \tag{A.34}$$

For $a \to 0$ the energy to momentum ratio lowers to zero $P/E \to 0$. For $a \to \infty$ the momentum to energy transfer asymptotically grows to 1. This is no surprise as for $a \to \infty$ the 3D Gaussian

becomes spatially homogeneous in y- and z-direction, which is the same as an one dimensional system. Additionally we will see in the next section that this transformation is the same as a Lorentz boost for high velocities in which the spherical Gaussian will be boosted to a slim disk.

A.5 Energy-Momentum Transfer Ratio for a Relativistic 3D Gaussian

In the last section the momentum over energy ratio for a spherical Gaussian in three dimensions was calculated. This calculation neglected any relativistic effects, resulting in a upper momentum to energy ratio of 1/2. Furthermore momentum and energy of any relativistic object would grow to infinity for $\beta \to 1$, which is not the case for the non-relativistic calculation in the last section. To address this issue, we will boost the Gaussian along the velocity direction. For simplicity we assume the velocity to be in line with our coordination-system in x-direction

$$\mathbf{v} = \begin{pmatrix} v \\ 0 \\ 0 \end{pmatrix} . \tag{A.35}$$

The non-relativistic form of the spherically symmetric 3D Gaussian becomes

$$\phi(\mathbf{x}, t) = A_0 \exp\left(\frac{-(x - vt)^2}{2\sigma_x^2}\right) \exp\left(\frac{-y^2 - z^2}{2\sigma_{yz}^2}\right) . \tag{A.36}$$

Both the space and time are boosted in x-direction:

$$x' = \gamma x , \tag{A.37}$$

$$t' = \gamma t , \tag{A.38}$$

$$1/\gamma = \sqrt{1 - \beta} , \tag{A.39}$$

$$\beta = \frac{v^2}{c^2} = v^2 . \tag{A.40}$$

Boosting (A.36) leads to

$$\phi(\mathbf{x}, t) = A_0 \exp\left(\frac{-\gamma^2 (x - vt)^2}{2\sigma^2}\right) \exp\left(\frac{-y^2 - z^2}{2\sigma^2}\right) . \tag{A.41}$$

Performing the same calculations for the energy and momentum as in the previous section, we arrive at the energy to momentum ratio with

$$\frac{P}{E} = \frac{2v}{3 - v^2} = \frac{-2\sqrt{\beta}}{3 - \beta} \ . \tag{A.42}$$

We have performed a Lorentz boost on the Gaussian, still equation (A.42) looks very similar to (A.31) with the difference of the minus sign. However, for $v \to 1$ we now get the correct relativistic limit

$$\max \left(\frac{P}{E} \right) \overset{\mathrm{v} \to 1}{=} 1 \ . \tag{A.43}$$

Figure A.5 shows the ratio P/E in dependence to the relativistic velocity. Additionally, the

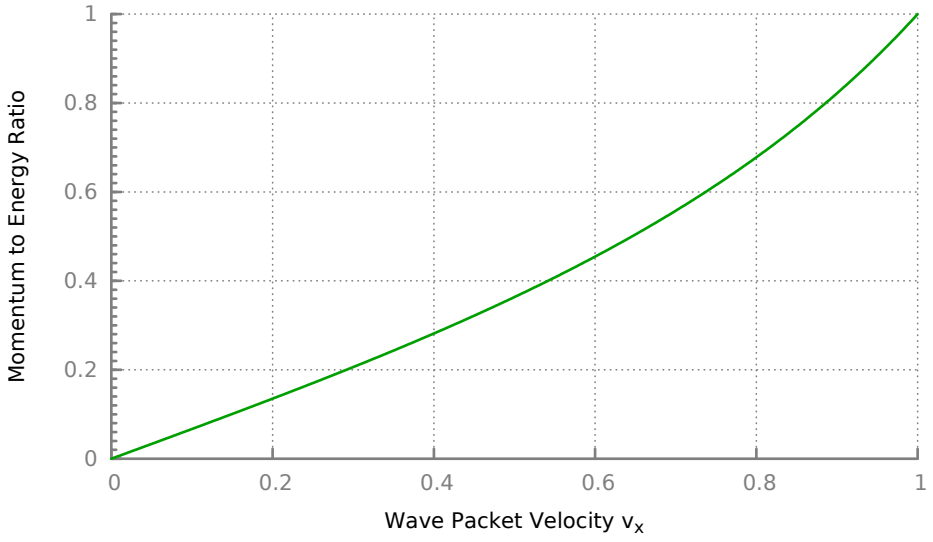

Figure A.5: Ratio of the momentum to energy transfer of a 3D spherical Gaussian with a Lorentz-boost.

energy and momentum of the Gaussian are now boosted and can reach arbitrary large values for $v \to 1$. In equation (A.41) x and t were boosted. This boost, which introduced an additional γ^2 in the equation could be absorbed in a boosted $\tilde{\sigma}_x$:

$$\tilde{\sigma}_x = \frac{\sigma}{\gamma} \tag{A.44}$$

This boost in x-direction can be reinterpreted in a smaller Gaussian width in x-direction, compressing the spherical Gaussian to a thin disk for high velocities $v \to 1$. In a numerical simulation the Lorentz-boost has to be employed in all three dimensions, extending (A.23) with

the general Lorentz-transformation

$$\phi(\mathbf{x},t) = A_0 \prod_i^3 \exp\left[-\frac{1}{2\sigma_i^2}\ \left(\sum_\mu^4 \Lambda_{\mu\nu} x^\nu\right)^2\right]\ . \tag{A.45}$$

However, for small velocities or small momentum to energy ratios, the non-boosted version can be used as an approximation. For $P/E < 0.3$ the error is about 18.6%. Additionally, one has to be careful with the numerics for high velocities. For $v \to 1$ the Gaussian becomes a slim disk which can lead to discretization artifacts if the effective $\tilde{\sigma}$ becomes of the order of magnitude of the grid size.

Appendix B

Numerical Sampling

Maybe life is random, but I doubt it.

Steven Tyler

Numerical Sampling Methods

In physics many systems are defined and described by distribution functions. Prominent distribution functions are the Gaussian distribution, the exponential distribution as well as Boltzmann, Fermi- or Bose-distributions.

Distribution functions are handy in statistical physics and many models define evolution equations for distribution functions. The Boltzmann function is a typical example for such a theory. Other models are the Fokker-Planck equation [153], the master equation or the Black-Scholes equation for stock-option pricing [154] and many more. For a given distribution function, one can derive time-evolution equations within these theories.

In general, distribution functions are continuous objects with a statistical interpretation. Most of the time, they are defined as probability density functions $f(x)$ with the following properties:

$$\text{Boundedness}: \quad \int \mathrm{d}x \; f(x) = c \; , \tag{B.1}$$

with $c = 1$ in case of a probability-density function or with a physical value for c, for example the particle number in case of the Boltzmann distribution.

For a probability distribution function, the expectation value for an observable $A(x)$ is defined as

$$\langle A \rangle = \int A(x) f(x) \mathrm{d}x \; . \tag{B.2}$$

This comes handy for analytic calculations, for numerical computations a discrete realization of a distribution function is needed. The process of generating a finite number of elements with properties which follow a given distribution function is called sampling

$$f(x) \xrightarrow{\text{Sampling}} \frac{1}{N}\sum_{i=1}^{N}\delta(x-x_i), \tag{B.3}$$

which reasembles the distribution function again in the continuous limit:

$$\lim_{N\to\infty}\frac{1}{N}\sum_{i}^{N}\delta(x-x_i) = f(x) \tag{B.4}$$

There is no single method for sampling, in fact it is an own discipline in numerical mathematics and various methods exist, depending on the properties of the functions to sample. All methods, which have been used in this thesis is listed in the following. The common point of all functions are the need for good random numbers.

Random-Number Generation

Sampling is directly related to random-number generation. In theory, a distribution function could be sampled with a deterministic pattern over the sampling range. However, for Monte-Carlo simulations one is interested in exploring the physical phase space of a model with probability methods. Therefore it is of interest to generate slightly different versions of a calculation, even though the initial conditions are the same. In general, the initial conditions are given by a distribution function and because of the too high numerical complexity of propagating the exact solution, the initial conditions are sampled and the subset of Monte-Carlo realizations are evaluated. Multiple runs with different sampling realizations lead to different results in the end which can be used for statistical analysis.

In all cases, Monte-Carlo calculations make heavy use of random numbers. For simulations, the generated random numbers should have a high statistical quality with a long period and for practical use should be fast in generation. In contrast to cryptographic applications, Monte Carlo simulations do not need an unpredictable stream of numbers.

A good choice for a general-purpose generator is the patent free Mersenne-Twister MT19937 [140]. It is based on a linear recurrence matrix on a finite field and has a period of $2^{219937}-1$. The chosen implementation implementation is the SSE2 optimized dSFMT implementation [155] which generated floating-point numbers in the interval $[0,1)$.

B.1 Inversion Method

The inversion method is a straight forward, numerically stable and fast method for the exact sampling of a distribution function. Its drawback is its limitation to distribution functions which have an invertible cumulative distribution function.

The cumulative distribution function for a random variable with $X \in \mathbb{R}$ with $F(x) = P(X \leq x)$ can be calculated from the probability distribution function $f(x)$ via an integration

$$F_X(x) = \int_{-\infty}^{x} f(\tau)\, \mathrm{d}\tau \ . \tag{B.5}$$

Per definition, $F_X(x) \in [0, 1]$.

For any random number ξ, the generated number X_f follows the distribution f if

$$X_f := F^{-1}(\xi) \quad \{\xi \in [0, 1]\} \ , \tag{B.6}$$

with ξ as an uniformly distributed random number. The following shows the sampling of an exponential function with the probability distribution function

$$f(x) = \exp(-\gamma x) \quad \text{for } x \in \mathbb{R}^+ \ , \tag{B.7}$$

and the normed cumulative distribution function

$$F(x) = \int_0^x \mathrm{d}x'\ f(x') = \frac{1}{\gamma}\left[1 - \exp(-\gamma x)\right] \ . \tag{B.8}$$

By inverting and substituting $\xi = 1 - \xi'$ the following generating function is defined

$$x = F^{-1}(\xi) = -\frac{\ln(\xi)}{\gamma} \quad \{\xi \in (0, 1]\} \ . \tag{B.9}$$

A sample of multiple x will follow an exponential distribution.

B.2 Accept-Reject Method

The Accept-Reject Method, or rejection-sampling [156] can be used to sample functions which can not directly be sampled with the inversion method. An example for such a function is the Boltzmann distribution

$$f(E) = E^2 e^{-E/T} \ , \tag{B.10}$$

which can be integrated but not inverted. The accept-reject method can be applied if an arbitrary distribution function $f(x)$ has an envelope function $g(x)$ and a constant k which fulfill

$$\forall x \in \mathbb{R} : f(x) \leq k \cdot g(x) \ . \tag{B.11}$$

The sampling is done in two steps, a random variable x_g is sampled according to $g(x)$, which acts as an candidate for the actual function $f(x)$. This candidate is accepted with the following probability

$$p = \frac{f(x_g)}{k \cdot g(x_g)} \ . \tag{B.12}$$

In case of the Boltzmann distribution function (B.10), a typical choice for the envelope function would be

$$g(x) = 2T^2 e^{-x/2T} \ , \tag{B.13}$$

$g(x)$ can be sampled with the inversion method.

B.3 Metropolis-Hastings Sampling

Metropolis-Hastings sampling is a generic method for sampling distribution functions which can not be sampled with the above methods. It is based on Markov chains (Markov chain Monte Carlo method, MCMC) and beside the sampling of distribution functions, it can be used to sample time-like distribution as well [157]. Interestingly, it was originally proposed for numerical equation of state calculation with canonical ensembles [158].

The idea of the algorithm is to perform a random walk on the distribution function. The probability of jumping from a position x_i to a possible candidate position x_c is weighted by the ratio of the probabilities given by the ratio of the distribution function

$$p = \frac{f(x_c)}{f(x_i)} \ . \tag{B.14}$$

The jump from x_i to x_c can be modeled in multiple ways, either by sampling x_c completely random, or by walking in Gaussian steps:

$$x_c = x_i + \frac{1}{2\sqrt{\sigma\pi}} \exp\left(-\frac{\xi^2}{2\sigma^2}\right) \tag{B.15}$$

Evaluation of a new candidate x_i is done a predefined number of rounds and has to be chosen as a trade off between sampling accuracy and calculation time. The following listing shows the algorithm in pseudo code:

```
E = initialGuess()
for round in range(NumberOfRounds):
    randomJump = randomGaussian()
    candidate = E + randomJump
    if randomUniform() > pdf(candidate)/pdf(E):
        E = candidate
```

In this thesis, the Metropolis-Hastings algorithm is used to sample particles according to the Boson- and Fermi-distributions.

B.4 Sampling of Gaussians

Random numbers which are Gaussian distributed are vastly needed for the simulation of noisy processes, like the Langevin-equation or for initial conditions. The Metropolis-Hastings algorithm needs a Gaussian random number for every iteration step. A suitable sampling method is the Box-Muller transform [159], however this makes heavy use of trigonometric functions. With some minor modifications, this method can be derived to the Marsaglia polar method [160], which is numerically more efficient and is used in this thesis. It generates two Gaussian random numbers at a single calculation step.

Two random variables are chosen with the condition

$$\xi' = \xi_x^2 + \xi_y^2 \leq 1 \quad \{\xi_x, \xi_y \in [-1, 1]\} \ . \tag{B.16}$$

The resulting independent random numbers are:

$$X_x = \xi_x \cdot \sqrt{\frac{-2\ln(\xi')}{s}} \ , \qquad X_y = \xi_y \cdot \sqrt{\frac{-2\ln(\xi')}{s}} \ . \tag{B.17}$$

Appendix C

Discrete Exponential Decay

> Wife walks in on husband, a string theorist, in bed with another woman. He shouts, "I can explain everything!"

In this section the mathematical properties and the numerical implementation of a discrete exponential decay are discussed.

The exponential decay is defined via the well known differential equation

$$\dot{y} = \frac{\mathrm{d}y}{\mathrm{d}t} = -\lambda y \tag{C.1}$$

and has the solution

$$y(t) = C\mathrm{e}^{-\lambda t} \ . \tag{C.2}$$

The exponential function is a smooth and arbitrary derivable function. Being fully deterministic, the exponential function has no statistical variance and the function itself matches its ensemble average

$$C\mathrm{e}^{-\lambda t} = \langle\langle C\mathrm{e}^{-\lambda t}\rangle\rangle \ . \tag{C.3}$$

In numerical simulations, especially in Monte-Carlo simulations, a statistical variance or some kind of random process desirable. Therefore the simulation and properties of a discrete, exponential like decay function are investigated in this section.

The discrete decay function $\hat{y}(t_i)$ should have the following properties:

- $\hat{y}$ should have a discrete update rule: $\hat{y}_{i+1} = y_i - \Delta y$ if a reaction happens, otherwise $\hat{y}_{n+1} = y_n$

- the ensemble average should be the one of an exponential function $\langle\langle \hat{y}_t \rangle\rangle = C \exp(-\gamma t)$

It should be clear, that a closed form for $\hat{y}$ can not be found, nevertheless we can define its statistical properties and how to simulate it.

Let us define the discrete exponential-like decay: We want to simualte a system with N_0 particles, so

$$\hat{y}(0) = N_0 \ . \tag{C.4}$$

A particle decay removes a ΔN from the system which can be seen as the pendant of a single particle leaving the system

$$\hat{y}_{i+1} \to \hat{y}_i - \Delta N \ . \tag{C.5}$$

The probability for a particle to decay with a time interval Δt is derived from the exponential law:

$$1 - \exp(-\gamma \Delta t) = \left(\gamma \Delta t - \frac{\gamma^2 \Delta t^2}{2!} + \frac{\gamma^3 \Delta t^3}{3!} + ... \right) \overset{\Delta t \ll 1}{\approx} \gamma \Delta t \ . \tag{C.6}$$

Each particle has the same, independent decay probability γ, so the decay probability for a single reaction scales linearly

$$p_t = \gamma N_t \Delta t \ , \tag{C.7}$$

with N_t as the number (or density) of particles present at time t. To simulate a discrete exponential decay with such a probability, Δt has to be small enough. Concretely we have to make sure that $p_t \ll 1$ and to neglect double decays in one time step $p_t^2 \ll p_t$ and $p_t^2 \lll 1$. A typically order of magnitude could be $10^{-2} > p_t$

Proof: $\langle\langle \hat{y}(t) \rangle\rangle = \exp(t)$

We can think about $\hat{y}$ as a finite number of particles which can decay independently from each other. First, a single, isolated particle is regarded. The decay probability of this particle should not vary in time

$$p_{\text{decay}}(t) = p \ . \tag{C.8}$$

We define $P(t)$ the probability to survive a given amount t without decaying. The particle is alive in the beginning, so we can state $P(0) = 1$. The probability to survive a given amount of time Δt is given in first order by

$$\text{probability to survive between } t \text{ and } t + \Delta t = \gamma \Delta t \tag{C.9}$$

and is valid for $\Delta t \ll 1$ and exact for $\Delta t \to \mathrm{d}t$.

Given the survive probability for a time step Δt and the start probability $P(t)$, we can derive

$$\begin{aligned} P(t+\Delta t) &= P(t)(1-p_0\Delta t) \\ \approx P(t) + \frac{\Delta P(t)}{\Delta t}\Delta t &= P(t) - P(t)p_0\Delta t \ , \qquad \text{(C.10)} \\ \frac{1}{P(t)}\frac{\Delta P(t)}{\Delta t} &= -p_0 \\ \Rightarrow P(t) &\approx C_0 \ \mathrm{e}^{-p_0 t} \ . \qquad \text{(C.11)} \end{aligned}$$

For $\Delta t \to \mathrm{d}t$, equation (C.10) recovers to the exponential law. Simulating equation (C.10) with $\Delta t \ll 1$ we get a decent approximation.

For a single particle we have shown that $\hat{Y}$ has the ensemble average as an exponential function. We now look at the ensemble average for multiple particles.

The decay of a single particle is statistically independent from all other particles, so we can solve the decay function for every particle independently: $\hat{Y} \to \hat{Y}_i$.

$$\hat{Y}(t) = \sum_{i=1}^{N} \hat{Y}_i(t) \qquad \text{(C.12)}$$

If $\hat{Y}_i$ is statistically independent of $\hat{Y}_j$, their ensemble average is also independent of each other:

$$\left\langle\left\langle \hat{Y}(t) \right\rangle\right\rangle = \left\langle\left\langle \sum_i^N \hat{Y}_i(t) \right\rangle\right\rangle = \sum \Delta N_i \mathrm{e}^{-p_i t} \ . \qquad \text{(C.13)}$$

All particles should be identical, so equation (C.13) can be simplified:

$$p_i = p_0, \qquad \Delta N_{i=1} = \Delta N \qquad \text{(C.14)}$$

$$\left\langle\left\langle \hat{Y}(t) \right\rangle\right\rangle = \sum_i^N \Delta N \mathrm{e}^{-p_0 t} = N \ \mathrm{e}^{-p_0 t} \qquad \text{(C.15)}$$

$$\qquad \text{(C.16)}$$

Under these assumptions, our discrete decay function shows the same ensemble average as the analytic exponential function, no matter how many particles we choose to simulate. We only have to make sure our numerical implementation properly simulates one particle decays.

Numerical Simulation

The numerical simulation of a discrete decay is straight forward:

```
# simple simulation of a discrete decay function
import random
t, dt, tStop = 0., 0.001, 300.
N = N0 = 100    # number of particles
deltaN = 1      # impact of one particle
gamma = 0.025   # decay rate
while t < tStop:
    prob = N * gamma * dt      # single event decay probability
    if prob > random.random(): # monte carlo sampling
        N -= 1
    t += dt
```

Figure C.1 shows some examples for different initial particle number N_0. Note how the decaying function $\hat{y}(t)$ approaches the smooth exponential for $N \gg 1$.

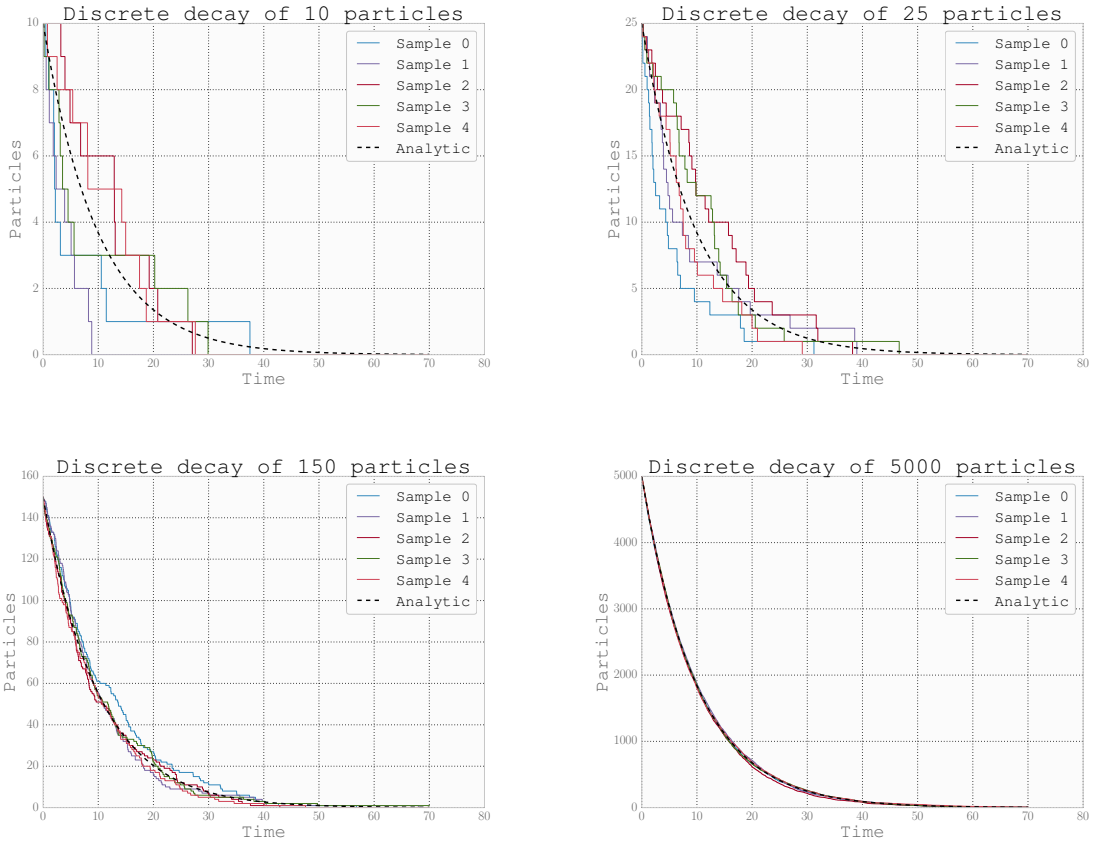

Figure C.1: simulation of a discrete, exponential like decay for different particle ensembles. For $N_{\text{part}} \to \infty$ the discrete decays recovers to an exponential decay.

Appendix D

Kinematics, Interactions and Decays

> The First Rule of Tautology Club is the first rule of Tautology Club.
>
> Tautology Club

This chapter will shortly discuss the kinematics of particle interactions and decays. A more detailed view of this discussion can be found in [161] or in the very good lecture notes [162].

D.1 Relativistic Kinematics

Some notation from special relativity:

$$\text{Lorentz metric tensor } g^{\mu\nu} = \text{diag}\,(1,-1,-1,-1)\ , \tag{D.1}$$

$$\text{spatial four vector } x^{\mu} = (t, \vec{x})\ , \tag{D.2}$$

$$\text{proper time } \mathrm{d}\tau = \mathrm{d}t/\gamma\ , \tag{D.3}$$

$$\text{Lorentz boost } \gamma^{-1} = \sqrt{1-(v/c)^2} = \frac{m}{E}\ , \tag{D.4}$$

$$\text{four velocity } u^{\nu} = \gamma\,(1, \vec{v})\ , \tag{D.5}$$

$$\text{four momentum } p^{\mu} = mu^{\mu} = \left(p^0 - E, \vec{p}\right)\ , \tag{D.6}$$

$$\text{energy momentum relation } p^2 = p^{\mu}p_{\mu} = E^2 - \vec{p}^2 = m^2\ . \tag{D.7}$$

D.2 Two-Particle Elastic Interactions

Elastic collisions are defined by several constraints: The particle number conservation, momentum conservation and mass conservation

$$\sum_j p_j^2 = \sum_j m_j^2 = \text{const} \ , \tag{D.8}$$

$$\sum_j \vec{p}_j = \text{const} \ . \tag{D.9}$$

The case for two particles is discussed in the following. The incoming particles are labeled 1 and 2, the outgoing 3 and 4. We assume that an interaction does not change the mass of the incoming particles

$$m_1 = m_3, \quad m_2 = m_4 \ . \tag{D.10}$$

Therefore energy-momentum conservation states

$$p_1 + p_2 = p_3 + p_4 \ . \tag{D.11}$$

In many kinematic calculations, the Mandelstam variables are very helpful

$$s = (p_1 + p_2)^2 \ , \tag{D.12}$$

$$t = (p_1 - p_3)^2 \ , \tag{D.13}$$

$$u = (p_1 - p_4)^2 \ . \tag{D.14}$$

The Lorentz invariant s variable is very handy as it defines square of the center-of-momentum energy:

$$s = (p_1 + p_2)^2 = (E_1^* + E_2^*)^2 = (E_1 + E_2)^2 - (\vec{p}_1 + \vec{p}_2)^2 \ . \tag{D.15}$$

with the particles energies in the center-of-momentum frame $E_{1,2}^*$. In the center-of-momentum frame where

$$p_1 + p_2 = 0 = p_3 + p_4 \ , \tag{D.16}$$

interactions become trivial in case of elastic scattering

$$E_1^* = E_3^* \ , \quad E_2^* = E_4^* \ . \tag{D.17}$$

We define a relative velocity

$$v_{12} = \left| \frac{\vec{p}_1^*}{E_1^*} - \frac{\vec{p}_2^*}{E_2^*} \right| = \left| \frac{\vec{p}_1^*}{E_1^*} - \frac{-\vec{p}_1^*}{E_2^*} \right| = \frac{|\vec{p}_1^*|}{E_1^* E_2^*} \left(E_1^* + E_2^* \right) \ . \tag{D.18}$$

which is needed fort the important Møller flux factor $v_{12}E_1^*E_2^*$. It is part of the particle flux within the cross section and a frame independent quantity.

D.3 Cross Section

The general differential cross section for two incoming particles and N_f particles in the final state is [11]

$$\mathrm{d}\sigma = \frac{1}{v_{12}}(2\pi)^2\delta^{(4)}\left(\sum_f^{N_f} p_f - p_1 - p_2\right)\,|M_{fi}|^2\,\frac{1}{2E_1}\frac{1}{2E_2}\prod_{j=f}\frac{\mathrm{d}^3p_j}{2E_j(2\pi)^3}\ . \tag{D.19}$$

In case of elastic scattering with two particles in the final state this equation can be simplified by evaluating some parts of the integrals in the center-of-momentum frame

$$\mathrm{d}\sigma^* = \frac{1}{2E_1E_2v_{12}}\,\frac{|\mathbf{p}_1|}{(2\pi)^2 4\sqrt{s}}\,\left|M\left(p_1,p_2\to p_3,p_4\right)\right|^2\mathrm{d}\Omega^*\ . \tag{D.20}$$

Having equals particles in all four states, we can simplify even further

$$\left(\frac{\mathrm{d}\sigma}{\mathrm{d}\Omega}\right)_{\mathrm{com}} = \frac{|M|^2}{64\pi^2E_*^2}\ . \tag{D.21}$$

Equation (D.21) is heavily used in the numerical model DSLAM. Employing a constant, isotropic cross section, (D.21) can be integrated to a total cross section. Using this total cross section, the interaction probability for two particles can be examined. Their outgoing momenta can be sampled isotropically in the center-of-momentum frame after the collision.

D.4 One Particle Decay

An unstable particle can decay into two or more outgoing particles. In our case, we think of the following process

$$\sigma \to \bar{\psi}\psi\ . \tag{D.22}$$

Particle decay can not be interpreted in terms of collision probabilities or geometric aspects, but rather in a differential rate for the decay to happen spontaneously. The decay rate for a unstable particle with momentum p_i and mass $m = \sqrt{s}$ into multiple particles can be derived from (D.19)

$$\mathrm{d}\Gamma = \frac{(2\pi)^4\delta^{(4)}\left(\sum^{N_f} p_f - p_i\right)}{2E_i}\,|M_{fi}|^2\prod_{j=f}\frac{\mathrm{d}^3p_j}{2E_j(2\pi)^3}\mathrm{d}\Omega\ . \tag{D.23}$$

Again, in case of two particles in the final state, we can simplify this to

$$\mathrm{d}\Gamma = \frac{|\mathbf{p}|}{32\pi^2 m^2} |M_{fi}|^2 \, \mathrm{d}\Omega \ . \tag{D.24}$$

Assuming an unporalized decay, the integration over phase space can be done

$$\Gamma = \frac{|\mathbf{p}|}{8\pi^2 m^2} |M_{fi}|^2 \ . \tag{D.25}$$

Equation (D.25) is again very useful for the calculations in the DSLAM model. However, the decay rate calculates the decay probability for a particle at rest. A fast moving particle has a boosted proper time, leading to an increase of it's life time. This boost has to calculated with $\Gamma/\gamma = \Gamma m/E$ or by using the velocity $v = p/E$.

The energy of the final state particles is easily derived from kinematic limits. For a better readability, the mass of the unstable particle is denoted as M and the mass of the final particles m_1 and m_2

$$E_1 = \frac{1}{2M}\left(M^2 + m_1 - m_2\right) \ , \tag{D.26}$$

$$\vec{p}_1^{\,2} = E_1^2 - m_1^2 = \frac{1}{4M^2}\left(M^4 - 2M^2(m_1^2 + m_2^2) + (m_1^2 - m_2^2)^2\right) \ . \tag{D.27}$$

For identical particles $m_1 = m_2$, we can simplify to

$$E_1 = E_2 = \frac{M}{2} \ , \tag{D.28}$$

$$\vec{p}_1^{\,2} = \vec{p}_2^{\,2} = \frac{M^2}{4} - m^2 \ . \tag{D.29}$$

The kinematic limit $2m < M$ has to be respected.

Appendix E

Generation of Correlated Random Fields

> Have i gone mad? I'm afraid so, but let me tell you something, the best people usualy are.
>
> Alice in Wonderland

For all numerical simulations a system must be properly initialized. These initial conditions are given by physical constraints or are motivated mathematically. In case of scalar fields, the initial conditions are not always trivial and can be complex models like temperature dependent Woods-Saxon potentials or in case of thermal nosy fields random distributions. In this section the initialization of scalar fields with Gaussian noise, Brownian noise, fractal noise and a thermal distribution like in the particle-field method are discussed. All distributions have a initial spatial correlation, not a time-like.

A spatial correlation of a scalar, three-dimensional field $\phi(\mathbf{x})$ with noisy excitations can be characterized by its power spectral density in Fourier space

$$S(\mathbf{k}) = |\mathcal{F}[\phi(\mathbf{x})](\mathbf{k})|^2 = \left| \int_{-\infty}^{\infty} \phi(\mathbf{k}) \cdot e^{i\mathbf{x}\cdot\mathbf{k}} \, \mathrm{d}^3\mathbf{x} \right|^2 . \tag{E.1}$$

A wide range of noises are characterized by assuming a power function for the power-spectral density

$$S(\mathbf{k}) \approx S_0 \cdot |\mathbf{k}|^{-\alpha} . \tag{E.2}$$

The so called color of noise is described by the parameter α. For $\alpha = 0$ the noise becomes uncorrelated and is called white or Gaussian noise, with a flat and constant $S(k) = S_0$. For

$\alpha = 2$ the noise is strongly correlated and is called Brownian noise, many physical processes can be described by such a noise distribution. For $\alpha \approx 1$ the distribution is called pink noise. Such distributions can be found in cloud formation, voice modeling or the simulation of planetary landscapes. Noises with negative α are also known but are very rare processes. All random distributions which can be characterized by (E.2) are scale-invariant. They have the same appearance, independent of the system size or the observation scale.

To generate correlated noise, the process of the Fourier analysis can be inverted. By generating a distribution in Fourier-space $\phi(\mathbf{k})$ with the intentional characteristic α and inverting the Fourier transformation, a randomly but correlated field is generated. The modes $\mathbf{k}$ can be shaped with the relation (E.2), while the phases of the modes in Fourier space can be selected randomly.

The output distribution $\phi(\mathbf{x})$ is purely real, therefore the Fourier amplitudes have to be consistent with the symmetry of the frequencies $\phi(\mathbf{k}) = \phi(-\mathbf{k})$.

The following listing shows a possible algorithm in pseudo-code for colored noises:

```
GridSize = 512
alpha = 1.

def shapeSpecturm(k):
    # function which generates a random Fourier modes
    # according to the desired color of noise
    amplitude = power(k, -alpha)
    phase = I * random() * 2. * Pi
    return amplitude * exp(phase)

# generate an empty complex field in Fourier space
fieldFourierSpace = newField((GridSize, GridSize), dtype=complex128)

# This parameter includes the frequency of the fild
# for the given mode in Fourier space
Frequencies = fftfreq(GridSize, d=1./GridSize)

# loop over all fourier modes for spectral shaping
for nx in range(0, GridSize):
    # only the positive frequencies are used here
    # because a real output is assumed
    for ny in range(0, GridSize/2):
            # calculate the Euclidean distance
            k = sqrt( power(Frequencies[nx], 2) + power(Frequencies[ny], 2))
            fieldFFT[nx][ny] = shapeSpecturm(k)
# inverse fourier transformation with the assumption of a real output
realField = realInverseFourier(fieldFFT)
```

Listing 1: Algorithm for generating a random initial condition for a given power spectrum in Fourier space

The function "shapeSpecturm" is the part in which the Fourier-modes are sampled according to their color of noise.

In case of the particle-field method, the thermal equilibrium distribution of the field is not a colored noise. Its field kinetic distribution $\dot{\phi}^2$ is given by the Gaussian

$$\frac{1}{2}\mathcal{F}\left|\dot{\phi}^2(\mathbf{x})\right|(\mathbf{k}) = \frac{k_B T}{2}\exp\left(-\frac{\mathbf{k}^2\sigma^2}{2}\right) , \tag{E.3}$$

In general it problematic to generate a field distribution $\phi(\mathbf{x})$ for a given kinetic energy distribution for $\dot{\phi}^2$ because the square in position space is a non-trivial function convolution in momentum space

$$\mathcal{F}\left|\dot{\phi}^2(\mathbf{x})\right|(\mathbf{k}) = \phi(\mathbf{k}) * \phi(\mathbf{k}) = \int \phi(\mathbf{k}') \cdot \phi(\mathbf{k}' - \mathbf{k})\, \mathrm{d}\mathbf{k}' \tag{E.4}$$

Luckily, the Gaussian shape in (E.3) can be trivially convoluted

$$\sqrt{\frac{\pi}{2}}\left(\exp\left(-\mathbf{k}^2\sigma^2\right) * \exp\left(-\mathbf{k}^2\sigma^2\right)\right) = \exp\left(-\frac{\mathbf{k}^2\sigma^2}{2}\right) \tag{E.5}$$

This result can directly be used to shape the Fourier modes for an initial random distribution with a given temperature and Gaussian width. Note that in difference to the colored noise distribution the Gaussian distribution has a length scale, given by σ.

```
def shapeSpecturmPhysical(k):
    # function which generates the Fourier modes
    # according to the thermal spectrum of the
    # particle-field's equilibrium distrubtion.
    # The amplitudes are given by the temperature
    # and the Gaussian shape of the interactions.
    T = 0.15
    sigma = 0.25  # given by the parameterization
    amplitude = T / 2 * exp(- power(k * sigmaEff, 2) / 2 )
    phase = random() * 2. * PI
    return amplitude * exp(phase)
```

Listing 2: Sampling of Fourier modes for the particle-field method to initialize a thermal and noisy field distribution.

Figure E.1 shows four examples for random initial conditions, both for colored noise and for the thermal initial field configuration in the case of the particle-field method.

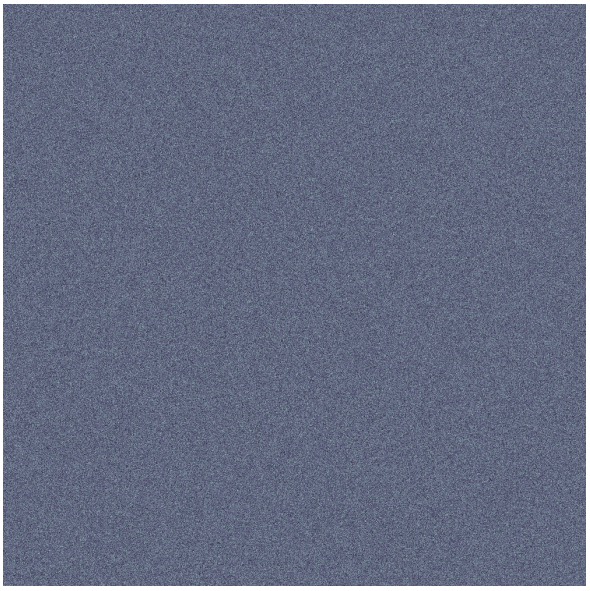

(a) White / Gaussian noise, $\alpha = 0$

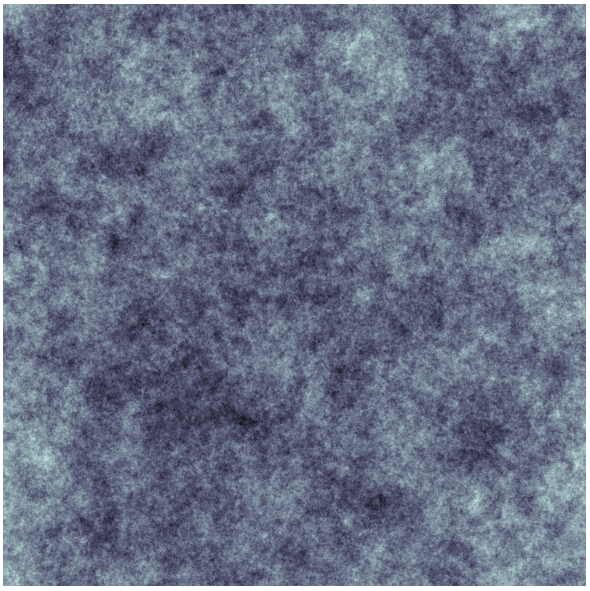

(b) Pink / fractal noise, $\alpha = 1$

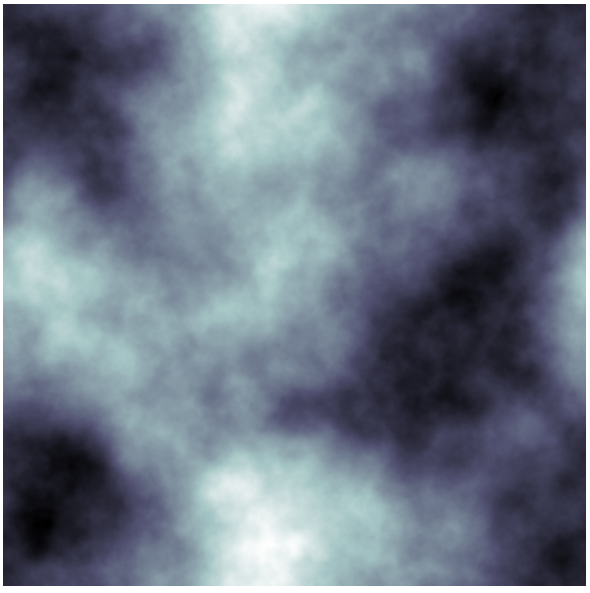

(c) Brownian noise, $\alpha = 2$

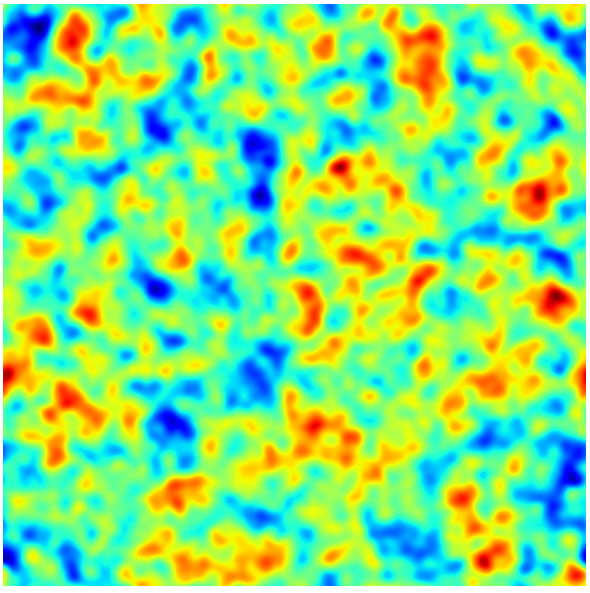

(d) Thermal spectrum given by the particle-field method. The distribution of the kinetic energy is a Gaussian in Fourier space.

Figure E.1: Examples of different noisy initial distributions. All field configurations have been generated by the method described in this section or by the code in Listing 1.

Bibliography

[1] Murray Gell-Mann. A schematic model of baryons and mesons. *Physics Letters*, 8(3): 214–215, 1964.

[2] George Zweig. A SU (3) model for strong interaction symmetry and its breaking. Version 1. Technical report, 1964.

[3] E. Bloom, D. Coward, H. DeStaebler, J. Drees, G. Miller, L. Mo, R. Taylor, M. Breidenbach, J. Friedman, G. Hartmann, and H. Kendall. High-Energy Inelastic e-p Scattering at 6 and 10 degree. *Phys. Rev. Lett.*, 23(16):930–934, Oct 1969. DOI: 10.1103/physrevlett.23.930. URL: http://dx.doi.org/10.1103/PhysRevLett.23.930.

[4] M. Breidenbach, J. I. Friedman, H. W. Kendall, E. D. Bloom, D. H. Coward, H. DeStaebler, J. Drees, L. W. Mo, and R. E. Taylor. Observed Behavior of Highly Inelastic Electron-Proton Scattering. *Phys. Rev. Lett.*, 23:935–939, Oct 1969. DOI: 10.1103/PhysRevLett.23.935. URL: http://link.aps.org/doi/10.1103/PhysRevLett.23.935.

[5] Miklos Gyulassy. Introduction to QCD thermodynamics and the quark-gluon plasma. *Progress in Particle and Nuclear Physics*, 15:403–442, Jan 1985. DOI: 10.1016/0146-6410(85)90076-6. URL: http://dx.doi.org/10.1016/0146-6410(85)90076-6.

[6] P Nason. Introduction to QCD. *CERN European Organisation for Nuclear Research-Reports-CERN*, pages 94–149, 1998.

[7] Ian Aitchison and Anthony Hey. *Gauge Theories in Particle Physics, Volume II*. Taylor & Francis, Dec 2003. DOI: 10.1201/9780849387760. URL: http://dx.doi.org/10.1201/9780849387760.

[8] Arthur Jaffe and Edward Witten. Quantum Yang-Mills Theory. *The millennium prize problems*, pages 129–152, 2006.

[9] Yoichiro Nambu. Quasi-Particles and Gauge Invariance in the Theory of Superconductivity. *Phys. Rev.*, 117:648–663, Feb 1960. DOI: 10.1103/PhysRev.117.648. URL: http://link.aps.org/doi/10.1103/PhysRev.117.648.

[10] J. Goldstone. Field theories with « Superconductor » solutions. *Nuovo Cim*, 19(1):154–164, Jan 1961. DOI: 10.1007/bf02812722. URL: http://dx.doi.org/10.1007/BF02812722.

[11] M.E. Peskin and D.V. Schroeder. *An Introduction to Quantum Field Theory*. Advanced book classics. Addison-Wesley Publishing Company, 1995. ISBN 9780201503975.

[12] Kenneth G. Wilson. Confinement of quarks. *Phys. Rev. D*, 10:2445–2459, Oct 1974. DOI: 10.1103/PhysRevD.10.2445. URL: http://link.aps.org/doi/10.1103/PhysRevD.10.2445.

[13] R. Hagedorn. Hadronic matter near the boiling point. *Il Nuovo Cimento A*, 56(4):1027–1057, Aug 1968. DOI: 10.1007/bf02751614. URL: http://dx.doi.org/10.1007/BF02751614.

[14] N. Cabibbo and G. Parisi. Exponential hadronic spectrum and quark liberation. *Physics Letters B*, 59(1):67 – 69, 1975. DOI: http://dx.doi.org/10.1016/0370-2693(75)90158-6. URL: http://www.sciencedirect.com/science/article/pii/0370269375901586.

[15] A. Chodos, R. L. Jaffe, K. Johnson, C. B. Thorn, and V. F. Weisskopf. New extended model of hadrons. *Phys. Rev. D*, 9:3471–3495, Jun 1974. DOI: 10.1103/PhysRevD.9.3471. URL: http://link.aps.org/doi/10.1103/PhysRevD.9.3471.

[16] T. Matsui and H. Satz. J/ψ suppression by quark-gluon plasma formation. *Physics Letters B*, 178(4):416 – 422, 1986. DOI: http://dx.doi.org/10.1016/0370-2693(86)91404-8. URL: http://www.sciencedirect.com/science/article/pii/0370269386914048.

[17] James D Bjorken. Energy loss of energetic partons in quark-gluon plasma. Technical report, 1982.

[18] Claudia Ratti, Michael A. Thaler, and Wolfram Weise. Phases of QCD: Lattice thermodynamics and a field theoretical model. *Phys. Rev. D*, 73:014019, Jan 2006. DOI: 10.1103/PhysRevD.73.014019. URL: http://link.aps.org/doi/10.1103/PhysRevD.73.014019.

[19] Stefan B. Rüster, Verena Werth, Michael Buballa, Igor A. Shovkovy, and Dirk H. Rischke. Phase diagram of neutral quark matter: Self-consistent treatment of quark masses. *Physical Review D*, 72(3), Aug 2005. DOI: 10.1103/physrevd.72.034004. URL: http://dx.doi.org/10.1103/PhysRevD.72.034004.

[20] D. Teaney, J. Lauret, and E. V. Shuryak. Flow at the SPS and RHIC as a Quark-Gluon Plasma Signature. *Phys. Rev. Lett.*, 86(21):4783–4786, May 2001. DOI: 10.1103/physrevlett.86.4783. URL: http://dx.doi.org/10.1103/PhysRevLett.86.4783.

[21] J. Adams et al. (STAR Collaboration). Experimental and theoretical challenges in the search for the quark–gluon plasma: The STAR Collaboration's critical assessment of the evidence from RHIC collisions. *Nuclear Physics A*, 757(1-2):102–183, Aug 2005. DOI:

10.1016/j.nuclphysa.2005.03.085. URL: http://dx.doi.org/10.1016/j.nuclphysa.2005.03.085.

[22] K. Adcox, et al. (PHENIX Collaboration). Formation of dense partonic matter in relativistic nucleus–nucleus collisions at RHIC: Experimental evaluation by the PHENIX Collaboration. *Nuclear Physics A*, 757(1-2):184–283, Aug 2005. DOI: 10.1016/j.nuclphysa.2005.03.086. URL: http://dx.doi.org/10.1016/j.nuclphysa.2005.03.086.

[23] Peter Braun-Munzinger and Johanna Stachel. The quest for the quark–gluon plasma. *Nature*, 448(7151):302–309, Jul 2007. DOI: 10.1038/nature06080. URL: http://dx.doi.org/10.1038/nature06080.

[24] Z. Fodor and S.D. Katz. A new method to study lattice QCD at finite temperature and chemical potential. *Physics Letters B*, 534(1-4):87–92, May 2002. DOI: 10.1016/s0370-2693(02)01583-6. URL: http://dx.doi.org/10.1016/S0370-2693(02)01583-6.

[25] Y. Aoki, G. Endrődi, Z. Fodor, S. D. Katz, and K. K. Szabó. The order of the quantum chromodynamics transition predicted by the standard model of particle physics. *Nature*, 443(7112):675–678, Oct 2006. DOI: 10.1038/nature05120. URL: http://dx.doi.org/10.1038/nature05120.

[26] Philippe de Forcrand and Owe Philipsen. The chiral critical point of N f = 3 QCD at finite density to the order $(\mu/T)^4$. *J. High Energy Phys.*, 2008(11):012–012, Nov 2008. DOI: 10.1088/1126-6708/2008/11/012. URL: http://dx.doi.org/10.1088/1126-6708/2008/11/012.

[27] Claudia Ratti, Szabolcs Borsányi, Zoltán Fodor, Christian Hoelbling, Sándor D. Katz, Stefan Krieg, and Kálmán K. Szabó. Recent results on QCD thermodynamics: lattice QCD versus Hadron Resonance Gas model. *Nuclear Physics A*, 855(1):253–256, Apr 2011. DOI: 10.1016/j.nuclphysa.2011.02.052. URL: http://dx.doi.org/10.1016/j.nuclphysa.2011.02.052.

[28] A. Bazavov, T. Bhattacharya, M. Cheng, C. DeTar, H.-T. Ding, Steven Gottlieb, R. Gupta, P. Hegde, U. M. Heller, F. Karsch, E. Laermann, L. Levkova, S. Mukherjee, P. Petreczky, C. Schmidt, R. A. Soltz, W. Soeldner, R. Sugar, D. Toussaint, W. Unger, and P. Vranas. Chiral and deconfinement aspects of the QCD transition. *Physical Review D*, 85(5), Mar 2012. DOI: 10.1103/physrevd.85.054503. URL: http://dx.doi.org/10.1103/PhysRevD.85.054503.

[29] M. Stephanov, K. Rajagopal, and E. Shuryak. Event-by-event fluctuations in heavy ion collisions and the QCD critical point. *Physical Review D*, 60(11), Nov 1999. DOI: 10.1103/physrevd.60.114028. URL: http://dx.doi.org/10.1103/PhysRevD.60.114028.

[30] M. Stephanov, K. Rajagopal, and E. Shuryak. Signatures of the Tricritical Point in QCD. *Phys. Rev. Lett.*, 81(22):4816–4819, Nov 1998. DOI: 10.1103/physrevlett.81.4816. URL: http://dx.doi.org/10.1103/PhysRevLett.81.4816.

[31] M. A. Stephanov. Non-Gaussian Fluctuations near the QCD Critical Point. *Phys. Rev. Lett.*, 102(3), Jan 2009. DOI: 10.1103/physrevlett.102.032301. URL: http://dx.doi.org/10.1103/PhysRevLett.102.032301.

[32] Boris Berdnikov and Krishna Rajagopal. Slowing out of equilibrium near the QCD critical point. *Physical Review D*, 61(10), Apr 2000. DOI: 10.1103/physrevd.61.105017. URL: http://dx.doi.org/10.1103/PhysRevD.61.105017.

[33] T. Anticic et al. (NA49 Collaboration). Energy dependence of transverse momentum fluctuations in Pb + Pb collisions at the CERN Super Proton Synchrotron (SPS) at 20 A to 158 A GeV. *Physical Review C*, 79(4), Apr 2009. DOI: 10.1103/physrevc.79.044904. URL: http://dx.doi.org/10.1103/PhysRevC.79.044904.

[34] Katarzyna Grebieszkow. Search for the critical point of strongly interacting matter in NA49. *Nuclear Physics A*, 830(1-4):547c–550c, Nov 2009. DOI: 10.1016/j.nuclphysa.2009.09.044. URL: http://dx.doi.org/10.1016/j.nuclphysa.2009.09.044.

[35] Maja Maćkowiak-Pawłowska and Andrzej Wilczek. Multiplicity fluctuations of identified hadrons in $p+p$ interactions at SPS energies. *J. Phys.: Conf. Ser.*, 509:012044, May 2014. DOI: 10.1088/1742-6596/509/1/012044. URL: http://dx.doi.org/10.1088/1742-6596/509/1/012044.

[36] Grzegorz Stefanek et al. Recent results from the search for the critical point of strongly interacting matter at the CERN SPS. *arXiv preprint arXiv:1411.2396*, 2014.

[37] B. Friman, C. Höhne, J. Knoll, S. Leupold, J. Randrup, and P. Senger R. Rapp. *The CBM Physics Book: Compressed Baryonic Matter in Laboratory Experiments*. Lecture Notes in Physics. Springer, 2011. ISBN 9783642132926.

[38] Peter Senger. The compressed baryonic matter experiment at FAIR. *Central European Journal of Physics*, 10(6):1289–1294, 2012.

[39] Claudia Höhne, CBM collaboration, et al. Physics of compressed baryonic matter. In *Journal of Physics: Conference Series*, volume 420, page 012016. IOP Publishing, 2013.

[40] J. Carlson, J. Kogut, and V. Pandharipande. Quark model for baryons based on quantum chromodynamics. *Physical Review D*, 27(1):233–243, Jan 1983. DOI: 10.1103/physrevd.27.233. URL: http://dx.doi.org/10.1103/PhysRevD.27.233.

[41] Carleton DeTar and Teiji Kunihiro. Linear sigma model with parity doubling. *Physical Review D*, 39(9):2805–2808, May 1989. DOI: 10.1103/physrevd.39.2805. URL: http://dx.doi.org/10.1103/PhysRevD.39.2805.

[42] L. Csernai and I. Mishustin. Fast Hadronization of Supercooled Quark-Gluon Plasma. *Phys. Rev. Lett.*, 74(25):5005–5008, Jun 1995. DOI: 10.1103/physrevlett.74.5005. URL: http://dx.doi.org/10.1103/PhysRevLett.74.5005.

[43] I.N. Mishustin and O. Scavenius. Dynamical generation of the constituent mass in expanding plasma. *Physics Letters B*, 396(1-4):33–38, Mar 1997. DOI: 10.1016/s0370-2693(97)00136-6. URL: http://dx.doi.org/10.1016/S0370-2693(97)00136-6.

[44] P. Rehberg, L. Bot, and J. Aichelin. Expansion and hadronization of a chirally symmetric quark-meson plasma. *Nuclear Physics A*, 653(4):415–435, Jul 1999. DOI: 10.1016/s0375-9474(99)00232-8. URL: http://dx.doi.org/10.1016/S0375-9474(99)00232-8.

[45] Nicholas Petropoulos. Linear sigma model and chiral symmetry at finite temperature. *Journal of Physics G: Nuclear and Particle Physics*, 25(11):2225, 1999.

[46] Jürgen Berges and Krishna Rajagopal. Color superconductivity and chiral symmetry restoration at non-zero baryon density and temperature. *Nuclear Physics B*, 538(1-2):215–232, Jan 1999. DOI: 10.1016/s0550-3213(98)00620-8. URL: http://dx.doi.org/10.1016/S0550-3213(98)00620-8.

[47] Jonathan T. Lenaghan, Dirk H. Rischke, and Jürgen Schaffner-Bielich. Chiral symmetry restoration at nonzero temperature in the $SU(3)_r \times SU(3)_l$ linear sigma model. *Physical Review D*, 62(8), Sep 2000. DOI: 10.1103/physrevd.62.085008. URL: http://dx.doi.org/10.1103/PhysRevD.62.085008.

[48] K. Paech, H. Stöcker, and A. Dumitru. Hydrodynamics near a chiral critical point. *Physical Review C*, 68(4), Oct 2003. DOI: 10.1103/physrevc.68.044907. URL: http://dx.doi.org/10.1103/PhysRevC.68.044907.

[49] Lorenzo Ferroni, Volker Koch, and Marcus B. Pinto. Multiple critical points in effective quark models. *Phys. Rev. C*, 82:055205, Nov 2010. DOI: 10.1103/PhysRevC.82.055205. URL: http://link.aps.org/doi/10.1103/PhysRevC.82.055205.

[50] Marlene Nahrgang, Christoph Herold, Stefan Leupold, Igor Mishustin, and Marcus Bleicher. The impact of dissipation and noise on fluctuations in chiral fluid dynamics. *Journal of Physics G: Nuclear and Particle Physics*, 40(5):055108, Apr 2013. DOI: 10.1088/0954-3899/40/5/055108. URL: http://dx.doi.org/10.1088/0954-3899/40/5/055108.

[51] Marlene Nahrgang, Stefan Leupold, Christoph Herold, and Marcus Bleicher. Nonequilibrium chiral fluid dynamics including dissipation and noise. *Physical Review C*, 84(2), Aug

2011. DOI: 10.1103/physrevc.84.024912. URL: http://dx.doi.org/10.1103/PhysRevC.84.024912.

[52] Marlene Nahrgang, Stefan Leupold, and Marcus Bleicher. Equilibration and relaxation times at the chiral phase transition including reheating. *Physics Letters B*, 711(1):109–116, May 2012. DOI: 10.1016/j.physletb.2012.03.059. URL: http://dx.doi.org/10.1016/j.physletb.2012.03.059.

[53] M. Gell-Mann and M. Lévy. The axial vector current in beta decay. *Il Nuovo Cimento*, 16(4):705–726, 1960. DOI: 10.1007/BF02859738. URL: http://dx.doi.org/10.1007/BF02859738.

[54] Nima Arkani-Hamed, Andrew G Cohen, Emanuel Katz, and Ann E Nelson. The Littlest Higgs. *J. High Energy Phys.*, 2002(07):034–034, Jul 2002. DOI: 10.1088/1126-6708/2002/07/034. URL: http://dx.doi.org/10.1088/1126-6708/2002/07/034.

[55] O. Scavenius, Á. Mócsy, I. N. Mishustin, and D. H. Rischke. Chiral phase transition within effective models with constituent quarks. *Physical Review C*, 64(4), Aug 2001. DOI: 10.1103/physrevc.64.045202. URL: http://dx.doi.org/10.1103/PhysRevC.64.045202.

[56] K Nakamura. Review of Particle Physics. *Journal of Physics G: Nuclear and Particle Physics*, 37(7A):075021, Jul 2010. DOI: 10.1088/0954-3899/37/7a/075021. URL: http://dx.doi.org/10.1088/0954-3899/37/7A/075021.

[57] K.A. Olive. Review of Particle Physics. *Chinese Phys. C*, 38(9):090001, Aug 2014. DOI: 10.1088/1674-1137/38/9/090001. URL: http://dx.doi.org/10.1088/1674-1137/38/9/090001.

[58] Henri Verschelde and Jeroen De Pessemier. Study of the O (N) linear\ sigma model at finite temperature using the 2PPI expansion. *The European Physical Journal C-Particles and Fields*, 22(4):771–779, 2002.

[59] Kenji Fukushima. Chiral effective model with the Polyakov loop. *Physics Letters B*, 591 (3-4):277–284, Jul 2004. DOI: 10.1016/j.physletb.2004.04.027. URL: http://dx.doi.org/10.1016/j.physletb.2004.04.027.

[60] B.-J. Schaefer, J. M. Pawlowski, and J. Wambach. Phase structure of the Polyakov-quark-meson model. *Physical Review D*, 76(7), Oct 2007. DOI: 10.1103/physrevd.76.074023. URL: http://dx.doi.org/10.1103/PhysRevD.76.074023.

[61] Kenji Fukushima. Phase diagrams in the three-flavor Nambu–Jona-Lasinio model with the Polyakov loop. *Physical Review D*, 77(11), Jun 2008. DOI: 10.1103/physrevd.77.114028. URL: http://dx.doi.org/10.1103/PhysRevD.77.114028.

[62] Hong Mao, Jinshuang Jin, and Mei Huang. Phase diagram and thermodynamics of the Polyakov linear sigma model with three quark flavors. *Journal of Physics G: Nuclear and Particle Physics*, 37(3):035001, Jan 2010. DOI: 10.1088/0954-3899/37/3/035001. URL: http://dx.doi.org/10.1088/0954-3899/37/3/035001.

[63] V. Skokov, B. Stokić, B. Friman, and K. Redlich. Meson fluctuations and thermodynamics of the Polyakov-loop-extended quark-meson model. *Physical Review C*, 82(1), Jul 2010. DOI: 10.1103/physrevc.82.015206. URL: http://dx.doi.org/10.1103/PhysRevC.82.015206.

[64] Christoph Herold, Marlene Nahrgang, Igor Mishustin, and Marcus Bleicher. Chiral fluid dynamics with explicit propagation of the Polyakov loop. *Physical Review C*, 87(1), Jan 2013. DOI: 10.1103/physrevc.87.014907. URL: http://dx.doi.org/10.1103/PhysRevC.87.014907.

[65] Rajan Gupta. Introduction to lattice QCD: Course. pages 83–219, 1997.

[66] G.P. Lepage. Lattice QCD for novices. pages 49–90, 1998.

[67] J. Smit. *Introduction to Quantum Fields on a Lattice*. Cambridge Lecture Notes in Physics. Cambridge University Press, 2002. ISBN 9780521890519. URL: https://books.google.de/books?id=KIHHW9NtbuAC.

[68] Carl-G. Källman. Mean-field QCD model for hot/dense matter. *Physics Letters B*, 134(5):363–367, Jan 1984. DOI: 10.1016/0370-2693(84)90017-0. URL: http://dx.doi.org/10.1016/0370-2693(84)90017-0.

[69] F. Green and F. Karsch. Mean field analysis of SU(N) deconfining transitions in the presence of dynamical quarks. *Nuclear Physics B*, 238(2):297–306, 1984. DOI: 10.1016/0550-3213(84)90452-8. URL: http://www.sciencedirect.com/science/article/pii/0550321384904528.

[70] Cheuk-Yin Wong. Dynamics of nuclear fluid. VIII. Time-dependent Hartree-Fock approximation from a classical point of view. *Phys. Rev. C*, 25:1460–1475, Mar 1982. DOI: 10.1103/PhysRevC.25.1460. URL: http://link.aps.org/doi/10.1103/PhysRevC.25.1460.

[71] G. Welke, R. Malfliet, C. Grégoire, M. Prakash, and E. Suraud. Collisional relaxation in simulations of heavy-ion collisions using Boltzmann-type equations. *Physical Review C*, 40(6):2611–2620, Dec 1989. DOI: 10.1103/physrevc.40.2611. URL: http://dx.doi.org/10.1103/PhysRevC.40.2611.

[72] A A Vlasov. THE VIBRATIONAL PROPERTIES OF AN ELECTRON GAS. *Soviet Physics Uspekhi*, 10(6):721, 1968. URL: http://stacks.iop.org/0038-5670/10/i=6/a=R01.

[73] Richard Lowry. Concepts and applications of inferential statistics. 2014.

[74] Chungsik Song and Volker Koch. Chemical relaxation time of pions in hot hadronic matter. *Physical Review C*, 55(6):3026–3037, Jun 1997. DOI: 10.1103/physrevc.55.3026. URL: http://dx.doi.org/10.1103/PhysRevC.55.3026.

[75] Scott Pratt and Kevin Haglin. Hadronic phase space density and chiral symmetry restoration in relativistic heavy ion collisions. *Physical Review C*, 59(6):3304, 1999.

[76] Stanislaw Mrówczyński and Berndt Müller. Reheating after supercooling in the chiral phase transition. *Physics Letters B*, 363(1-2):1–4, Nov 1995. DOI: 10.1016/0370-2693(95)01188-v. URL: http://dx.doi.org/10.1016/0370-2693(95)01188-V.

[77] AD Dolgov and DP Kirilova. On particle creation by a time-dependent scalar field. Technical report, Joint Inst. for Nuclear Research, Dubna (USSR). Lab. of Theoretical Physics, 1989.

[78] Gert Aarts and Jan Smit. Particle production and effective thermalization in inhomogeneous mean field theory. *Physical Review D*, 61(2), Dec 1999. DOI: 10.1103/physrevd.61.025002. URL: http://dx.doi.org/10.1103/PhysRevD.61.025002.

[79] M. Beneke, A. P. Chapovsky, A. Signer, and G. Zanderighi. Effective Theory Approach to Unstable Particle Production. *Phys. Rev. Lett.*, 93:011602, Jul 2004. DOI: 10.1103/PhysRevLett.93.011602. URL: http://link.aps.org/doi/10.1103/PhysRevLett.93.011602.

[80] G. Breit and E. Wigner. Capture of Slow Neutrons. *Phys. Rev.*, 49:519–531, Apr 1936. DOI: 10.1103/PhysRev.49.519. URL: http://link.aps.org/doi/10.1103/PhysRev.49.519.

[81] Arno R. Bohm and Yoshihiro Sato. Relativistic resonances: Their masses, widths, lifetimes, superposition, and causal evolution. *Phys. Rev. D*, 71:085018, Apr 2005. DOI: 10.1103/PhysRevD.71.085018. URL: http://link.aps.org/doi/10.1103/PhysRevD.71.085018.

[82] D. Boyanovsky, H. J. de Vega, R. Holman, and J. Salgado. Nonequilibrium Bose-Einstein condensates, dynamical scaling, and symmetric evolution in the large $\boldsymbol{N}$ Φ^4 theory. *Phys. Rev. D*, 59:125009, May 1999. DOI: 10.1103/PhysRevD.59.125009. URL: http://link.aps.org/doi/10.1103/PhysRevD.59.125009.

[83] Roger Woods and David Saxon. Diffuse Surface Optical Model for Nucleon-Nuclei Scattering. *Physical Review*, 95(2):577–578, Jul 1954. DOI: 10.1103/physrev.95.577. URL: http://dx.doi.org/10.1103/PhysRev.95.577.

[84] Björn Engquist and Andrew Majda. Absorbing boundary conditions for numerical simulation of waves. *Proceedings of the National Academy of Sciences*, 74(5):1765–1766, 1977.

[85] Dan Givoli. High-order local non-reflecting boundary conditions: a review. *Wave Motion*, 39(4):319 – 326, 2004. DOI: http://dx.doi.org/10.1016/j.wavemoti.2003.12.004. URL: http:

//www.sciencedirect.com/science/article/pii/S0165212503001203. New computational methods for wave propagation.

[86] R. M. Feshchenko and A. V. Popov. Exact transparent boundary condition for the three-dimensional Schrödinger equation in a rectangular cuboid computational domain. *Phys. Rev. E*, 88:053308, Nov 2013. DOI: 10.1103/PhysRevE.88.053308. URL: http://link.aps.org/doi/10.1103/PhysRevE.88.053308.

[87] Abdellatif Abada and Michael C. Birse. Coherent amplification of classical pion fields during the cooling of droplets of quark plasma. *Physical Review D*, 55(11):6887–6899, Jun 1997. DOI: 10.1103/physrevd.55.6887. URL: http://dx.doi.org/10.1103/PhysRevD.55.6887.

[88] Abdellatif Abada and Jörg Aichelin. Chiral Phase Transition in an Expanding Quark-Antiquark Plasma. *Phys. Rev. Lett.*, 74(16):3130–3133, Apr 1995. DOI: 10.1103/physrevlett.74.3130. URL: http://dx.doi.org/10.1103/PhysRevLett.74.3130.

[89] Carsten Greiner and Dirk-Hermann Rischke. Shell-like structures in an expanding quark-antiquark plasma. *Phys. Rev. C*, 54:1360–1365, Sep 1996. DOI: 10.1103/PhysRevC.54.1360. URL: http://link.aps.org/doi/10.1103/PhysRevC.54.1360.

[90] Matthew J. Turk, Britton D. Smith, Jeffrey S. Oishi, Stephen Skory, Samuel W. Skillman, Tom Abel, and Michael L. Norman. yt: A multi-code analysis toolkit for astrophysical simulation data. *ApJS*, 192(1):9, Dec 2010. DOI: 10.1088/0067-0049/192/1/9. URL: http://dx.doi.org/10.1088/0067-0049/192/1/9.

[91] D.V. Ahluwalia. Wave-particle duality at the Planck scale: freezing of neutrino oscillations. *Physics Letters A*, 275(1-2):31–35, Oct 2000. DOI: 10.1016/s0375-9601(00)00578-8. URL: http://dx.doi.org/10.1016/S0375-9601(00)00578-8.

[92] Linda E Reichl and Ilya Prigogine. *A modern course in statistical physics*, volume 186. University of Texas press Austin, 1980.

[93] Zhe Xu and Carsten Greiner. Thermalization of gluons in ultrarelativistic heavy ion collisions by including three-body interactions in a parton cascade. *Physical Review C*, 71(6), Jun 2005. DOI: 10.1103/physrevc.71.064901. URL: http://dx.doi.org/10.1103/PhysRevC.71.064901.

[94] Eugene P. Gross and E. Atlee Jackson. Kinetic Models and the Linearized Boltzmann Equation. *Phys. Fluids*, 2(4):432, 1959. DOI: 10.1063/1.1724415. URL: http://dx.doi.org/10.1063/1.1724415.

[95] TH Dupree. A perturbation theory for strong plasma turbulence. *Physics of Fluids (1958-1988)*, 9(9):1773–1782, 1966.

[96] Charles K Birdsall and A Bruce Langdon. *Plasma physics via computer simulation*. CRC Press, 2004.

[97] Jürgen Berges and Jürgen Cox. Thermalization of quantum fields from time-reversal invariant evolution equations. *Physics Letters B*, 517(3-4):369–374, Oct 2001. DOI: 10.1016/s0370-2693(01)01004-8. URL: http://dx.doi.org/10.1016/S0370-2693(01)01004-8.

[98] Fred Cooper, Salman Habib, Yuval Kluger, and Emil Mottola. Nonequilibrium dynamics of symmetry breaking in $\lambda\Phi^4$ theory. *Phys. Rev. D*, 55:6471–6503, May 1997. DOI: 10.1103/PhysRevD.55.6471. URL: http://link.aps.org/doi/10.1103/PhysRevD.55.6471.

[99] Gert Aarts and Jürgen Berges. Nonequilibrium time evolution of the spectral function in quantum field theory. *Physical Review D*, 64(10), Oct 2001. DOI: 10.1103/physrevd.64.105010. URL: http://dx.doi.org/10.1103/PhysRevD.64.105010.

[100] Jürgen Berges, Szabolcs Borsányi, and Julien Serreau. Thermalization of fermionic quantum fields. *Nuclear Physics B*, 660(1-2):51–80, Jun 2003. DOI: 10.1016/s0550-3213(03)00261-x. URL: http://dx.doi.org/10.1016/S0550-3213(03)00261-X.

[101] S. Juchem, W. Cassing, and C. Greiner. Quantum dynamics and thermalization for out-of-equilibrium φ^4 theory. *Phys. Rev. D*, 69:025006, Jan 2004. DOI: 10.1103/PhysRevD.69.025006. URL: http://link.aps.org/doi/10.1103/PhysRevD.69.025006.

[102] Don S. Lemons and Anthony Gythiel. Paul Langevin's 1908 paper "On the Theory of Brownian Motion" ["Sur la théorie du mouvement brownien," C. R. Acad. Sci. (Paris) 146, 530–533 (1908)]. *American Journal of Physics*, 65(11):1079–1081, 1997. DOI: 10.1119/1.18725. URL: http://scitation.aip.org/content/aapt/journal/ajp/65/11/10.1119/1.18725.

[103] Patrick Milan, Matthias Wächter, and Joachim Peinke. Turbulent Character of Wind Energy. *Phys. Rev. Lett.*, 110(13), Mar 2013. DOI: 10.1103/physrevlett.110.138701. URL: http://dx.doi.org/10.1103/PhysRevLett.110.138701.

[104] J-P Bouchaud and Rama Cont. A Langevin approach to stock market fluctuations and crashes. *The European Physical Journal B-Condensed Matter and Complex Systems*, 6(4):543–550, 1998.

[105] A. Bonasera, F. Gulminelli, and J. Molitoris. The Boltzmann equation at the borderline. A decade of Monte Carlo simulations of a quantum kinetic equation. *Physics Reports*, 243(1–2):1–124, 1994. DOI: 10.1016/0370-1573(94)90108-2. URL: http://www.sciencedirect.com/science/article/pii/0370157394901082.

[106] Jørgen Randrup and Bernard Remaud. Fluctuations in one-body dynamics. *Nuclear Physics A*, 514(2):339–366, Jul 1990. DOI: 10.1016/0375-9474(90)90075-w. URL: http://dx.doi.org/10.1016/0375-9474(90)90075-W.

[107] Ph. Chomaz, G.F. Burgio, and J. Randrup. Inclusion of fluctuations in nuclear dynamics. *Physics Letters B*, 254(3–4):340–346, 1991. DOI: 10.1016/0370-2693(91)91166-S. URL: http://www.sciencedirect.com/science/article/pii/037026939191166S.

[108] Carsten Greiner and Stefan Leupold. Stochastic Interpretation of Kadanoff–Baym Equations and Their Relation to Langevin Processes. *Annals of Physics*, 270(2):328–390, 1998. DOI: 10.1006/aphy.1998.5849. URL: http://www.sciencedirect.com/science/article/pii/S0003491698958493.

[109] Carsten Greiner and Berndt Müller. Classical fields near thermal equilibrium. *Phys. Rev. D*, 55:1026–1046, Jan 1997. DOI: 10.1103/PhysRevD.55.1026. URL: http://link.aps.org/doi/10.1103/PhysRevD.55.1026.

[110] Tamás S. Biró and Carsten Greiner. Dissipation and Fluctuation at the Chiral Phase Transition. *Phys. Rev. Lett.*, 79(17):3138–3141, Oct 1997. DOI: 10.1103/physrevlett.79.3138. URL: http://dx.doi.org/10.1103/PhysRevLett.79.3138.

[111] Zhe Xu and Carsten Greiner. Stochastic treatment of disoriented chiral condensates within a Langevin description. *Physical Review D*, 62(3), Jul 2000. DOI: 10.1103/physrevd.62.036012. URL: http://dx.doi.org/10.1103/PhysRevD.62.036012.

[112] Dirk H. Rischke. Forming disoriented chiral condensates through fluctuations. *Phys. Rev. C*, 58:2331–2357, Oct 1998. DOI: 10.1103/PhysRevC.58.2331. URL: http://link.aps.org/doi/10.1103/PhysRevC.58.2331.

[113] D. Boyanovsky, H. J. de Vega, R. Holman, D.-S. Lee, and A. Singh. Dissipation via particle production in scalar field theories. *Phys. Rev. D*, 51:4419–4444, Apr 1995. DOI: 10.1103/PhysRevD.51.4419. URL: http://link.aps.org/doi/10.1103/PhysRevD.51.4419.

[114] Julian Schmidt, Alex Meistrenko, Hendrik van Hees, Zhe Xu, and Carsten Greiner. Simulation of stationary Gaussian noise with regard to the Langevin equation with memory effect. *Physical Review E*, 91(3), Mar 2015. DOI: 10.1103/physreve.91.032125. URL: http://dx.doi.org/10.1103/PhysRevE.91.032125.

[115] Li. Numerical studies of the Klein-Gordon-Schrödinger equations. Master's thesis, Sichuan University, 2006.

[116] Gerald Beresford Whitham. *Linear and nonlinear waves*, volume 42. John Wiley & Sons, 2011.

[117] Lev Kofman, Andrei Linde, and Alexei A. Starobinsky. Reheating after Inflation. *Phys. Rev. Lett.*, 73:3195–3198, Dec 1994. DOI: 10.1103/PhysRevLett.73.3195. URL: http://link.aps.org/doi/10.1103/PhysRevLett.73.3195.

[118] Ioannis Bouras. *Investigation of relativistic shock waves and Mach cones in a partonic cascade*. PhD thesis, 2013. URL: http://d-nb.info/1046974955/04. Frankfurt (Main), Univ., Diss., 2013.

[119] I. Senitzky. Dissipation in Quantum Mechanics. The Harmonic Oscillator. *Physical Review*, 119(2):670–679, Jul 1960. DOI: 10.1103/physrev.119.670. URL: http://dx.doi.org/10.1103/PhysRev.119.670.

[120] R.P Feynman and F.L Vernon. The theory of a general quantum system interacting with a linear dissipative system. *Annals of Physics*, 24:118–173, Oct 1963. DOI: 10.1016/0003-4916(63)90068-x. URL: http://dx.doi.org/10.1016/0003-4916(63)90068-X.

[121] Hermann Grabert, Ulrich Weiss, and Peter Talkner. Quantum theory of the damped harmonic oscillator. *Zeitschrift für Physik B Condensed Matter*, 55(1):87–94, Mar 1984. DOI: 10.1007/bf01307505. URL: http://dx.doi.org/10.1007/BF01307505.

[122] Peter Riseborough, Peter Hanggi, and Ulrich Weiss. Exact results for a damped quantum-mechanical harmonic oscillator. *Physical Review A*, 31(1):471–478, Jan 1985. DOI: 10.1103/physreva.31.471. URL: http://dx.doi.org/10.1103/PhysRevA.31.471.

[123] William Coffey, Yu P Kalmykov, and John T Waldron. *The Langevin equation: with applications to stochastic problems in physics, chemistry, and electrical engineering*, volume 14. World Scientific, 2004.

[124] M. Toda, R. Kubo, N. Saito, and N. Hashitsume. *Statistical Physics II: Nonequilibrium Statistical Mechanics*. Series C, English Authors. Springer Berlin Heidelberg, 1991. ISBN 9783540538332.

[125] A. Einstein. Über die von der molekularkinetischen Theorie der Wärme geforderte Bewegung von in ruhenden Flüssigkeiten suspendierten Teilchen. *Annalen der Physik*, 322(8):549–560, 1905. DOI: 10.1002/andp.19053220806. URL: http://dx.doi.org/10.1002/andp.19053220806.

[126] T. Lindstrom. Fractional Brownian Fields as Integrals of White Noise. *Bulletin of the London Mathematical Society*, 25(1):83–88, Jan 1993. DOI: 10.1112/blms/25.1.83. URL: http://dx.doi.org/10.1112/blms/25.1.83.

[127] Norbert Wiener. Generalized harmonic analysis. *Acta Mathematica*, 55(1):117–258, 1930. DOI: 10.1007/BF02546511. URL: http://dx.doi.org/10.1007/BF02546511.

[128] L.P. Pitaevskii and E.M. Lifshitz. *Physical Kinetics*. Number Bd. 10. Elsevier Science, 2012. ISBN 9780080570495. URL: https://books.google.de/books?id=DTHxPDfV0fQC.

[129] L.D. Landau and E.M. Lifshitz. *Course of Theoretical Physics*. Elsevier Science, 1980. ISBN 9781483103372.

[130] Thomas Huckle and Stefan Schneider. *Numerische Methoden*. Examen-Press. Springer London, Limited, 2006. ISBN 9783540303183.

[131] Wolfgang Dahmen and Arnold Reusken. *Numerik Für Ingenieure und Naturwissenschaftler*. Springer-Lehrbuch. Springer London, Limited, 2008. ISBN 9783540764939.

[132] K. Jarrod Millman and Michael Aivazis. Python for Scientists and Engineers. *Computing in Science & Engineering*, 13(2):9–12, 2011. DOI: 10.1109/MCSE.2011.36. URL: http://scitation.aip.org/content/aip/journal/cise/13/2/10.1109/MCSE.2011.36.

[133] Travis E. Oliphant. Python for Scientific Computing. *Computing in Science & Engineering*, 9(3):10–20, 2007. DOI: 10.1109/MCSE.2007.58. URL: http://scitation.aip.org/content/aip/journal/cise/9/3/10.1109/MCSE.2007.58.

[134] Stefan van der Walt, S Chris Colbert, and Gaël Varoquaux. The NumPy Array: A Structure for Efficient Numerical Computation. *Computing in Science & Engineering*, 13(2):22–30, Mar 2011. DOI: 10.1109/mcse.2011.37. URL: http://dx.doi.org/10.1109/MCSE.2011.37.

[135] Eric Jones, Travis Oliphant, Pearu Peterson, et al. SciPy: Open source scientific tools for Python, 2001–. URL: http://www.scipy.org/. [Online; accessed 2014-09-24].

[136] Stefan Behnel, Robert Bradshaw, Craig Citro, Lisandro Dalcin, Dag Sverre Seljebotn, and Kurt Smith. Cython: The Best of Both Worlds. *Computing in Science & Engineering*, 13 (2):31–39, Mar 2011. DOI: 10.1109/mcse.2010.118. URL: http://dx.doi.org/10.1109/MCSE.2010.118.

[137] M. Frigo and S.G. Johnson. FFTW: an adaptive software architecture for the FFT. In *Acoustics, Speech and Signal Processing, 1998. Proceedings of the 1998 IEEE International Conference on*, volume 3, pages 1381–1384 vol.3, May 1998. DOI: 10.1109/ICASSP.1998.681704.

[138] M. Galassi and B. Gough. *GNU Scientific Library: Reference Manual*. GNU manual. Network Theory, 2009. ISBN 9780954612078. URL: http://www.gnu.org/software/gsl/.

[139] Jorge J More, Burton S Garbow, and Kenneth E Hillstrom. User guide for MINPACK-1. Technical report, CM-P00068642, 1980.

[140] Makoto Matsumoto and Takuji Nishimura. Mersenne twister: a 623-dimensionally equidistributed uniform pseudo-random number generator. *ACM Transactions on Modeling and Computer Simulation (TOMACS)*, 8(1):3–30, 1998.

[141] Mutsuo Saito and Makoto Matsumoto. SIMD-oriented fast Mersenne Twister: a 128-bit pseudorandom number generator. In *Monte Carlo and Quasi-Monte Carlo Methods 2006*, pages 607–622. Springer, 2008.

[142] François Panneton, Pierre L'ecuyer, and Makoto Matsumoto. Improved long-period generators based on linear recurrences modulo 2. *ACM Trans. Math. Softw.*, 32(1):1–16, Mar 2006. DOI: 10.1145/1132973.1132974. URL: http://dx.doi.org/10.1145/1132973.1132974.

[143] John D. Hunter. Matplotlib: A 2D Graphics Environment. *Computing in Science & Engineering*, 9(3):90–95, 2007. DOI: 10.1109/MCSE.2007.55. URL: http://scitation.aip.org/content/aip/journal/cise/9/3/10.1109/MCSE.2007.55.

[144] Thomas Williams, Colin Kelley, and many others. Gnuplot 4.4: an interactive plotting program. http://gnuplot.sourceforge.net/, March 2010.

[145] Zhe Xu and Carsten Greiner. Elliptic flow of gluon matter in ultrarelativistic heavy-ion collisions. *Physical Review C*, 79(1), Jan 2009. DOI: 10.1103/physrevc.79.014904. URL: http://dx.doi.org/10.1103/PhysRevC.79.014904.

[146] John Charles Butcher. *The numerical analysis of ordinary differential equations: Runge-Kutta and general linear methods*. Wiley-Interscience, 1987.

[147] Uri M. Ascher, Steven J. Ruuth, and Raymond J. Spiteri. Implicit-explicit Runge-Kutta methods for time-dependent partial differential equations. *Applied Numerical Mathematics*, 25(2-3):151–167, Nov 1997. DOI: 10.1016/s0168-9274(97)00056-1. URL: http://dx.doi.org/10.1016/S0168-9274(97)00056-1.

[148] Salvador Jiménez and Luis Vázquez. Analysis of Four Numerical Schemes for a Nonlinear Klein-Gordon Equation. *Applied Mathematics and Computation*, 35(1):61–94, Jan 1990. DOI: 10.1016/0096-3003(90)90091-g. URL: http://dx.doi.org/10.1016/0096-3003(90)90091-G.

[149] Zhang Fei and Luis Vázquez. Two energy conserving numerical schemes for the Sine-Gordon equation. *Applied Mathematics and Computation*, 45(1):17–30, Sep 1991. DOI: 10.1016/0096-3003(91)90087-4. URL: http://dx.doi.org/10.1016/0096-3003(91)90087-4.

[150] Bengt Fornberg. On the instability of leap-frog and Crank-Nicolson approximations of a nonlinear partial differential equation. *Mathematics of Computation*, 27(121):45–57, 1973.

[151] Fred Cooper and Graham Frye. Single-particle distribution in the hydrodynamic and statistical thermodynamic models of multiparticle production. *Physical Review D*, 10(1):186–189, Jul 1974. DOI: 10.1103/physrevd.10.186. URL: http://dx.doi.org/10.1103/PhysRevD.10.186.

[152] Felix Reining. Untersuchung von Scherfluss und -viskosität in einer partonsichen Kaskade. Diplomarbeit, Institut für theoretische Physik - Goethe Universität Frankfurt am Main, 2009.

[153] Andrei Kolmogoroff. Über die analytischen Methoden in der Wahrscheinlichkeitsrechnung. *Mathematische Annalen*, 104(1):415–458, 1931.

[154] Robert C. Merton. Theory of Rational Option Pricing. *The Bell Journal of Economics and Management Science*, 4(1):141, 1973. DOI: 10.2307/3003143. URL: http://dx.doi.org/10.2307/3003143.

[155] Hiroshima University Mutsuo Saito, Makoto Matsumoto. double precision SIMD oriented Fast Mersenne Twister(dSFMT), 2013. URL: http://www.math.sci.hiroshima-u.ac.jp/~%20m-mat/MT/SFMT/index.html.

[156] John Von Neumann. Various techniques used in connection with random digits. *Applied Math Series*, 12(36-38):1, 1951.

[157] Siddhartha Chib and Edward Greenberg. Understanding the metropolis-hastings algorithm. *The american statistician*, 49(4):327–335, 1995.

[158] Nicholas Metropolis, Arianna W Rosenbluth, Marshall N Rosenbluth, Augusta H Teller, and Edward Teller. Equation of state calculations by fast computing machines. *The journal of chemical physics*, 21(6):1087–1092, 1953.

[159] G. E. P. Box and Mervin E. Muller. A Note on the Generation of Random Normal Deviates. *The Annals of Mathematical Statistics*, 29(2):610–611, 06 1958. DOI: 10.1214/aoms/1177706645. URL: http://dx.doi.org/10.1214/aoms/1177706645.

[160] G. Marsaglia and T. A. Bray. A Convenient Method for Generating Normal Variables. *SIAM Review*, 6(3):pp. 260–264, 1964. URL: http://www.jstor.org/stable/2027592.

[161] R. Hagedorn. *Relativistic kinematics: a guide to the kinematic problems of high-energy physics*. Mathematics Lecture Note Series. W. A. Benjamin, 1973.

[162] V. Chiochia C. Anastasiou L. Baudis. Lecture Notes: Particle Physics Phenomenology 1. November 2012. URL: http://www.itp.phys.ethz.ch/education/hs10/ppp1/.

Danke!

Die Verleihung des akademischen Doktorgrades soll die Fähigkeit zum selbstständigen, wissenschaftlichen Arbeiten attestieren. So schön das klingt, so wenig lässt sich eine Promotion als einzelne Person bewälltigen. Es braucht vielfältige Unterstützung, Betreuung und Beratung.

Großen Dank geht daher zuerst an meinen Betreuer Prof. Dr. Carsten Greiner. Vielen Dank für die Aufnahme in deine Arbeitsgruppe, die Unterstützung, die wunderbare Zeit, die vielen tollen Konferenzen und natürlich danke für die fachliche, thematische und finanzielle Ermöglichung dieser Arbeit. Ich weiß zu schätzen, dass viele Dinge während meiner Uni-Zeit nicht selbstverständlich waren und wir bei dir gute Physik machen konnten.

Besonderen Dank geht auch an Dr. Hendrik van Hees für die vielen fruchtbaren Diskussionen, Hilfestellungen, und Tipps. Nicht unwichtig für das Entstehen dieser Arbeit waren auch die vielen Tassen Kaffee aus deiner Maschine!

Danke auch an meine Arbeitsgruppe, mit denen ich viele schöne Jahre verbringen konnte, ihr seid wirklich eine tolle Truppe und ich werde euch vermissen. Oliver, Ioannis, Jan, Andrej, Kai, Hendrik, Florian, Max, Gerhard, Moritz, Alex, Frank, Felix, Julian, Philipp und natürlich auch Denise!

Für das mühevolle und geduldige korrigieren meiner Arbeit möchte Hendrik, Katharina und Max danken. Ich weiß, das meine Texte manchmal nicht einfach sind.

Prof. Dr. Jürgen Schaffner-Bielich möchte ich ganz herzlich für die Begutachtung meiner Arbeit danken!

Danke an Petra, dass du so viel Geduld während meiner Promotion mit mir und den damit verbundenen Launen hattest.

Sehr gefreut hat mich auch, dass ich meine Hündin mit ins Institut nehmen konnte und sich alle so lieb um sie gekümmert, mit ihr gespielt und das arme dünne Tier versorgt haben. Besonders danken möchte ich hier Daniela und Hendrik, ihr habt nicht nur Naddi glücklich gemacht.

Danke an Prof. Dr. Henner Büsching für die tollen und wirklich guten Lecture Weeks. Ich muss nicht erwähnen, dass die Abende mit einem guten Wein das Beste daran waren!

Sehr dankbar bin ich auch für die finanzielle und inhaltliche Unterstützung durch die Helmholtz Research School for Quark Matter studies (H-QM), die Helmholtz Graduate School for Hadron and Ion Research (HGS-HIRe), das Helmholtz International Center for FAIR (HIC4FAIR), das Land Hessen, der Goethe-Universität Frankfurt und das Bundesministerium für Bildung und Forschung (BMBF). Numerische Berechnungen wurden im Rechenzentrum des Center for Scientific Computing (CSC) an der Goethe-Universität Frankfurt durchgeführt.

Zuletzt möchte ich noch ganz besonders meinen Eltern und Großeltern danken! Ohne euch hätte ich diesen Weg niemals gehen und bewältigen können. Vielen Dank für die langwierige und uneingeschränkte Unterstützung. Ich weiß das sehr zu schätzen und habe euch sehr lieb!

Deutsche Zusammenfassung

E.1 Einleitung

Das Gebiet der modernen Kernphysik beschäftigt sich mit dem Aufbau, der Struktur und Dynamik von Kernmaterie. Der Begriff Kernmaterie beinhaltet nicht nur die bekannten Teilchen wie Protonen und Neutronen, aus der sich die um uns herum stabile Materie zusammensetzt, sondern auch exotische Materie und Elementarteilchen, die sich nur in Forschungseinrichtungen bei großen Energien erzeugen lässt. Eine typische Frage- und Aufgabenstellung ist die Untersuchung der Eigenschaften sowohl dieser einzelnen Teilchen als auch deren Wechselwirkungen im Kollektiv und in gebundenen Zuständen. Die Werkzeuge in der Kernphysik können in experimentelle und theoretische Methoden unterschieden werden, beide liefern mit völlig unterschiedlichen Ansätzen und Ideen Antworten und Daten zu denselben physikalischen Fragen und Phänomenen. Experimentell sind Beschleuniger-Experimente sehr erfolgreich um in das Innere der Materie zu "blicken". Forschungsbeschleuniger wie der Large Hadron Collider LHC am CERN in Genf oder der Relativistic Heavy Ion Collider RHIC in Brookhaven beschleunigen Schwerionen, wie einzelne Blei- oder Gold-Ionen, auf nahezu Lichtgeschwindigkeit und bringen diese anschließend zur Kollision. Bei steigenden Geschwindigkeit steigt die Energie, die bei einem Zusammenstoß zweier Kerne frei wird. Die geringe Größe dieser Systeme führt zu einer extrem hohen Energiedichte. Aktuelle Beschleuniger erzeugen damit eine effektive Temperatur der Kernmaterie von über einer Billionen Grad Celsius und stellen Bedingungen wie kurz nach dem kosmischen Urknall da. Bei solchen Temperaturen und Energien wird die Energie durch Erzeugung neuer Elementarteilchen mit unterschiedlichen Massen und Impulsen umgesetzt. Je höher die Energiedichte, umso mehr und schwerere Teilchen können erzeugt werden. Die dabei entstehenden Elementarteilchen, gebundene Zustände oder Resonanzen können allerdings selten direkt beobachtet werden, da sie instabil und damit kurzlebig sind. Sie zerfallen in einer Kaskade von weiteren Teilchen, pro Kollision können so über tausend weitere Elementarteilchen entstehen. Komplexe Detektoren beobachten die Spuren dieser Übergänge, aufwendige Analysen in Rechencluster erlauben einen Rückschluss auf den genauen Hergang einer solchen Kollision und Zerfallskaskade. Untersucht man systematisch viele dieser Kollisionen mit statistischen Mitteln, lassen sich Aussagen über die entstandenen Teilchen und deren Wechselwirkungen untereinander ableiten.

Solche Untersuchungen lassen sich allerdings nicht rein aus dem Experiment heraus gestalten, da für die Auswertung der rohen Detektordaten immer ein gewisses theoretisches Verständnis zur Ableitung mathematischer Beschreibungen benötigt wird. Der theoretische Ansatz zur Untersuchung von Kernmaterie ist die Formulierung einer Theorie zur Beschreibung aller Elementarteilchen. Diese einheitliche Theorie wird das Standard Modell der Kernphysik genannt und beschreibt die Bausteine der Materie und die Wechselwirkungsteilchen der elementaren Naturkräften. Insgesamt kennen wir vier Elementarkräfte: die Gravitation, die elektromagnetische Kraft, die schwache Kernkraft und die starke Kernkraft. Das Standardmodell fasst die drei letzten Kräfte in einer Theorie zusammen, wobei jede Kraft von einer eigenen Untertheorie beschrieben wird.

Diese Arbeit ist von theoretischer Natur und befasst sich mit der starken Kernkraft, die dazugehörige Theorie wird Quanten Chromodynamik (QCD) genannt. Die starke Kernkraft ist unter anderem verantwortlich für die Stabilität von Atomkernen. Atomkerne bestehen aus Protonen und Neutronen, diese wiederum bestehen aus weiteren Elementarteilchen, den Quarks. Sie existieren in sechs verschiedenen Familien mit den Namen up, down, strange, charm, beauty und top. Quarks existieren niemals als frei Teilchen, sie können nur in neutralen, gebundenen Objekten vorkommen. Der verantwortliche Mechanismus wird Farbeinschluss (Color-Confinement) genannt. Mathematisch hat jedes Quark einen von drei möglichen Zuständen, der in der QCD Farbe genannt wird (rot, grün, blau). Alle gebundenen Objekte müssen Farbneutral sein, also aus allen drei Farben (wie bei beispielsweise Protonen) oder aus einer Farbe und deren Antifarbe bestehen. Gebunden werden solche Objekte von den Trägern der starken Kraft, den Gluonen. Diese Austauschteilchen ändern die Farbzustände zwischen den Quarks und sorgen somit für eine effektive Anziehung der Teilchen. Die Wechselwirkung lässt sich in einer Lagrange-Gleichung innerhalb der Quantenfeldtheorie formulieren, ist mathematisch aber so komplex, dass diese Gleichung seit 40 Jahren der aktiven Forschung unterliegt und bis heute große Rätsel aufwirft.

Eines dieser Rätsel ist die Masse von gebundener Kernmaterie. Die Masse eines Protons ist seit langem bekannt und sehr genau vermessen. Mit Teilchenbeschleuniger lies sich nachweisen, dass Protonen selbst aus drei gebundenen Quarks bestehen. Erstaunlicherweise weicht die Masse der einzelnen Quarks stark von der zu erwartenden Masse an und beträgt lediglich 1.5% der Masse des Protons, obwohl genau diese drei Quarks das Proton definieren. Theoretisch sollten sogar alle Elementarteilchen masselos sein, die Grundmasse der Quarks wird durch den Higgs-Mechanismus erklärt, die restlichen 98,5% entstehen in einem dynamischen Prozess zwischen Quarks und Gluonen.

Erklärt werden kann dieses Verhalten mit dem Mechanismus der spontanen Brechung der chiralen Symmetrie. Diese Symmetrie ist eine fundamentale Eigenschaft der QCD und beschreibt die mathematische Relation von links- und rechtshändigen Wellenfunktionen von Teilchen und Anti-Teilchen. Bei bestehender Symmetrie können beide Arten von Wellenfunktionen mathematisch separat beschrieben werden, eine Mischung der Arten ist nicht möglich und damit auch keine Bindung untereinander. In der QCD besteht diese Symmetrie allerdings nicht vollständig. Sie

ist bereits schwach, aber explizit, durch den Higgs-Mechanismus gebrochen, zusätzlich kann sie spontan brechen. Eine spontane Brechung liegt vor, wenn die mathematischen Gleichungen die Symmetrie vorweisen, das gesamte System aber in einen asymmetrischen Zustand fällt und dadurch die Symmetrie gebrochen wird. Dies kann geschehen, wenn der asymmetrische Zustand energetisch günstiger ist. Genau dies geschieht in der QCD. Bei hohen Temperaturen ist die chirale Symmetrie gegeben, ab einer kritischen Temperatur durchläuft Kernmaterie einen Phasenübergang von der restaurierten zur gebrochenen Symmetrie, dabei erhält die Materie ihre bekannte Masse. Ein zweiter Aspekt ist bei hohen Temperaturen interessant, da neben dem chiralen Phasenübergang auch ein Übergang bei dem sogenannten Farbeinschluss stattfindet. Die sonst gebundenen Quarks und Gluonen können bei sehr hohen Temperaturen aufbrechen und sich in einem Plasma aus Farbladungen quasi-frei bewegen. Dieser Zustand wird Quark-Gluon-Plasma (QGP) genannt und kann als eigener Aggregatzustand von Materie aufgefasst werden. Die Untersuchung dieses Zustandes ist Gegenstand aktueller Forschung.

E.2 Untersuchung des dynamischen linearen-σ-Modells

Diese Arbeit untersucht das Phänomen dieses chiralen Symmetriebruch. Ziel war es den Übergang zwischen den beiden Symmetriephasen dynamisch nachzustellen und dabei dessen Eigenschaften zu untersuchen. Der Übergang zwischen den beiden Phasen lässt sich mit klassischen thermodynamischen Mitteln und Theorien zu Phasenübergängen beschreiben. Eine Kernfrage ist dabei, mit welcher Ordnung sich der Übergang beschreiben lässt. Ein Übergang erster Ordnung ähnelt dabei den Eigenschaften des Übergangs von Wasser zur Gasphase. Beide Phasen können dabei nebeneinander in lokalen Blasen existieren, der Übergang selbst findet bei einer genau definierbaren Temperatur statt. Bei einem Übergang zweiter Ordnung gibt es keine Phasenkoexistenz, stattdessen zeigt das System skaleninvarianz, Fluktuationen und Korrelationenlängen zeigen divergentes Verhalten am Phasenübergang. Auch möglich ist die Existenz eines kritischen Punktes im Phasendiagramm, an dem die erste Ordnung Phasenübergangslinie enden und in einen Übergang zweiter Ordnung übergeht. Die Untersuchung der Ordnung eines Phasenübergangs ist insofern interessant, dass sich durch diese makroskopischen Beschreibungen mikroskopische Eigenschaften der Materie und des Quark-Gluonen Plasmas ableiten lassen.

Eine Behandlung der vollen QCD Theorie ist in diesem Kontext leider nicht möglich, da sie sich aus mathematischen Gründen nicht lösen lässt. Umgangen wurde dieses Problem, indem nicht die QCD, sondern eine verwandte, effektiven Theorie untersucht wurde. Eine effektive Theorie stellt einige grundlegenden Eigenschaften wie die chirale Symmetrie nach und reduziert dabei die Komplexität durch mehrere Vereinfachungen. Ein solches Modell ist das lineare σ-Modell, das lediglich zwei gleichartige Quark-arten und keine Gluonen oder Farbladungen beinhaltet. Die chirale Symmetrie wird durch ein skalares Feld, das sowohl als Ordnungsparameter des Phasenübergangs als auch Masse erzeugendes Wechselwirkungsfeld dient. Dieses Modell wurde

vereinfacht und numerisch in einer eigenen Transport-Simulation realisiert. Alle Quantenfelder wurden dabei als klassische Felder, Quarks als klassische Teilchen beschrieben. Das Ergebnis ist das 3+1 dimensionale DSLAM Modell. Die Felder werden durch partielle Differentialgleichungen propagiert, Teilchen können elastisch miteinander stoßen und wechselwirken außerdem über langwellige und ortsabhängige Potentiale mit den Feldern.

In ersten Rechnungen wurden die thermodynamischen Eigenschaften des Modells mit denen des linearen σ-Modell verglichen und Tests auf numerische Stabilität durchgeführt. Um das Verhalten am chiralen Phasenübergang zu untersuchen, wurden verschiedene Rechnungen mit Temperaturänderung oder -Sprüngen durchgeführt. Das Medium in der heißen, chiral restaurierten Phase wurde schlagartig abgekühlt, was das chirale σ-Feld in die chiral gebrochene Phase überführen sollte. Hierbei zeigten sich zwei unerwartete Phänomene. Eine reine Temperaturänderung der Quarks ohne Änderung der Teilchenzahl treibt das chirale Feld noch mehr in die Richtung der chiral restaurierten Phase, was genau gegenteilig dem erwarteten Verhalten ist. Bei Rechnungen mit einem Temperatursprung, in dem sich auch die Quarkdichte änderte, wurde das σ-Feld in Richtung chiral gebrochener Phase getrieben. Allerdings wurde das Gesamtsystem in eine kohärente Schwingung versetzt, in der chirale Feld stark gegen die chirale Dichte der Quarks schwingt. Diese globale Schwingung des Systems kann nicht mit den implementierten Gleichungen des mittleren Feld des Modells gedämpft werden.

Beide Beobachtungen lassen sich durch das fehlen chemischer Prozesse erklären. Ein solcher Prozess wäre der Zerfall eines skalaren σ-Teilchens in ein Quark- und Antiquark Paar $\sigma \to \bar{\psi}\psi$, das Gleiche gilt für den inversen Prozess der Quark Annihilation $\bar{\psi}\psi \to \sigma$. Diese Prozesse verändern die Teilchendichte und damit die Anzahl der Quarks im System, außerdem können sie Energie von den Quarks zu den σ-Teilchen transferieren und umgedreht.

Weitere Untersuchungen in dieser Arbeit haben gezeigt, welche quantitativen Auswirkungen die thermische und chemische Verteilung auf die Gleichgewichts Eigenschaften des Gesamtsystems haben. Abweichungen dieser beiden Komponenten von den Gleichgewichtsverteilungen können sowohl die Temperatur der Phasenübergangs als auch dessen Ordnung ändern. Solche Nichtgleichgewichts-Abweichungen sind typischerweise zu erwarten, wenn das Quark-Gluon Plasma schnell expandiert und dabei thermische und chemische Prozesse unterschiedlich schnell ablaufen. Außerdem ist noch nicht völlig klar, wie schnell das Quark-Gluon Plasma thermalisiert, nachdem es durch eine Schwerionen Kollision erzeugt worden ist. Der Materiezustand kurz nach einer solchen Kollision wird als hochgradig nicht-thermisch angenommen.

Um das Problem chemischer und thermischer zu Untersuchen, wurde die erste Version des DSLAM Modells mit Quarkpaar Erzeugung- und Vernichtungsprozessen erweitert. Je ein Quark und Antiquark können ein skalares σ erzeugen, und umgedreht. Mit dem erweiterten Modell wurden die Rechnungen mit variabler Temperatur erneut durchgeführt. Hierbei zeigte sich eine effektive Equilibrierung des Systems, außerdem konnte die dynamische Entstehung von Fluktuationen

beobachtet werden. Diese bauen sich rein durch die mikroskopischen Wechselwirkungen zwischen den Quarkteilchen und dem skalaren σ-Feld auf.

Das letzte betrachtete System stellt ein einfaches Modell für das Quark-Gluonen Plasma kurz nach einer Schwerionenkollision da. Heiße Quarkmaterie befindet sich ein einer kugelähnlichen Verteilung und kann frei in den Raum expandieren. Untersucht wird dabei die zeitliche und räumliche Entwicklung der Teilchen- und Feldverteilung, sowie dessen Endzustände. Dabei werden auch Rechnungen mit und ohne chemische Wechselwirkungen zwischen Feld und Teilchen verglichen. Es zeigt sich, dass sich in allen Szenarien starke Nichtgleichgewichtsverteilungen einstellen und sich der chirale Ordnungsparameter nicht verhält wie in thermischen Rechnungen. Der Grund liegt in der raschen Expansion, in der das System keine Zeit hat sich adiabatisch der Temperatur und Volumenänderung anzupassen. Ein Unterschied zwischen den verschiedenen Ordnungen des Phasenübergangs lassen sich kaum feststellen. Wiederholt man die Rechnungen allerdings mit chemischen Prozessen, lässt sich ein starker qualitativer Unterschied im Vergleich zu den Rechnungen ohne chemische Prozesse feststellen. Durch diese Prozesse stellen sich viel stärkere räumliche und zeitliche Fluktuationen in den Verteilungen ein. Die Stärke der Fluktuationen steigt mit stärke der Wechselwirkungen zwischen Teilchen und Felder, dabei zeigen sich die stärksten Fluktuationen bei Systemen, die im thermischen Verhalten einen Phasenübergang erster Ordnung zeigen, statt wie klassisch angenommen mit zweiter Ordnung. Ein weiteres Phänomen war die Bildung von lokalen Blasen, in denen kalte Quarks kondensierten und über lange Zeiträume stabil gefangen blieben.

In dieser Arbeit konnte die Wirkung von Nichtsgleichgewichtseffekte auf das Verhalten des linearen σ-Modells und dessen chiralen Phasenübergang untersucht werden. Diese Effekte sind allerdings so stark, dass sich in hochdynamischen Systemen wie die Expansion eines Feuerballs keine eindeutigen Signaturen für die Unterscheidung zwischen den verschiedenen möglichen Ordnungen im chiralen Phasenübergangs finden ließen.

E.3 Das Teilchen-Welle Verfahren

Neben den physikalischen Fragestellung zum chiralen Phasenübergang hat sich diese Arbeit auch mit einem numerischen Fragen beschäftigt. Um Wechselwirkungen zwischen Quarks und den chiralen Feldern in der Simulation zu behandeln, musste dafür eion neues numerisches Verfahren entwickelt werden. Teilchen und Wellen haben eine unterschiedliche mathematische Beschreibung, die eine direkte Zuordnung deren Eigenschaften nicht möglich machen, eine Wechselwirkung muss daher immer zusätzlich mathematisch und physikalisch modelliert werden. Bekannte Verfahren wie die Vlasov-Gleichung koppeln Felder und Teilchen über kontinuierliche Potentiale, die Langevin-Gleichung nutzt dagegen eine stochastische und kontinuierliche Beschreibung.

Innerhalb dieser Arbeit war es aber nötig ein Verfahren zu finden, mit dem ein Quarkpaar zerstören und dessen Erhaltungsgrößen auf ein klassisches Feld in Form eines diskreten Quants übertragen lassen, Gleiches gilt für den inversen Prozess. Ein solcher Prozess ist ein diskretes Ereignis und lässt sich schwer mit kontinuierlichen Prozessen darstellen, wenn man keine statistische Mittelung über viele gleichzeitige Ereignisse durchführen möchte.

Die Lösung dieses Problems ergab sich aus der Kombination zweier einzelner Verfahren, beide sind durch den Welle-Teilchen Dualismus motiviert. Das erste Verfahren erlaubt es mit Hilfe von Gaußschen Wellenpaketen die Energie- und Impulsdichte eines Feldes beliebig zu ändern. Dabei kann sowohl eine exakte Menge an Energie und Impuls hinzugefügt oder auch entfernt werden. Diese Feldmanipulation geschieht dabei in einer räumlich beschränkten Region auf dem Feld, motiviert durch die räumlich beschränkte Reichweite einer diskreten Wechselwirkung. Interessanterweise ergeben in diesem Verfahren automatische physikalisch-mathematische Schranken, z.B. darf der übertragene Impuls nicht größer als die Übertragene Energie sein. Dieses erste Verfahren erlaubt es also Wechselwirkungen durch Energie- und Impulsänderungen darzustellen.

Das zweite Verfahren werden die möglichen Wechselwirkungen zwischen Teilchen und Feldern physikalisch motiviert und modelliert. Dabei werden aus dem Feld lokale Energie- und Impulsdichten abgeleitet, aus diesen kann eine lokale Verteilungsfunktion angenommen werden. Diese Verteilungsfunktion wird genutzt um einzelne, virtuelle Teilchen zu würfeln, die zerfallen oder wechselwirken können. Hierbei können mikroskopische Wirkungsquerschnitte genutzt werden, um Wechselwirkungswahrscheinlichkeiten zu berechnen. Im Falle einer Wechselwirkung wird der Energie- und Impulsübertrag berechnet und mit der ersten Methode auf das Feld transferiert oder entfernt.

Diese Teilchen-Welle Methode ist so generisch, dass sie nicht nur für diese Arbeit, sondern für viele mögliche numerische Simulationen angewendet werden kann.